Computational Studies of Reactivity, Selectivity, and Non-Classical Pathways in Organic and Organometallic Systems

By

WENTAO GUO

DISSERTATION

Submitted in partial satisfaction of the requirements for the degree of

DOCTOR OF PHILOSOPHY

in

Chemistry

in the

OFFICE OF GRADUATE STUDIES

of the

UNIVERSITY OF CALIFORNIA

DAVIS

Approved:

---

Dean J. Tantillo, Chair

---

Lee-Ping Wang

---

Alexie A. Stuchebrukov

Committee in Charge

2024

Dedicated to my family (Huanhuan Tang, Zujun Guo), DJ, *Xiaoqi* and *Yuanzi*

# Contents

**Abstract**

This dissertation explores a broad spectrum of modern computational chemistry techniques to address mechanistic questions in organic reactions. It delves into the thermodynamic and kinetic aspects of these reactions while also examining the roles of dynamic effects and tunneling in influencing organometallic reaction outcomes. Key areas of focus include elucidating reaction mechanisms from kinetic, thermodynamic, and dynamic perspectives, understanding reaction pathways and the origins of selectivity, investigating byproduct formation in catalytic reactions, and developing strategies to mitigate these byproducts.

Chapter 1 introduces the physical chemistry methods used to tackle these questions, providing a concise overview of the fundamentals of computational chemistry, physical organic chemistry, and the theoretical assumptions applied to the following chapters.

The next three chapters concentrate on dirhodium-catalyzed reactions from various systems and perspectives. In Chapter 2, the project examines a previously reported lactonization reaction complicated by post-transition state bifurcation (PTSB). Here, traditional transition state theory (TST) falls short in accurately predicting product yield and selectivity. *Ab initio* molecular dynamics (AIMD) simulations offer a framework to rationalize selectivity origins, revealing the interplay between thermodynamic and dynamic preferences. The study of larger catalysts illustrates how a lowered barrier for byproduct recombination can lead to the formation of $\beta$-lactones.

Chapter 3 investigates another C-H insertion reaction that is combined with a Cope rearrangement (CHCR). A PTSB effect is proposed to be at play, leading to competing C-H insertion and CHCR products. However, further AIMD simulations reveal multiple accessible channels after the transition state, resulting in byproducts that cannot revert to either CH or CHCR products. An analysis of vibrational modes uncovers a "dynamic mismatching" effect, where the reaction is driven away from producing a downhill product and instead becomes trapped in flat energy regions, ultimately leading to byproduct formation.

Chapter 4 presents a study on a C-C activation reaction forming cyclopropanation products and dimerized byproducts. This chapter specifically focuses on a mixed-ligand dirhodium catalyst where one acetate ligand is replaced with a PhTCB group. This tethered, axially coordinated ligand system (TACLS) has been reported to enhance selectivity toward the desired product but lacks a detailed mechanistic study. The mixed-ligand design allows for the dissociation of the PhTCB ligand to form either a stabilizing $\pi - \pi$ stacking interaction with the substrate in a unique three-benzene sandwich structure, or a free ylide as a key intermediate. A comprehensive DFT study was employed to uncover and formulate the reaction mechanism.

Chapter 5 explores the formation and rearrangement of a non-classical carbonation – barbaralyl cation ($C_9H_9^+$). Computational studies on proposed stationary structures reveal two highly delocalized minima, one of $C_s$ symmetry and the other of $D_{3h}$ symmetry, affirmed by quantum chemistry-based NMR predictions. Partial and total rearrangement cycle was found to proceed through a $C_2$ and $C_{2v}$ symmetric transition structure. AIMD simulations initiated from the $D_{3h}$ $C_9H_9^+$ structure revealed its connection to six minima, due to the six-fold symmetry of the PES. The effects of tunneling and boron substitution on this complex reaction network were also examined.

Chapter 6 discusses heavy atom tunneling in organic synthesis. The contribution of quantum mechanical tunneling to the rates of several radical coupling reactions, which are key steps in natural product total syntheses, was computed using density functional theory. The results indicate that tunneling plays a significant role in the rates and should be considered when designing complex synthetic schemes.

**Acknowledgments**

"This is not a swan song," I reminded myself countless times throughout my Ph.D. journey, especially during moments when the end seemed unreachable. Often, I found myself raising the bar, pushing my limits when things felt too smooth or when I craved more intensity. This self-imposed pressure sometimes led to tears and burnout, but I have no regrets about the decisions I've made along the way. I am proud of the strength I've shown, and I am deeply grateful to the people who have supported me – it's their unwavering encouragement that has helped me grow stronger over time.

First and foremost, I want to express my heartfelt thanks to my PI, Professor Dean Tantillo. He introduced me to the fascinating world of physical organic chemistry through his exceptional CHE 233 class. As the PI in our research group, Dean has always been open-minded and supportive, offering encouragement during our discussions about my research projects. He has empowered me to explore topics that genuinely interest me, reminding me that I have the right to pursue my own path. Beyond being an inspiring mentor, Dean is a caring friend who has listened to my frustrations and provided valuable insights – not just about being a student or researcher, but about navigating life as a Ph.D. and scientist. His guidance has been invaluable, and I am truly thankful for his presence in my academic and personal journey.

I would also like to extend my thanks to my collaborators: Prof. Regan Thomson (Northwestern University), Prof. Jared Shaw (UC Davis), Jingyang Zhang (Tsinghua University), Neha Jha and Prof. Manmohan Kapur (Indian Institute of Science Education and Research Bhopal), Andrew Mitchell (Illinois State University), Andre Sanchez and Prof. Thomas Maimone (UC Berkeley), Myriam Mikhael and Prof. Sarah E Wengryniuk (Temple University). Their collaboration and insights have significantly contributed to my research, and I am truly grateful for the opportunity to work with them.

In addition, I want to acknowledge the support I received from many professors. I am especially grateful to Prof. Lee-Ping Wang and Prof. Alexei Stuchebrukhov, who served

on my dissertation committee, as well as to my QE committee members, Prof. Dylan Murray and Prof. Roland Faller. Their knowledge, discussions, and suggestions provided the foundation and inspiration I needed to complete my Ph.D. Outside my Ph.D. program, I would like to extend special thanks to Prof. Duncan Temple Lang, Prof. Jie Peng, and Prof. Miles Lopes from the Statistics department. They encouraged me to pursue a double MS in statistics and guided me on my path to data science. Their mentorship expanded my knowledge base and helped me integrate data engineering and data science tools into my computational chemistry research.

Last, but certainly not least, I want to thank my parents, Huanhuan Tang and Zujun Guo, my partner Dongjie Chen, and my friend Yushi Gao, for their support throughout my life and Ph.D. journey. Their emotional support has been the cornerstone of my resilience. I also extend my gratitude to *Xiaoqi*, *Yuanzi*, Xiaohei, Guigui, Xiaoguai, and Tuanzi, who have been my source of joy and comfort during the toughest times. Moreover, I appreciate the support from the people I met at DP Technology Company, especially the HAL9K group, where I had a great summer internship with individuals who are passionate about the future of AI in science.

## Publication List

(1) **Guo, Wentao**, W.-Y. Kong and D. Tantillo, "Revisiting a Classic Carbocation–DFT, Coupled-Cluster, and ab initio Molecular Dynamics Computations on Barbaralyl Cation Formation and Rearrangements", *Chemical Science*, 2024, Accepted

(2) **Guo, Wentao**, E. Robinson, R. Thomson, and D. Tantillo, "Heavy Atom Quantum Mechanical Tunneling in Total Synthesis", *Organic Letters*, 2024, 26, 22, 4606–4609

(3) **Guo, Wentao** and D. J. Tantillo, "Running Wild Through Dirhodium Tetracarboxylate-Catalyzed Combined CH(C)-Functionalization/Cope Rearrangement Landscapes: Does Post-Transition-State Dynamic Mismatching Influence Product Distributions?" *Journal of the American Chemical Society*, 2024, 146, 10, 7039–7051

(4) S. Banjare, S. Afreen, W.-Y. Kong, **Guo, Wentao**, et al., "Cobalt-Catalyzed Deacylative Ipso-C-C Bond Functionalization: An Approach Towards Indole-Acylolins and Its Photophysical Studies", *Journal of Organic Chemistry*, 2024, 89, 13, 9187–9197

(5) Z. Feng, **Guo, Wentao**, W.-Y. Kong, et al., "Analogies between Photochemical Reactions and Ground State Reactions with Post-Transition State Bifurcations – Prospects for Rational Design", *Nature Chemistry*, 2024

(6) F. Wang, **Guo, Wentao**, M. Cheng, S. Yuan, H. Xu, and Z. Gao, "Mmpolymer: A Multimodal Multitask Pretraining Framework for Polymer Property Prediction", *Proceedings of the 30th ACM International Conference on Information & Knowledge Management*, 2024

(7) L. Yao, **Guo, Wentao**, Z. Wang,, et al., "Node-Aligned Graph-to-Graph: Elevating Template-Free Deep Learning Approaches in Single-Step Retrosynthesis", *JACS Au*, 2024, 4, 3, 992–1003.

(8) J. Zhang, W.-Y. Kong, **Guo, Wentao**, et al., "Combined Computational and Experimental Study Reveals Complex Mechanistic Landscape of Bronsted Acid-catalyzed Silane-dependent P=O Reduction," *Journal of the American Chemical Society*, 2024, 146, 20, 13983–13999

(9) S. N. Angles, **Guo, Wentao**, K. Darko, et al., "Net Intermolecular Silyloxypryrone-Based (5+2) Cycloadditions Utilizing Amides as Enabling and Cleavable Tethers", *Organic Letters*, vol. 25, no. 39, pp. 7137–7141, 2023.

(10) N. Jha, **Guo, Wentao**, W.-Y. Kong, D. J. Tantillo, and M. Kapur, "Regiocontrol *via* Electronics: Insights into a Ru-Catalyzed, Cu-Mediated Site-Selective Alkylation of Isoquinolones *via* a C- C Bond Activation of Cyclopropanols", *Chemistry–A European Journal*, vol. 29, e202301551, 55 2023.

(11) J. P. Mancinelli, W.-Y. Kong, **Guo, Wentao**, D. J. Tantillo, and S. M. Wilkerson-Hill, "Borane-Catalyzed C–F Bond Functionalization of gem-Difluorocyclopropenes Enables the Synthesis of Orphaned Cyclopropanes", *Journal of the American Chemical Society*, vol. 145, no. 31, pp. 17389–17397, 2023.

(12) A. Sanchez, A. Gurajapu, **Guo, Wentao**, et al., "A Shapeshifting Roadmap for Polycyclic Skeletal Evolution", *Journal of the American Chemical Society*, vol. 145, pp. 13452–13461, 2023.

(13) A. T. Merrill, **Guo, Wentao**, and D. J. Tantillo, "Enabling Tools and Techniques for Organic Synthesis: A Practical Guide to Experimentation, Automation, and Computation", in Wiley, 2023, ch. NMR Prediction with Computational Chemistry, *ISBN: 9781119855644*.

(14) A. J. Youman, S. N. Rokey, J. P. Grabowski, **Guo, Wentao**, et al., "Experimental and Theoretical Investigation of the Synchronicity of Ambident Silyloxypryrone-Based (5+2) Cycloadditions", *The Journal of Organic Chemistry*, vol. 88, no. 9, pp. 5972–5981, 2023.

(15) **Guo, Wentao**, S. R. Hare, S.-S. Chen, C. M. Saunders, and D. J. Tantillo, "C–H Insertion in Dirhodium Tetracarboxylate-Catalyzed Reactions despite Dynamical Tendencies toward Fragmentation: Implications for Reaction Efficiency and Catalyst Design", *Journal of the American Chemical Society*, vol. 144, no. 37, pp. 17219–17231, 2022.

(16) S. I. Corrie, A. C. Pearce, J. P. Grabowski, K. A. Randolph, **Guo, Wentao**, et al., "Boron-Tethered Oxidopyrilium-Based [5+ 2] Cycloadditions", *Tetrahedron Letters*, vol. 107, p. 154094, 2022.

(17) T. Nanda, S. K. Banjare, W.-Y. Kong, **Guo, Wentao**, et al., "Breaking the Monotony: Cobalt and Maleimide as an Entrant to the Olefin-Mediated Ortho C–H Functionalization", *ACS Catalysis*, vol. 12, no. 19, pp. 11651–11659, 2022.

(18) Y. Li, K. Zhou, **Guo, Wentao**, and M. Cui, "$^{18}$F-Labeled 2-Phenylbenzotriazoles with Chiral Dihydroxyl Side Chains as $\beta$-Amyloid Imaging Probes", *Bioorganic & Medicinal Chemistry*, vol. 29, p. 115884, 2021.

(19) M. Mikhael, **Guo, Wentao**, D. J. Tantillo, and S. E. Wengryniuk, "Umpolung Strategy for Arene C- H Etherification Leading to Functionalized Chromanes Enabled by I (III) N-Ligated Hypervalent Iodine Reagents", *Advanced Synthesis & Catalysis*, vol. 363, no. 21, pp. 4867–4875, 2021.

(20) Y. Li, K. Wang, K. Zhou, **Guo, Wentao**, et al., "Novel D–A–D Based Near-Infrared Probes for the Detection of $\beta$-Amyloid and Tau Fibrils in Alzheimer's Disease", *Chemical Communications*, vol. 54, no. 63, pp. 8717–8720, 2018.

CHAPTER 1

# Introduction

## 1.1. Fundamental Theoretical Concepts

Computational chemistry's foundations are deeply intertwined with the history of physics, tracing back to the 19th century when the concept of molecular structures and energies was first introduced. This groundbreaking idea, primarily attributed to the pioneering work of Ludwig Boltzmann, Josiah Willard Gibbs, and Max Planck, marked a pivotal moment in the scientific understanding of physical and chemical reactions. Their contributions, along with those of many other luminaries in the history of science, laid the theoretical groundwork for explaining these reactions from a theoretical perspective. Over the subsequent decades, the field has experienced remarkable growth, driven by two primary factors: the rapid development of experimental techniques capable of capturing invisible microscopic changes and converting them into human-readable signals and data, and the dramatic boost in computational efficiency through advanced algorithms and materials. This confluence of experimental prowess and computational power has led to the steady growth and ultimate prosperity of computational chemistry as a discipline.

Though modern computational chemists stand on the shoulders of pioneers who opened doors for them, they need not master all the wisdom and knowledge inherited from history's fruits. Thanks to developers and engineers who have encapsulated complex equations and computations into software packages, the barrier to entry has been significantly lowered. However, a deep understanding of fundamental concepts still leads researchers to more profound insights and enables them to effectively pass this knowledge on to future generations of scientists. This understanding not only enhances their own work but also contributes to the continued growth and evolution of the field. Though not comprehensive, the key ideas

in physical chemistry and how they shed light on organic reactivity are briefly introduced in this section.

**1.1.1. First-Principles Methods.** Quantum mechanics (QM) forms the foundation of first-principles methods in computational chemistry. These *ab initio* approaches solve the electronic Schrödinger equation without relying on empirical parameters. Quantum mechanics postulates that observable properties can be determined through mathematical equations. [**1**]

1.1.1.1. *Schrödinger equation.* For chemists, the most crucial observable is energy ($E$), which is described by the Schrödinger equation: [**2**]

$$\hat{H}\Psi = E\Psi \tag{1.1}$$

The energy operator Hamiltonian ($\hat{H}$) consists of the kinetic (KE, $K$) and potential energy (PE, $E$). While the $\Psi$ (Psi) is the wavefunction, which contains all the information about the quantum state of the system. The Hamiltonian is written as:

$$\hat{H} = -\sum_{k} \frac{\hbar^2}{2M_k}\nabla_k^2 - \sum_{i} \frac{\hbar^2}{2m_e}\nabla_i^2 + \sum_{k<l} \frac{Z_k Z_l e^2}{r_{kl}} + \sum_{i<j} \frac{e^2}{r_{ij}} - \sum_{i,k} \frac{Z_I e^2}{r_{ik}} \tag{1.2}$$

where $i$ and $j$ refers to electrons, $k$ and $l$ for nuclei; $m_e$ is the mass of eletron; $M_k$ is the mass of nucleus $k$; $e$ is the electron charge; $Z$ is the atomic number; $r_{ab}$ refers to the distance between two particles; and $\nabla^2$ is the Laplacian operator. Note that this is a time-independent format of the Schrödinger equation. For any given system that is in a stationary state, solving this equation yields the allowed energy states ($E_i$, eigenvalue) and corresponding wavefunctions ($\Psi_i$, eigenfunction).

In computational chemistry, various approximation methods are employed to solve the Schrödinger equation for molecular systems, as exact solutions are only possible for the simplest cases such as the hydrogen atom or $H_2^+$ ion. When dealing with complex molecular

systems, the mathematical problem set of solving *just* a linear differential equation becomes intractable not only for humans but also for conventional computing methods. This is due to the exponential scaling of the problem: the number of independent variables in the equation is $3N$, where $N$ is the number of electrons in the system. As molecular size increases, this leads to a rapid escalation in computational complexity known as the "curse of dimensionality." To overcome the prohibitive computational cost, researchers have developed a range of approaches that trade some degree of accuracy for faster computations. These methods, which include variational methods, coupled cluster theory, and perturbation theory, aim to strike a balance between accuracy and computational efficiency. [**3**, **4**]

1.1.1.2. *Ab initio molecular structure.* Before diving into related methods, it is essential to first understand how wavefunctions and Hamiltonian connect to molecular structure. In quantum chemistry, Atomic Orbital (AO) and Molecular Orbital (MO) theories provide the foundation for understanding electronic structure. Atomic orbitals describe the wavefunctions of electrons in isolated atoms, indicating regions of space where electrons are likely to be found. When atoms combine to form molecules, their atomic orbitals interact and merge, forming molecular orbitals. This interaction is described by the Linear Combination of Atomic Orbitals (LCAO) method, where molecular orbitals are expressed as linear combinations of atomic orbitals:

$$\psi_i = \sum_j c_{ij}\phi_j \tag{1.3}$$

Here, $\psi_i$ is the $i$-th molecular orbital, $\phi_j$ represents the $j$-th atomic orbital, and $c_{ij}$ are coefficients that indicate the contribution of each atomic orbital to the molecular orbital. Variational Principle, a fundamental concept in quantum mechanics finds the best possible approximation of the molecular orbitals. The principle states that the trial wavefunction (in this case, the molecular orbital) should be chosen such that the expectation value of the Hamiltonian (which corresponds to the energy of the system) is minimized. Mathematically,

this is expressed as:

$$E = \frac{\langle \Psi | \hat{H} | \Psi \rangle}{\langle \Psi | \Psi \rangle} \tag{1.4}$$

where $E$ is the energy of the system, $\Psi$ is the trial wavefunction, and $\hat{H}$ is the Hamiltonian operator. By adjusting the coefficients $c_{ij}$ in the LCAO method, we can find the optimal molecular orbitals that minimize the energy, leading to a more accurate description of the electronic structure. [**5**]

One application of the LCAO method and the Variational Principle specifically for conjugated $\pi$-electron systems is Hückel Theory. [**6**] In Hückel Theory, only the $\pi$-electrons are considered, and the atomic orbitals involved are the p-orbitals perpendicular to the plane of the molecule. The resulting molecular orbitals are then used to calculate the energy levels and properties of the $\pi$-electron system.

The overall electronic wavefunction of a molecule, denoted as $\Psi$, is constructed from molecular orbitals. Specifically, $\Psi$ is represented as an antisymmetrized product of these orbitals, typically in the form of a Slater determinant. This formulation ensures compliance with the Pauli exclusion principle and is fundamental to the Hartree-Fock (HF) method, which will be discussed in detail in the next subsection:

$$\Psi(\mathbf{r}_1, \mathbf{r}_2, \ldots, \mathbf{r}_n) = \frac{1}{\sqrt{n!}} \begin{vmatrix} \psi_1(\mathbf{r}_1) & \psi_2(\mathbf{r}_1) & \cdots & \psi_n(\mathbf{r}_1) \\ \psi_1(\mathbf{r}_2) & \psi_2(\mathbf{r}_2) & \cdots & \psi_n(\mathbf{r}_2) \\ \vdots & \vdots & \ddots & \vdots \\ \psi_1(\mathbf{r}_n) & \psi_2(\mathbf{r}_n) & \cdots & \psi_n(\mathbf{r}_n) \end{vmatrix} \tag{1.5}$$

This wavefunction concept and orbital theory are central to solving the Schrödinger equation and serve as the basis for many computational chemistry methods.

On the other hand, to make the equation solvable, the Born-Oppenheimer (B-O) approximation is employed. This approximation leverages the significant difference in mass between

electrons and nuclei, where electrons are much lighter and thus move much faster than nuclei. As a result, the nuclei are treated as stationary at fixed positions during the calculation, effectively decoupling their motion from that of the electrons. This allows the wavefunction to be considered dependent only on the positions of the electrons for a given arrangement of nuclei.

For a molecule, the total Hamiltonian $\hat{H}$ can be expressed as:

$$\hat{H} = \hat{T}_e + \hat{T}_n + \hat{V}_{ee} + \hat{V}_{nn} + \hat{V}_{en} \tag{1.6}$$

The corresponding time-independent Schrödinger equation for the molecular system is:

$$\hat{H}\Psi(\mathbf{r}, \mathbf{R}) = E\Psi(\mathbf{r}, \mathbf{R}) \tag{1.7}$$

Where: $\Psi(\mathbf{r}, \mathbf{R})$ is the total wavefunction, dependent on the electronic coordinates $\mathbf{r}$ and nuclear coordinates $\mathbf{R}$. $E$ is the total energy of the system.

The B-O approximation simplifies this by assuming that the electronic wavefunction can be solved independently for fixed nuclear positions $\mathbf{R}$. The total wavefunction is then expressed as a product of electronic $\psi(\mathbf{r}; \mathbf{R})$ and nuclear $\chi(\mathbf{R})$ wavefunctions:

$$\Psi(\mathbf{r}, \mathbf{R}) = \psi(\mathbf{r}; \mathbf{R})\chi(\mathbf{R}) \tag{1.8}$$

The electronic Schrödinger equation is then:

$$\hat{H}_e\psi(\mathbf{r}; \mathbf{R}) = E_e(\mathbf{R})\psi(\mathbf{r}; \mathbf{R}) \tag{1.9}$$

Where $\hat{H}_e$ is the electronic Hamiltonian for fixed nuclear positions:

$$\hat{H}_e = \hat{T}_e + \hat{V}_{ee} + \hat{V}_{en} \tag{1.10}$$

This equation is solved for the electronic wavefunction $\psi(\mathbf{r};\mathbf{R})$ and the electronic energy $E_e(\mathbf{R})$, which depends parametrically on the nuclear positions $\mathbf{R}$.

Once $E_e(\mathbf{R})$ is known, it can be used to solve the nuclear Schrödinger equation, where the nuclei are treated as moving in the potential energy surface defined by $E_e(\mathbf{R})$:

$$\left(\hat{T}_n + E_e(\mathbf{R}) + \hat{V}_{nn}\right)\chi(\mathbf{R}) = E\chi(\mathbf{R}) \tag{1.11}$$

However, the Born-Oppenheimer (BO) approximation breaks down when the motion of electrons and nuclei in a molecule can no longer be considered completely separate, typically occurring when electronic states are very close in energy or when there is a significant coupling between electronic and nuclear motions. This is often observed in photochemistry reactions and situations involving conical intersections and surface crossings. In such cases, non-adiabatic dynamics methods are necessary to account for the coupling between electronic and nuclear motions. Computational approaches like surface hopping algorithms are employed to handle these complex situations where the B-O approximation is no longer valid. [**7**]

Besides, in many chemical systems, a single Slater determinant provides an adequate description of the electronic wavefunction. These situations, often involving near-degeneracies or strong electron correlation, require multiconfigurational methods for accurate description. [**8**] Multiconfigurational methods, such as the Complete Active Space Self-Consistent Field (CASSCF) approach, use multiple Slater determinants to represent the wavefunction. [**9**] This allows for a more flexible and accurate description of systems with complex electronic structures.

It's worth noting that while multiconfigurational methods and non-adiabatic dynamics are distinct concepts, they often appear together in the study of complex chemical systems, as many situations that require a multiconfigurational description of the wavefunction also involve a breakdown of the B-O approximation.

1.1.1.3. *HF and DFT.* Modern physical chemistry is increasingly centered around Hartree-Fock (HF), post-HF methods, and DFT. The Hartree-Fock (HF) approach is a fundamental starting point in quantum chemistry calculations, providing an approximate solution to the electronic Schrödinger equation. As described in the above section, the HF method is distinguished by its representation of the overall electronic wavefunction of a molecule using a single Slater determinant. This approach is fundamental to HF theory and sets it apart from other wavefunction-based methods. [**10**, **11**] The Self-Consistent Field (SCF) procedure iteratively refines the HF solution until convergence is achieved. While this approach captures a significant portion of the electronic energy, it neglects electron correlation beyond exchange. This limitation has led to the development of post-HF methods that use more complex wavefunction ansatzes to improve upon the HF description, including Configuration Interaction (CI), [**12**] Coupled Cluster (CC), [**4**] and Møller-Plesset perturbation theory (MP2, MP3, etc.). [**13**] These techniques incorporate electron correlation effects, leading to more accurate descriptions of molecular properties.

The most prevalent and cost-efficient method is density functional theory (DFT). Its origins can be traced to 1964 when the Hohenberg-Kohn theorems postulate that ground state properties are determined by electron density. [**14**] The following year, Kohn and Sham introduced a practical method for DFT calculations. [**15**] Subsequent decades saw the development of increasingly accurate functionals. [**16**, **17**] The essential idea of DFT is that the ground-state properties of a many-electron system can be described by its electron density $\rho(\mathbf{r})$, rather than the many-body wavefunction $\Psi(\mathbf{r}_1, \mathbf{r}_2, \ldots, \mathbf{r}_N)$, which depends on the coordinates of all $N$ electrons. The electron density is a simpler quantity, depending only on three spatial coordinates, irrespective of the number of electrons.

In the context of DFT, a *functional* is a mathematical mapping of a function (in this case, the electron density) to a scalar value, such as energy that aligns with the concept of Hamiltonian:

$$E[\rho] = T[\rho] + V_{\text{ext}}[\rho] + J[\rho] + E_{\text{xc}}[\rho] \tag{1.12}$$

Where: $T[\rho]$ is the kinetic energy functional; $V_{\text{ext}}[\rho]$ is the external potential energy functional, typically representing the interaction with nuclei; $J[\rho]$ is the Coulomb energy functional, accounting for the classical self-repulsion of a charge distribution; $E_{\text{xc}}[\rho]$ is the exchange-correlation energy functional, which includes all the complex quantum mechanical interactions not captured by the simpler terms.

Jacob's Ladder is a metaphor used in DFT to describe the hierarchy of approximations to the exchange-correlation functional term $E_{\text{xc}}[\rho]$. [**18**] As one ascends the ladder (from right to left in Figure 1.1), the approximations become more sophisticated, and the accuracy of the computed electronic structure improves. The ladder has five rungs, each representing a different level of approximation:

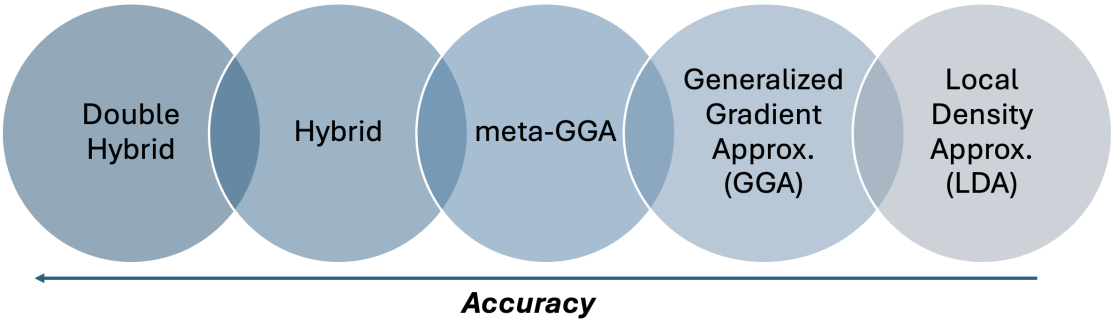


FIGURE 1.1. Jacob's ladder

(1) **Local Density Approximation (LDA):** the exchange-correlation energy is based solely on the local electron density $\rho(\mathbf{r})$.

(2) **Generalized Gradient Approximation (GGA):** incorporating the gradient of the electron density $\nabla\rho(\mathbf{r})$.

(3) **Meta-Generalized Gradient Approximation (Meta-GGA):** including the second derivative (Laplacian) of the electron density and the kinetic energy density.

(4) **Hybrid Functionals:** a mixture of exact exchange energy from Hartree-Fock theory with the exchange-correlation energy from GGA or Meta-GGA functionals.

(5) **Double Hybrid Functionals:** A perturbative treatment of electron correlation is added to the hybrid functional framework, providing the most accurate approximations available within the DFT framework.

Besides the development of Jacob's Ladder, there are other important advancements in DFT that address specific shortcomings of traditional functionals. [**19**] Among them, the treatment of dispersion interactions and the accurate description of long-range effects have been developed. Empirical dispersion corrections, such as Grimme's DFT-D methods, add pairwise atomic potentials to account for van der Waals interactions that are poorly described by standard functionals. [**20**, **21**] Range-separated functionals represent another significant development, partitioning the electron-electron interaction into short-range and long-range components. [**22**] This approach allows for the optimal combination of DFT exchange at short range with exact Hartree-Fock exchange at long range, addressing issues like the self-interaction error and improving the description of charge-transfer excitations. These developments, while not part of the original Jacob's Ladder framework, have greatly expanded the applicability and accuracy of DFT methods in computational chemistry.

The accuracy of DFT also depends on the size of the basis set. A *basis set* is a set of functions used to represent the wavefunctions of electrons in a molecule. Basis sets are often composed of atomic orbitals (such as Gaussian or Slater-type orbitals) centered on the nuclei of atoms. These orbitals serve as the building blocks for constructing molecular orbitals in DFT. Larger basis sets generally provide more accurate results but are computationally more expensive by introducing electrons in the outer shells. Though more efficient, smaller basis set may lead to basis set superposition error (BSSE): An artifact that can occur due to the incompleteness of finite basis sets, leading to an overestimation of binding energies or an underestimation of intermolecular distances.

**1.1.2. Thermo Corrections.** While quantum mechanics provides a foundation for describing molecular systems at the microscopic level, thermodynamics bridges the gap between these molecular-scale phenomena and observable, macroscopic properties. Temperature, in

particular, plays a pivotal role in determining the behavior of chemical systems, influencing reaction rates, equilibrium constants, and the distribution of molecular conformations. In computational chemistry, statistical mechanics provides the theoretical framework to connect microscopic properties calculated from quantum mechanical methods to macroscopic thermodynamic observables.

The bridges between the microscopic and macroscopic worlds are partition functions and free energy calculations. Partition functions ($Q$) are fundamental quantities in statistical mechanics that encapsulate the statistical properties of a system in thermodynamic equilibrium. They are defined as:

$$Q = \sum_i g_i e^{-E_i/kT} \tag{1.13}$$

where $g_i$ is the degeneracy of energy level $E_i$, $k$ is the Boltzmann constant, and $T$ is the temperature. Partition functions allow us to calculate various thermodynamic properties, including internal energy, entropy, and free energy.

In DFT methods, the molecule's geometry is first optimized to find a stationary point on the potential energy surface where the energy gradient is zero. The nature of this stationary point is determined by the eigenvalues of the Hessian matrix (second derivatives of energy with respect to coordinates). If all eigenvalues are positive, the structure is a local minimum; if there is exactly one negative eigenvalue, it represents a first-order saddle point (transition state, TS). The frequency calculation also provides vibrational frequencies and zero-point vibrational energies (ZPVE). Additionally, this calculation enables the computation of translational, rotational, and vibrational partition functions.

The final corrected Gibbs free energy ($G$) is obtained by combining enthalpy ($H$) and entropy ($S$) according to $G = H - TS$, where T is temperature. These thermodynamic corrections are typically calculated at standard temperature (298.15 K) and pressure (1 atm). The harmonic oscillator approximation is employed for vibrational modes, which can introduce

errors for low-frequency modes. For more complex systems or processes involving multiple conformations or states, molecular dynamics (MD) simulations offer a powerful alternative approach to free energy calculations. These MD-based methods are introduced in the next subsection.

**1.1.3. MD simulation.** Molecular Dynamics (MD) simulation is a powerful computational technique used to study the physical movements of atoms and molecules in real time. Rather than treating the molecule as a stationary structure on the potential energy surface, MD simulation acknowledges the reality that atomic and molecular motions are continuous and dynamic, occurring at timescales too fast to observe. MD simulations are based on classical mechanics, typically using Newton's equations of motion:

$$\mathbf{F}_i = m_i \mathbf{a}_i = m_i \frac{d^2 \mathbf{r}_i}{dt^2} \tag{1.14}$$

where $\mathbf{F}_i$ is the force acting on particle $i$, $m_i$ is its mass, $\mathbf{a}_i$ is its acceleration, and $\mathbf{r}_i$ is its position. The force on each particle is derived from a potential energy function $U(\mathbf{r}_1, \mathbf{r}_2, ..., \mathbf{r}_N)$:

$$\mathbf{F}_i = -\nabla_i U(\mathbf{r}_1, \mathbf{r}_2, ..., \mathbf{r}_N) \tag{1.15}$$

The description of potential energy may have multiple patterns. In AIMD, also known as BOMD (Born-Oppenheimer Molecular Dynamics), the force is computed *on-the-fly* as it is the first derivative of energy. Energy can also be defined based on a force field, which typically includes terms for bonded (bond stretching, angle bending, dihedral rotations) and non-bonded (van der Waals, electrostatic) interactions:

$$U = U_{\text{bond}} + U_{\text{angle}} + U_{\text{dihedral}} + U_{\text{vdW}} + U_{\text{electrostatic}} \tag{1.16}$$

To simulate the dynamics (trajectory propagation), we need to numerically integrate the equations of motion to propagate the system over time. Popular algorithms used for this purpose include: [**23**]

**Verlet Algorithm:**

$$\mathbf{r}(t+\Delta t) = 2\mathbf{r}(t) - \mathbf{r}(t-\Delta t) + \frac{\mathbf{F}(t)}{m}\Delta t^2 \tag{1.17}$$

**Leap-Frog Algorithm:**

$$\mathbf{v}\left(t+\frac{\Delta t}{2}\right) = \mathbf{v}\left(t-\frac{\Delta t}{2}\right) + \frac{\mathbf{F}(t)}{m}\Delta t \tag{1.18}$$

$$\mathbf{r}(t+\Delta t) = \mathbf{r}(t) + \mathbf{v}\left(t+\frac{\Delta t}{2}\right)\Delta t \tag{1.19}$$

**Velocity Verlet Algorithm:**

$$\mathbf{r}(t+\Delta t) = \mathbf{r}(t) + \mathbf{v}(t)\Delta t + \frac{\mathbf{F}(t)}{2m}\Delta t^2 \tag{1.20}$$

$$\mathbf{v}(t+\Delta t) = \mathbf{v}(t) + \frac{\mathbf{F}(t)+\mathbf{F}(t+\Delta t)}{2m}\Delta t \tag{1.21}$$

To initiate an MD simulation, the sampling of the starting geometry and velocities is crucial for ensuring the physical and chemical relevance of the simulation. Classical sampling typically involves drawing initial conditions from a Maxwell-Boltzmann distribution at a given temperature, ensuring that the system's kinetic energy is properly initialized. *Quasi*-classical sampling can involve preparing specific vibrational states or ensuring that certain reaction coordinates have predefined properties, allowing for more targeted exploration of the system's phase space. In the following section, we will show that for specific reaction systems, *quasi*-classical AIMD is critical for rationalizing the reaction outcomes.

Two commonly used ensembles in MD simulations are the NVE Ensemble (Microcanonical Ensemble) and NVT Ensemble (Canonical Ensemble). NVE ensemble conserves the total energy (E) of the system, where the number of particles (N) and volume (V) are kept constant. It is often used to simulate isolated systems where energy exchange with the environment is negligible. NVT ensemble maintains a constant number of particles (N), volume (V), and temperature (T), allowing the system to exchange energy with a thermal bath.

For complex systems or processes, advanced free energy calculation methods, all rooted in MD simulations, provide powerful tools for exploring energy landscapes and thermodynamic properties. These MD-based approaches enable the calculation of free energy differences between states by extensively sampling the configurational space of the system. Thermodynamic Integration and Free Energy Perturbation, pioneered by Zwanzig and others, use MD simulations to gradually transform the system from one state to another, allowing for the calculation of free energy differences along the transformation path. [**24**, **25**]

For systems with high energy barriers or multiple relevant states, MD-based enhanced sampling techniques are crucial. Umbrella Sampling, which uses biasing potentials in MD simulations to sample configurations that would be rarely visited in unbiased simulations, and metadynamics, which enhances sampling by adding history-dependent biasing potentials to the MD simulation, are two prominent examples of such methods. [**26**, **27**] These approaches gradually fill energy minima and reveal the underlying free energy landscape.

By facilitating the exploration of complex free energy landscapes, these MD-based methods enable the study of rare events, reaction mechanisms, conformational changes, and phase transitions. Leveraging the power of MD simulations, these approaches provide insights into the thermodynamics and kinetics of complex molecular systems that would be inaccessible through traditional experimental or computational methods.

## 1.2. Organic Reactivity and Kinetics

**1.2.1. Reaction Profile.** Every chemical reaction, when broken down into elementary steps, can be explained by a sequence of energy changes associated with chemical transformations (bond breaking/formation). The energies obtained from computational chemistry calculations can be used to construct a detailed reaction profile, providing valuable insights into the reaction mechanism and energetics (Figure 1.2).

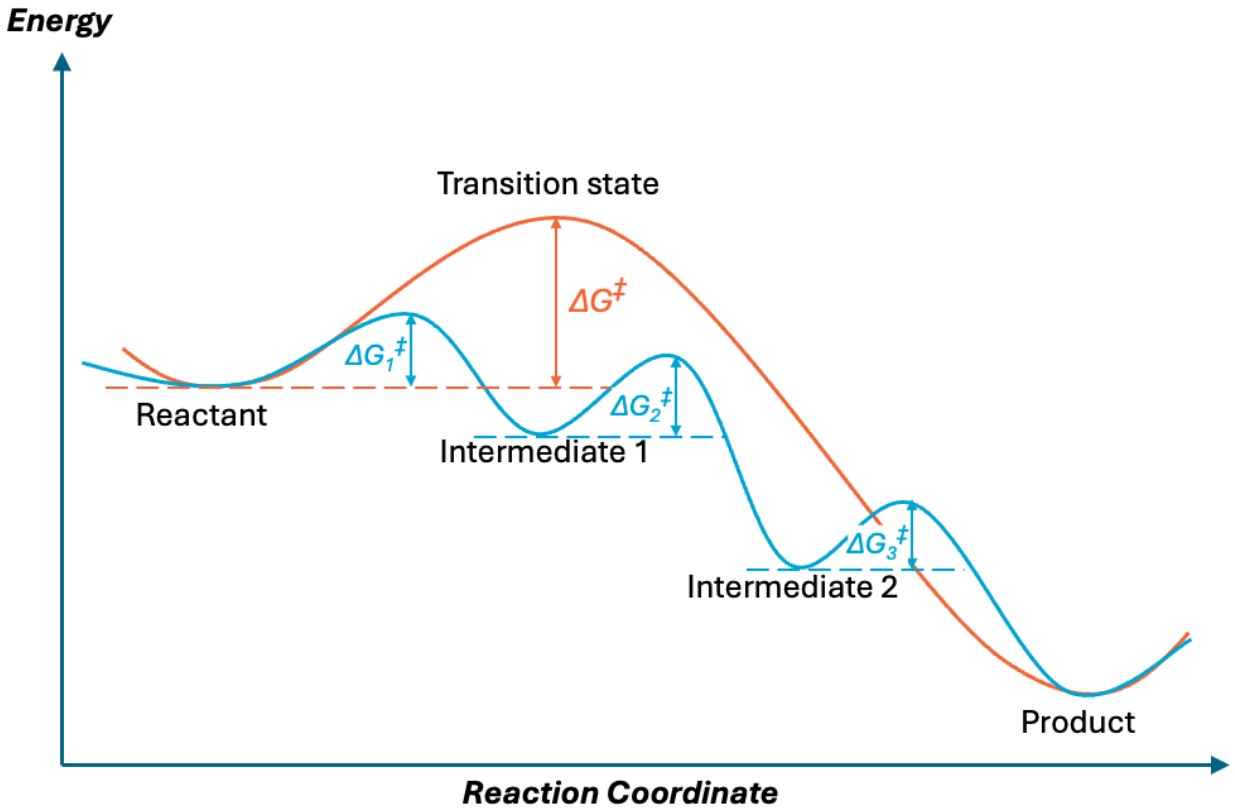


FIGURE 1.2. Reaction profile (in terms of Gibbs free energy) of two reaction pathways that connect reactant and product through one or multiple TS.

To construct a reaction profile, a reaction coordinate representing the structural changes is defined as the x-axis, while energy (typically potential energy or Gibbs free energy) is plotted on the y-axis. Computational methods identify and characterize stationary points along this reaction coordinate, including reactants, products, transition states, and intermediates. The computed energies reveal crucial information about the reaction:

(1) Activation barrier (here, in terms of Gibbs free energy) ($\Delta G^{\ddagger} = G_{\mathrm{TS}} - G_{\mathrm{R}}$): Related to the reaction rate, indicating how quickly reactants transform into products.

(2) Reaction energy ($\Delta G_{\mathrm{rxn}} = G_{\mathrm{P}} - G_{\mathrm{R}}$): Determines the equilibrium constant and overall thermodynamic favorability of the reaction.

(3) Intermediate stabilities: Provides insights into the reaction mechanism and potential rate-limiting steps.

While the PES is often visualized as a three-dimensional plot for human readability, it's important to note that the total degrees of freedom for a molecule with $N$ atoms is $3N - 6$ (or $3N - 5$ for linear molecules). To illustrate the reaction process effectively, the hyperdimensional surface is typically projected onto a lower-dimensional space, often using:

(1) One or two key geometric parameters (e.g., bond distances or angles)

(2) Mass-weighted collective variables

(3) Principal component analysis (PCA) of atomic motions

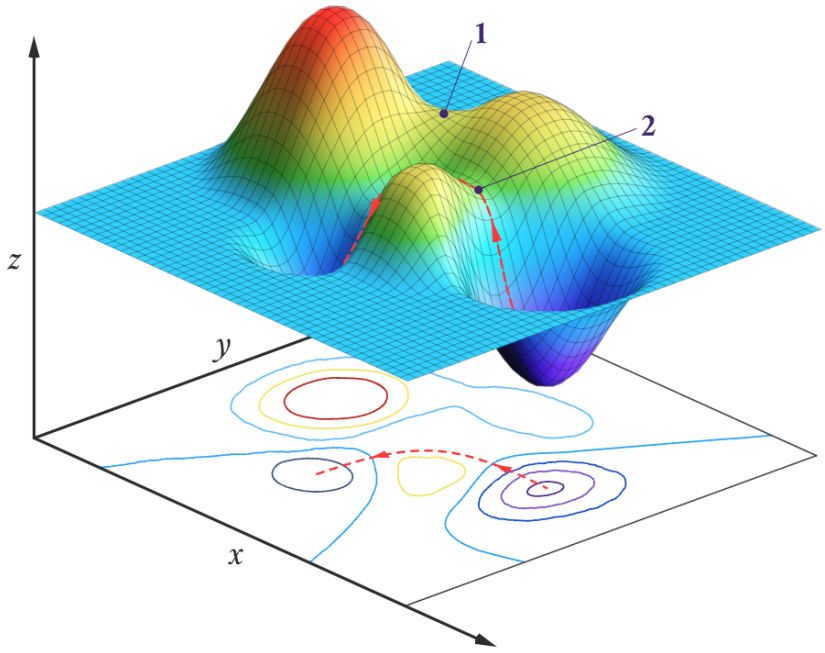


FIGURE 1.3. A 2D contour map and corresponding 3D PES. the IRC is labeled as a red dash line. (CC BY-NC; Ümit Kaya *via* LibreTexts)

Another common approach is intrinsic reaction coordinate (IRC) calculations, which provide a more complete picture of the minimum energy path (MEP) connecting reactants, transition states, and products in this high-dimensional space. [**28**, **29**]

**1.2.2. Transition State Theory and Kinetics.** Transition State Theory (TST) provides a framework for understanding and predicting reaction rates based on the properties of reactants and the transition state. The central postulate of TST is the existence of the equilibrium between reactants and the transition state.

The rate constant $k$ for a reaction according to TST is given by:

$$k = \kappa \frac{k_B T}{h} \exp\left(-\frac{\Delta G^{\ddagger}}{RT}\right) \tag{1.22}$$

where $\kappa$ is the transmission coefficient (often assumed to be 1); $k_B$ is Boltzmann's constant; $T$ is the absolute temperature; $h$ is Planck's constant; $\Delta G^{\ddagger}$ is the Gibbs free energy of activation; $R$ is the gas constant. The exponential term represents the probability of forming the transition state, while the pre-exponential factor ($\frac{k_B T}{h}$) represents the frequency of attempts to cross the barrier.

TST defines how kinetic effects control the outcome of a reaction - when two barriers are in front of the reactant, it more likely passes the lower one, leading to a kinetically favored product in a limited time. Selectivity refers to the preferential formation of one product over others in a chemical reaction and it is a crucial concept in organic synthesis and catalysis. There are several types of selectivity, such as Chemoselectivity (preference for reaction at one functional group over others); Regioselectivity (preference for one direction of chemical bond making or breaking over other directions); and Stereoselectivity (preference for forming one stereoisomer over another).

TST provides a theoretical basis for understanding and predicting selectivity. The relative rates of competing reaction pathways determine the product distribution. According to TST, the ratio of rate constants for two competing pathways A and B is:

$$\frac{k_A}{k_B} = \exp\left(-\frac{\Delta\Delta G^{\ddagger}}{RT}\right) \tag{1.23}$$

where $\Delta\Delta G^{\ddagger}$ is the difference in activation-free energies between pathways A and B. Note that we assume the reversing barrier is high – the selectivity is only kinetically controlled. This relationship allows us to predict yield and selectivity based on computed activation energies. For example, at room temperature (298.15 K), a difference of 1.4 kcal/mol in $\Delta G^{\ddagger}$ leads to a 10:1 product ratio. It is important to note that this 1.4 kcal/mol difference is comparable to the error margin of current widely adopted DFT methods. This similarity in magnitude indicates that achieving an excellent match between experimentally observed product ratios and DFT predictions is challenging. Consequently, computational chemists are often more confident in predicting whether selectivity exists rather than precisely determining the ratio between two competing products. This limitation underscores the importance of interpreting computational results within the context of their inherent uncertainties and emphasizes the need for experimental validation of theoretical predictions.

## 1.3. Beyond Transition State Theory

Though TST is a powerful theoretical model for reactivity explanation, it's important to note that factors such as solvent effects, non-statistical dynamic effects, entropy, and quantum mechanic effects can complicate the picture.

**1.3.1. Solvent Effect.** Most chemical reactions occur in solution rather than in vacuum or gas phase. In computational chemistry simulations, two primary approaches are used to incorporate solvent effects on the solute: implicit and explicit solvation models. The fundamental difference between these approaches lies in the level of detail at which the solvent molecules are described.

In explicit solvation models, each solvent molecule is represented at an atomic or molecular level, with individual interactions between solute, solvent, and other solvent molecules explicitly considered. This approach allows for a more accurate representation of solvent-solute interactions, such as hydrogen bonding, $\pi - \pi$ stacking, and the formation of solvent shells around the solute (cage effect) [**30**]. Explicit models can capture dynamic effects, local inhomogeneities, and specific interactions that are crucial for certain phenomena like proton transfer or conformational changes [**31**, **32**].

In contrast, implicit solvation models treat the solvent as a continuous medium, approximating its effects through an electrostatic potential that surrounds the solute. [**33**] This continuum representation of the solvent reduces the complexity of the system by eliminating the need to model individual solvent molecules explicitly. While implicit models may not capture specific solvent-solute interactions with the same level of detail as explicit models, they can still provide a good approximation of the overall solvent effects on molecular properties and energetics. Popular implicit models include the Polarizable Continuum Model (PCM), the Conductor-like Screening Model (COSMO) and Universal Solvation Model Based on Solute Electron Density (SMD). [**34**, **35**, **36**]

To balance accuracy and computational efficiency, hybrid solvation models combining explicit and implicit solvation have been developed. These mixed models typically involve

explicit treatment of a limited number of solvent molecules. [**37**] By selectively incorporating explicit solvent molecules in critical regions, such as those involved in key interactions or reactive sites, hybrid models aim to capture important solvent effects while maintaining computational feasibility. An example of a hybrid approach is the QM/MM method, where the solute and a few solvent molecules are treated quantum mechanically, while the rest of the system is described by molecular mechanics. [**38**, **39**]

The solvent impact on reactions is complicated, for example, polar solvents increase the rate of SN2 reactions by stabilizing the charged nucleophile without excessively solvating it, effectively lowering the barrier. In extreme cases, the solvent-induced stabilization of what would be a transition state in the gas phase can transform it into a stable intermediate on the PES. This transformation can alter the reaction mechanism, shifting it from a concerted process to a stepwise [**40**, **41**]

**1.3.2. Variational Transition State Theory.** The understanding and computation of thermodynamic correction terms are critical in TST. However, the location of the transition structures (TS) based on conventional TST is typically determined on the PES rather than the free energy surface. Consequently, the saddle point identified by algorithms using DFT does not necessarily reflect the true "bottleneck" structure on the free energy surface. To address this inconsistency, variational transition state theory (VTST) refines the structure by redefining the dividing surface that separates reactants from products.

VTST incorporates a variational approach to optimize the location of the transition structure. Instead of fixing the transition state at a saddle point, VTST defines it variationally as the phase-space hypersurface that minimizes the one-way flux or maximizes the free energy of activation. This approach allows for a more accurate determination of the transition state, particularly in complex reactions where the conventional TST assumptions may not hold.

The fundamental rate constant in conventional TST can also be expressed as:

$$k_{\mathrm{TST}} = \frac{k_B T}{h} \frac{Q^{\ddagger}}{Q_{\mathrm{r}}} e^{-\frac{\Delta G^{\ddagger}}{RT}} \tag{1.24}$$

where $k_B$ is the Boltzmann constant, $T$ is the temperature, $h$ is Planck's constant, $Q^{\ddagger}$ is the partition function of the transition state, $Q_{\mathrm{r}}$ is the partition function of the reactants, and $\Delta G^{\ddagger}$ is the Gibbs free energy of activation.

In VTST, the transition state is not fixed at a specific point but is instead variationally optimized by minimizing the rate constant over possible dividing surfaces. The variational principle can be mathematically expressed as:

$$k_{\mathrm{VTST}} = \min_{s} \left( \frac{k_B T}{h} \frac{Q^{\ddagger}(s)}{Q_{\mathrm{r}}} e^{-\frac{\Delta G^{\ddagger}(s)}{RT}} \right) \tag{1.25}$$

Here, $s$ is the reaction coordinate, and the minimization is performed over all possible dividing surfaces $s$ to find the optimal one that provides the smallest rate constant. This process ensures that the chosen transition state surface corresponds to the most significant dynamical bottleneck for the reaction.

The assumptions behind VTST include the local-equilibrium assumption, which posits that species in the transition state are in equilibrium with the reactants, and the no-recrossing assumption, which asserts that any system passing through the transition state does so only once before stabilizing as reactants or products. The refinement of the TS structure offers a better geometry for starting downhill molecular dynamic simulation which minimizes the amount of recrossing trajectories. [**42**, **43**]

**1.3.3. Tunneling.** Quantum mechanical tunneling, quantified by the transmission factor $\kappa$, can be computed using *ab initio* methods and assumptions. This effect may significantly influence reaction rates, particularly at low temperatures. The tunneling correction to the rate constant is incorporated as a transmission coefficient, $\kappa(T)$, modifying the rate

expression as follows:

$$k_{\mathrm{VTST}} = \kappa(T) \min_{s} \left( \frac{k_B T}{h} \frac{Q^{\ddagger}(s)}{Q_{\mathrm{r}}} e^{-\frac{\Delta G^{\ddagger}(s)}{RT}} \right) \tag{1.26}$$

In this thesis, tunneling calculations are based on Variational Transition State Theory. This approach accounts for the quantization of motion along the reaction coordinate, incorporating both quantum mechanical tunneling and nonclassical reflection. [**44**]

For approximating the accurate quantum tunneling in reaction rate, the multidimensional tunneling VTST model includes the small-curvature tunneling (SCT), large-curvature tunneling (LCT), and zero-curvature tunneling (ZCT) approximations. Each model represents a different approach to estimating the effect of quantum tunneling on reaction rates, with SCT assuming minimal curvature along the reaction path, LCT accounting for significant curvature, and ZCT simplifying the scenario by neglecting curvature altogether. These models are employed based on the specific characteristics of the reaction under study, allowing for a more accurate representation of tunneling effects in various reaction scenarios.

**1.3.4. Non-Statistical Dynamic Effect.** Non-statistical dynamic effects fall outside the scope of TST in two primary situations:

(1) **Bifurcating Surface:** This occurs when the potential energy surface (PES) involves a non-unique channel or pairing between one TS and two minima. Specifically, this happens in the post-TS or pre-TS region where a valley-ridge inflection point leads to a bifurcation, or even trifurcation, of the surface (due to symmetry, see Chapter 5).

(2) **Non-Equilibrium Effects and Entropic Intermediates:** These effects occur when the molecule gains momentum through either an uphill or downhill process that drives or even traps it in a region away from the expected minimum on the PES. This region may correspond to an entropic hidden intermediate that is not explicitly capturable on the PES.

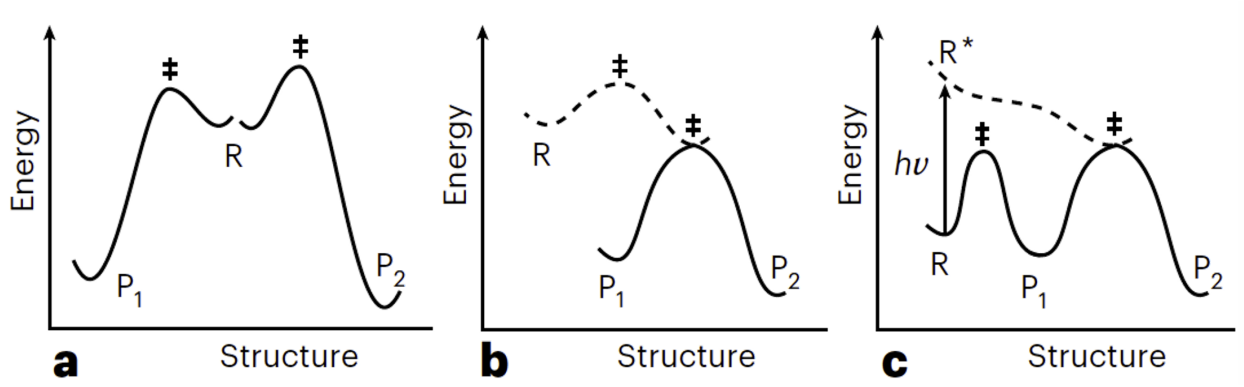


FIGURE 1.4. Energy profile of selectivity model. (a) Two separate TS correspond to P1 and P2; (b) Ground state reaction with PTSB involved; (c) photochemical reaction with group state excitation involved. [**45**]

The first case is known as post-transition state bifurcation (PTSB) and the number of reactions that have been verified with it is increasing. [**46**, **47**, **47**, **48**, **49**, **50**, **51**, **52**, **53**, **54**] In this scenario, a single *ambimodal* TS can lead to two different minima on one side of the dividing surface without encountering any intermediates. Therefore, the selectivity between two competing products is no longer determined by the energy of the TS. Reactions of this type are typically concerted but asynchronous, with an IRC that features a shoulder, indicating a platform along the reaction pathway. More technically, this corresponds to the valley-ridge inflection (VRI) area on the PES. PTSB challenges the conventional understanding of reaction mechanisms, where product distribution is usually thought to depend on the relative energies of competing TSs. Instead, in bifurcating systems, the dynamics of how the molecule navigates the PES after passing through the TS play a critical role in determining the reaction outcome. PTSB has been observed in ground-state reactions and photochemical reactions, where surface hopping from a higher energy surface to a lower one can naturally lead to a branched surface at the intersection region (Figure 1.4). [**45**] Understanding these dynamics requires detailed trajectory studies from MD simulations to capture the full complexity of the reaction pathway.

The second case, involving non-equilibrium effects and entropic traps, underscores the limitations of the equilibrium assumption in TST. In reality, kinetic energy and momentum can

cause the reaction to deviate from the expected path, leading the molecule into regions of phase space that TST cannot account for. [**55**, **56**] These regions may represent transient states or entropic intermediates that are not apparent on a static PES but can significantly influence reaction dynamics and outcomes. For example, a dynamic matching effect occurs when the momentum at the TS aligns with the direction of one PTSB product, showing a clear preference. Conversely, a mismatching effect, as introduced in Chapter 3, occurs when the momentum drives the reaction toward a byproduct or a non-IRC product. Additionally, the momentum may even cause the molecule to "fly" over shallow minima on the surface, utilizing the extra kinetic energy gained from the downhill pathway. This phenomenon is related to the timescale of intramolecular vibrational energy redistribution (IVR), which typically takes about 1 to 10 picoseconds to transfer excess energy to the environment — equilibrium takes time. [**57**]

The entropic intermediate, which can be captured by VTST, may hinder the reaction by trapping it in the intermediate region and redistributing the energy and momentum gained during the process. [**43**, **53**] In general, not only the shape of the surface but also the entropy and momentum collectively determine the non-equilibrium fate of the molecule after it overcomes the TS. In this thesis, we demonstrate that reaction outcomes are not only influenced by these factors but can also be manipulated by understanding these non-statistical dynamic effects, thereby enhancing the yield and selectivity of organic reactions.

CHAPTER 2

# C–H Insertion in Dirhodium Tetracarboxylate-catalyzed Reactions Despite Dynamical Tendencies toward Fragmentation: Implications for Reaction Efficiency and Catalyst Design

Rh-catalyzed C-H insertion reactions aimed at forming $\beta$-lactones are complicated by post-transition state bifurcations (PTSB), where identical transition states can lead to the formation of ketones, ketenes *via* fragmentation, and the desired product $\beta$-lactones. In such scenarios, traditional transition state theory (TST) fails to predict product yield and selectivity accurately. To address this, we employed *ab initio* molecular dynamics (AIMD) simulations, providing a framework to rationalize the origins of selectivity. Weak interactions between the catalyst and substrate were studied using energy decomposition and non-covalent interaction analyses which unmasked an important role of the 2-bromophenyl substituent that has been used in multiple $\beta$-lactone-forming C-H insertion reactions. Our study revealed distinct behaviors between small and large catalysts, with the latter providing a means of overcoming dynamically preferred fragmentation by lowering the barrier for recombination of the product fragments in the grip of the large catalyst active site cavity. Consequently, this work displays the risks and insufficiency of oversimplification in both mechanistic studies and catalyst design, underscoring the importance of involving non-TST computational models and complete catalyst models for understanding and predicting organometallic reaction outcomes.[1]

[1]This chapter is adapted from *J. Am. Chem. Soc.* **2022**, 144, 37, 17219–17231 [**58**, **59**], with permission. The project was initiated by Stephanie Hare and Carla Saunders, who explored the reaction mechanism. Shu-Sen Chen contributed by supporting the AIMD simulations using an ORCAdyn script, which employs ORCA for force computations instead of *Gaussian16*. While their results are not explicitly included in this thesis, their contributions are acknowledged here.

## 2.1. Introduction

A core enabling technology for C–C bond formation in the field of organometallic chemistry involves C–H insertion with metal-bound carbenes. Free carbenes typically have short lifetimes, but metal carbenes (also referred to as *metal-carbenoids*, although arguments against this terminology have been advanced), [**60**] where the two non-bonded electrons at the carbene center form a metal-carbon bond, which is accompanied by varying degrees of back-bonding from the metal that induces double bond character, can be long-lived. [**61**, **62**, **63**] Despite this perturbation from the electronic structure of a free carbene, metal carbenes still undergo many reactions typical of free carbenes, but do so in a more readily controllable manner. Chief among these are insertions – into both $\pi$-bonds (e.g., cyclopropanation) [**64**, **65**, **66**] and $\sigma$-bonds (e.g., C–H insertion, 1,2-shifts) [**67**, **68**, **69**, **70**] and ylide formation. [**71**, **72**, **73**]

Among the many transition metal catalysts for carbene reactions that have been discovered and utilized, dirhodium carboxylates (and their close relatives) are perhaps the most prominent class in the realm of synthetic organic chemistry. [**70**, **74**, **75**, **76**] Various computational studies on $Rh_2L_4$-promoted carbene reactions have been published, but many mechanistic questions remain to be answered. [**77**, **78**, **79**, **80**, **81**]

A particular facet of reactivity in need of further understanding is the role of non-statistical dynamic effects in controlling product distributions for dirhodium catalytic systems. Previously, we proposed that a post-transition state bifurcation (PTSB) is involved in $\beta$-lactone formation promoted by dirhodium tetracarboxylates that harms the yield of the desired product by opening the cryptical post-TS channel to ketene + ketone fragmentations (Scheme 2.1). [**46**]

As described in Chapter 1, reactions with PTSBs involve a single *ambimodal* transition state structure (TSS) that leads directly to two products *via* pathways that monotonically decrease in potential energy (e.g., TS1 in Scheme 2.2), i.e., no potential energy surface (PES) minima separate the ambimodal TSS from either product. In this circumstance, traditional transition

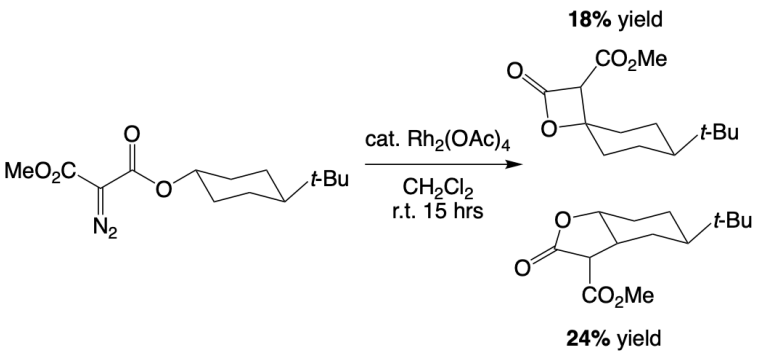


SCHEME 2.1. Previously investigated reaction with a PTSB. [**46**, **86**]

state theory (TST) cannot predict the product distribution, since both products share a transition state (dividing surface) – product selectivity must result from a non-statistical dynamic effect. [**47**, **48**, **50**, **51**, **53**, **56**, **82**, **83**] Consequently, molecular dynamics (MD) simulations initiated from the *ambimodal* TSS are typically used to reveal kinetic preferences for the formation of one product over the other, which result from the momentum possessed by reacting molecules as they pass through the transition state/dividing surface. [**84**, **85**] We argued that the PTSB for the reaction shown in Scheme 2.1 allows leakage to side products, thereby reducing the yields of desired $\beta$-lactones (Scheme 2.2). [**86**] Consistent with this model, experimental evidence for the fragmentation products we predict would arise *via* the PTSB was reported. This example shows how failing to detect a PTSB can preclude rational reduction of unwanted side products.

## 2.2. Computational Methods and Tools

**2.2.1. Structure Optimization.** All structure optimizations and energy calculations were performed with *Gaussian16 Rev. C.01.* [**87**] Density functional theory (DFT) optimizations were carried out using B3LYP-D3(0) and a mixed basis set consisting of 6-31G(d) for C, H, O, and Br and LANL2DZ for Rh. [**20**, **88**, **89**, **90**, **91**, **92**, **93**, **94**] Single point energy calculations were performed based on optimized structures using M06/6-311G(d,p)+LANL2DZ and B3LYP-D3(0)/6-311g(d,p). [**95**, **96**] These and similar combinations have been used

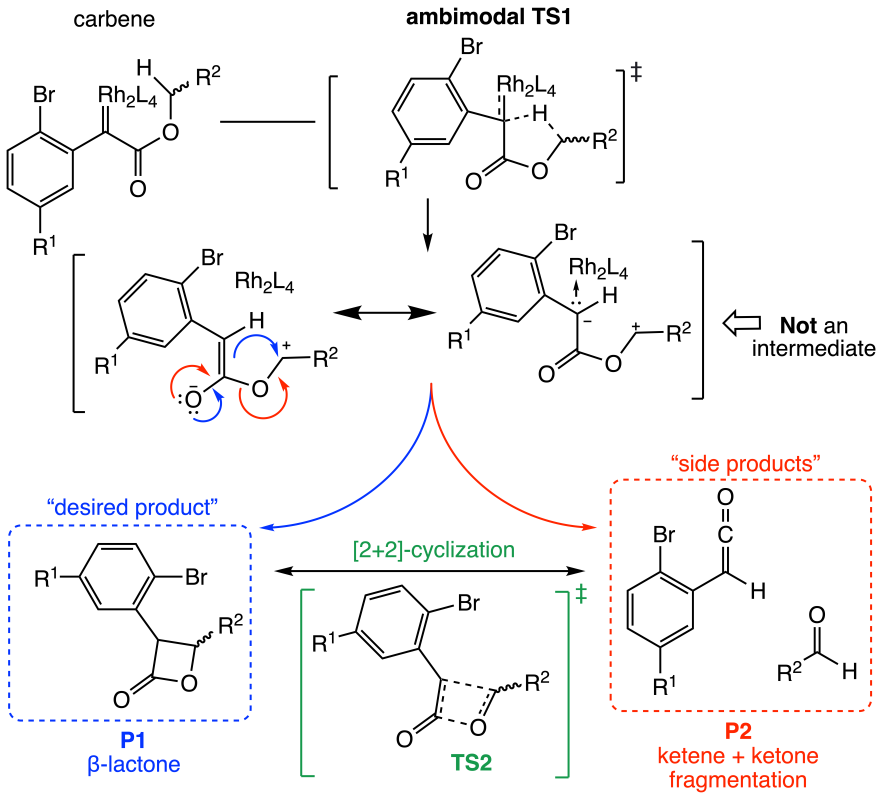


SCHEME 2.2. PTSB involved in $\beta$-lactone formation. An ambimodal transition structure (TS1), whose imaginary frequency corresponds to 1,4-H shift, precedes a PTSB that leads to both $\beta$-lactones and fragmentation products. [**46**]

previously to successfully describe related reactions. [**91**, **97**, **98**, **99**, **100**] Other functional and basis set combinations were used for benchmarking, e.g., MN15 and def2-TZVP (see Appendix 7.1.1). [**101**, **102**, **103**] These tests indicated that the relatively inexpensive B3LYP-D3(0)/6-31G(d)-LANL2DZ was sufficient for our purposes. Wavefunction stability was tested for optimized stationary points and no instabilities were found. Triplet states were calculated to have much higher energies than singlets. TSSs were found to possess only one imaginary vibrational frequency and were further characterized with intrinsic reaction coordinate (IRC) analysis, which smoothly connected all stationary points along reaction pathways. [**28**, **29**, **104**]

**2.2.2. *Ab initio* MD Simulation.** *Quasi*-classical *ab initio* molecular dynamics (AIMD) trajectories were obtained using Singleton's *Progdyn* package in the NVE ensemble at 298K. [**83**] The selectivity between the formation of $\beta$-lactone and fragmentation products was determined by comparing the number of trajectories that connect Rh-carbene reactant to product minima (see Supporting Information for additional details). Tests indicated that TSSs were insufficient for running AIMD with the systems studied here, since recrossing was not minimized, i.e., variational transition states (VTSs) differed considerably from TSSs. [**44**] Consequently, we used VTSs, located using the RODS method in Polyrate/Gaussrate, to initiate our downhill MD simulations. [**105**, **106**]

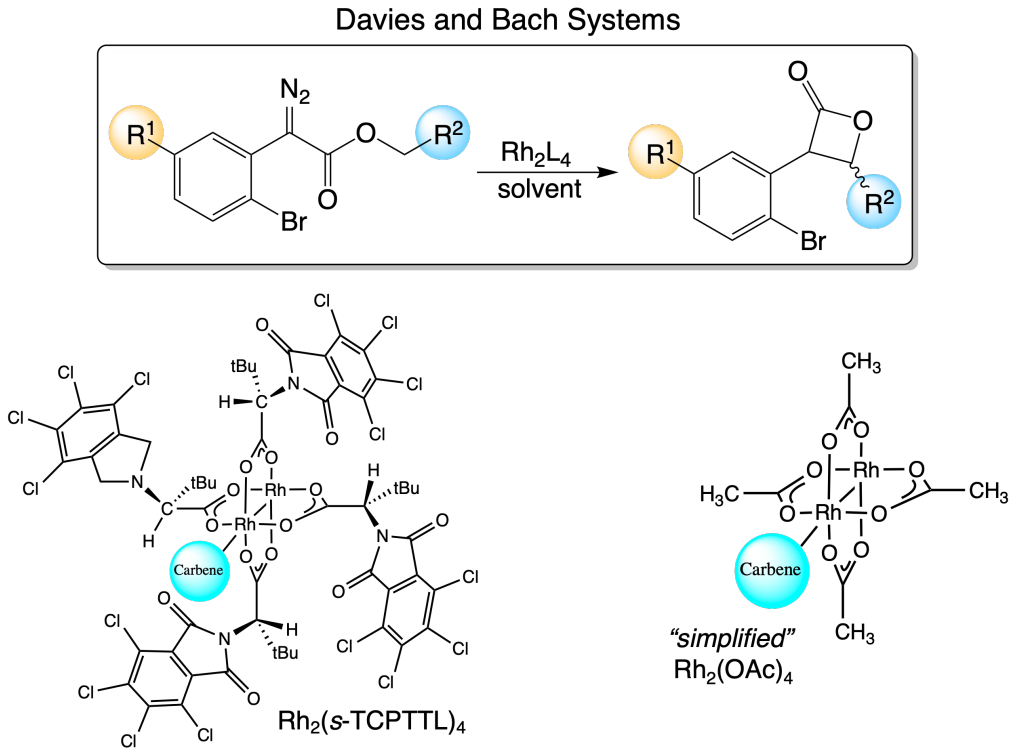


| Name | $Rh_2L_4$[a] | $Rh_2L_4$[b] | $R^{1(a)}$ | $R^{2(a)}$ | $R^{2(b)}$ | solvent[a] | yield | *cis*:*trans* |
|---|---|---|---|---|---|---|---|---|
| Davies-Me | $Rh_2$(*s*-TCPTTL)$_4$ | $Rh_2(OAc)_4$ | OMe | Me | Me | DCM | 83% | 1:8.3 |
| Davies-Ph | $Rh_2$(*s*-TCPTTL)$_4$ | $Rh_2(OAc)_4$ | OMe | Ph | Ph | DCM | 72% | >19:1 |
| Bach-*i*Pr | $Rh_2(OAc)_4$ | $Rh_2(OAc)_4$ | H | *i*Pr | *i*Pr | PhH | 43% | 1:24 |
| Bach-ethyl | $Rh_2(OAc)_4$ | $Rh_2(OAc)_4$ | H | *n*Pr | eth | PhH | 66% | 1:7.3 |

FIGURE 2.1. Summary of experimental reactions studied in this work. [a]Catalysts and substrate in experiment. [b]Simplified model in computational calculations.

**2.2.3. Non-Covalent Interactions.** The origins of differing reactivity were analyzed using multiple approaches. First, we employed the non-covalent interaction (NCI) methodology developed by Yang and co-workers. [**107**, **108**] NCI analysis characterizes weak interactions according to electron density topology based on the reduced density gradient (RDG) on 3D cubic grids. The Laplacian of the density is used to distinguish attractive (positive value) and repulsive (negative value) interactions. In general, RDG isosurfaces are plotted and colored according to the type of interactions. In 2017, the related Independent Gradient

Model (IGM) was introduced. [**109**] In IGM analysis, intermolecular interaction regions are defined accurately, and intramolecular interactions can be shielded to allow for analysis of local interactions between fragments. We implemented both RDG and IGM analysis with the *Multiwfn* package to characterize specific regions of weak interactions. [**110**]

**2.2.4. Energy Decomposition Analysis.** In addition, the activation strain/distortion-interaction model championed by Bickelhaupt and Houk was applied to separate the energy required to distort the reactants into geometries they have in TSSs (so-called "activation strain" or "distortion energy") and the interaction energies between molecular substructures. [**111**, **112**, **113**] The origins of interaction energies were interpreted using energy decomposition analysis (EDA). [**99**] After sampling various approaches, we decided to use the second-generation ALMO-EDA, which is based on absolutely localized molecular orbitals (ALMO), as implemented in *Q-Chem 5.3*. [**114**, **115**, **116**] With this method, interaction energy is decomposed into permanent electrostatics, Pauli repulsion, dispersion, polarization, and charge transfer terms. Other EDA methods may, of course, lead to different bonding models. Detailed activation strain/distortion-interaction and EDA results can be found in the Appendix 7.1.4.

## 2.3. Analysis of Model System - Structures and IRCs

**2.3.1. Conformational Studies.** The $\beta$-lactone forming C–H insertion reactions reported by Davies and Bach shown in Figure 2.1 were studied using some simplifications. [**117**, **118**] Between the two groups, substrates containing ethyl, benzyl, neopentyl, and n-butyl groups were used. We used these groups as is, except for the n-butyl group, which was truncated to n-propyl. The Bach group's substrates included a 2-bromophenyl group, while the Davies' group's substrates also included a methoxy group *para* to the bromine. These four model substrates are named "Davies-Me", "Davies-Ph", "Bach-*i*Pr" and "Bach-ethyl", as a combination of their discoverer and substituent $R^2$. While the Bach group used $Rh_2(OAc)_4$

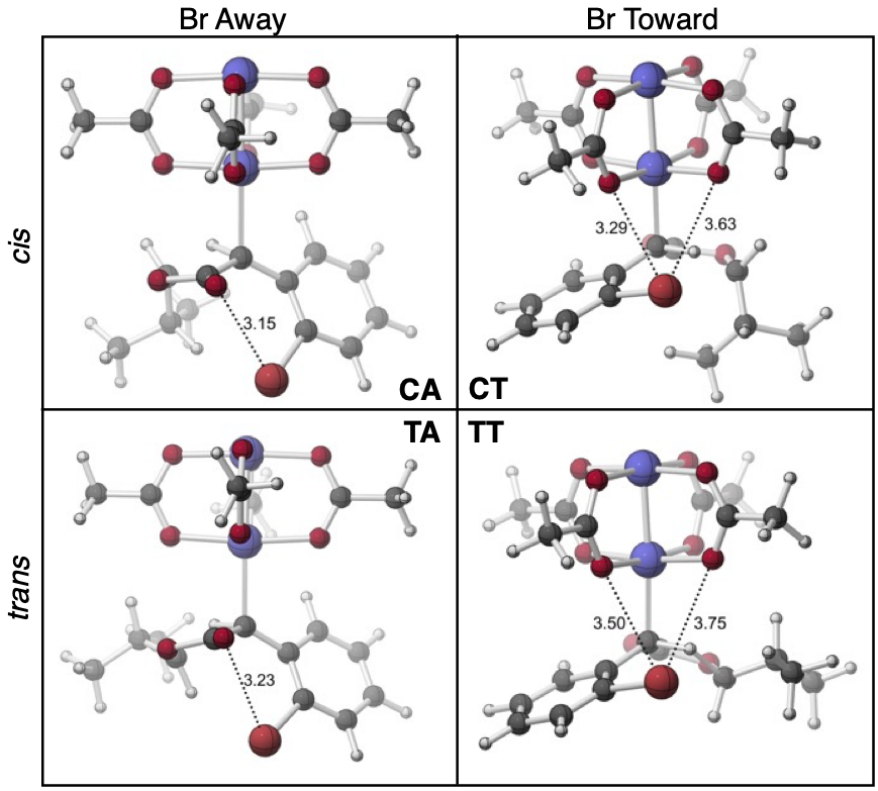


FIGURE 2.2. Four forms of the dirhodium tetraacetate carbene examined, differing in the orientation of the bromophenyl (bromine away or toward the acetates) and the orientation of the alkyl chain (whether C–H insertion will lead to a *cis* or *trans* lactone).

as the catalyst, the Davies group used $Rh_2(s\text{-TCPTTL})_4$. We used $Rh_2(OAc)_4$ for all substrates in our initial study (Figure 2.2), both for simplicity, and so we can compare differences arising solely from substrates.

For each substrate, we considered four forms of the C–H insertion TSS (shown in Figure 2.2). First, these differ in terms of which diastereotopic hydrogen transfers, i.e., whether a *cis* or *trans* $\beta$-lactone results (labeled with a C or T, respectively). Second, they differ in the conformation of the bromophenyl group, i.e., whether the bromine atom is oriented toward or away from the acetate ligands on rhodium (labeled with a T or A, respectively). We also considered methoxy group rotation in the Davies systems and alkyl group rotations in the Bach systems, but these were found to have minimal effects on our results.

| Name | *cis* | | *trans* | | *cis*:*trans* | *cis*:*trans* |
|---|---|---|---|---|---|---|
| | BrA | BrT | BrA | BrT | (exp) | (calc) |
| Davies-Me | 17.1 (17.7) | 9.5 (10.2) | 16.0 (17.0) | 8.4 (9.5) | 1:8.3 | 1:8 (1:3) |
| Davies-Ph | 13.3 (14.5) | 7.4 (8.7) | 15.6 (17.0) | 5.4 (6.8) | >19:1 | **1:29 (1:25)** |
| Bach-ipr | 17.4 (18.4) | 10.8 (11.9) | 16.2 (17.4) | 9.2 (10.8) | 1:24 | 1:15 (1:6) |
| Bach-eth | 17.2 (17.6) | 10.0 (10.4) | 16.3 (16.8) | 8.7 (8.9) | 1:7.3 | 1:9 (1:12) |

TABLE 2.1. Computed activation free energies (kcal/mol), along with predicted and experimental *cis*/*trans* product ratios for $\beta$-lactones. Geometry optimization and thermal corrections are under B3LYP-D3(0)/6-31G(d)+LANL2DZ level. Single point energies are under B3LYP-D3(0)/6-311G(d,p)+LANL2DZ and M06/6-311G(d,p)+LANL2DZ (in parentheses).

First, we discuss *cis*/*trans* selectivity. We optimized structures of Rh-carbene reactants and C–H insertion TSSs for all systems (e.g., Figure 2.3). Based on free energy barriers (Table 2.1), trans products were predicted to predominate, which matches with experimental observations for three of the four systems examined. The inconsistency between theory and experiment for the Davies-Ph system likely comes from the simplification of the catalyst in our initial computational model (*vide infra*), suggesting that the match for the other Davies system might be coincidental. Nonetheless, the large (6-10 kcal/mol) preference for TSSs with the bromine atom oriented towards the acetate groups of $Rh_2(OAc)_4$ was striking and warranted further investigation (*vide infra*).

**2.3.2. IRC Reveals Potential PTSB Effect.** Though they have similar geometries and imaginary vibrations, IRC calculations on TSs for C–H insertion did not always lead to the same types of products; for the Davies-Me system, IRCs for all four TSSs led to $\beta$-lactones, but for the other three systems, IRCs for some TSSs led to $\beta$-lactones and IRCs for others led to fragmentation products. This type of behavior is consistent with the presence of PTSBs. The gradient of energy change along these IRCs changes from high to low after the TSS, i.e., "shoulders" are observed, another behavior often found for systems with PTSBs. [**46**] We also located TSSs for interconversion of $\beta$-lactones and fragmentation

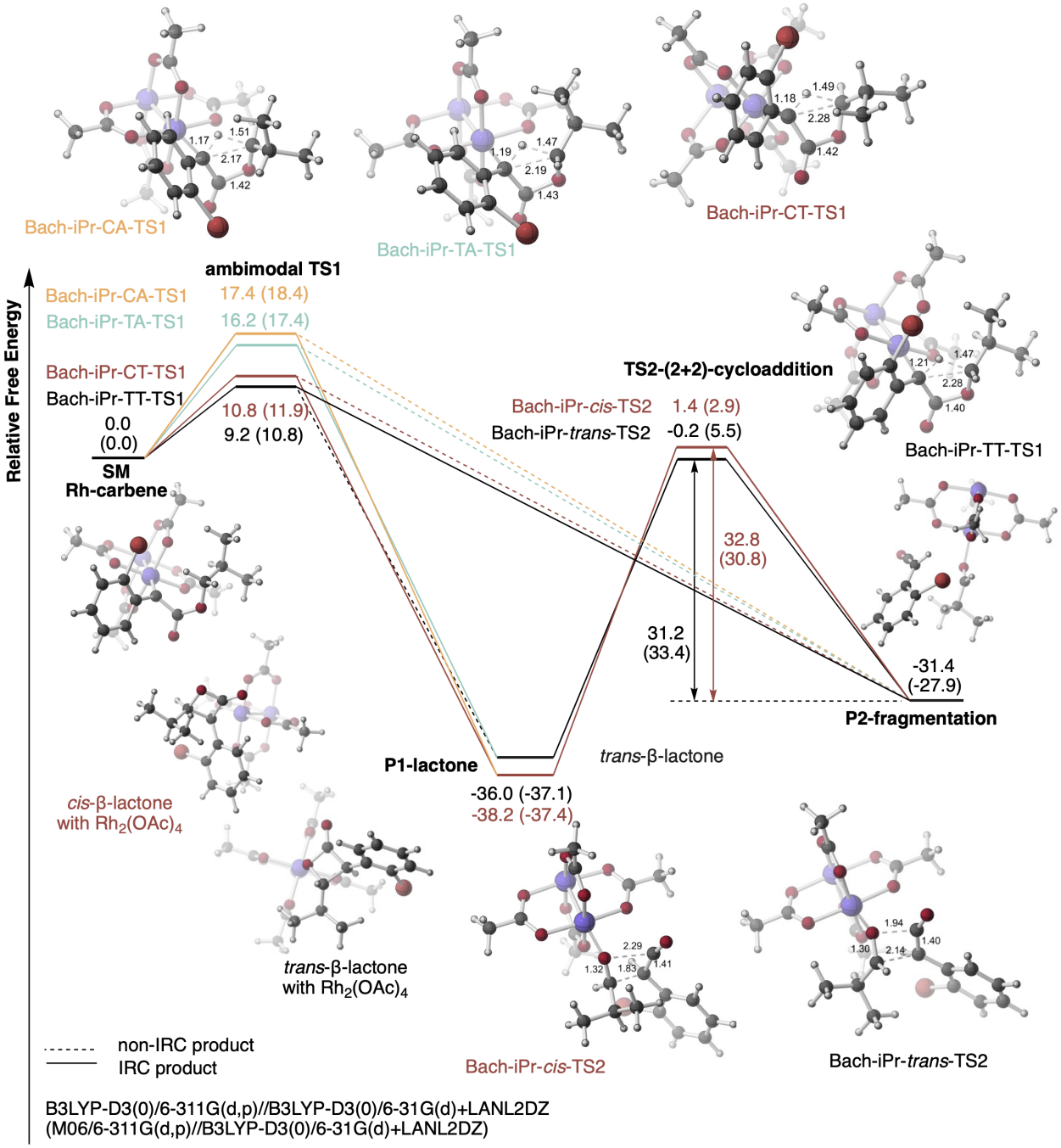


FIGURE 2.3. Computed reaction profile for $\beta$-lactone formation and fragmentation for the Bach-*i*Pr system. 3D structures were visualized with *CYLview*. [**119**] Relative energies are in kcal/mol and distances are in Å.

products (**TS2** in Scheme 2.2 and Figure 2.3). In general, these (2+2) cycloadditions are

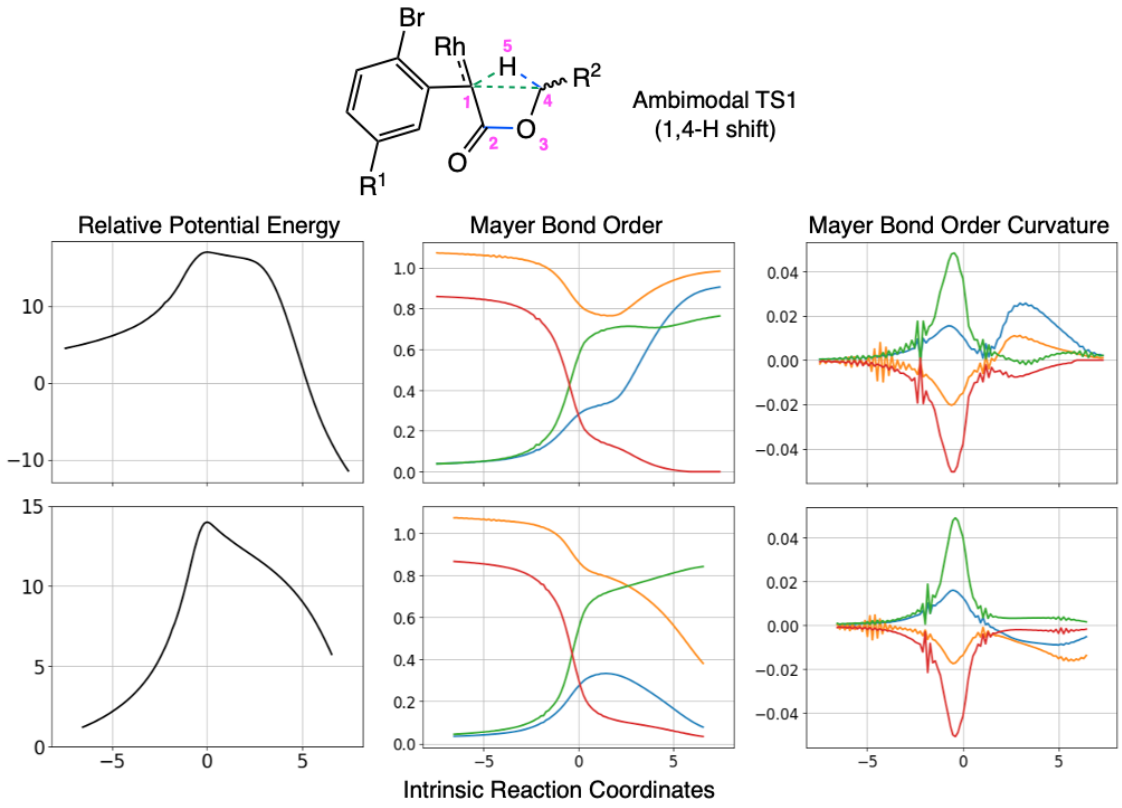


FIGURE 2.4. Bond orders along IRCs near TS1 for the Bach-*i*Pr-CT (middle) and the Bach-*i*Pr-TT (bottom) systems. Left: Relative potential energy profile along the reaction pathway. Middle: Mayer Bond order profile. Right: Mayer bond order curvature profile. Critical atoms for bond order plotting are illustrated on the top. Red: C4-H5; Orange: C2-O3; Green: C1-H5; Blue: C1-C4.

predicted to have barriers ≥30 kcal/mol for converting fragmentation products to $\beta$-lactones, suggesting that there is little hope of recovering from unwanted fragmentation.

To characterize the synchronicity of bond-making/breaking events, we computed Mayer bond orders along the IRCs. [**110**, **120**] Values for the key C–H bonds that are broken and made, as well as the C–C bond that forms if the C–H insertion completes and the C–O bond that breaks if fragmentation occurs, are shown in Figure 2.4. Naturally, as the hydrogen shifts, one C–H bond weakens as the other strengthens. These bonds have the same bond order just before the TS. For the Bach-*i*Pr-CT system, whose IRC leads to $\beta$-lactone, the C–C bond gradually increases in strength, but the "rate" of change decreases in the shoulder region of the IRC. In this same region, the bond order of the C–O bond, which does not break along

| | SM-P1 | SM-P2 | SM-SM | P-P |
|---|---|---|---|---|
| VTST | 33% | 47% | 9% | 11% |
| TST | 30% | 43% | 21% | 6% |

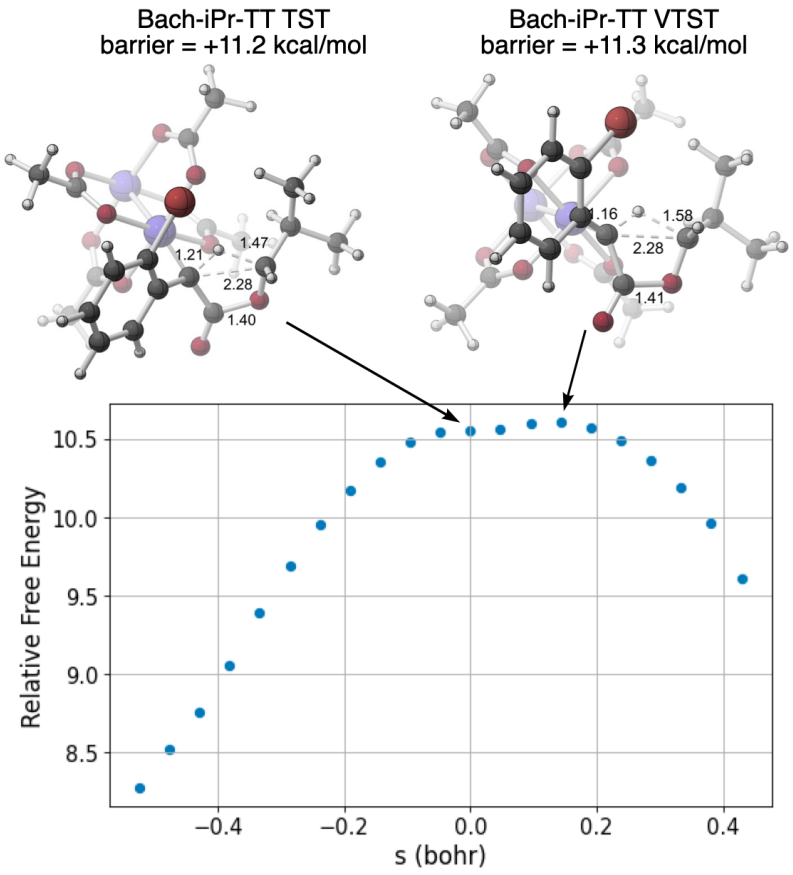


FIGURE 2.5. Comparison of TSSs (i.e., first-order stationary points on PESs) and VTSSs. Top: trajectory results. Bottom: Transition structure and variational transition structure highlighted with energies along the free energy curve.

this IRC, dips. Together, these behaviors again hint that there may be an exit from this region of the PES that leads to fragmentation. For the Bach-*i*Pr-TT system, whose IRC leads to fragmentation products, very similar behavior is observed until the shoulder region where the C–C stops forming and the C–O bond now continues on to break.

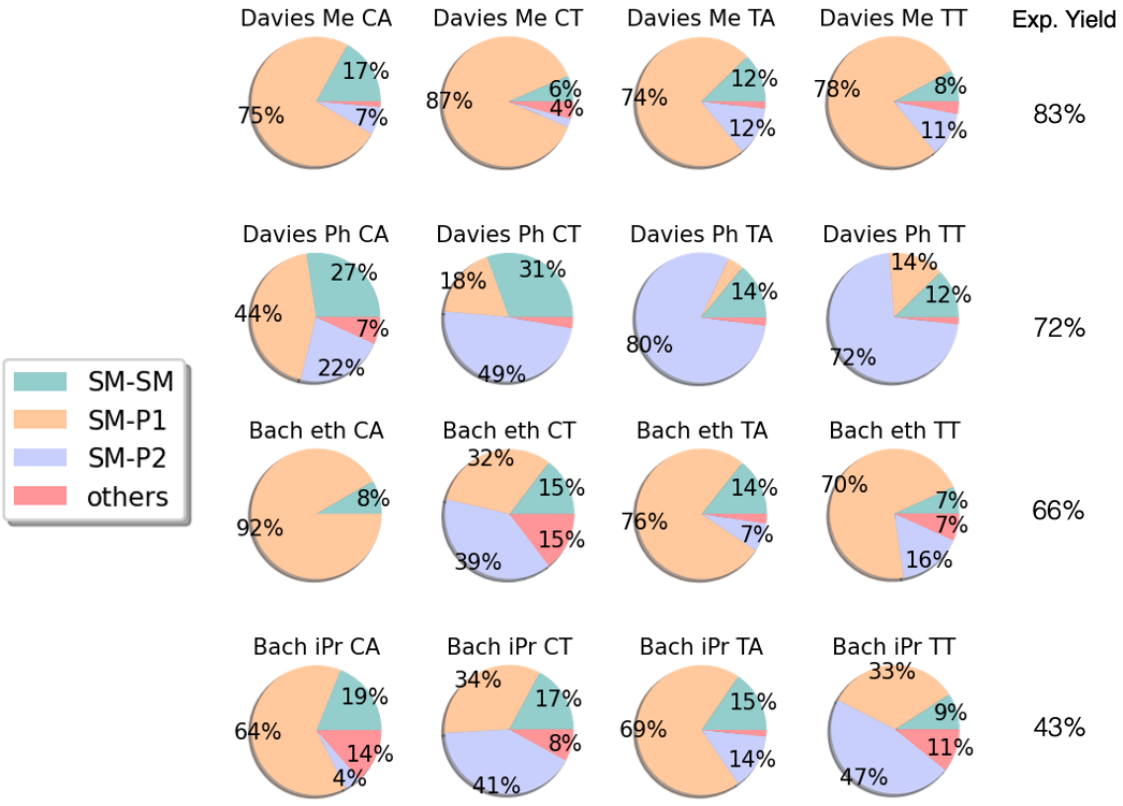


FIGURE 2.6. Distribution of products from downhill AIMD trajectories. "Exp. Yield" corresponds to yield of the $\beta$-lactone product (P1).

## 2.4. Dynamic Effect

**2.4.1. AIMD Results.** Confident that PTSBs were involved in these reactions based on our IRC-based investigations, we undertook *quasi*-classical AIMD simulations. [**85**] These were initiated from VTSs; as shown in Figure 2.5. VTSs are "later" than TSSs. The P1:P2 ratio derived from counting trajectories initiated from TSSs and VTSs is very consistent, but using the "later" VTSs decreases recrossing (SM-SM) trajectories (9% vs. 21%). [**44**, **56**] Key observations from our AIMD simulations are summarized below.

First, linear alkyl chains as C–H sources are predicted to lead to higher proportions of $\beta$-lactone (P1) products (Figure 2.6, top) compared to branched chains (Figure 2.6, bottom). This prediction is qualitatively consistent with the higher experimental yields of $\beta$-lactones reported for the Davies-Me (83%) and Bach-eth (66%) systems compared to those for the

Davies-Ph (72%) and Bach-*i*Pr (41%) systems, although reported yields are generally associated with considerable uncertainties.

Second, in most cases, the dynamically preferred product is predicted to be the IRC product, but not always. For the Davies-Ph-CT system, fragmentation is predicted by AIMD simulations to predominate, but the IRC leads to the $\beta$-lactone. However, there is uncertainty that the trajectory sampling is insufficient.

Third, for the Bach-*i*Pr system, the dynamically preferred product is predicted to differ for bromine-away and bromine-towards transition states. All four transition state conformations examined possess PTSBs, but the selectivity here arises from conformationally controlled non-statistical dynamic behavior. The conformational difference amounts to a rotation of an aryl ring of the substrate but changes the predicted major product. And, in this case, it is the two lower energy transition state conformations that have dynamical preferences for undesired side products. Identifying this effect opens the door to rationally changing substrates (or catalysts) to avoid side products that arise from PTSBs.

Fourth, the proportion of trajectories leading to fragmentation products appears to be severely overestimated for the Davies-Ph system. While this scenario could be the result of a solvent cage effect, as we have surmised previously, [**46**] that effect would be expected to be felt approximately equally for all four systems. Consequently, we suspected that the full-sized $Rh_2$(*s*-TCPTTL)$_4$ catalyst might eliminate the PTSB or utilize its bulk to dramatically modulate selectivity (*vide infra*).

**2.4.2. Conformational Preferences – the Dilemma.** In general, bromine-toward transition states face a dilemma, they are lower in energy than bromine-away transition states (kinetically favored) but have stronger dynamical tendencies to fragment. But why? Naturally, one might imagine that the energy difference between bromine-toward and bromine-away conformations arises from a favored interaction between bromine and $Rh_2(OAc)_4$This interaction somehow affects momentum during trajectories.

**2.4.3. Halogen bonding?** To look for energetically favorable (attractive) non-covalent interactions between the bromine and the $Rh_2(OAc)_4$ catalyst unit in TSs, we generated RDG plots (e.g., Figure 2.7). As a representative case, we discuss here the Bach-*i*Pr system. For the Bach-*i*Pr-TT TS, we observed an isosurface that appears to correspond to two Br$\cdots$O halogen bonds and a weak donor/acceptor interaction between Br and Rh. [**121**, **122**, **123**] The Br$\cdots$O bond distances are 3.3-3.4Å, which is in the range associated with weak halogen bond interactions. [**124**, **125**] This TS also possesses a shortened carbene-metal bond of 2.18 Å. In contrast, for the Bach-*i*Pr TA TS, bromine interacts with the adjacent ester functional group with Br$\cdots$O distances of 3.26Å, but not other heteroatoms; the C–Rh bond in the Bach-*i*Pr-TA TS is also longer at 2.29Å. Replacing the bromine with a methyl group eliminates the energy difference between the toward and away conformations (see Appendix 7.1.2), consistent with the conformational preference not being a result of a simple steric effect.

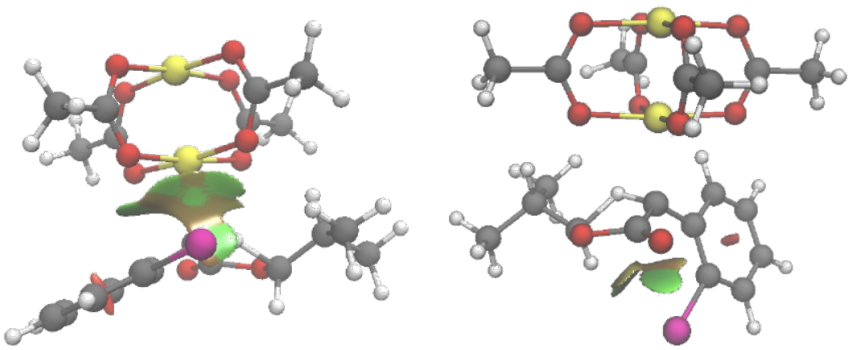

FIGURE 2.7. RDG plots for Bach-*i*Pr-TT (left) and Bach-*i*Pr-TA (right) TSs. Plotted with VMD. [**126**]

**2.4.4. When/Where Does Branching Occur?** To determine how close to the TS branching occurs, we analyzed our AIMD trajectories using geometric parameters that can distinguish reactants, *ambimodal* TSs, $\beta$-lactones (P1), and fragmentation products (P2). We chose the sum of C1–C4 and C1–H5 distances for one collective variable and the sum of C2–O3 and C1–H4 distances for the other. As a representative case, plots for the four conformations examined for the Bach-*i*Pr system are shown in Figure 2.8. The vectors connecting reactants to ambimodal TSs point in the direction of $\beta$-lactones for all four conformations,

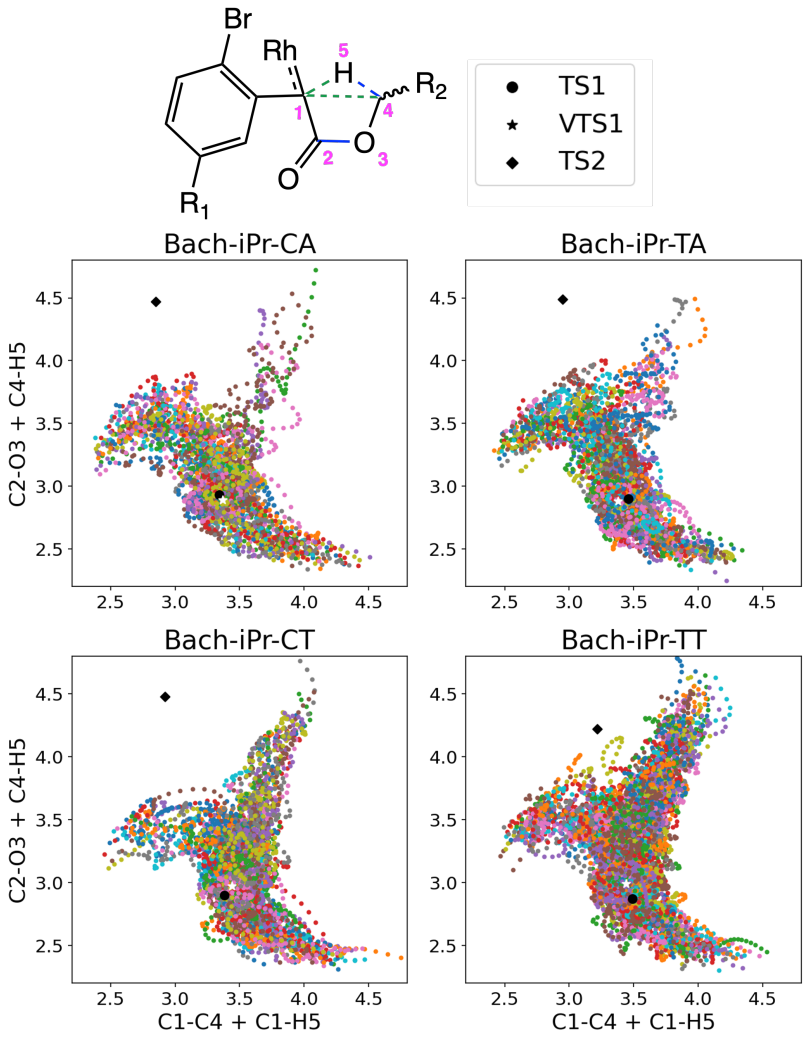


FIGURE 2.8. Plots of trajectory paths in terms of collective variables. The positions of **TS1** (black dot), **VTS1** (white star), and **TS2** (black oblique) are marked on each graph.

yet $\beta$-lactones are not the dynamically preferred products in all cases (see Figure 2.6, fourth row). The trajectories are not well-separated in the vicinity of the *ambimodal* TSs (**TS1**). Instead, they explore a fairly broad swath of that area before settling on one or the other product well. These observations are consistent with flat regions of the PESs close to the ambimodal TSs, lacking well-defined valley-ridge inflection points.

## 2.5. Construction of Potential Energy Surfaces

Studies on reactions with PTSBs have emphasized the influence of PES shape on dynamic selectivity. [**127**, **128**, **129**] However, the construction of PESs for reactions of species with many degrees of freedom has long been a difficult problem. [**130**, **131**, **132**] Here we employ a modification of the procedure recently described by Chuang et al. for the construction of 2-dimensional PESs for reactions with PTSBs. In that protocol, an "artificial reaction path" that connects the ambimodal TS to the TS for interconversion of the two product minima arising from a PTSB is constructed. While the reported procedure proved impractical to implement for the complex systems examined here, it inspired us to implement a similar but simplified (i.e., more approximate) approach.

| TS1s | | C-Rh bond length | IRC/ARC connectivity |
|---|---|---|---|
| **IRC** | **CA** | 2.32Å | SM - P1 |
| | **CT** | 2.29Å | SM - P1 |
| | **TA** | 2.29Å | SM - P1 |
| | **TT** | 2.18Å | SM - P2 |
| **ARC** | **CA'** | 2.18Å | P2 - P2 |
| | **CT' (same as CT)** | 2.29Å | SM - P2 |
| | **TA'** | 2.19Å | SM - P2 |
| | **TT'** | 2.24Å | P1 - P1 |

TABLE 2.2. C–Rh distances in ambimodal TSSs and corresponding artificial TSSs, along with products of IRCs and ARCs.

From our study of bond orders (*vide supra*), we realized that bromine-toward TSs are more likely to have IRCs that lead to fragmentation and to have stronger and shorter C–Rh bonds. [**133**] Therefore, for TSs with IRCs that lead to $\beta$-lactones, we slightly stretched the C–Rh bond and reoptimized with a fixed C–Rh distance. For TSs with IRCs that lead to fragmentation we slightly shortened the C–Rh bond and re-optimized. IRC calculations were run on the resulting "artificial" TSs (not fully optimized stationary points!) and these IRCs indeed led to the alternative products. The results of this procedure are summarized in Table 2.2. The new reaction coordinates, which we call "artificial reaction coordinates" (ARCs), accomplish our goal: providing a reasonable path to the non-IRC product arising

from an *ambimodal* TS. For some entries in Table 2.2, both sides of an ARC turned out to be the same (perhaps because the IRC calculation is initiated on the product side of the actual TS), but this is of no consequence since all we need is one half, i.e., the path from a point near the *ambimodal* TS to the non-IRC product. Then, inspired by the protocol of Chuang et al., we constructed PESs by using IRCs and ARCs as the two axes and interpolating between them (see Appendix 7.1.3).

In Figure 2.9, we present such PESs for the *ambimodal* **TS1**s of the Bach-*i*Pr system. As suggested by the data in Figure 2.8, the regions near the TSs (bottom right corner of each plot) are fairly flat. For transition state conformations for which $\beta$-lactones (**P1**) are dynamically preferred, i.e., bromine-away transition states, the post-TSS PES is tilted toward the $\beta$-lactone minimum (Figure 2.9, left), For transition state conformations for which fragmentation products (**P2**) are dynamically preferred, i.e., bromine-toward transition states, the post-TS PES is less tilted (Figure 2.9, right), and the magnitude of the selectivity predicted by AIMD simulations is not large (Figure 2.9, chart, and Figure 2.6, bottom right).

Various tools for predicting products of reactions with PTSBs based on similarities between stationary points exist. [**127**, **134**] The classic tool for doing so is Carpenter's Newton program, which compares the products to the imaginary eigenvector of the ambimodal TSS. [**135**] In the cases described here, this approach does not lead to correct predictions, e.g., for the Bach-*i*Pr-CA TS, the Newton prediction is opposite in sign and magnitude to the AIMD results (Figure 2.9 table). This observation, along with the related observation noted above, implies that ballistic behavior is not responsible here for product selectivity, i.e., the vibrational modes activated as the transition state is passed are not coupled ("matched") to those that distinguish $\beta$-lactone formation from fragmentation. This scenario makes sense here, in that the 1,4-hydrogen transfer and C–C bond formation/C–O bond cleavage events occur asynchronously (see Figure 2.4).

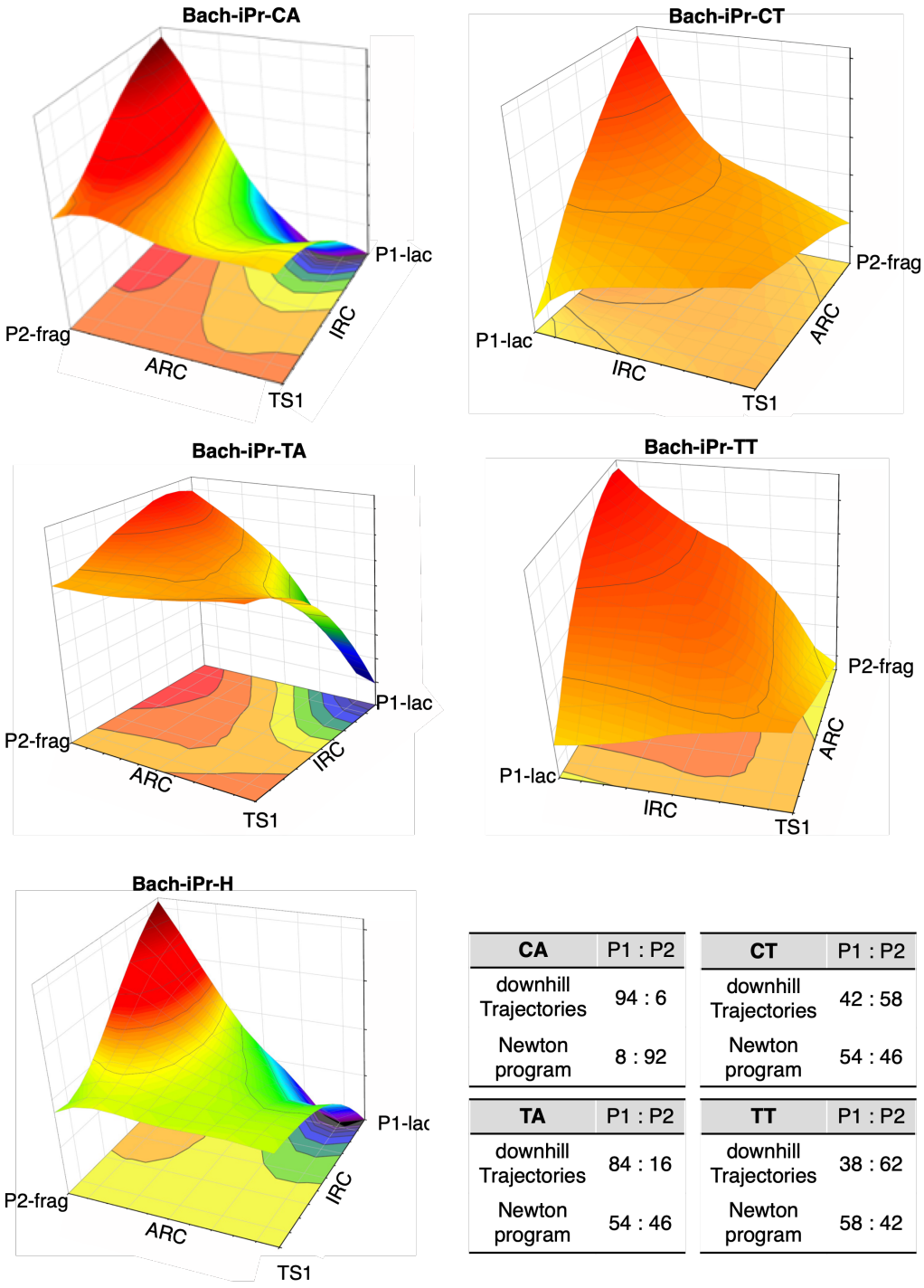


| CA | P1 : P2 |
|---|---|
| downhill Trajectories | 94 : 6 |
| Newton program | 8 : 92 |

| CT | P1 : P2 |
|---|---|
| downhill Trajectories | 42 : 58 |
| Newton program | 54 : 46 |

| TA | P1 : P2 |
|---|---|
| downhill Trajectories | 84 : 16 |
| Newton program | 54 : 46 |

| TT | P1 : P2 |
|---|---|
| downhill Trajectories | 38 : 62 |
| Newton program | 58 : 42 |

FIGURE 2.9. PESs, AIMD results, and predictions from Newton program for Bach-*i*Pr system.

## 2.6. Davies System with Full Catalyst

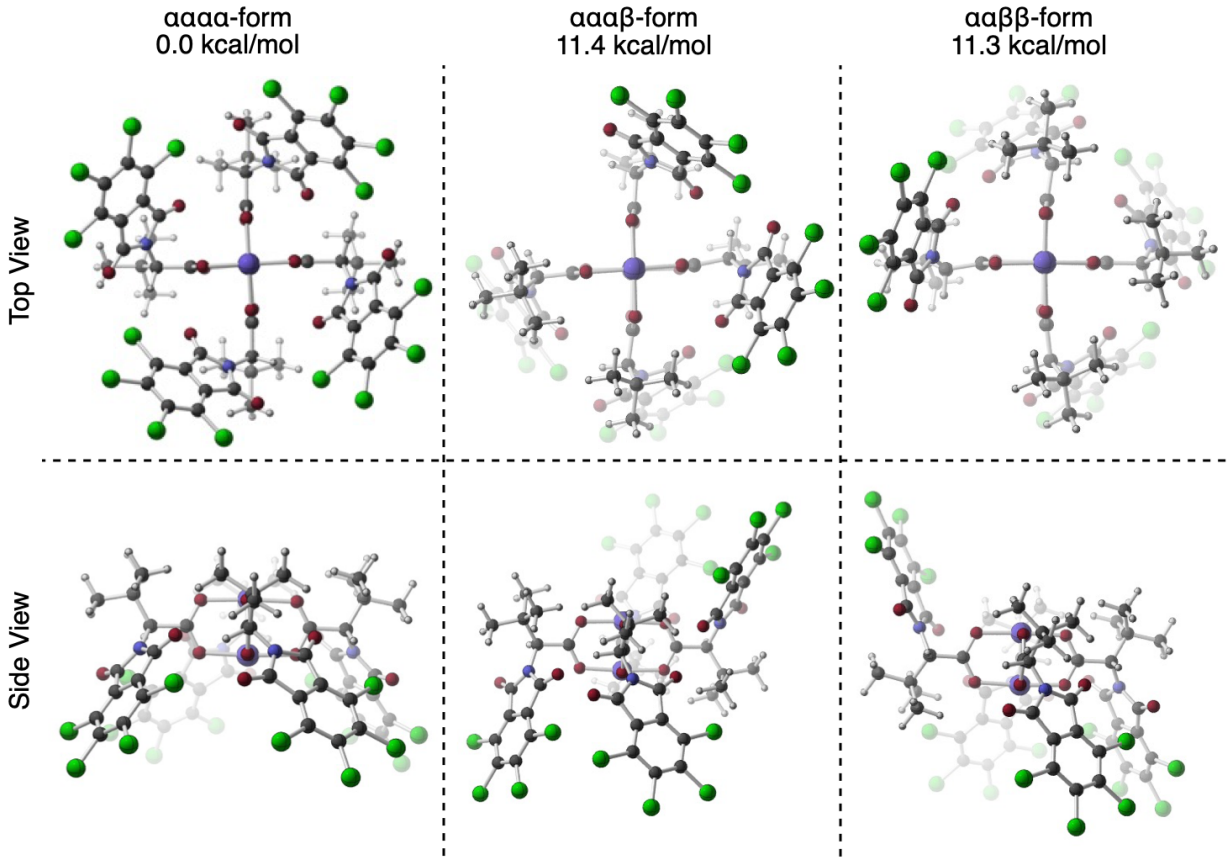


FIGURE 2.10. 3D structures of $Rh_2$($s$-TCPTTL)$_4$ $\alpha\alpha\alpha\alpha$-, $\alpha\alpha\alpha\beta$- and $\alpha\alpha\beta\beta$-conformers

As noted above, our predictions for the Davies-Ph system are not consistent with the reported experimental results – we predict an incorrect *cis*/*trans* ratio (Table 2.1) and far too much fragmentation (Figure 2.6). Possible reasons for this discrepancy include:

(1) There is no PTSB with $Rh_2$($s$-TCPTTL)$_4$.

(2) A PTSB still exists but our AIMD simulation method is flawed.

(3) A PTSB still exists, our AIMD simulation results are correct (fragmentation is dynamically preferred), but $\beta$-lactone can be easily formed by (2+2)-cycloaddition of the fragmentation products in the presence of $Rh_2$($s$-TCPTTL)$_4$ (but not $Rh_2$(OAc)$_4$ as shown above).

To settle this issue, we re-examined the Davies-Ph system using the full bulky $Rh_2$($s$-TCPTTL)$_4$ catalyst. [**136**, **137**]

First, we reoptimized the geometries of the competing TSs. The geometry of $Rh_2$($s$-TCPTTL)$_4$ is more complex than that of $Rh_2(OAc)_4$ in that multiple conformations of the carboxylate ligands are possible (e.g., $\alpha\alpha\alpha\alpha$-, $\alpha\alpha\alpha\beta$- and $\alpha\alpha\beta\beta$-conformations). We compute that the dominant form is $\alpha\alpha\alpha\alpha$ by at least 10 kcal/mol over other forms (see Figure 2.10). Shown at the top of Figure 2.12 are the competing $\alpha\alpha\alpha\alpha$-TSSs with $Rh_2$($s$-TCPTTL)$_4$ along with their relative energies. While the TT TS was preferred with $Rh_2(OAc)_4$ (Table 2.1), the CT TS is preferred with $Rh_2$($s$-TCPTTL)$_4$ which now aligns with the experimentally observed preference for the *cis* product).

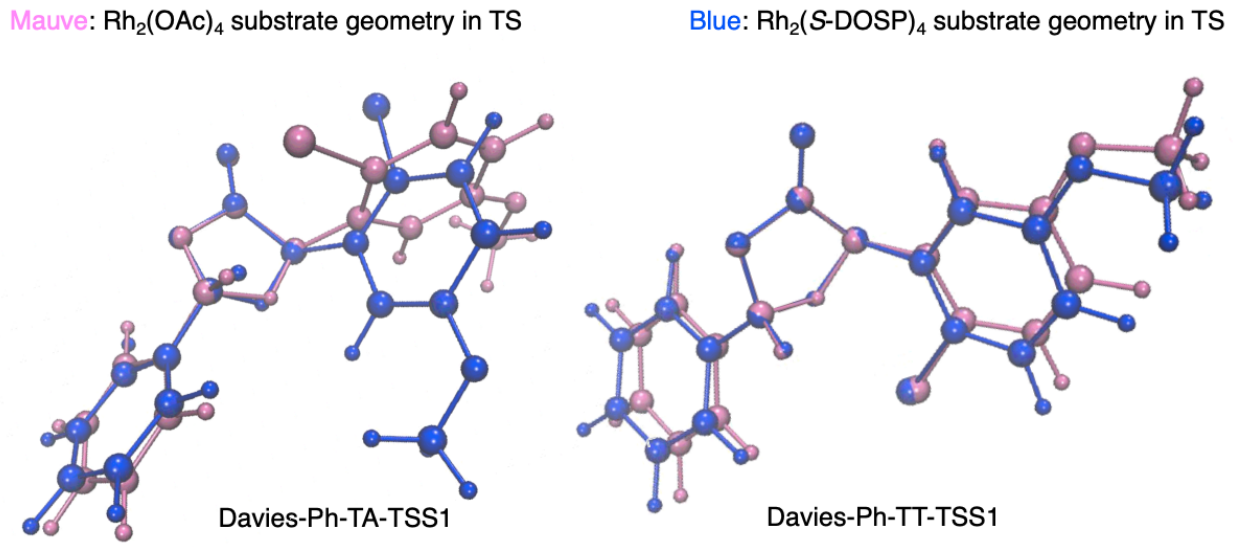


FIGURE 2.11. Structure alignment between "relaxed" substrate geometry and "strained" geometry. The energy differences between TT- and TA- substrate are 0.3 kcal/mol ($Rh_2(OAc)_4$) and 8.4 kcal/mol ($Rh_2$($s$-TCPTTL)$_4$)

The shape of $Rh_2$($s$-TCPTTL)$_4$ can be likened to a hand that grips the carbene with four N-tetrachlorophthaloyl claws. These claws provide a more restricted environment than that provided by $Rh_2(OAc)_4$. A simple hypothesis that would explain the preference for *cis* substrates is the shorter the length of the substrate, the easier it is to fit into the restricted cavity without experiencing strain.

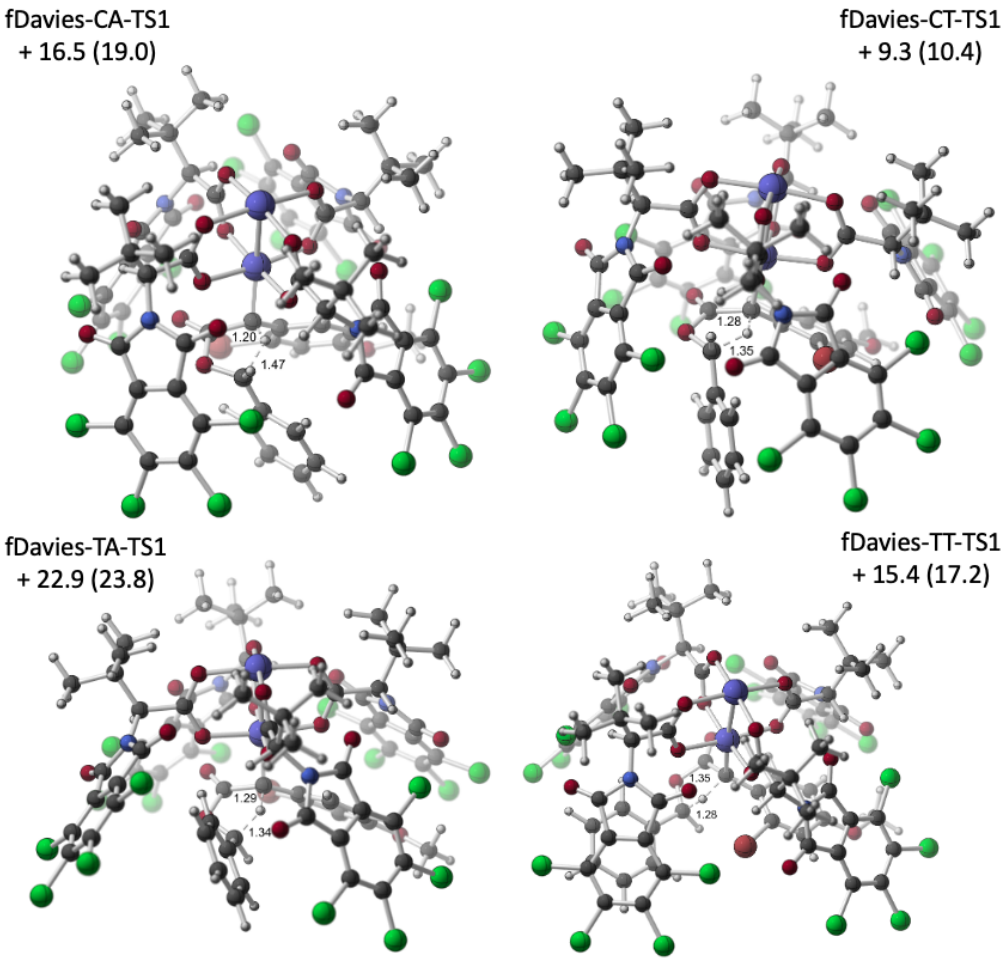


FIGURE 2.12. 3D structures of fDavies-TS1s visualized by *CYLview 1.0* with critical bond lengths in Å.

As a crude measure of the length of CT and TT TSs, we consider the distance between the methoxy group and the *para*-H on the substrate phenyl group. The difference between these lengths is approximately 2 Å. But IGM analysis in Figure 2.13 suggests that this model is too simple and non-covalent interactions play a major discriminatory role. As shown in Figure 2.13, there appears to be a larger region of $\pi - \pi$ interaction in the CT TS. Moreover, we notice that in the absence of halogen bonding due to the small room in the center of Rh atoms and tetracaboxylates, BrToward-TS1s retains its lower energy due to a less distorted (more "relaxed") structure. As shown in Figure 2.11, the geometry of BrToward TS1 is

almost unchanged when it is placed inside the $Rh_2$(*s*-TCPTTL)$_4$. However, the structure of TA folds to fit in the active site.

In addition to the preference for *cis* geometries, the conformational preference for having the bromine oriented toward the catalyst core still exists (Figure 2.12). As shown in Figure 2.13, not only does Br$\cdots$O halogen bonding exist in both bromine-toward TSSs, but a Br-$\pi$ interaction with an isoindoline ring also is present for the CT TSS.

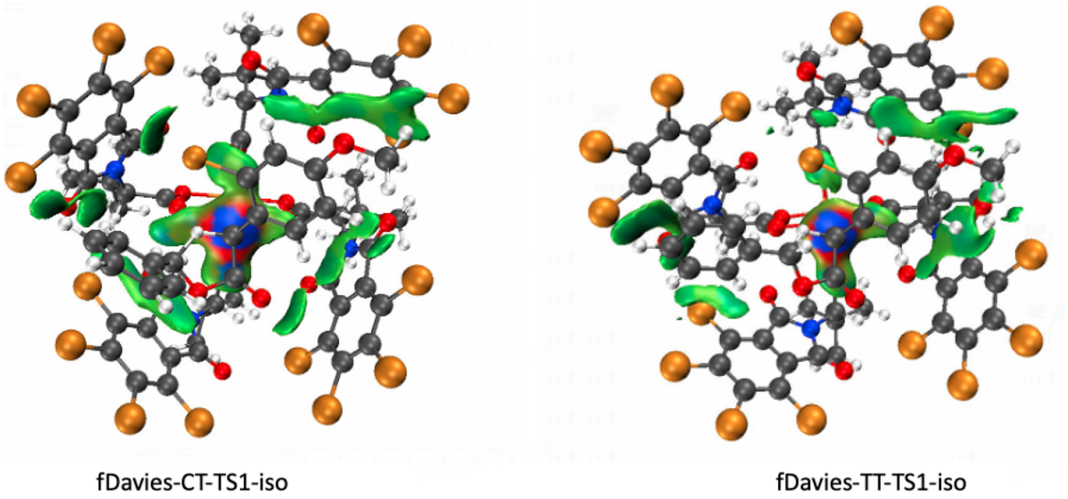


FIGURE 2.13. IGM plots for fDavies-Ph-CT (left) and fDavies-Ph TT (right) TS1s.

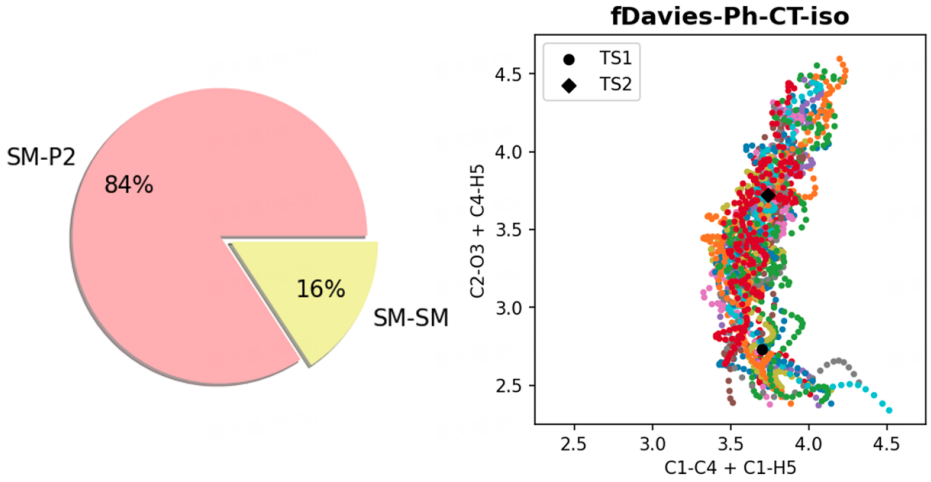


FIGURE 2.14. Left: Distribution of products from downhill AIMD trajectories for fDavies-Ph-CT transition state. Right: Plot of trajectory paths in terms of collective variables for the fDavies-Ph-CT. P1: $\beta$-lactone; P2: fragmentation.

What of the dynamic behavior of the Davies-Ph CT and CA transition states with the full $Rh_2(s\text{-TCPTTL})_4$ catalyst? As shown in Figure 2.14, no $\beta$-lactone-forming trajectories were found for the CT transition state. As shown in Figure 2.14, the trajectories sample the fragmentation side of the IRC almost exclusively. These results do not appear to match the experimental observations at all.

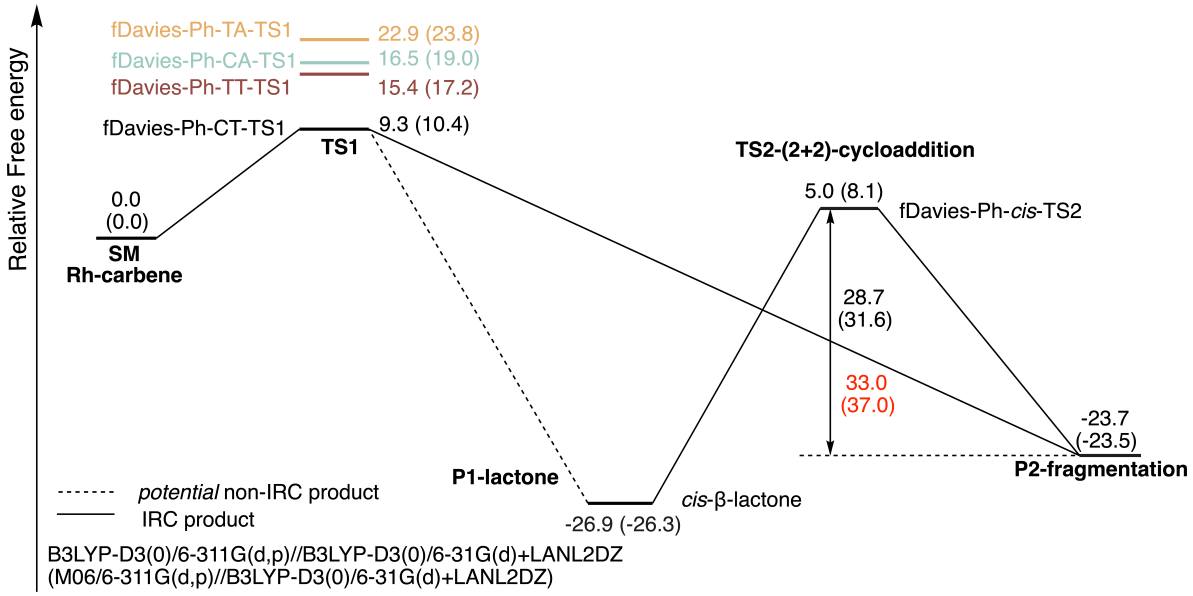


FIGURE 2.15. Energy profile of fDavies systems. The Davies-Ph-CT-TS2 relative barrier to P2-fragmentation is highlighted in red for comparison with fDavies-Ph-CT-TS2.

Where does this leave us? A PTSB appears to remain but is severely biased toward fragmentation if our AIMD results are to be believed. For the $Rh_2(OAc)_4$ systems, we found that product interconversion was accompanied by too high a barrier to be relevant (e.g., Figure 2.3). However, with $Rh_2(s\text{-TCPTTL})_4$, that is not the case! The barrier for (2+2)-cycloaddition, which allows fragments to recombine and form $\beta$-lactones, is reduced to only 28.7 kcal/mol for the bound fragmentation products, as shown in Figure 2.15.

The distortion of the ketone + ketene to their geometries, when bound to $Rh_2(s\text{-TCPTTL})_4$, was described as the relative single point energy to the geometries when bound to $Rh_2(OAc)_4$. As shown in Figure 2.16, the substrate's energy gets around 7 kcal/mol lowered at the fragmentation stage. While at the (2+2)-TS2, the energy of the substrate is favored by

3 kcal/mol when it is attached to the $Rh_2$(*s*-TCPTTL)$_4$. Note that the pocket of $Rh_2$(*s*-TCPTTL)$_4$ is held fairly rigid by a series Cl···O halogen bond between the four ligands. [**136**] As long as the fragments recombine more rapidly than they are released to bulk solvent, then $\beta$-lactone should predominate.

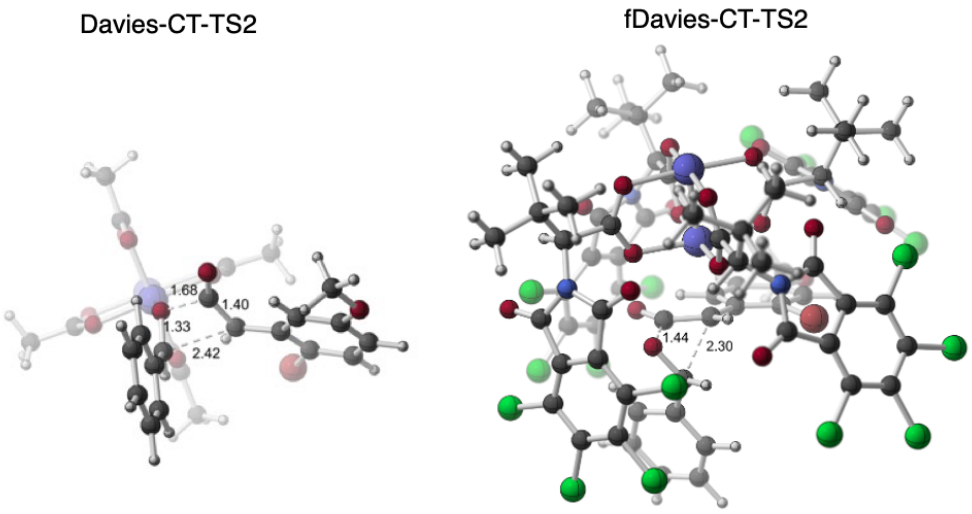


| | fragmentation geometry (Hartree) | ΔE (kcal/mol) | TS2 geometry (Hartree) | ΔE (kcal/mol) |
|---|---|---|---|---|
| Substrate with $Rh_2(OAc)_4$ | -3417.547590 | 0.0 | -3417.508542 | 0.0 |
| Substrate $Rh_2$(*s*-TCPTTL)$_4$ | -3417.536061 | 7.2 | -3417.513269 | -3.0 |

FIGURE 2.16. Top: 3D structure of Davies-CT-TS2 and fDavies-CT-TS2 depicted by *CYLView 1.0* with critical bond length labeled in Å. Bottom: Relative distortion energies of the substrate in the geometry of fragmentations and TS2 (the energy with $Rh_2(OAc)_4$ was taken as the reference).

Thus, the bulky ligands of $Rh_2$(*s*-TCPTTL)$_4$ have several effects that lead to the final success of its functionality. First, $Rh_2$(*s*-TCPTTL)$_4$ switch the inherent preference for *trans* products to *cis*. Also, though it induces a dynamic preference for fragmentation, it significantly reduces the barrier to the recombination of fragmentation products. This reduction in the barrier is so pronounced that the kinetic preference for forming these fragmentation products is overridden by a thermodynamic preference for their conversion to $\beta$-lactones.

## 2.7. Conclusions

In an effort to test the generality of the idea that PTSBs intervene in dirhodium tetracarboxylate-promoted lactone-forming C–H insertion reactions, we discovered:

(1) Yes, these PTSBs are widespread in this class of reactions.

(2) Subtle conformational preferences in transition states (e.g., conformations of aryl groups) can have dramatic effects on the dynamical outcome of reactions with PTSBs.

(3) Changing the size and shape of ligands on the catalyst not only can affect dynamical tendencies (i.e., by affecting the balance between momentum and forces related to PES shape), but can override them by opening up avenues for thermodynamic equilibration.

While some of these concepts are not new, we hope that their demonstration in the context of complex organometallic reactions such as those described here will encourage their broad application both in deriving models to explain observed reactivity (both rationalizing ratios of desired products and accounting for undesired side products) and in designing new chemistry. For example, if the reactions described here were developed with PTSBs in mind, perhaps one could have gotten out in front of yield-reducing fragmentation pathways. Admittedly, controlling how molecules navigate PTSBs is not yet a reliably rational process, [**138**, **139**] but we show here that one could predict that frag-mentation would dominate for the large $Rh_2$(*s*-TCPTTL)$_4$ catalyst and then one could have chosen to embrace that since one also could have predicted that rebound to the desired product would be rapid. That was not the order of events that occurred in the development of this reaction, but such a process could be followed in the future. In addition, as a result of following that process, we arrive now at the prediction that $Rh_2$(*s*-TCPTTL)$_4$ also might promote $\beta$-lactone formation by starting with ketones and ketenes (if competing reactions do not interfere) – a prediction that we hope will be put to the test.

CHAPTER 3

# Running Wild through Dirhodium-Catalyzed Combined CH(C)-Functionalization/Cope Rearrangement Landscapes: Does Post-Transition-State Dynamic Mismatching Influence Product Distributions?

A special type of C-H functionalization can be achieved through C-H insertion combined with Cope rearrangement (CHCR) in the presence of dirhodium catalysts. This type of reaction was studied using density functional theory and *ab initio* molecular dynamics (AIMD) simulations, the results of which pointed to the dynamical origins of low yields observed in experiments. These studies not only reveal intimate details of the complex reaction network underpinning CHCR reactions, but they further cement the generality of the importance of non-statistical dynamic effects in controlling $Rh_2L_4$-promoted reactions.[1]

## 3.1. Introduction

As we have mentioned in Chapter 2, the mechanisms of $Rh_2L_4$-catalyzed C-H functionalization reactions have been extensively investigated through a combination of experimental and density functional theory (DFT)-based computational studies, which have provided valuable insights into the electronic structure of the key [Rh] carbene intermediate, $N_2$ extrusion and C-H insertion transition structures (TSs), and the roles of both the metals and ligands of the catalyst in facilitating reaction. [**77**, **78**, **79**, **141**, **142**, **143**, **144**, **145**, **146**] In general, but not always, H-transfer and C–C bond formation are combined into a concerted process in which these events can occur synchronously or asynchronously. In some cases (the number is growing), post-transition state bifurcations (PTSBs) [**47**, **49**, **50**, **51**, **52**, **53**, **54**]

[1]This chapter is adapted from *J. Am. Chem. Soc.* **2024**, 146, 10, 7039–7051 [**140**], with permission.

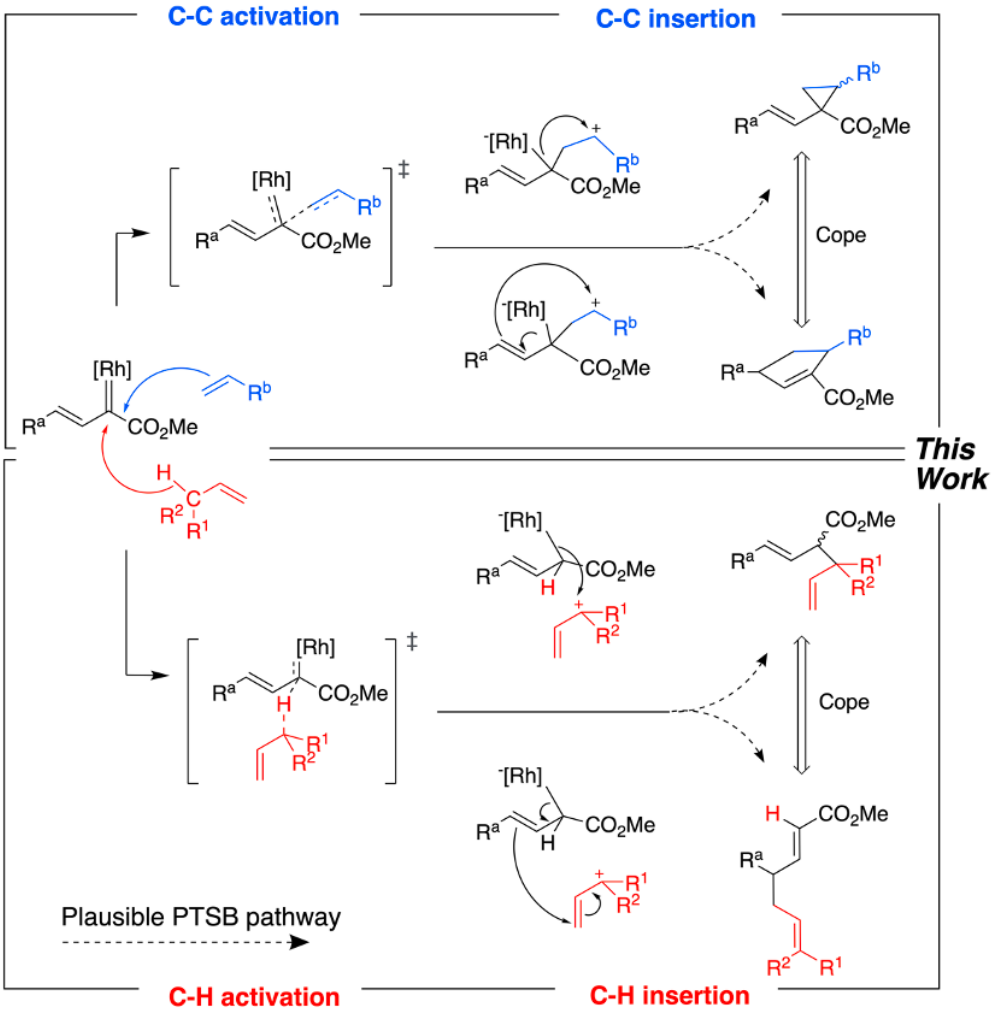


SCHEME 3.1. C-H and C-C activation of C-C $\pi$ bond-containing substrate facilitated by [Rh] carbene with plausible PTSB dynamic behavior. [Rh] = Rh2L4. Structures with curved arrows are not discrete intermediates but are shown to help readers connect TSs to products.

have been found to result in two downhill pathways from an apparent TS for C-H insertion. [**46**, **58**, **70**, **147**, **148**] For example, we have shown $Rh_2L_4$-promoted $\beta$-lactonization involve an ambimodal TS followed by pathways downhill in potential energy that lead to the lactone product or fragmentation products in Chapter 2.

In Chapter 3, we examine another seminal, case of a PTSB intruding on a $Rh_2L_4$-catalyzed C-H insertion reaction (Scheme 3.1, bottom), along with a related cyclopropanation reaction (Scheme 3.1, top), employing AIMD simulations to characterize the non-statistical dynamic

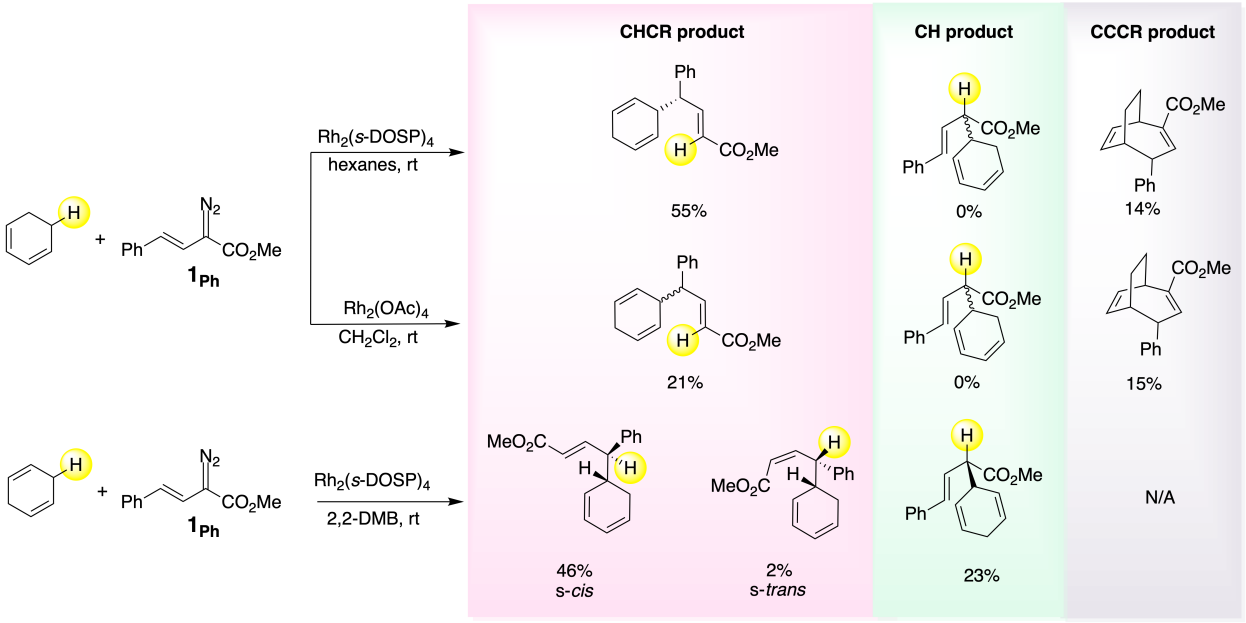


SCHEME 3.2. Selected experimental results. [**148**, **149**, **150**]

effects that control product selectivity. It is perhaps not surprising that we now believe that PTSBs are common in $Rh_2L_4$-promoted reactions.

Among the large realm of Rh-catalyzed C-H activation reactions, one called the CHCR reaction, discovered by Davies' group in 1998, has been extensively studied and explored using various chiral dirhodium catalysts due to its high enantioselectivity and diastereoselectivity. [**147**] Experiments and DFT calculations from Davies, Autschbach, and co-workers revealed that [Rh] carbene insertion into allylic C–H bonds likely involves a PTSB leading to two products that are related by a Cope rearrangement, leading them to dub this process "combined C-H functionalization/Cope rearrangement" (CHCR). [**147**, **148**, **149**] Computations indicated that C-H insertion and C–C bond formation occurred asynchronously with the computed IRC leading to the CHCR product (the major product found experimentally), however, the reaction coordinate involved a flat region. Experimental outcomes with some less selective substrates and $Rh_2L_4$ catalysts are shown in Scheme 3.2. These results are indeed consistent with the presence of a PTSB, and here we aim to provide results from AIMD simulations that confirm that both products are directly accessible from the C-H

insertion transition state for these reactions and provide insights into the factors controlling selectivity. [**84**] In addition, the presence of C=C $\pi$ bonds in the reactants leads to a competition between C-H and C=C functionalization; Scheme 3.2 shows that products of C=C functionalization are also sometimes observed. We also explore whether the TS for C–C bond formation is followed by a bifurcation that provides pathways to two C–C functionalized products, one a cyclopropane, that are also related by a Cope rearrangement, another reaction studied experimentally by Davies and co-workers. [**151**, **152**] We refer to this reaction as a "combined C-C functionalization/Cope rearrangement" (CCCR).

These networks of reactions are much more complex than those encountered in previous AIMD studies on $Rh_2L_4$-promoted $\beta$-lactone formation *via* C-H insertion in chapter 2. As a result, the work described here not only bears on the generality of non-statistical dynamic effects in $Rh_2L_4$-promoted reactions, but also tests the limits of our modeling approaches.

## 3.2. Computational Methods

**3.2.1. Structures.** The details of structure optimization and single point corrections are slightly different from chapter 2. Instead of using 6-311G(d,p) functional, the diffusion function was added as 6-311+G(d,p) to describe the electronic structure more accurately, especially for ionic complexes with significant electron delocalization. In simulations involving solvent, the DCM environment was represented using the Polarizable Continuum Model (PCM) for both DFT calculations and AIMD simulations. [**153**, **154**] Transition structures were identified by the presence of only one imaginary vibrational frequency, and their connection to minima was confirmed *via* IRC analysis. [**28**, **29**] Coordinates for all computed structures are available at ioChem-BD repository https://iochem-bd.bsc.es/browse/review-collection/100/315418/. [**155**]

**3.2.2. AIMD.** The same AIMD simulations protocol in Chapter 2 was run for *quasi*-classical downhill trajectory, using Singleton's Progdyn package in the NVE ensemble at room temperature (298.15 K) with a time step of 1 fs. [**83**] Moreover, we performed three

types of dynamic simulations: *quasi*-classical downhill, classical downhill, and uphill. [**156**, **157**] *Quasi*-classical simulations involved providing zero-point energy (ZPE) to each vibrational mode. However, the time required to form a product in some systems exceeded 1 ps (1000 steps), causing us to worry about ZPE leakage effects. [**158**] Therefore, we also employed classical MD.

We attempted to initiate uphill dynamics from [Rh] carbenes by stretching the C–H bond that would break in the insertion reaction, but this approach was unsuccessful. Although the barrier for C-H functionalization is only 4 kcal/mol relative to the Rh-carbene, it requires over 30 kcal/mol of energy to shift the hydride. The failure of uphill dynamics might be attributed to the way we add energy to the system: the initial energy is added to the breaking C and H atoms following the vector corresponding to the bond-stretching movement. However, the actual hydride shift occurs along a parabolic trajectory. Considering the artifact caused by additional energy to the system in the long term, we chose downhill MD instead.

## 3.3. Parent System

**3.3.1. Selectivity or not?** We first discuss a simplified reaction, involving methyl 2-methylenebut-3-enoate bound to $Rh_2(HCO_2)_4$ and cyclohexadiene as substrate in the gas phase. The same setup was previously reported in Davies and coworkers' work, where four different conformations of C-H insertion TSs were reported. In addition to the s-*cis*/s-*trans*(referring to the Rh-C-C=C dihedral angle) and chair-like/boat-like (referring to the six atoms involved in the Cope rearrangement) geometries discussed in the previous work, we observed that the orientation of the carbonyl oxygen of the seemingly innocuous ester (in/out labels indicate whether oxygen is inside or outside the gap between 1,3-cyclohexadiene and the [Rh] carbene) also played a critical role in determining product selectivity. C-H insertion TSs with cyclohexadiene in other orientations were explored, but these were higher in energy (see Appendix 7.2.1).

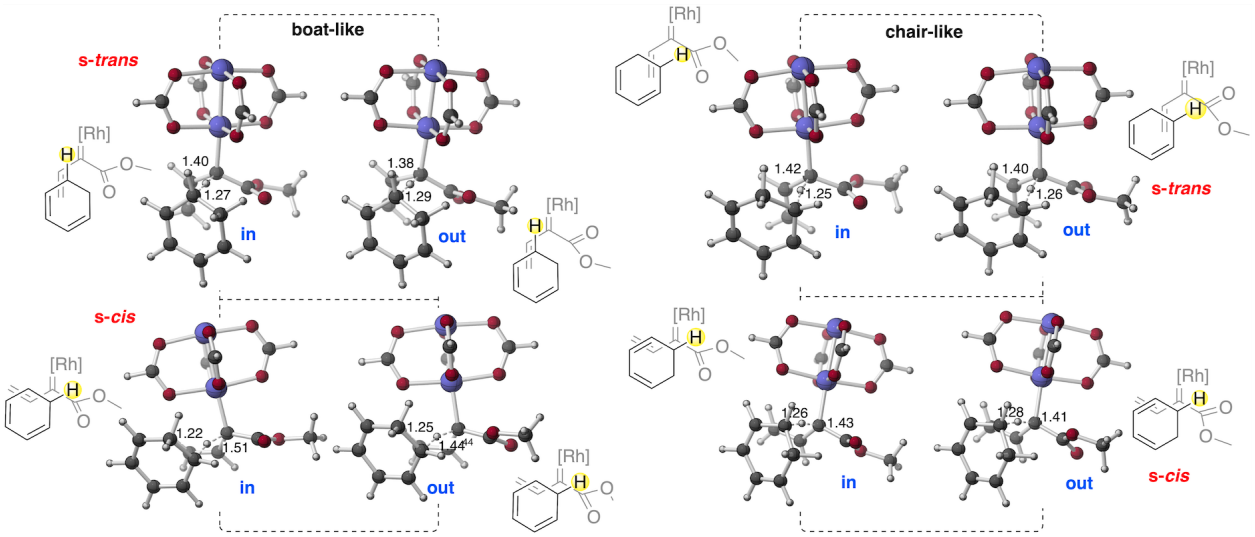


FIGURE 3.1. Model system C-H insertion TS conformations with key bond lengths in Å. See Appendiex 7.2.2 for geometries of C-C activation TSs

The data in Table 3.1 indicate that chair-like C-H insertion transition states are consistently lower in free energy than boat-like transition states, which is consistent with the DFT studies from Davies and coworkers. [**148**] However, in that all barriers for C-H insertion are low, we suspected that s-*cis* versus s-*trans* selectivity might be determined prior to C-H insertion, i.e., barriers for interconversion of s-*cis* and s-*trans* species might be higher than those for reaction. The s-*cis* and s-*trans* interconversion were also discussed in Davies's work while they focused on the post-Rh-carbene stage. The possibilities are outlined in Scheme 3.3, which also shows computed energies. The process of switching from s-*cis* to s-*trans* at the [Rh] carbene stage involves a barrier of approximately 9 kcal/mol, which is indeed greater than the barriers computed for C-H activation (Table 3.1). Consequently, the formation of the carbene from the diazo precursor is not inconsequential with regard to selectivity. The s-*cis* and s-*trans* diazo compounds are predicted to differ in energy by 1.7 kcal/mol. Their interconversion is associated with TS ($\mathbf{TS1}_H$) whose energy is comparable to the TSs for $N_2$ extrusion ($\mathbf{TS2}_{H-cis}$ and $\mathbf{TS2}_{H-trans}$). $N_2$ extrusion is also predicted to be very exergonic and releases a gas, so it is expected to be irreversible. While all of these considerations complicate matters, considering the accuracy and expected error bars associated with DFT

| **conformation** | s-*cis* | | | | s-*trans* | | | |
|---|---|---|---|---|---|---|---|---|
| | chair | | boat | | chair | | boat | |
| | in | out | in | out | in | out | in | out |
| $\Delta G^{\ddagger}$ | 5.3 | 5.2 | 8.8 | 7.5 | 5.9 | 6.4 | 7.6 | 7.2 |
| **IRC product** | CHCR | CHCR | CHCR | CHCR | CHCR | CHCR | elimination | CHCR |

TABLE 3.1. $\Delta G^{\ddagger}$ and IRC products for the C-H activation TSs shown in Figure 1. Energies are in kcal/mol and are relative to the $G_{1,3-cyclohexadiene}$ + the best $G_{Rh-carbene}$ form at the B3LYP-D3(0)/6-311+G(d,p)+LANL2DZ//B3LYP-D3(0)/6-31G(d)+LANL2DZ level of theory in the gas phase.

methods of the type used, it is most prudent to predict that little, if any, selectivity is expected. We point out these issues, though, because such a copout may not be possible for other systems.

**3.3.2. Reaction coordinates.** As shown in Table 3.1, an elimination product, benzene, was unexpectedly observed when running an IRC from the trans-boat-in C-H insertion TS (**TS**$4_{H-trans-boat-in}$ in Figure 3.2). The formation of the elimination product involves the shift of a proton from the $sp^3$ carbon of the cyclohexadiene not involved in C-H insertion to the nearby oxygen of $CO_2Me$ (in addition to the hydride shift from the other $sp^3$ carbon to the carbene carbon). Thus, the geometry of this TS must have a short H$\cdots$O distance to access the elimination channel. Among the eight possible conformers, only **TS4**$_{H-cis-chair-in}$ and **TS4**$_{H-trans-boat-in}$ satisfy this requirement, yet their IRCs lead to different products. Is a PTSB involved? To help answer this question, we plotted the two IRCs together in Figure 3.2, with respect to the distances for the O–H and C–C bonds that would form in elimination and CHCR products, respectively. Both O–H and C–C bonds are shorter in the geometry of **TS4**$_{H-cis-chair-in}$ (whose IRC leads to the CHCR product) than in **TS4**$_{H-trans-boat-in}$, its IRC showing that the O and H initially approach each other but then move apart as the C–C bond forms through a pathway that descends steeply in energy. In contrast, O and H move towards each other throughout the IRC for **TS4**$_{H-trans-boat-in}$, which describes a longer region of relatively constant energy.

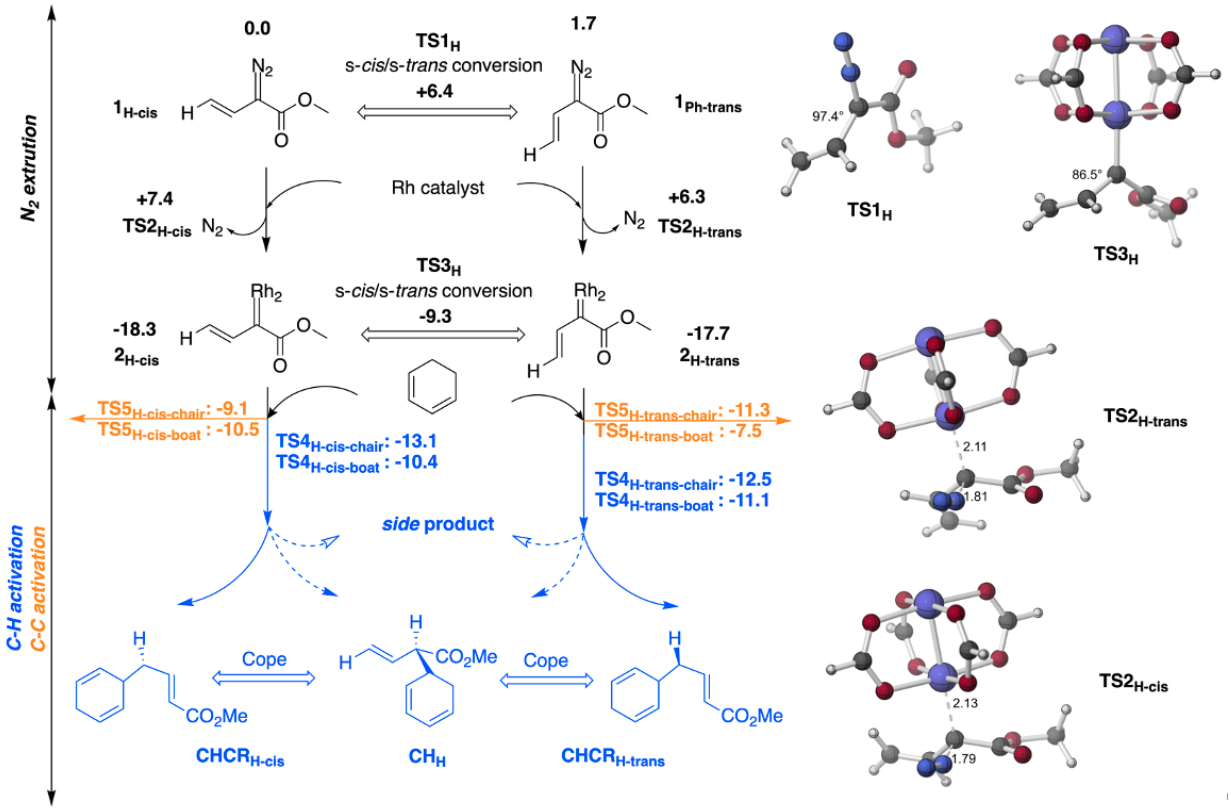


SCHEME 3.3. Energy profile of the parent system C-H and C-C activation with key TSs. Relative free energies were computed at the B3LYP-D3(0)/6-311+G(d,p)+LANL2DZ//B3LYP-D3(0)/6-31G(d)+LANL2DZ level of theory (gas phase). As the in and out conformations have very similar energies, only the energy of the lower energy one is presented. Selected distances on TSs are shown in Å. Dihedral angles for s-*cis*to s-*trans*conversion TSs are labeled as well. For more information on the formation of CCCR products (orange), see Appendix 7.2.2.

In both cases, flat regions of potential energy are observed, which correspond to structures labeled as *NOT an intermediate* in Figure 3.2, although whether or not such structures have significant lifetimes and can be characterized as entropic intermediates remains to be seen. [**43**, **159**, **160**] The presence of a "shoulder" on the IRC is a common feature for TSs **TS4**, even when their geometries are not conducive to the formation of an elimination product, but what does this feature suggest that multiple products are accessible from each **TS4**? Answering this question requires AIMD simulations.

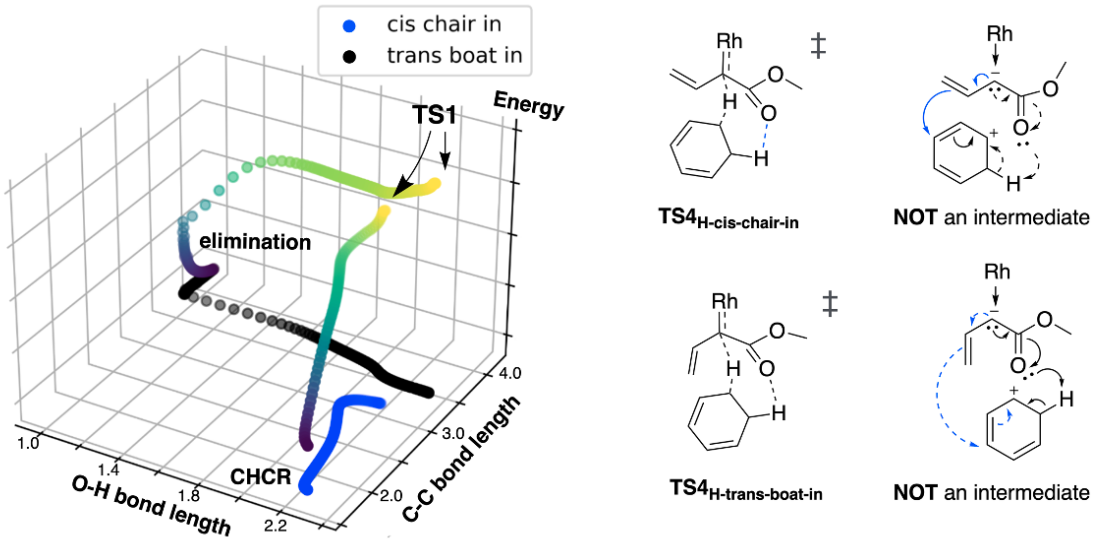


FIGURE 3.2. IRCs and their projections of the $\mathbf{TS4}_{H-cis-chair-in}$ and the $\mathbf{TS4}_{H-trans-boat-in}$ boat-like TSSs' on the direction of the product side color by the energy. The C-C bond and O-H bond formation correspond to the CHCR and elimination of cyclohexadiene, respectively. Critical bonds and arrows are colored by the corresponding products: black-**elimination**; blue-**CHCR**.

**3.3.3. Dynamical Tendencies.** AIMD simulations were carried out, starting from both $\mathbf{TS4}_{H-cis-chair-in}$ and $\mathbf{TS4}_{H-trans-boat-in}$, revealing several dynamic behaviors:

(1) For both TSs, four different product minima were found to be linked to the [Rh] carbene: the **CHCR** product, the **elimination** product, a **CH*** product (same molecular structure as the direct C-H insertion product but resulting from a formal 1,5-sigmatropic rearrangement step following hydride transfer), and a **ketene acetal** product. As shown in Scheme 3.4, all four products can be rationalized as arising from the "*NOT an intermediate*" ion pair associated with the shoulder region of the IRCs discussed above, consistent with this region of the potential energy surface being flat and having multiple exit channels.

(2) The dynamically preferred products are the IRC products (Table 3.1 and pie charts in Scheme 3.4).

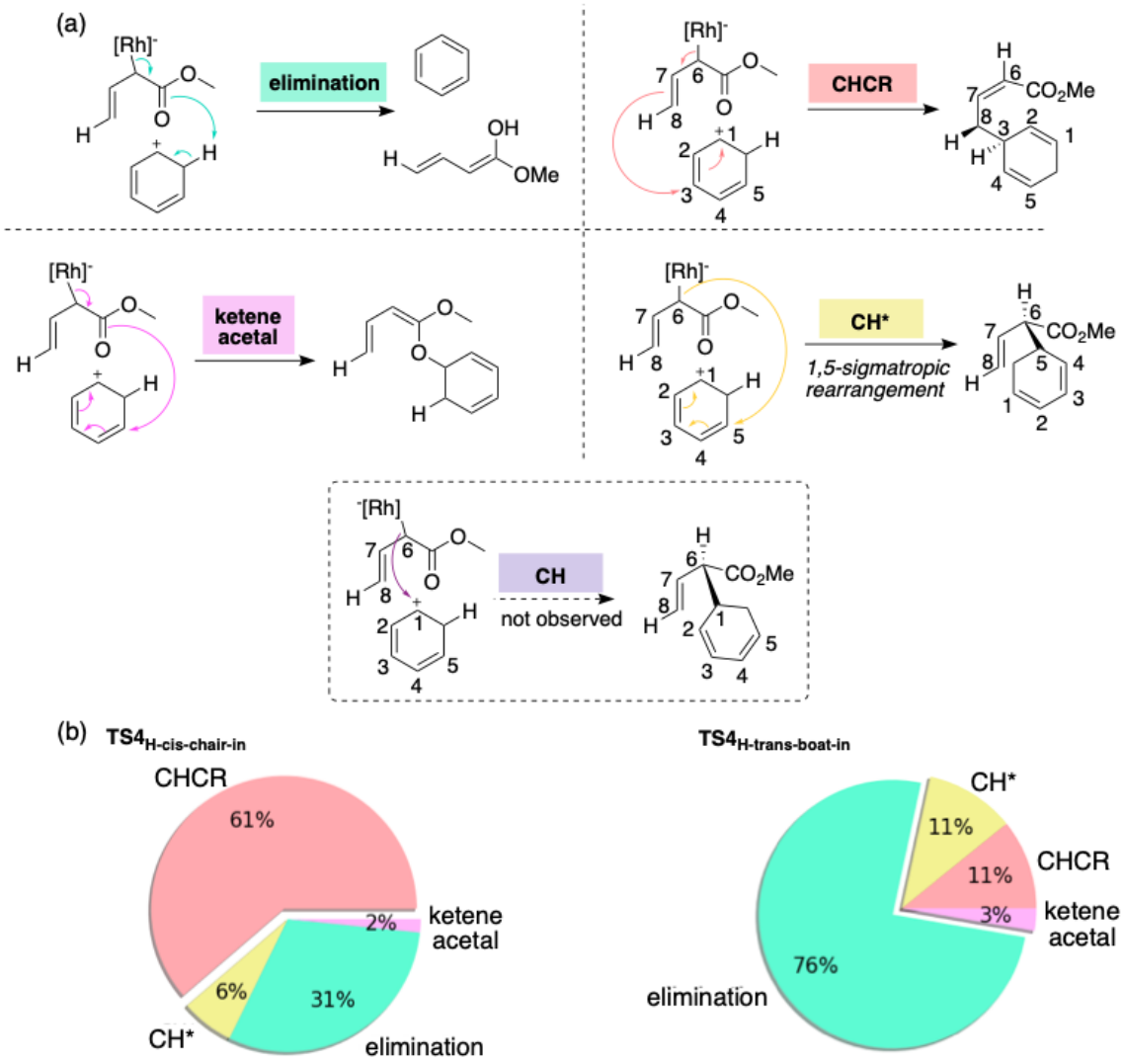


SCHEME 3.4. Top: Products found in AIMD simulations, arrow pushing mechanisms for each from the "NOT an intermediate" ion pair. To distinguish **CHCR**, **CH***, and **CH** products, atomic indexes are labeled on the ChemDraw structures. [Rh] = $Rh_2(HCO_2)_4$ Bottom: Product distributions from AIMD simulations.

(3) None of the trajectories lead directly to the C-H insertion product or even show a tendency to do so (details in the Appendix 7.2.3).

(4) The time necessary for product formation shows substantial variability for both TSs (Figure 3.3), again consistent with a flat energy surface and/or an entropic intermediate. For example, the time required for the formation of an elimination product from $\mathbf{TS4}_{H-trans-boat-in}$ ranges from 60 to 450 fs.

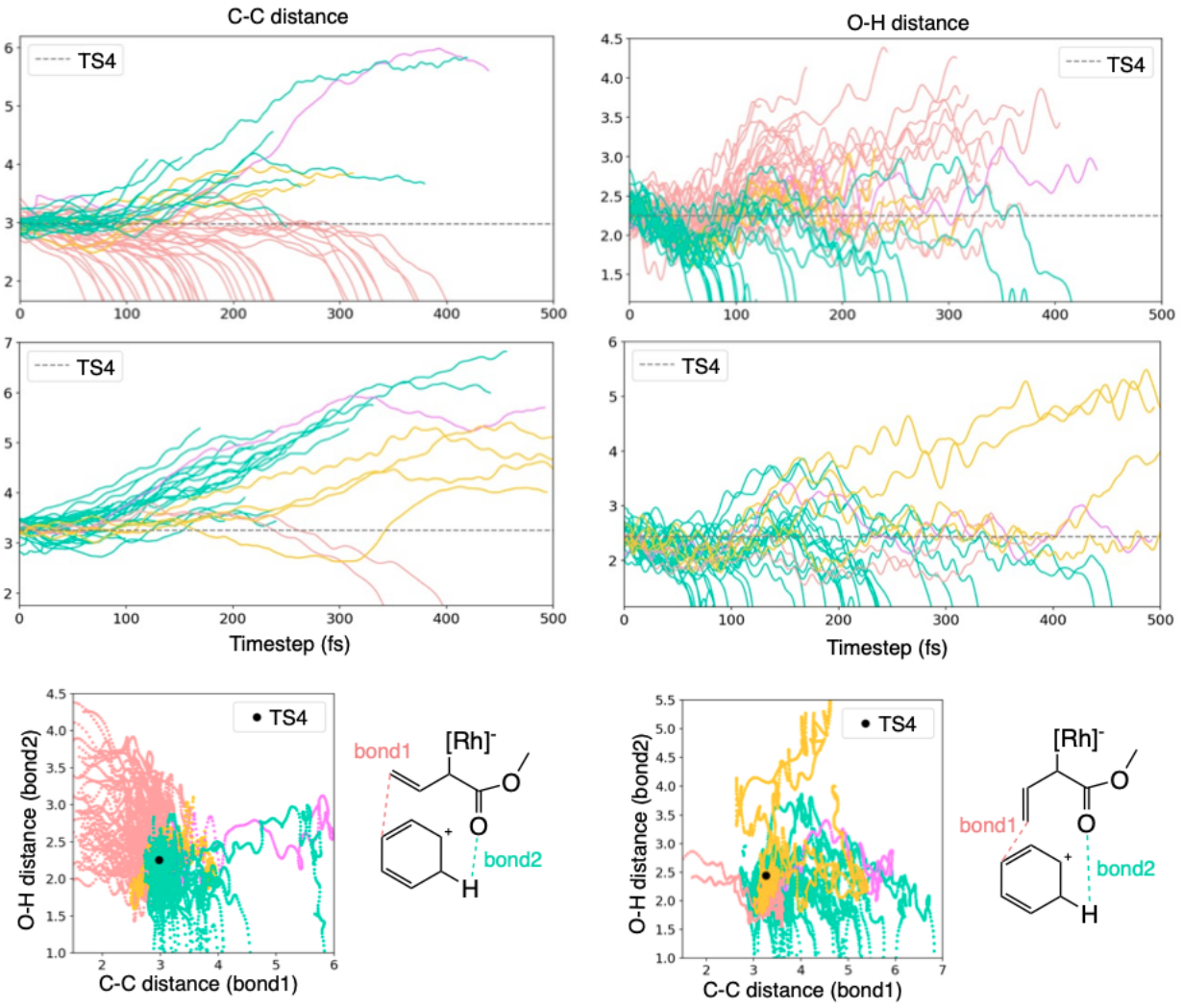


FIGURE 3.3. Plots of trajectories from $\mathbf{TS4}_{H-cis-chair-in}$ (top) and $\mathbf{TS4}_{H-trans-boat-in}$ (bottom), in terms of the C-C (CHCR product) and O-H (elimination product) distance. Left: C-C distance versus time. Middle: O-H distance versus time. Right: 2D projections of trajectories. Color represents the product of corresponding trajectories: **CHCR** in pink, **elimination** in mint, **ketene acetal** in magenta, **CH*** in yellow.

(5) The ion pair generally explores a broad region close to each TS before settling into a minimum, as revealed by the 2D trajectory projections in Figure 3.3 (right). This observation is consistent with the fact that the key O–H and C–C bonds are not directly involved in the hydride shift, minimizing the likelihood of a ballistic (momentum) effect (additional details can be found in the Appendix 7.2.3). [**135**]

While the lack of a ballistic effect implies that the initial momentum of the system does not have a direct impact on the dynamic effects, it may still affect the behavior of the non-statistical intermediate in subsequent trips.

(6) Two special cases were observed in which proton migration was assisted by $HCO_2$ ligands during elimination from $\mathbf{TS4}_{H-trans-boat-in}$. Four consecutive stages were observed in these cases (e.g., Figure 3.4): hydride shift (fast, 0-11 fs), counter-clockwise rotation of the protonated benzene (slow, 11-180 fs), deprotonation by $HCO_2$ (fast, 180-185 fs), OH group reorientation (slow, 185-288 fs), and proton shuttling to the carbonyl O (fast, 288-293 fs). These trajectories suggest that even in the absence of an appropriate initial elimination pose, there is still a possibility that the proton is captured by a carboxylate before any C–C bond is formed.

To investigate the general importance of putative ion pair entropic intermediate $\mathbf{IM}_H$, we examined $\mathbf{TS4}_{H-cis-chair-out}$ and $\mathbf{TS4}_{H-trans-chair-in}$ with AIMD simulations. The acidic proton in the former is far from both the catalyst and the ester group, while the acidic proton in the latter is located away from the ester group but in between two $HCO_2$ ligands. These two TSs also have low relative energies (Table 3.1). The AIMD simulations for $\mathbf{TS4}_{H-cis-chair-out}$ produced only the CHCR product, whereas those for $\mathbf{TS4}_{H-trans-chair-in}$ led to four different products (Figure 3.5, left). The four products included two new products, a product of direct C-H insertion (**CH**) and $\mathbf{IM}_H$ as an endpoint; **CH*** and **ketene acetal**

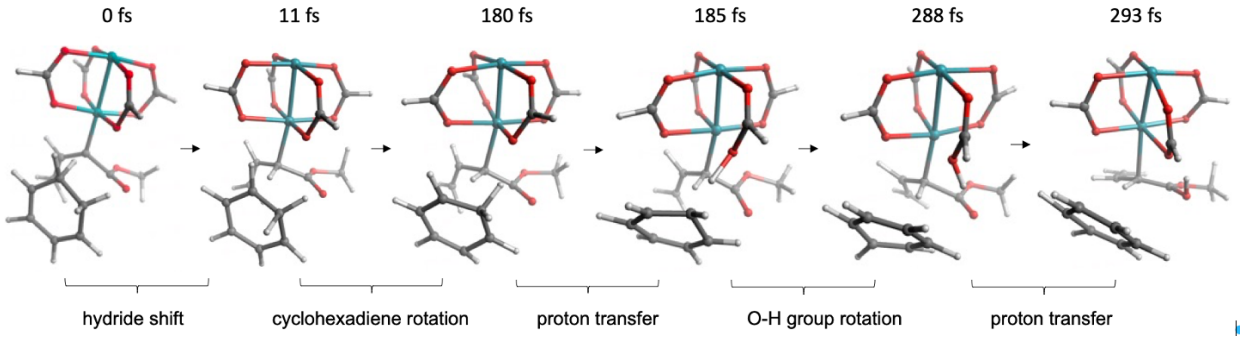


FIGURE 3.4. Snapshots taken from a trajectory in which an $HCO_2$ ligand facilitates elimination for $\mathbf{TS4}_{H-trans-boat-in}$.

products were not observed. Here, $\mathbf{IM}_H$ was confirmed to be a minimum on the potential energy surface by optimizing the endpoints of $\mathbf{IM}_H$-forming trajectories. We hypothesize that the emergence of this shallow intermediate (which will be converted to product structures at longer times) is due to two CH $\cdots$ O hydrogen bonds between CH protons on the cyclohexadienyl cation substructure and oxygens of $HCO_2$ groups on the catalyst and/or the ester (Figure 3.5, right). Additionally, the perpendicular pose of the carbanion and protonated benzene makes it inaccessible to either the C-H insertion or CHCR exit channels.

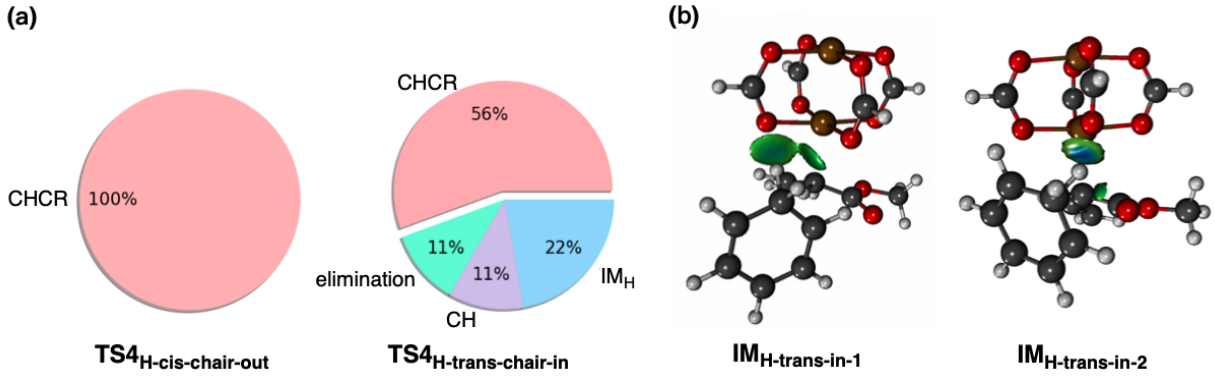


FIGURE 3.5. Left: Product distribution from AIMD simulations for $\mathbf{TS4}_{H-cis-chair-out}$ and $\mathbf{TS4}_{H-trans-chair-in}$. Right: IGMH graph for two $\mathbf{IM}_H$ minima (isovalue = 0.005) depicted by Multiwfn and VMD. [**110**, **126**] The hydrogen bonds in $\mathbf{IM}_{H-trans-in-1}$ are between two $HCO_2$ groups and the acidic H, while in $\mathbf{IM}_{H-trans-in-2}$ one hydrogen bond involves the carbanion ester.

Though the trajectories show considerable variability, there is one common trait observed among all of them: no matter their initial geometry, the terminal alkene rotates clockwise after the hydride shift. To understand why, we examined the vibrations corresponding to the imaginary frequencies of the TSs. These are visualized for two TSs in Figure 3.6. These vibrations lead to the terminal alkene rotating away from the hexadiene into a mutually perpendicular orientation that impedes the formation of both CHCR and direct C-H insertion products. In contrast to dynamic matching, [**56**, **82**, **156**, **160**, **161**, **162**] where the momentum possessed by a molecule as it falls down the energy hill after passing the transition state is used to enhance the formation of a subsequent product, here that momentum

actively drives trajectories away from products, allowing the ion pair structure to persist. We propose the term *"dynamic mismatching"* for such an effect, i.e., when post-TS momentum drives a trajectory away from the product of an IRC rather than towards it. Note that this effect is distinct from the increase in "flexibility" that leads to entropic intermediates. This effect is more detrimental to the s-*trans* TSs, as their terminal carbons are moving quickly away from the cyclohexadiene. Consequently, more time is required for the cyclohexadienyl cation to become appropriately aligned to form the **CHCR** product. Indeed, for $\mathbf{TS4}_{H-trans-chair-in}$, **CHCR** product-forming trajectories are on average (397 fs), longer than those for $\mathbf{TS4}_{H-cis-chair-in}$ (214 fs) (see Appendix 7.2.3).

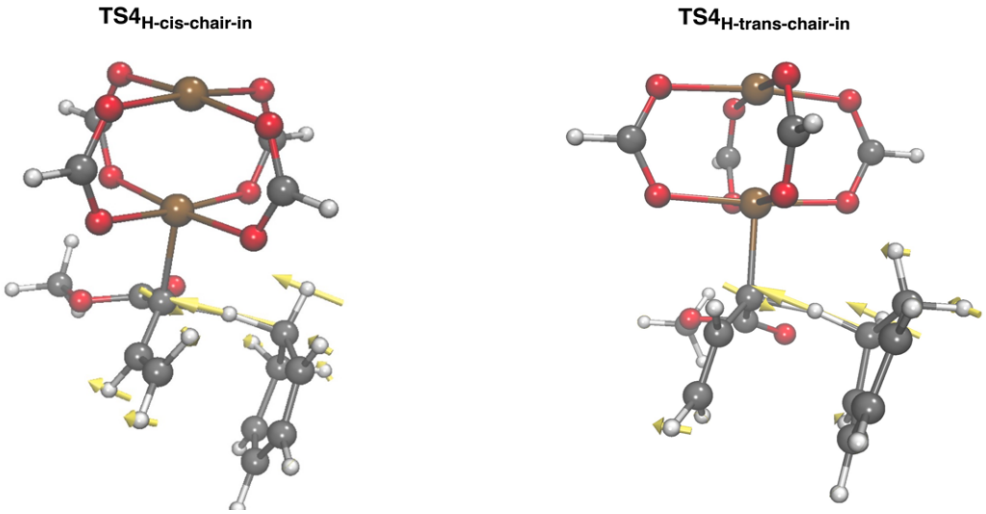


FIGURE 3.6. Vector representation of the imaginary vibrational mode, visualized by VMD. [**126**]

### 3.4. Putting It All Together

The results of our AIMD simulations make it clear that the reactivity of this system is far more complex than combined C-H insertion and Cope rearrangement. Based on our AIMD results, we sought out additional PES minima and have identified a total of six that can be reached from the C-H activation TS (Scheme 3.5): direct C-H insertion (**CH**), Cope rearrangement combined with CH insertion (**CHCR**), 1,5-sigmatropic rearrangement combined with C-H insertion (**CH***), ion pair intermediate ($\mathbf{IM}_H$), C–O bond formation (**ketene**

**acetal**), and **elimination** (benzene) products. Note that we do not consider this scenario to reflect a "post-transition-state hexafurcation"; rather it reflects an energy surface with flat regions having multiple exit channels, consistent with the early calculations on reaction coordinates from Davies and Autschbach (see Appendix 7.2.4 for details on AIMD simulations initiated with other stationary points and IRCs, which often have *shoulders*). [**148**] Given the complex nature of the potential energy surfaces involved, it is challenging (and we would argue, not so useful) to capture all stationary points in a classic 2-dimensional energy profile (energy versus structure). Instead, we summarize the connectivity between minima and TSs in Scheme 3.5 through the use of various types of arrows: double-headed arrows (not resonance arrows!) link the minima for which we have identified a TS for their interconversion, whereas conventional single-headed arrows indicate structures connected to **TS4** by AIMD trajectories alone (see Appendix 7.2.5 for an alternative dimensionality-reducing approach based on principal component analysis). The top of Scheme 3.5 shows the s-*trans*-chair-in system, for which we were able to locate two $\mathbf{IM}_{H-trans}$ minima and eight TSs that connect products. The two geometries of $\mathbf{IM}_{H-trans}$ originate from either a clockwise or counter-clockwise rotation following the initial hydride shift event. To indicate how this rotation impacts branching in dynamics simulations, the arrows surrounding the post-$\mathbf{TS4}_{trans-chair-in}$ structure are drawn clockwise or counter-clockwise based on the sense of rotation in trajectories that lead to the products at the end of those arrows. While the **CH*** product could potentially be achieved *via* a clockwise reaction pathway, we did not observe any trajectories leading to its formation in this system. Initially, we discovered that $\mathbf{IM}_{H-trans-in-2}$ is linked to two types of elimination processes (where the proton is transferred to either the ester group or $HCO_2$ ligand) and the **ketene acetal** *via* $\mathbf{TS6}_{H-trans}$, $\mathbf{TS7}_{H-trans}$, and $\mathbf{TS8}_{H-trans}$. While $\mathbf{TS7}_{H-trans}$ is higher in potential energy than $\mathbf{IM}_{H-trans-in-2}$, it is actually slightly lower in free energy than $\mathbf{IM}_{H-trans-in-2}$. A similar reaction network is observed

for the s-*cis*-chair-in system (Scheme 3.5, bottom), although it is slightly simpler. For example, only one $\mathbf{IM}_{H-cis-chair-in}$ minimum was found, but no trajectories were trapped in this structure.

### 3.5. Phenyl Substitution

Replacing one terminal hydrogen of the simple system described above with a phenyl group and $HCO_2$ ligands with OAc ligands leads to a system that was reported by Davies in 2007 (Scheme 3.2, center). [**51**] For reactant $\mathbf{1}_{Ph}$ (Figure 3.7), a 1.4:1 ratio of CHCR:CCCR products, with a combined yield of 36%, was observed. To determine whether the relatively low yield (21%) of CHCR products might be the result of dynamic mismatching, comprehensive DFT calculations on the potential energy surface for this system and AIMD simulations were carried out with the PCM solvation model.

Adding a phenyl group to the substrate alkene leads to a more challenging interconversion between s-*cis* and s-*trans* Rh-carbene $\mathbf{2}_{Ph}$, which now is predicted to have a free energy barrier (*via* $\mathbf{TS3}_{Ph}$) of approximately 16 kcal/mol (Scheme 3.7). In contrast, the predicted barrier for s-*cis*/s-*trans* interconversion of $\mathbf{1}_{Ph}$ remains low. This difference is likely a result of steric clashes with the ligands on the catalyst that restrict the rotation of the styrenyl group. Since the barrier for interconversion of the [Rh] carbenes is higher than those for conversion to products, selectivity should come from the $N_2$ extrusion process, for which no significant preference for s-*cis* versus s-*trans* $\mathbf{TS2}_{Ph}$ is predicted. Thus, we expect both the *cis* and *trans* low-energy chair-like **TS4**s to contribute essentially equally when predicting product distributions from AIMD simulations.

A challenge with running *quasi*-classical AIMD simulations for this system was that approximately 10% of all trajectories did not form products within 1000 fs. This may reflect the presence of an entropic intermediate differing from $\mathbf{IM}_{Ph}$, but given the risk of ZPE leakage, we also carried out classical downhill AIMD simulations. The outcomes of both *quasi*-classical (with trajectories that did not form products not included) and classical AIMD simulations are presented in Figure 3.8.

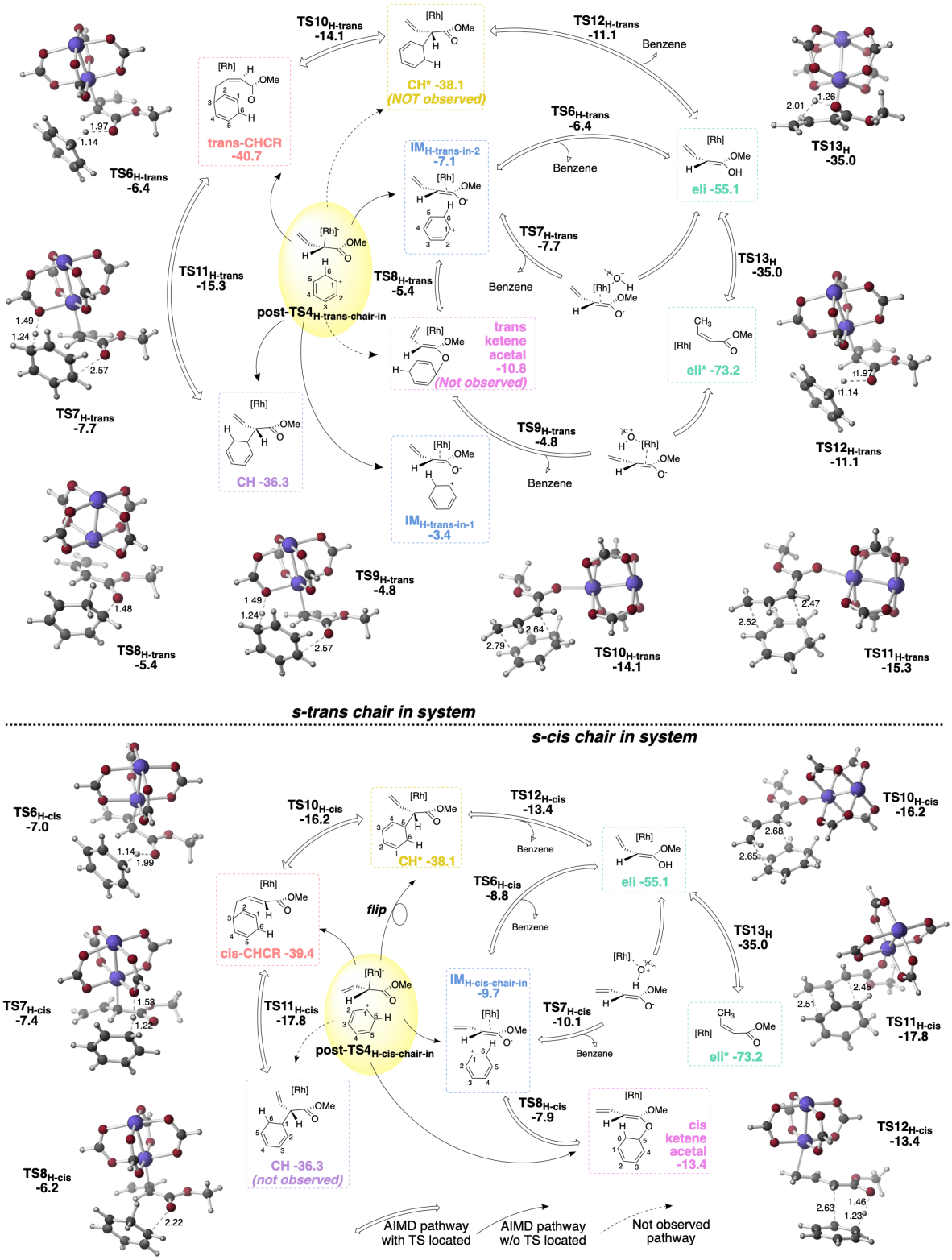


SCHEME 3.5. Reaction networks for s-*trans*-chair-in and s-*cis*-chair-in systems. Free energies relative to the best [Rh] carbene/1,3-cyclohexadiene complex are shown (kcal/mol).

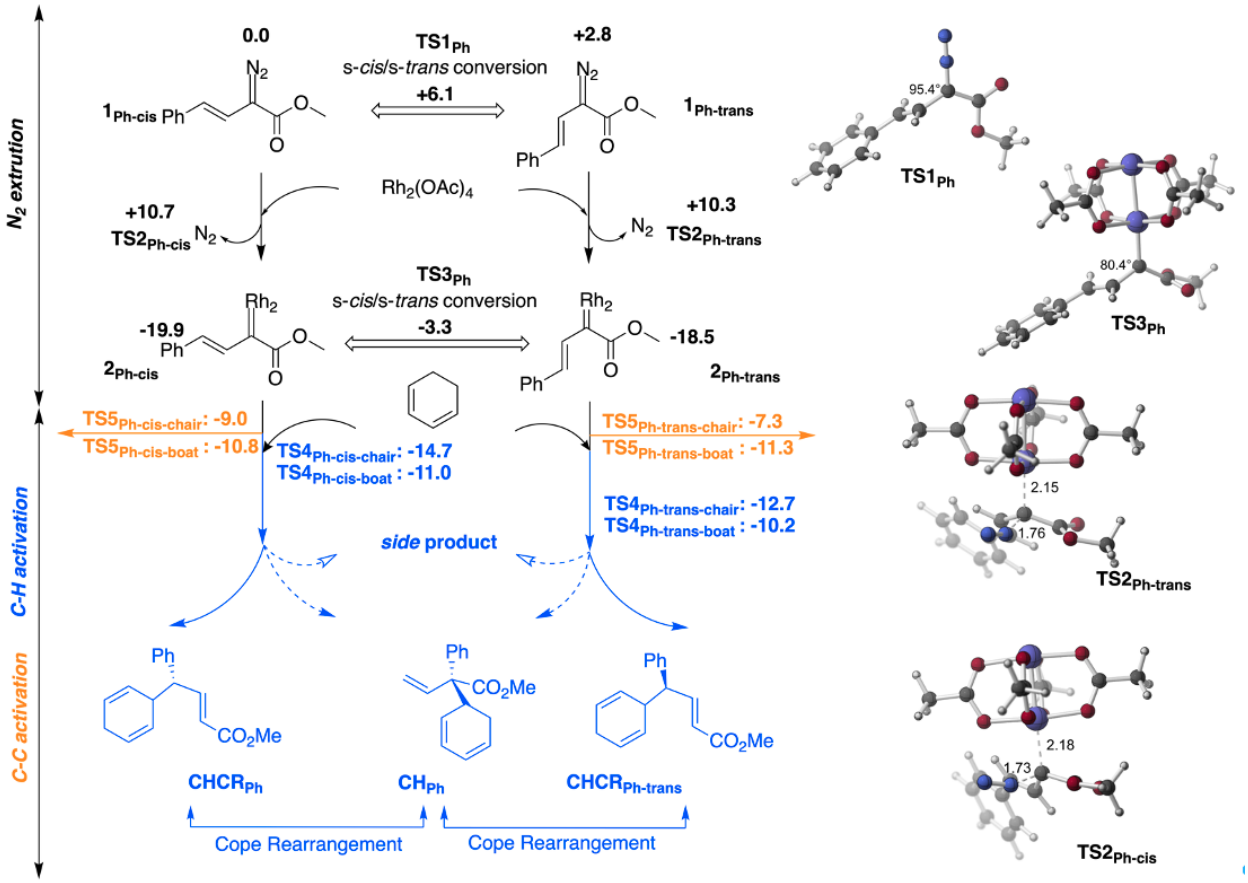


FIGURE 3.7. Energy profile of the phenyl-substituted system. Relative free energies were computed at PCM(DCM)-B3LYP-D3(0)/6-311+G(d,p)+LANL2DZ//PCM(DCM)-B3LYP-D3(0)/6-31G(d)+LANL2DZ level of theory. As the in and out conformations have very similar energies, only the energy of the lower energy one is presented. Selected distances on TSs are shown in Å. [**119**]

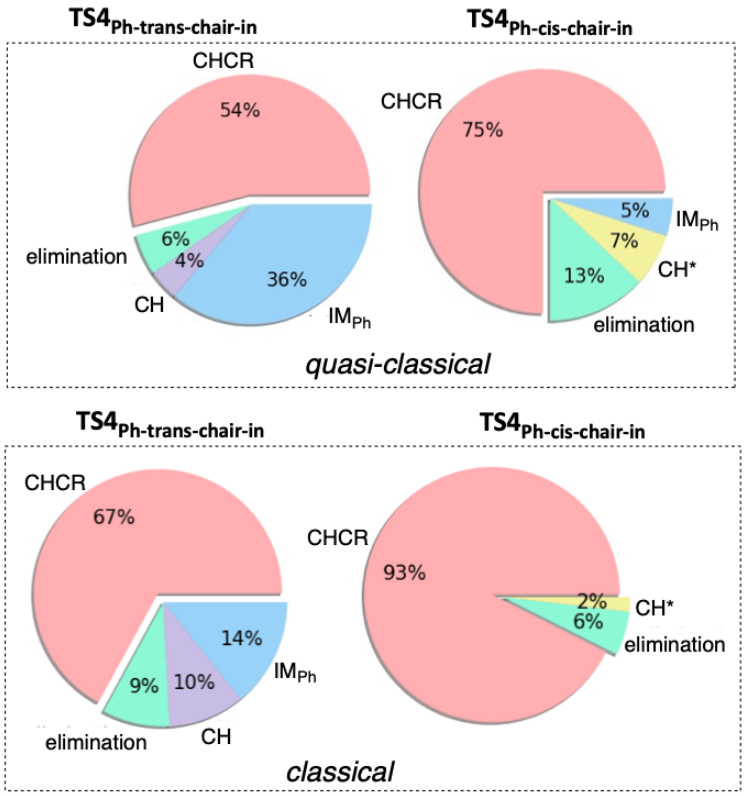


FIGURE 3.8. Results of AIMD simulations initiated from $\mathbf{TS4}_{Ph-trans-chair-in}$ and $\mathbf{TS4}_{Ph-cis-chair-in}$. int = $\mathbf{IM}_{Ph}$, which is parallel to the $\mathbf{IM}_{H}$, containing a phenyl group at R group instead of H.

In the classical simulations, all trajectories managed to terminate within 1000 fs. This, in turn, boosted the proportion of trajectories forming the CHCR product, seemingly since the kinetic energy of the system is not sufficiently large and distributed appropriately for the molecule to explore around the $\mathbf{IM}_{trans-Ph}$ region, but instead remains localized around the minimum energy path leading to the CHCR product.

For s-*trans* $\mathbf{TS4}_{Ph-trans-chair-in}$, the product distribution from *quasi*-classical AIMD simulations is similar to that of the model system (Figure 3.5), but again, removing ZPE increases CHCR product formation.

Overall, combining the results from the s-*trans* and s-*cis* systems, more CHCR products are expected for the phenyl-substituted system, but the nature of the potential energy surface and associated dynamic behavior is expected to lead to very little C-H insertion product

(none was observed experimentally) and a non-trivial amount of side products (consistent with the experimentally reported low yield). Comparing to the model system, the mismatching effect could be alleviated due to the phenyl substituent, which is not as easy to rotate as H. Note also that TSs leading to CCCR products (**TS5**) may be close enough in free energy to compete as well (Figure 3.7 and Appendix 7.2.2).

## 3.6. A Larger Catalyst

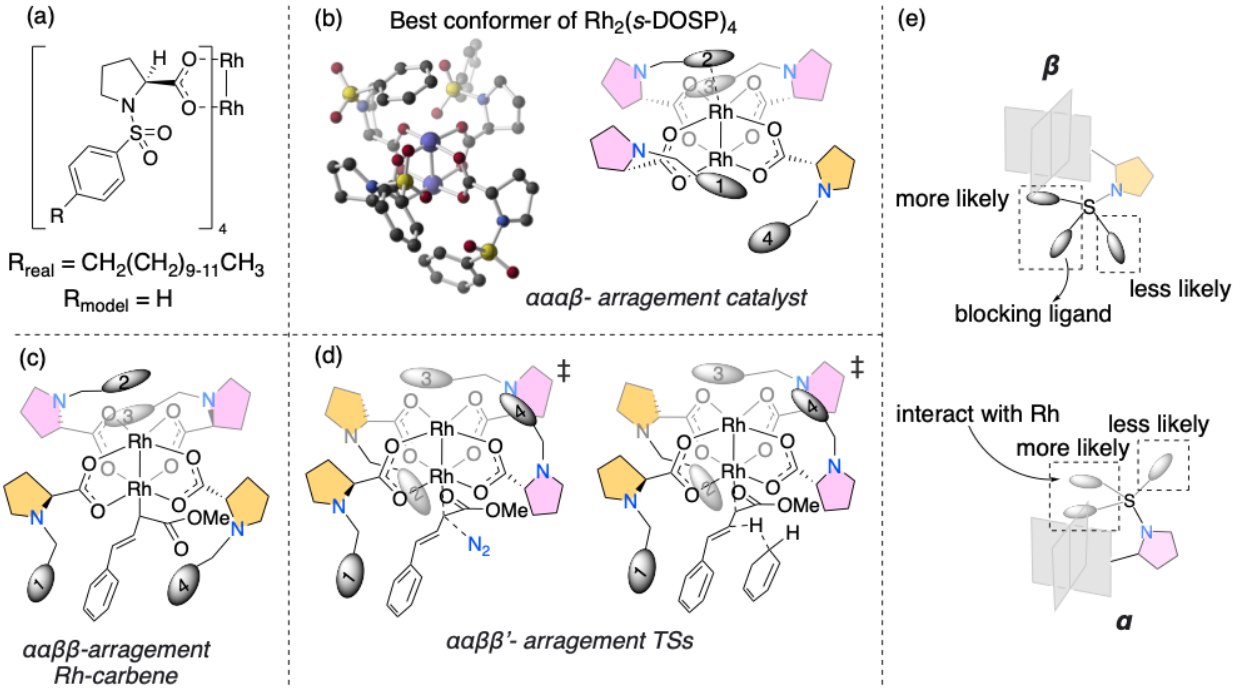


FIGURE 3.9. (a) $Rh_2$($S$-DOSP)$_4$ simplification used for calculations. (b) The lowest energy $Rh_2$($S$-DOSP)$_4$ geometry and schematic illustration of the lowest energy Rh-carbene geometry. (c) Schematic illustration of the lowest energy Rh-carbene geometry. (d) Schematic illustration of the lowest energy $N_2$ extrusion and C-H activation TSs geometry. (e) Schematic illustration of the plausible conformations of $Rh_2$($S$-DOSP)$_4$ and its flexible ligands

In contrast to the $Rh_2(OAc)_4$-catalyzed reaction just described, Davies and co-workers observed a good yield (63%) of CHCR product when using $Rh_2$($S$-DOSP)$_4$ as catalyst (Scheme 3.2, top). [**64**] Again, no simple C-H insertion product was reported. To characterize the role of $Rh_2$($S$-DOSP)$_4$ we employed a model that truncates the long alkyl chains

of the ligands (Figure 3.9a). The selectivity obtained with $Rh_2$(*S*-DOSP)$_4$ was previously proposed to originate from a favored $\alpha\alpha\alpha\beta$-ligand arrangement, common for $Rh_2L_4$ catalysts with bulky ligands. [**163**, **164**] However, unlike other common ligands that are fairly rigid, such as TCPTTL, the pyrrolidine and benzene sulfonyl groups of DOSP have considerable rotational flexibility. [**58**, **76**, **165**] Thus, it is perhaps not surprising that our conformational searches on $Rh_2$(*S*-DOSP)$_4$ led to no ligand orientations that can be described simply as either pointing upwards or downwards with respect to the Rh-Rh unit. We explored the geometrical space of $Rh_2$(*S*-DOSP)$_4$, the [Rh] carbene, and the $N_2$ extrusion TS using xTB-CREST. [**166**] The lowest energy conformer of $Rh_2$(*S*-DOSP)$_4$ has an asymmetrical geometry that we tentatively refer to as $\alpha\alpha\alpha\beta$ (Figure 3.9b; see Appendix 7.2.6 for other conformers). In the absence of a bound carbene, one benzene ring tends to interact with Rh, but the ligands alter their arrangement to accommodate the substrate, maximizing weak interactions while minimizing steric hindrance with an $\alpha\alpha\beta\beta$ geometry (e.g., Figure 3.9c). Another $\alpha\alpha\beta\beta$ geometry (also called $\alpha\alpha\beta'\beta'$) is preferred for the $N_2$ extrusion TS structure, with one side of the substrate shielded and the other side left open (Figure 3.9d). Additionally, the shielding ligand promotes an out conformation of the [Rh] carbene, wherein the carbonyl oxygen is oriented toward the shielded direction. A similar geometry is expected for the C-H functionalization TSs as cyclohexadiene approaches (Figure 3.9d). Moreover, the *S*-DOSP ligands, serving as steric blocking groups, may prevent mismatching due to the rotation no matter if a s-*cis* or s-*trans* conformation. In short, the DOSP ligands provide a malleable binding site.

While AIMD simulations on this system are beyond the scope of this study due to the size and, significantly, flexibility of $Rh_2$(*S*-DOSP)$_4$, we can propose a hypothesis on the origins of increased selectivity for this system based on the geometries and energies of key structures. While no strong preference was predicted for the s-*trans* or s-*cis* carbene with $Rh_2(OAc)_4$ (Figure 3.7), the s-*cis* [Rh] carbene is predicted to be 6 kcal/mol lower energy than the s-*trans* [Rh] carbene with $Rh_2$(*S*-DOSP)$_4$ as a result of selective noncovalent interactions with the

ligands, and these same interactions are likely to hinder s-*cis*/s-*trans* interconversion, This strong preference for s-*cis* binding with $Rh_2$(*S*-DOSP)$_4$ is also reflected in the energies of the $N_2$ extrusion TSs, where s-*cis* dominates with a 4 kcal/mol energy barrier. Even though both s-*cis* and s-*trans* carbenes lead to CHCR products, we've shown above that the s-*cis* conformation results in a higher selectivity for the formation of CHCR products over side-products in AIMD simulations, for both the simple model system and the phenyl-substituted system with $Rh_2(OAc)_4$. If this dynamical preference persists with $Rh_2$(*S*-DOSP)$_4$, the bias induced by the ligand for the s-*cis* conformation may well be the indirect source of enhanced CHCR product formation.

### 3.7. Conclusions

The results of our quantum chemical calculations, both static and dynamic – which add to a growing number of quantum chemistry-based dynamics simulations on metal-catalyzed reactions [**46**, **58**, **148**, **160**, **167**, **168**, **169**, **170**, **171**] – have revealed exceedingly complex reaction networks for Davies' $Rh_2L_4$ promoted C–H(C) functionalization/Cope rearrangements. These results confirm Davies and Autschbach's original proposal of a flat potential energy surface with a PTSB and showcase the even greater complexity of the reaction network tied to this surface and the dynamical behavior of the molecules faced with traversing it. Of particular note, the importance of s-*cis*/s-*trans* ratios in preparing trajectories to launch was revealed, as was the importance of flat regions of the post-TS PESs, which may contain entropic intermediates. The "dynamic mismatching" concept was introduced as a twist on Carpenter's dynamic matching concept, and a tentative model of the origins of increased selectivity with DOSP ligands was put forth. The general importance of post-transition state dynamics for controlling selectivity in $Rh_2L_4$-promoted reactions now seems quite clear.

CHAPTER 4

# Flexibility, $\pi - \pi$ Stacking, and Ylide Stabilization: A DFT Study on the Cyclopropanation Selectivity of Mixed-Ligand Rhodium(II) Catalysts

Recent experimental work has demonstrated the potential of mixed-ligand Rh(II) paddlewheel complexes to enhance cyclopropanation yields and selectivity compared to traditional catalysts with identical ligands like $Rh_2(OAc)_4$. In this chapter, we explore the mechanistic basis for the improved performance of $Rh_2(OAc)_3$(PhTCB). The mixed-ligand design offers increased catalyst flexibility, enabling the dissociation of the PhTCB ligand from the vacant Rh site and the formation of stabilizing $\pi - \pi$ stacking interactions with the substrate in a three-benzene sandwich structure. Along the reaction pathway, the Rh-carbene intermediate forms an explicit C-S bond, resulting in an ylide structure that represents a deep energy minimum. The unique functionality of the $Rh_2(OAc)_3$(PhTCB) catalyst arises from its ability to modulate the energetic landscape and promote cyclopropanation while suppressing side reactions. These computational insights highlight the power of mixed-ligand Rh(II) catalysts and provide a framework for the rational design of improved Rh paddlewheel catalysts. [1]

## 4.1. Introduction

In Chapters 2 and 3, we explored dirhodium-catalyzed C-H insertion reactions, revealing the asynchronous nature of hydride shift and subsequent bond formation. Our detailed investigation of potential PTSB effects uncovered cryptic channels that divert reaction pathways from desired products ($\beta$-lactones and CHCR products, respectively). These studies highlight the

[1]This chapter presents a collaborative project with Professor Ampofo K. Darko's research group. The experimental work was conducted by Paul Pitcher, from Darko's group. Wang-Yeuk Kong contributed to the conformational searching, mechanisms brainstorming, and benchmarkings.

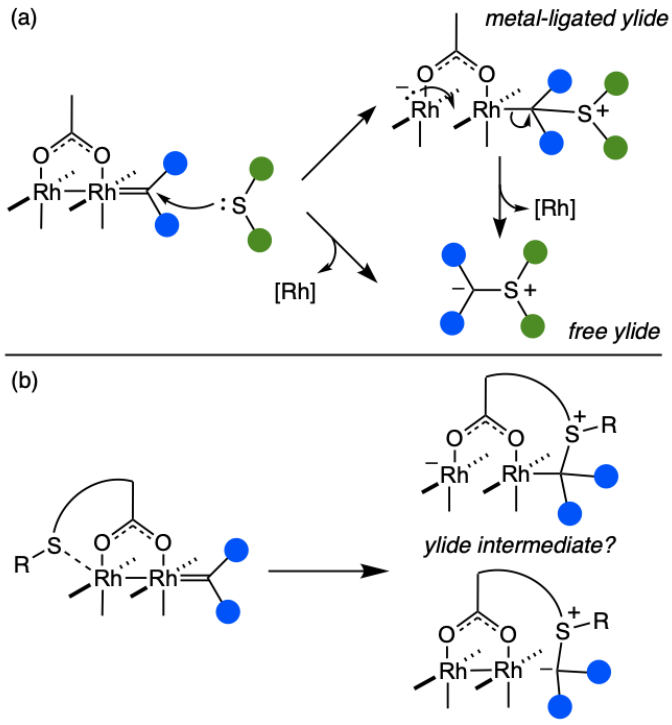


SCHEME 4.1. (a) General mechanism of ylide intermediate generated from a [Rh]-carbene and sulfide. (b) Proposed ylide intermediate formation specific to $Rh_2(OAc)_3$(PhTCB)catalyst, highlighting the role of the SPh ligand on the asymmetric catalyst.

limitations of relying solely on thermodynamic considerations in organometallic reactions. By analyzing the dynamic trajectories, vibrational modes, and post-TS PES, we demonstrated that the outcome is influenced by both momentum effects and catalyst-substrate interactions, which can be manipulated to control reaction outcomes. Here, we extend our investigation to a dirhodium-catalyzed cyclopropanation reaction, briefly introduced in Chapter 3. While no dynamic effects have been confirmed for this reaction, it may involve an intriguing process given by the unique properties of the catalysts $Rh_2(OAc)_3$(PhTCB). Sulfur-containing compounds play a pivotal role in organometallic chemistry, particularly in reactions involving ylide intermediates. These transformations have garnered attention due to their ability to facilitate asymmetric sigmatropic rearrangements, such as the [1,2]-sigmatropic Stevens rearrangement and the [2,3]-sigmatropic Doyle-Kirmse rearrangement. [**172**, **173**, **174**, **175**, **176**, **177**, **178**] A key point of debate in the field centers on the

nature of the ylide intermediate: whether it exists as a free species or remains coordinated to the metal center throughout the reaction (scheme 4.1). [**141**, **179**, **180**, **181**, **182**] Elucidating this mechanistic detail is crucial for optimizing reaction performance and expanding the scope of these valuable transformations.

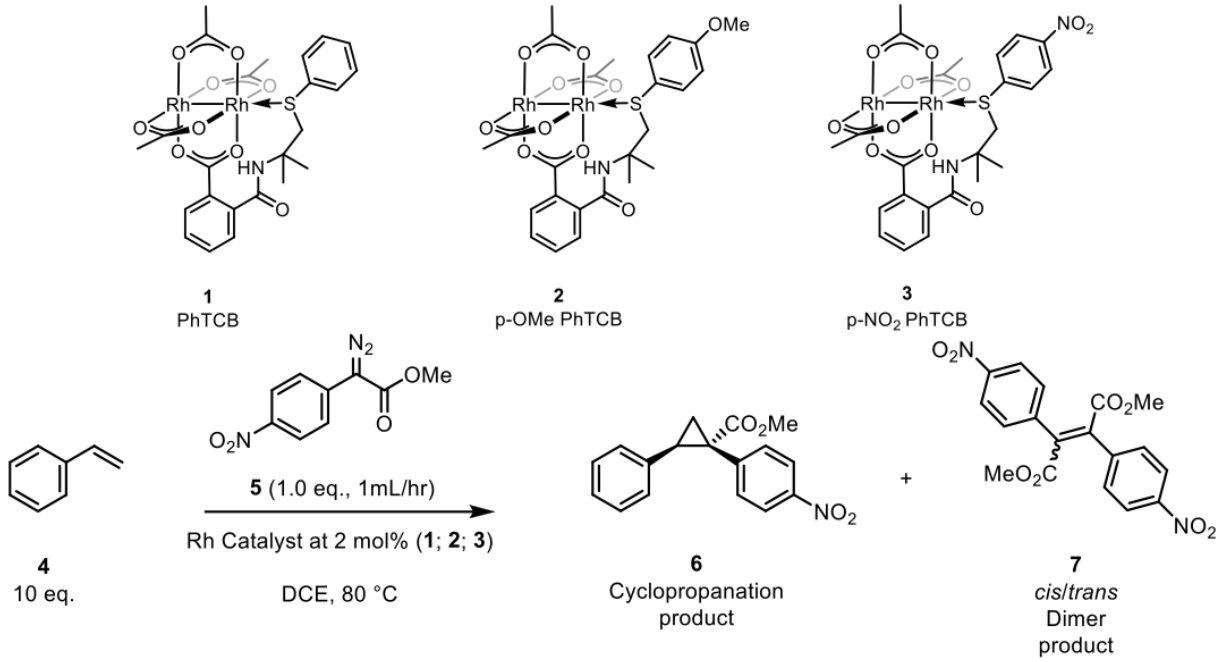


| entry | Rh catalyst | Catalyst (mol%) | Yield (%)[a] | 6/7[b] |
|---|---|---|---|---|
| **1** | 1 | 1.75 | 75 | >100:1[c] |
| **2** | 2 | 2 | 69 | >100:1[c] |
| **3** | 3 | 2 | 61 | 78:1 |
| **4** | $Rh_2(OAc)_4$ | 2 | 49 | 5.4:1 |

FIGURE 4.1. Cyclopropanation reactions catalyzed by $Rh_2(OAc)_3$(PhTCB) and $Rh_2(OAc)_4$.[a]Yields obtained from an average of two reactions. $^1$H NMR using mesitylene as an internal standard was used in order to obtain yields. [b]Ratio of two products was determined using $^1$H NMR. [c]The ratio calculated was beyond standard NMR detection limits.

Meanwhile, the double-Rh center trait of Rh(II) paddlewheel complexes has led to the exploration of tethered, axially coordinated ligands (TACLs). This design stems from the *remote control* effect on the vacant axial position, which can be coordinated by a solvent molecule, another carbene, or even part of the ligand. [**183**, **184**, **185**, **186**] Preliminary results from Darko's lab have shown that thioether-appended TACLs can significantly enhance

the efficiency and yields of diazo-mediated reactions compared to $Rh_2(OAc)_4$ (as shown in Figure 4.1). However, the origin of this improved performance remains unclear.

The prevailing hypothesis suggests that coordination on the distal Rh remotely modulates the catalytic mechanism by adjusting the Rh centers. To validate the postulate, we use DFT to investigate mixed-ligand Rh catalysts featuring a sulfur atom, which is designed to occupy the axial-coordination position. Interestingly, this opens up the possibility that following $N_2$ extrusion, the metal carbene, and even the C-C activation step may involve a sulfonium intermediate with the TACL rather than the Rh (Scheme 4.1b). It's worth noting that four-TACL-substituted dirhodium catalysts may be unable to capture the ylide intermediate due to steric hindrance between the ligands. This scenario also presents a possibility where the catalyst remains intimately involved throughout the reaction, potentially offering new avenues for control and selectivity in sulfur-mediated organometallic transformations. By applying advanced computational methods, we aim to elucidate the mechanistic details of this reaction, potentially uncovering novel insights into the broader class of dirhodium-catalyzed transformations.

## 4.2. Computational Methods

DFT calculations for this study were performed using *Gaussian16 C.01*. [**87**] Geometry optimizations were carried out using the B3LYP functional with Grimme's D3 dispersion correction (B3LYP-D3(0)), employing the def2-SV(P) basis set. [**88**, **89**, **90**, **103**, **187**] Single-point energy calculations on the optimized structures were subsequently conducted at the SMD(DCE)-PWPB95-D4/def2-TZVPP level of theory using *ORCA 5.0.4*. [**188**] These functional/basis set combinations have also been previously benchmarked and successfully applied to similar reaction systems. [**189**] The dichloromethane (DCM) solvent environment was modeled using the SMD implicit solvation model at single-point energy correction. *Quasi*-harmonic thermochemical corrections at 353.15 K and 1.0 M concentration were computed using the *GoodVibes* software package. [**36**] Transition state structures were identified

by the presence of a single imaginary vibrational frequency, and their connections to relevant minima were confirmed through IRC analyses. [**28**, **29**]

To identify the optimal conformations for each stationary structure, we employed both CREST from xTB and GOAT from the latest version of *ORCA 6.0*. All conformers within a 10 kcal/mol energy window were subsequently optimized using DFT calculations to determine the lowest energy structure.

### 4.3. Mechanism Investigation with $Rh_2(OAc)_4$

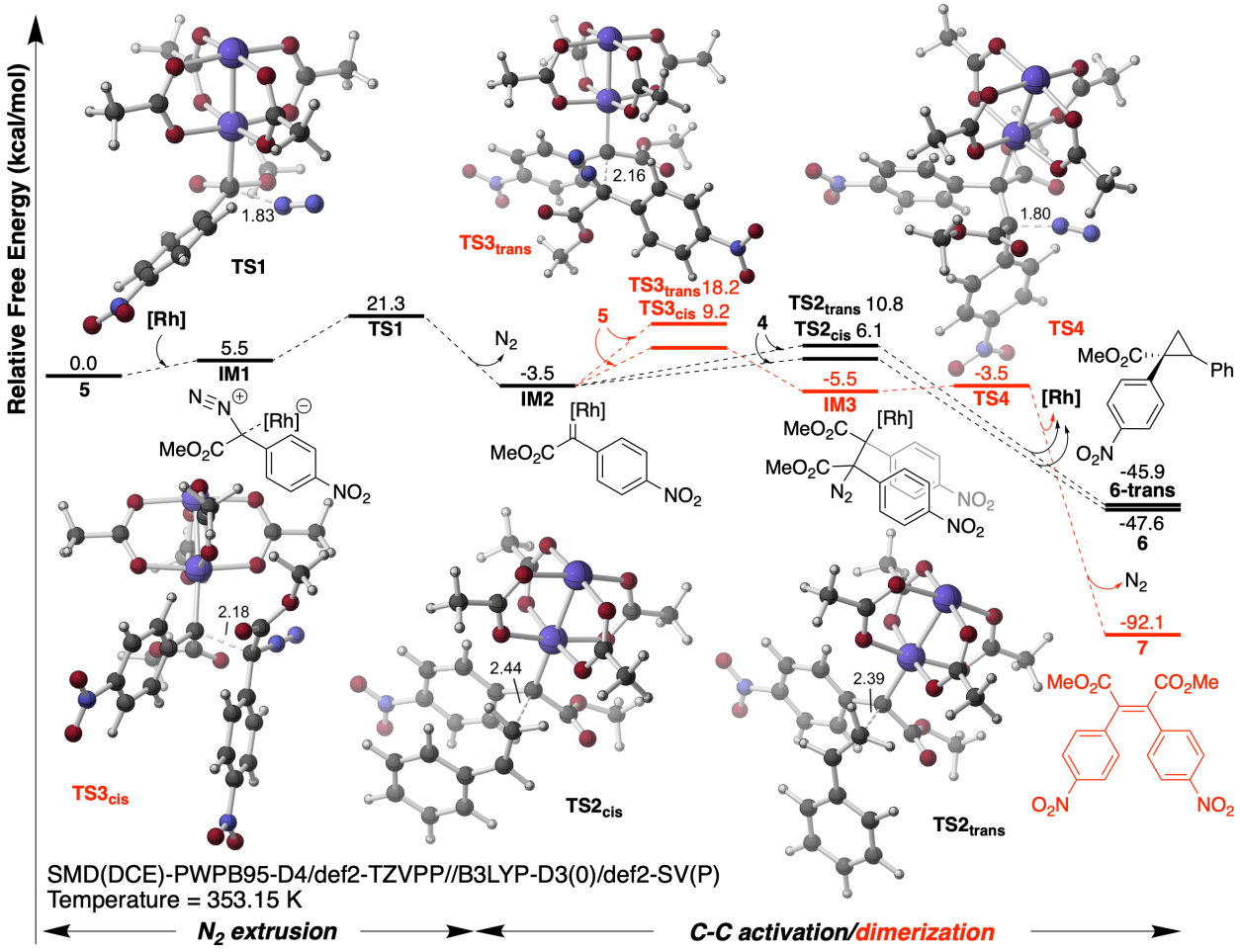


FIGURE 4.2. Energy profile of $Rh_2(OAc)_4$ catalyzed cyclopropanation v. dimerization under SMD(DCE)-PWPB95-D4/def2-TZVPP//B3LYP-D3(0)/def2-SV(P) at 353.15K.

First, we investigated the mechanism using the simple catalyst $Rh_2(OAc)_4$, which provides a straightforward model despite its moderate selectivity (5.4:1 of **6**/**7** ratio). Computational analysis confirmed $N_2$ extrusion as the rate-determining step, with a 21.3 kcal/mol barrier. Post Rh-carbene generation, two pathways compete: cyclopropanation *via* C-C activation (compound **4** + **5**), and dimerization (compound **5** + **5**). Cyclopropanation yields **6** through $\mathbf{TS2}_{cis}$ ($\Delta G^{\ddagger}$ = 9.6 kcal/mol, relative to **IM2**) Dimerization proceeds *via* $\mathbf{TS3}_{cis}$, followed by another $N_2$ leaving **TS4** to generation **7** in a *cis* form. The *trans*-cyclopropanation $\mathbf{TS2}_{trans}$ is higher than these two TS ($\Delta G^{\ddagger}$ = 14.3 kcal/mol, relative to **IM2**), due to the lack of a $\pi - \pi$ stacking pose. Combining the three TSs with the highest $\mathbf{TS3}_{trans}$ ($\Delta G^{\ddagger}$ = 21.7 kcal/mol, relative to **IM2**), no *trans* products are expected to be observed in the experiment. An alternative pathway involving direct C-N bond formation (**TS3'**) presents a higher barrier than TS3 ($\Delta G^{\ddagger}$ = 14.7 kcal/mol), requiring subsequent rearrangement to form **7** (Details in Appendix 4.7).

### 4.4. Dual Mechanistic Pathways Revealed by 1 and 1-carbene

The investigation of $Rh_2(OAc)_3$(PhTCB) began with exploring its structure (compound **1**). The optimal conformations benefit from the Z-form of the amide and an explicit S-Rh coordination bond, as illustrated in Figure 4.3. The relative positioning of the amide and $OAc^-$ ligands also determines the energetics. Conformer 2 emerges as the lower energy structure, despite conformer 1 featuring two hydrogen bonds between the amide hydrogen and $OAc^-$. Conformers 3 and 4 are less favorable: conformer 3 adopts the E-form of the amide, incurring a 7.8 kcal/mol energy penalty, while conformer 4 exhibits a dissociated S-Rh structure with a Ph coordination geometry, resulting in a 5.5 kcal/mol higher energy. Next, we identified the optimal structure of the Rh-carbene intermediate, which is the key precursor for the cyclopropanation step. Four distinct structural patterns were proposed:

(1) Pattern A: The carbene center and sulfur atom occupy opposite coordination sites on the rhodium center.

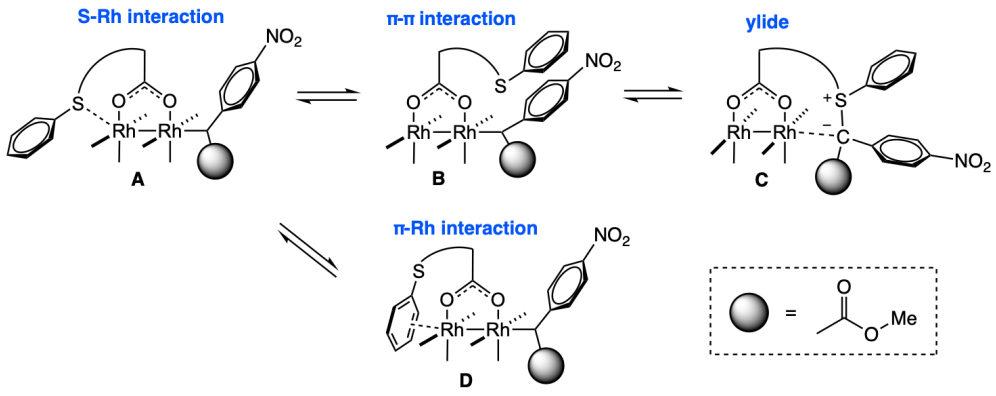


SCHEME 4.2. Illustration of the four possible intermediate structures at the carbene stage.

(2) Pattern B: The sulfur dissociates from rhodium, allowing the PhTCB ligand to twist and approach the carbene center.

(3) Pattern C: Following sulfur dissociation from rhodium and ligand twisting, an S-C bond forms, generating an ylide intermediate.

(4) Pattern D: The sulfur dissociates from rhodium, allowing the phenyl on the PhTCB ligand to coordinate with the vacant Rh (similar to conformer 4 in Figure 4.3)

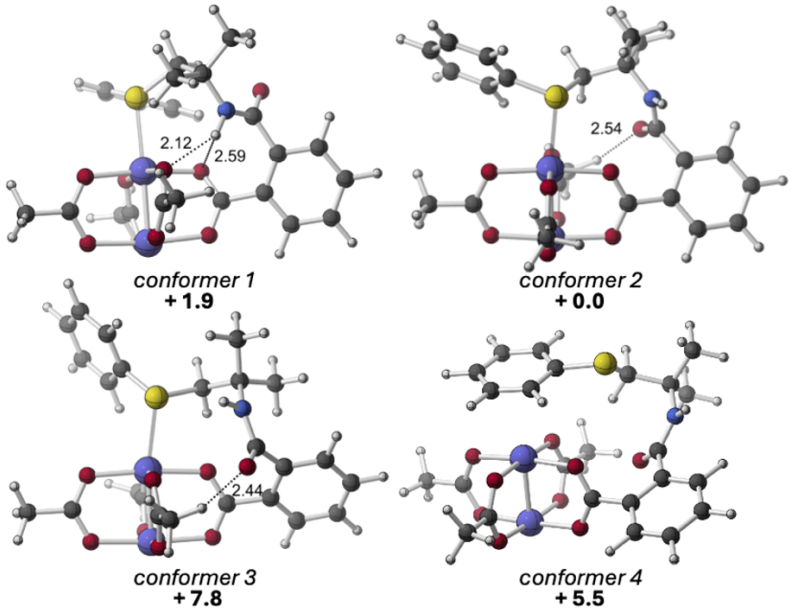


FIGURE 4.3. Representative conformers of $Rh_2(OAc)_3$(PhTCB) with relative free energies labeled.

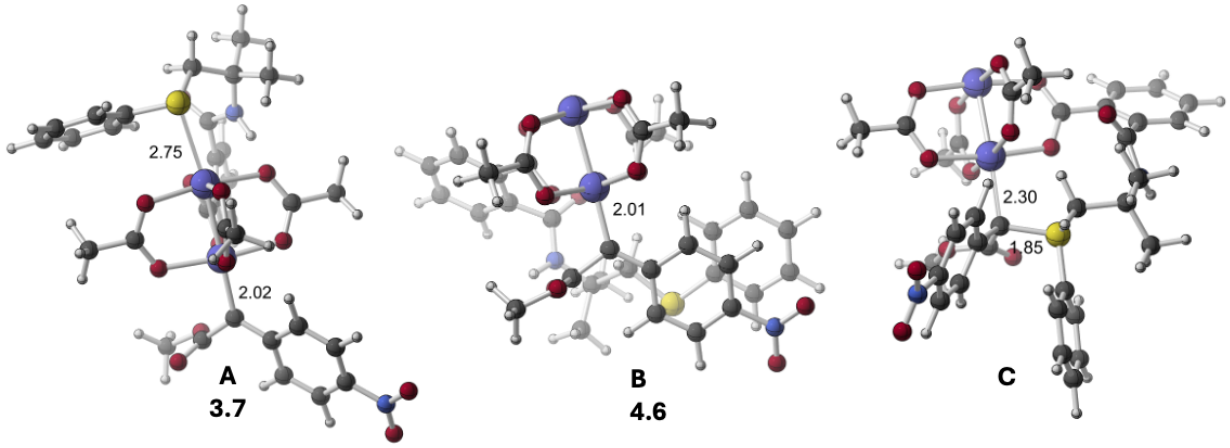


| | Pattern A | Pattern B | Pattern C | Pattern D |
|---|---|---|---|---|
| Rh-S | 2.75 Å | - | - | - |
| Rh-Rh | 2.48 Å | 2.47 Å | 2.46 Å | 2.47 Å |
| Rh-C | 2.02 Å | 2.01 Å | 2.30 Å | 1.99 Å |
| ΔG | 3.7 | 4.6 | -19.8 | 4.0 |

FIGURE 4.4. The structure and relative free energies of three Rh-carbene geometries visualized by *CYLView 1.0* with key bond length labeled and summarized in the table below. $\Delta G$ is under SMD(DCE)-PWPB95-D4/def2-TZVPP//B3LYP-D3(BJ)/def2-SV(P) at 353.15K in kcal/mol.

Scheme 4.2 illustrates four possible intermediates present at the Rh-carbene stage. Four structures correspond to patterns A, B, C, and D with their relative free energies displayed in Figure 4.4. Only pattern A has been considered in the dirhodium-catalyzed reaction mechanism, the other three are first proposed and verified in this DFT study. In the initial catalyst stage, the S-Rh bond length in **1** is approximately 2.52 Å, which elongates to 2.75 Å in the carbene stage of pattern A. Despite benefiting from $\pi - \pi$ stacking between the substrate and PhTCB ligand, pattern B is about 1 kcal/mol higher in energy than Pattern A. This energy difference likely stems from the distortion of the PhTCB ligand. The ylide structure in Pattern C exhibits significantly lower energy than the other patterns, representing a deep energy minimum along the reaction pathway.

Pattern D initially exhibits an energy over 5 kcal/mol higher than Pattern A in the catalyst structure. However, this energy difference diminishes in the carbene stage. (conformer 2 v. conformer 4 in Figure 4.3) This energy shift correlates with weakened Rh-SPh interactions

following carbene attachment, as the opposite Rh center becomes more nucleophilic. Consequently, the S-Rh coordination appears to be dynamic rather than static throughout the catalytic cycle, contrary to what one might initially assume.

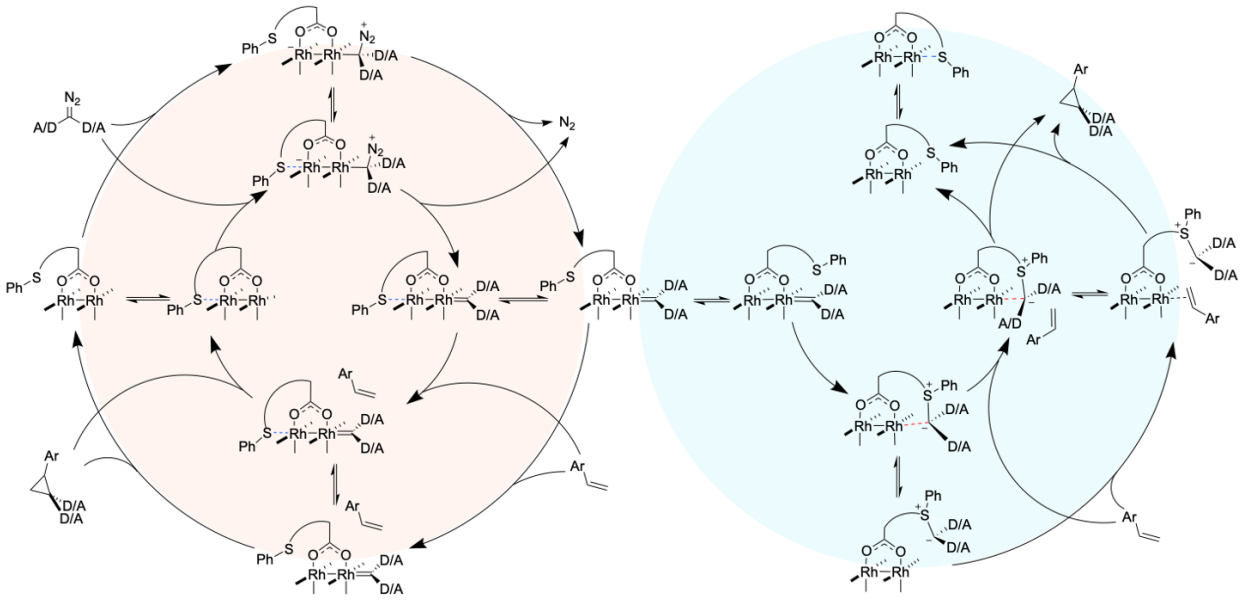

FIGURE 4.5. Catalytic mechanism of $Rh_2(OAc)_3$(PhTCB) elucidated in this study. The primary catalytic cycle (left) depicts the configuration where PhTCB occupies the axial position opposite to the reaction site. An alternative mechanism is illustrated in the outer cycle, involving S-Rh bond cleavage and potential non-covalent interactions between PhTCB and the *p*-$NO_2$Ph acceptor group on the carbene substrate.

Considering the above results, we question the assumption that the tethered ligand merely serves as a remote controller to adjust the reactivity of the dirhodium catalyst. Here, we propose a more nuanced scenario for the asymmetric catalytic system mediated by **1** with two plausible mechanistic pathways:

(1) Non-ylide pathway that leads to three possible configurations - the SPh group remaining in position, sulfur dissociating to allow phenyl coordination with rhodium, or the phenyl group engaging in stacking with the substrate's *p*-$NO_2$Ph group (orange cycle on the left side in scheme 4.5). This pathway proceeds without ylide formation or associated deep energy minimum traps.

(2) A ylide-mediated pathway where, following S-Rh bond dissociation, the PhTCB ligand nucleophilically attacks the carbene center, forming a ylide structure (blue cycle on the left side in scheme 4.5). This may be followed by C-Rh bond dissociation, with ethyldiazoacetate subsequently reacting with either a free or metal-ligated ylide through an inner-sphere mechanism to generate **6** and **7**.

## 4.5. Non-Ylide Mechanism

The initial $N_2$ extrusion step was confirmed to proceed primarily *via* pattern A (details in Appendix 7.3.1), with an S-Rh coordinated transition state (**TS1-A**) exhibiting a 28.1 kcal/mol barrier. Pattern B showed a slightly higher energy barrier (**TS1-B**, $\Delta G^{\ddagger} = +29.9$ kcal/mol), while pattern D had the highest energy among the three (**TS1-D**, $\Delta G^{\ddagger} = +30.3$ kcal/mol) due to the weaker electron donating phenyl than thiol. Besides, no transition state for $N_2$ extrusion was identified for pattern C. Given these competing barriers, all leading to $N_2$ extrusion but in different conformations, the intermediate generated after this step is predominantly the pattern A Rh-carbene. This conclusion is based on the relative energies of the TSs and the principle of kinetic control. Structures are depicted in Appendix 7.3.1.

To further investigate the interconversion of different **1**-carbene geometries in Scheme 4.2, we identified transition structures corresponding to S-Rh bond dissociation and C-S bond formation (Figure 4.6). Following the formation of **IM2-A**, the S-Rh bond dissociates readily with a low barrier of 0.8 kcal/mol (**TS(A-D)**) relative to **IM2-A**, forming **IM2-D**. Subsequently, we posit that the PhTCB ligand possesses sufficient flexibility to approach the carbene, with a conformational change barrier lower than the rate-determining $N_2$ extrusion **TS1-A** to form **IM2-B**.

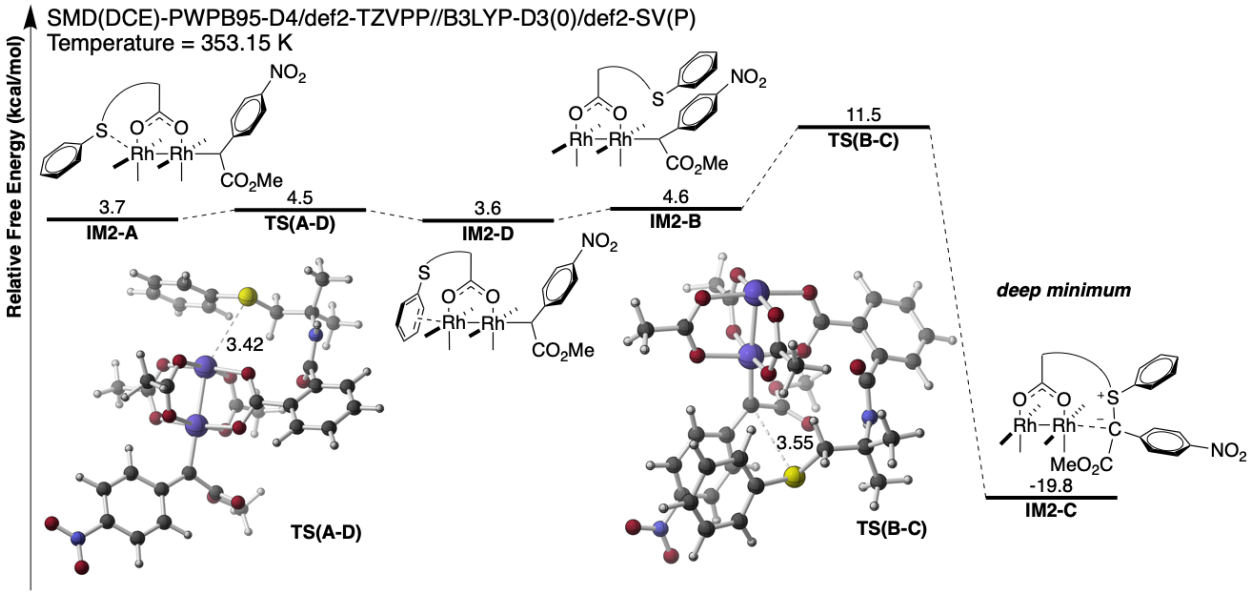


FIGURE 4.6. Energy profile of the ylide formation mechanism catalyzed by $Rh_2(OAc)_3$(PhTCB) under SMD(DCE)-PWPB95-D4/def2-TZVPP//B3LYP-D3(0)/def2-SV(P) at 353.15K. TSs are visualized by CYLView 1.0 with critical bond length labeled in Å.

After that, S-C bond formation requires overcoming a 8 kcal/mol barrier (relative to **IM2-D**) to generate the ylide **IM2-C**. Ultimately, the Rh-carbene forms a highly stable ylide structure, which is around 20 kcal/mol lower in energy than the starting material. The interconversion between carbene geometries ultimately leads to a thermodynamically favored ylide intermediate – a deep energy minimum. This discovery presents a challenging scenario: all subsequent C-C activation barriers are elevated by approximately 20 kcal/mol. This stands in stark contrast to the $Rh_2(OAc)_4$ system depicted in Figure 4.2, where the Rh-carbene **IM2**'s energy is merely 3.5 kcal/mol lower than that of the reactant.

To proceed with the following C-C activation *via* patterns A, B, and D, the S-C bond must cleave. However, under the reaction conditions of 80 °C, this process encounters a formidable barrier of 31.3 kcal/mol. The subsequent C-C activation transition states for patterns A, B, and D demand even higher energy (Figure 4.7). The three **TS2** barriers are within a 2 kcal/mol difference, with pattern D exhibiting a slightly lower barrier ($\Delta G^{\ddagger}$ = 32.0 kcal/mol). Additionally, we computed the stepwise dimerization process, encompassing

**TS3** and **TS4**. The results reveal that the energy difference between the competing barriers for cyclopropanation versus dimerization is approximately 6 kcal/mol. (4 kcal/mol difference was observed in the $Rh_2(OAc)_4$ system). Another observation reveals that the energies of **TS3-B(cis)** and **TS3-D(cis)** are much higher than that of **TS3-A(cis)**. This suggests that the alternative conformers we have proposed, aside from the "remote control" model, not only fail to facilitate the formation of byproduct **7**, but actually elevate the energy barrier significantly.

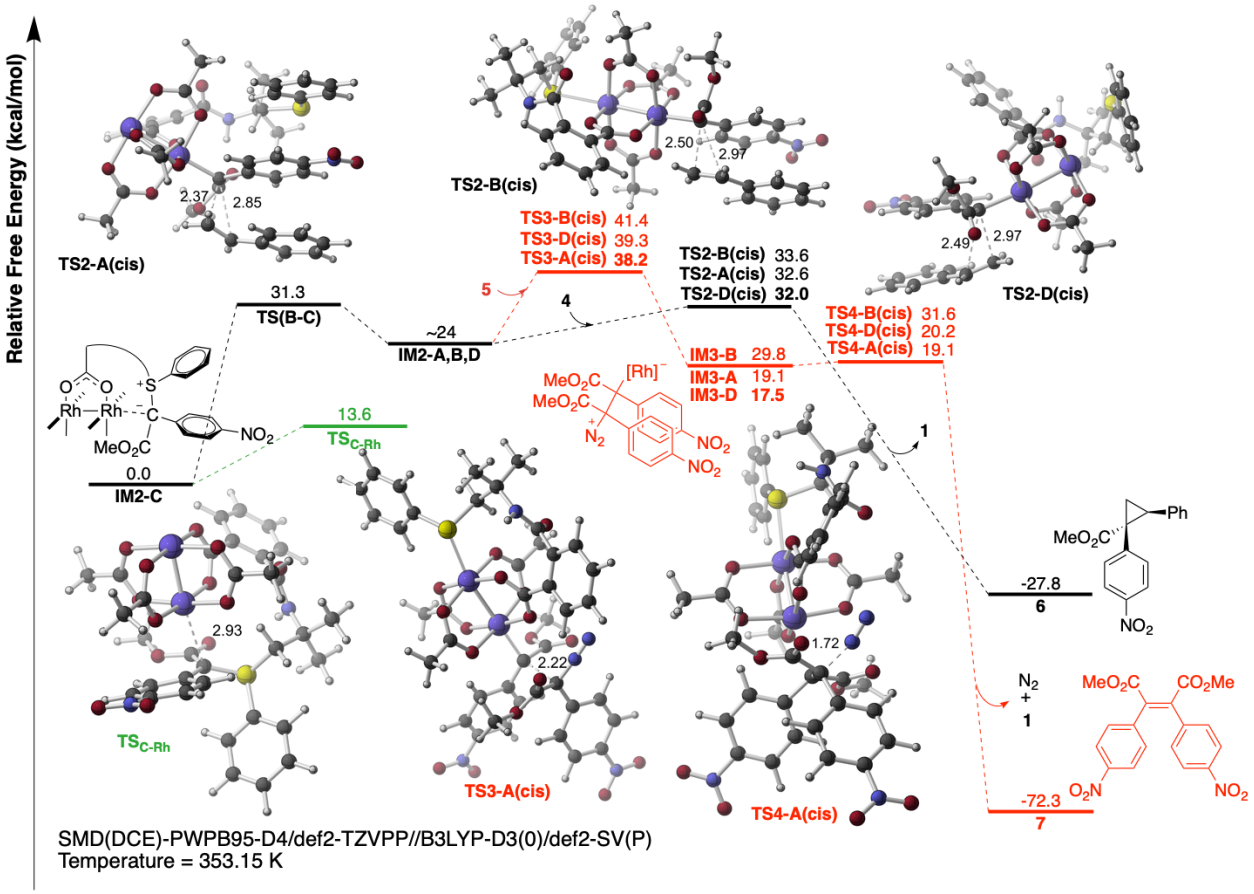


FIGURE 4.7. Energy profile of the non-ylide mechanism catalyzed by $Rh_2(OAc)_3$(PhTCB) under SMD(DCE)-PWPB95-D4/def2-TZVPP//B3LYP-D3(0)/def2-SV(P) at 353.15 K. High-energetic TS are visualized in Appendix 7.3.2. The deep minimum **IM2-C** is set as the reference point (zero) for relative free energies, providing a clearer view of the heights of the rate-determining and selectivity-determining barriers. Critical bond lengths in Å are labeled in the TS visualized by *CYLView 1.0*.

### 4.6. Free ylide or not?

Is this a dead end? Computationally, all molecules appear trapped in this deep energy well, yet experimentally, they proceed to form cyclopropanation and dimerization products. This apparent contradiction demands a closer examination of the reaction mechanism. We first attempted to position styrene near the reactive site. The C-C activation transition state exhibits a structure with a dissociated C-Rh bond. Therefore, we located the **TS5** for cleaving the Rh-C bond, which is approximately 14 kcal/mol (green lines in Figure 4.7), significantly lower than the **TS(B-C)** for breaking the S-C bond.

Consequently, cyclopropanation likely proceeds *via* a mechanism involving a "*quasi*-free" ylide intermediate (Scheme 4.1). It's crucial to note that since the thiophenyl group is part of the catalyst, a truly "free" ylide does not exist. Instead, the catalyst remains in close proximity throughout the reaction, maintaining interaction with the ylide.

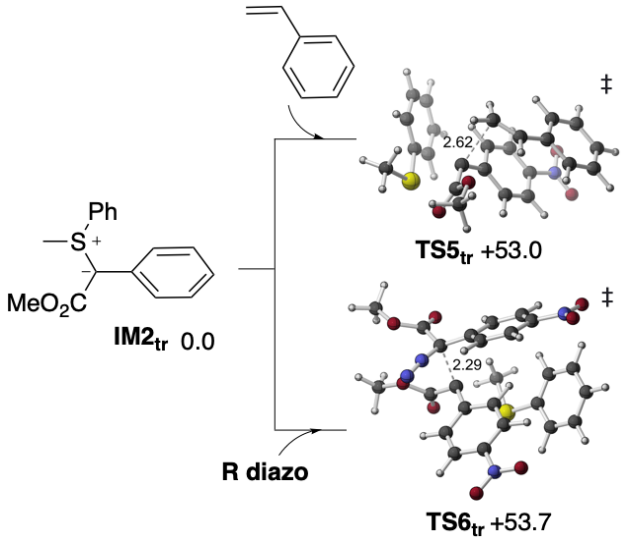


FIGURE 4.8. TS and free energy barriers of C-C coupling from truncated free ylide.

To quickly assess the accessibility of the C-C activation barrier, we explored $\mathbf{TS5}_{tr}$ using a truncated catalyst model (*tr* refers to truncated), incorporating only the SPh group as a representative of the full catalyst. However, this simplification yields prohibitively high

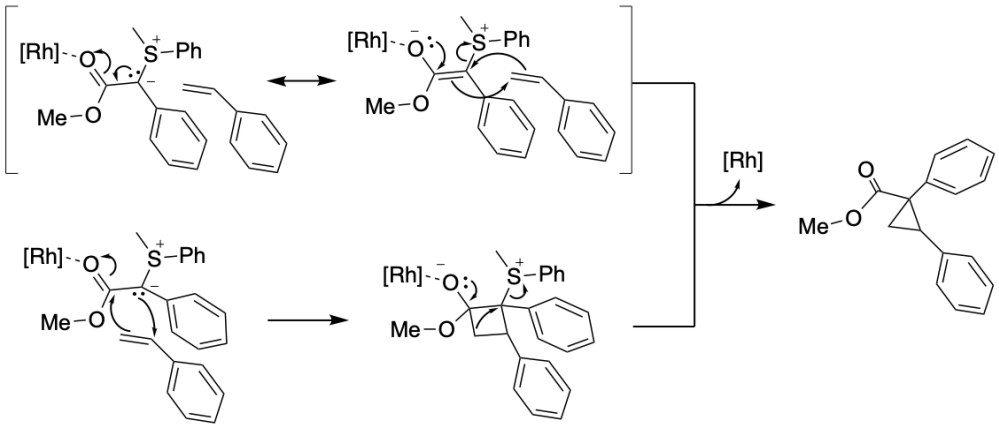


SCHEME 4.3. Schemetic illustration of the outer-sphere C-C activation mechanisms.

barriers exceeding 53 kcal/mol for both cyclopropanation ($\mathbf{TS5}_{tr}$) and dimerization ($\mathbf{TS6}_{tr}$), see Figure 4.8), with negligible selectivity when the paddlewheel center is omitted.

To reintroduce the catalyst into the system, we first examined the cyclopropanation **TS7** with Rh coordinated to the $CO_2Me$ group, which corresponds to an "outer-sphene" geometry. While the barriers are no longer as high as those of the truncated free ylide, the best transition state identified through comprehensive conformational searching (as described in the method section) still exhibited a barrier exceeding 40 kcal/mol (see Scheme 4.3).

An alternative mechanism involves Rh coordination with styrene to facilitate C-C coupling from the ylide, which corresponds to the outer cycle on the right side of Scheme 4.1 in blue. The TS geometry can be described as an inner-sphere structure in which the catalyst becomes a *clip* that holds the styrene at the center. This configuration determines the *cis*/*trans* selectivity based on the relative positioning of styrene between [Rh] and the ylide substrate. Our preliminary exploration has reduced the barrier to 35.6 kcal/mol, comparable to $\mathbf{TS3}_{cis}$ in Figure 4.7.

**4.6.1. What's Next? – A Pre-Conclusion.** Current findings suggest that our proposed conformers are essential for understanding how $Rh_2(OAc)_3$(PhTCB) catalyzes the C-C activation reaction. We discovered that a deep ylide structure can block all plausible transition states we had initially proposed. However, by uncovering this previously overlooked

possibility, we have discovered a more comprehensive catalytic cycle (Scheme 4.5). Additionally, the $Rh_2(OAc)_3$(PhTCB) catalyst forces the ylide into a "*quasi*-free" state – though with a low dissociation barrier of 13.6 kcal/mol, the $Rh_2(OAc)_3$(PhTCB) is a part of the ylide. Although the [Rh] center does not directly coordinate with the sulfur atom anymore, it may still exert an influence on the reaction. In summary, our mechanistic analysis reveals a delicate balance between ylide formation, metal coordination, and substrate interaction, which is crucial for understanding the observed reactivity and selectivity in this catalytic system.

Another possibility is that the transformation from **IM2-D** to **IM2-B** requires overcoming an energy barrier higher than 8.6 kcal/mol ($G_{\text{TS2-D(cis)}} - G_{\text{IM2-D}}$), which is the relative energy of **TS2-D(cis)** with respect to **IM2-D** without encountering the ylide intermediate **IM2-C**. Currently, the formation of **IM2-C** is energetically favored with a lower barrier of 6.9 kcal/mol ($G_{\text{TS(B-C)}} - G_{\text{IM2-D}}$) when the PhTCB rotational barrier is neglected. However, quantifying the energy required for conformational changes in this case is challenging, as it cannot be described by a single transition state. Based on our results now, we would presume that most of the Rh-carbene may fall to the deep well of the ylide.

Moreover, even after the formation of ylide **IM2-C**, the catalyst retains a vacant coordination site on Rh, which will catalyze the subsequent $N_2$ extrusion and cyclopropanation processes. In this scenario, the ylide modulates the electron density of the Rh center, such that the *remote control* now involves the entire ylide moiety rather than solely the sulfur atom.

### 4.7. Why not B3LYP for SPE Correction

The most critical structure we have discovered is undoubtedly the knotty ylide intermediate. To assess the stability of this "well" and validate the robustness of our theoretical methods, we employed two additional functionals widely used in organometallic chemistry, B3LYP and PBE0, to reevaluate the S-C bond dissociation barrier. Our findings indicate that the energy of this challenging minimum varies depending on the functional used for single-point energy correction.

As shown in Figure 4.6, breaking the S-C bond of the ylide requires an energy barrier of over 31 kcal/mol (formidable under 80 °C) when using the PWPB95-D4 functional. However, with the same basis set (def2-TZVPP), single-point corrections performed using B3LYP-D3(0) and PBE-D3(0) yield significantly lower energy barriers of 21.5 and 28.9 kcal/mol, respectively. Consequently, the subsequent barriers for C-C activation are also lowered, and the stability of the ylide is underestimated by these two functionals. Benchmark work on ylide bond dissociation by Truhlar [**190**] has shown that among the DFT functionals considered, PBE0-D3(0) is one of the most accurate, with a Mean Signed Error (MSE) of -2.2 kcal/mol, while B3LYP-D3(0) exhibits a larger error of -7.84 kcal/mol. The trend of barrier height here is consistent with previous benchmark studies, alleviating concerns about the PWPB95-D4 functional that we chose.

So what happens if B3LYP-D3(0) is used for this system? You might get a seemingly perfect answer — but it would be **wrong**. After generating the ylide intermediate, the barrier predicted by B3LYP-D3(0) can easily allow a reversal back to **IM1-A** and **IM1-B**. The subsequent C-C activation would then proceed primarily through the cyclopropanation pathway, as the **TS2** is low enough to occur (around 25 kcal/mol, as shown in Figure 4.9). Meanwhile, the **TS3** barriers remain significantly high, nearly identical to those in Figure 4.7. This computational outcome can perfectly explain why $Rh_2(OAc)_3$(PhTCB) exhibits excellent selectivity in experiments, based on these kinetic barriers. However, this result is an artifact – a case of accidentally getting the right answer with the wrong computational approach. While B3LYP with dispersion corrections is widely regarded as a robust functional for organometallic systems, it falls short in this scenario due to its deficiency in describing ylide intermediates. This isn't a fault of B3LYP itself; rather, it underscores the critical importance of selecting the appropriate computational method. It also serves as a cautionary reminder of the risks associated with uncritical theory selection.

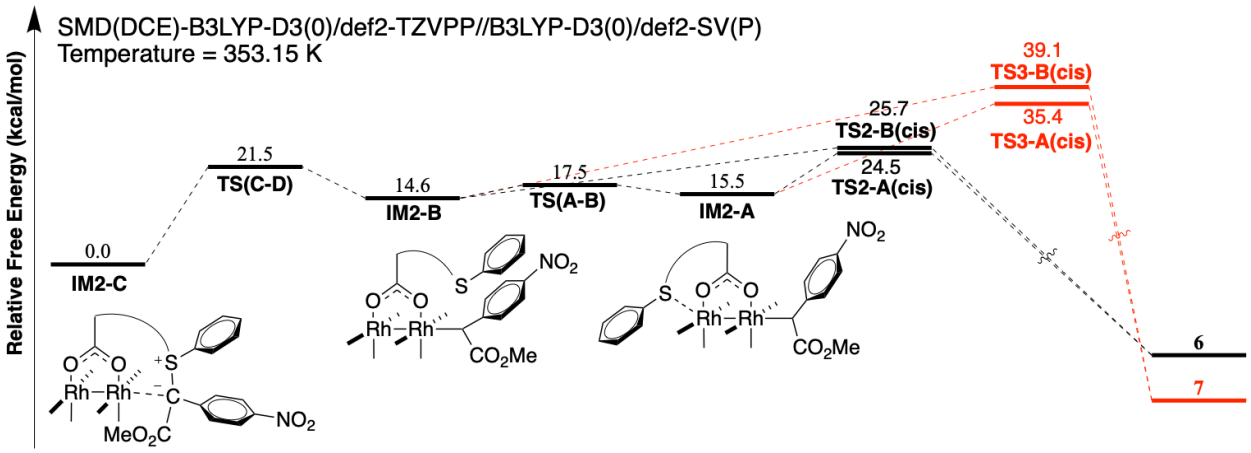


FIGURE 4.9. Free energy profile of the after-ylide mechanism catalyzed by $Rh_2(OAc)_3$(PhTCB) using B3LYP-D3(0) as the SPE functional at 353.15 K.

CHAPTER 5

# Revisiting a Classic Carbocation - DFT, Coupled-Cluster, and *ab initio* Molecular Dynamics Computations on Barbaralyl Cation Formation and Rearrangements

Density functional theory computations were used to model the formation and rearrangement of the barbaralyl cation ($C_9H_9^+$). Two highly delocalized minima were located for $C_9H_9^+$, one of $C_s$ symmetry and the other of $D_{3h}$ symmetry, with the former having lower energy. Quantum chemistry-based NMR predictions affirm that the lower energy structure is the best match with experimental spectra. Partial scrambling was found to proceed through a $C_2$ symmetric transition structure associated with a barrier of only 2.3 kcal/mol. The full scrambling was found to involve a $C_{2v}$ symmetric transition structure associated with a 5.0 kcal/mol barrier. *Ab initio* molecular dynamics simulations initiated from the $D_{3h}$ $C_9H_9^+$ structure revealed its connection to six minima, due to the six-fold symmetry of the potential energy surface. The effects of tunneling and boron substitution on this complex reaction network were also examined.[1]

## 5.1. Introduction

A question driving many classic studies in the realm of physical organic chemistry is how many minima exist for a particular structure? For example, does a particular structure reside in one well or two on a PES, with the two in the latter case rapidly interconverting through a low barrier? This question is intimately tied to the degree of delocalization in organic structures.

[1]This chapter has been accepted by *Chemical Science*. The benchmarking results and metadynamics computations presented herein are attributed to Wang-Yeuk Kong.

The most famous examples of this type of issue involve "the nonclassical ion problem" (i.e., cyclic 3-center 2-electron delocalization) [**191**, **192**, **193**, **194**, **195**, **196**] and the search for "stable transition states" for Cope reactions (i.e., neutral homoaromaticity) [**197**, **198**, **199**, **200**]. But if barriers between minima are very low (how low depends on the temperature) it doesn't really matter if these barriers exist, i.e., very shallow minima and a flat PES are not expected to show differences in dynamical behavior. [**53**] Consequently, some felt and feel that such issues were not worthy of investigation and even forcefully complained that discussions (which often devolved into viperous arguments) may well have irreparably damaged the field of physical organic chemistry. Nonetheless, the one-well-or-two issue has led to many insights into electronic structure and associated reactivity that remain relevant today, raising their heads in contexts ranging from natural product biosynthesis to transition metal-promoted C-H insertion. [**201**, **202**, **203**, **204**]

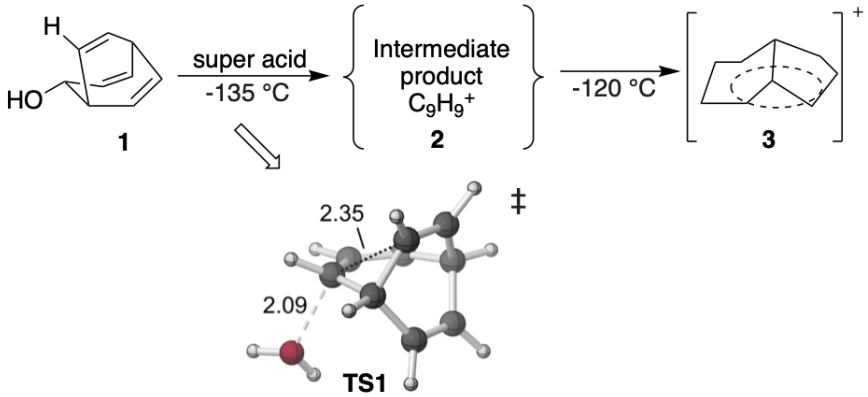


SCHEME 5.1. Previous experiments on $C_9H_9^+$ cations. [**205**] The transition state TS1 is visualized using *CYLview 1.0*, [**119**] with critical bond lengths labeled in Å. The C–O bond breaks first, and the C–C bond formation occurs subsequently in an asynchronous manner (see Appendix 7.4.2 for details).

Here we address structural and reactivity/dynamic issues for a classic carbocation with a putative nonclassical structure for which the number and identities of minima on its PES have long been uncertain: the barbaralyl cation (Scheme 5.1). As demonstrated by our computational results, this carbocation brings together the concepts of hyperconjugation (acyclic 3-center 2-electron delocalization), [**206**, **207**] nonclassical bridging (cyclic 3-center 2-electron

delocalization) [**191**, **192**, **193**, **194**, **195**, **196**], through-bond coupling, [**208**] homo/sigma-aromaticity, [**197**, **198**, **199**, **200**, **209**, **210**, **211**, **212**] sigmatropic shifts with low/no barriers (stable transition states?), [**197**, **198**, **199**, **200**, **213**] synchronicity, [**214**, **215**] entropic intermediates, [**43**] fluxionality, [**203**, **216**, **217**, **218**] non-statistical dynamic effects on caldera/mesas, [**140**, **219**, **220**, **221**, **222**] post-transition state bifurcations (PTSBs), [**53**, **55**, **219**, **223**, **224**, **225**, **226**], inter-transition state roaming, [**53**, **156**, **227**] and tunneling. [**228**, **229**, **230**, **231**] We cannot think of another carbocation, or any structure, that showcases so many principles of structure and reactivity, ranging from those appreciated a half-century ago or more to those only recently being recognized.

**5.1.1. $C_9H_9^+$ Barbaralyl cation.** The $C_9H_9^+$ barbaralyl cation has been studied both experimentally and computationally for decades. In 1970, Winstein and co-workers reported that $C_9H_9^+$ (**2**) could be generated by reacting bicyclo[3.2.2]-nona-3,6,8-trien-2-ol (**1**) at -135 °C with superacid ($FSO_3H$-$SO_2ClF$ in $CD_2Cl_2$) (Scheme 5.1) (following up on earlier solvolysis studies with a different substrate by Schleyer and co-workers). [**205**, **232**] Subsequently, NMR experiments led to various insights into the structure of **2**. A key observation was that, at -135 °C both the $^1H$ and $^{13}C$ NMR spectra of **2** contain only a single peak: a singlet at 6.6 ppm for $^1H$ and a peak at 118.5 ppm for $^{13}C$. [**233**, **234**] These results indicate that either nine CH groups are equivalent in the geometry of **2** or rapid equilibration during the NMR experiment leads to complete scrambling of all CHs. Since a regular polyhedron with nine vertices does not exist, and since cyclononatetraenyl cation possesses $8\pi$ electrons – a number associated with antiaromaticity or a Möbius topology, [**210**, **211**, **235**] it is very likely that fluxional isomerization is the cause of the simplicity of the NMR spectra. [**233**, **234**] In contrast, bullvalene ($C_{10}H_{10}$) only interchanges its CH groups when the temperature is raised to over 100 °C. [**236**] Moreover, as the temperature was decreased to -150 °C, the 118.5 ppm $^{13}C$ NMR signal of **2** split to two peaks at 101 and 152 ppm with a 6:3 integration ratio, consistent with a rearrangement that slows at low temperature. [**233**, **234**]

These experiments provide important constraints on the nature of the rearrangement and associated barrier heights.

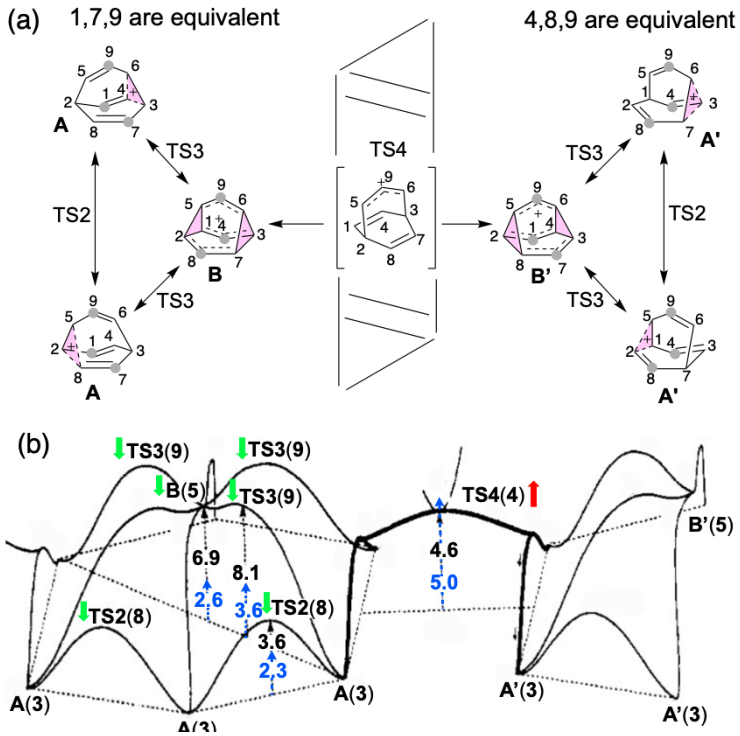


FIGURE 5.1. (a) Outline of the computed mechanism of barbaralyl cation scrambling. The equivalent carbons in the middle are highlighted with grey circles for the partial scrambling process. (b) Energy profile depicted by Albert in 1993 based on MP4(SDQ)/6-31G(d) results (reproduced with permission from ref [**237**]). Relative free energies determined here with DLPNO-CCSD(T)/CBS//CAM-B3LYP/6-31G(d) at 138.15 K (-135 °C) have been added (blue). Green and red arrows have also been added to indicate whether the energies increased or decreased compared to the previous results. Numbers in parentheses are the structure numbers from ref [**237**].

While the first computational study was reported at the MINDO/3 level in 1989, [**238**] Cremer and co-workers proposed a "pound cake"-shaped PES with two types of minima and three transition structures (Figure 5.1) in 1993 on the basis of calculations conducted at the MP4(SDQ)/6-31G(d) level of theory. [**237**] More recently, Werstiuk revisited this PES along with QTAIM-DI-VISAB analysis at the B3PW91/aug-cc-pVTZ and CCSD(full)/6–31+G(d,p)

levels of theory. [**239**] Other related works have examined the topology of the barbaralyl cation [**240**, **241**, **242**] and the less fluxional barbaralyl radical [**241**] and barbaralone. [**218**, **243**]

Here, we focus on the fluxionality of barbaralyl cation. A comprehensive benchmarking study using prevalent quantum mechanical methods was carried out, since the PES in question has rather flat regions. In addition, *ab initio* molecular dynamics (AIMD) simulations were used to characterize rearrangements. [**50**, **53**, **222**, **224**, **225**, **226**, **244**, **245**] Our results indicate that the highly delocalized nature of $C_9H_9^+$ structures gives rise to an unusual PES that supports complex dynamic effects. Beyond shedding light on the specific case of the barbaralyl cation itself, this study also points to potentially general considerations for the interplay of structure, stability, and dynamics in fluxional systems. [**197**, **198**, **199**, **216**, **217**, **218**, **246**, **247**, **248**]

### 5.2. Computational Methods

Initially, we performed geometry optimization using the M06-2X/def2-TZVP level of theory [**95**, **103**] with *Gaussian 16 C.01*, [**87**] due to its widely acknowledged robustness for molecules composed of main group elements [**249**] and its previous use for carbocations. [**250**, **251**, **252**, **253**, **254**] Single point energy corrections were then computed at the DLPNO-CCSD(T)/CBS level of theory using *ORCA 5.0.4*. [**255**, **256**, **257**] Basis set extrapolation to the complete basis set (CBS) limit was performed using the focal point analysis approach employing def2-TZVPP and def2-QZVPP basis sets. [**103**, **258**, **259**] The TightPNO cutoff was used for the local coupled cluster calculations and iterative triples corrections were used. [**260**] *Quasi*-harmonic thermochemical corrections were obtained using the *GoodVibes* package. [**187**, **261**] With this approach, one transition structure reported previously (**TS2**) was not found. [**237**, **239**] Consequently, an extensive benchmarking study was carried out. After examining geometries and energetics with density functionals and two basis sets (6-31G(d) and def2-SVP) (based on DLPNO-CCSD(T)/CBS//$\omega$B97X-D/def2-TZVP results as **TS2** cannot be located with M06-2X functional, see Appendix 7.4.1), it became clear

that different functionals lead to divergent conclusions with regard to the relative energies of structures and existence of stationary points on PES).

Although absolute energy differences were not large, i.e., the flatness of the PES was consistently reproduced, interpretation of NMR data requires quite accurate energies. Among the different levels of theory investigated, the CAM-B3LYP range-separated hybrid functional with the 6-31G(d) Pople basis set provided the best agreement with the relative electronic energies obtained at the DLPNO-CCSD(T)/CBS level for this specific system.* [**92**, **262**, **263**, **264**][2] Consequently, results from this level of theory are discussed below. For results with M06-2X/6-31G(d), see Appendix 7.4.7. IRC calculations were carried out at the CAM-B3LYP/6-31G(d) level of theory. [**28**, **104**, **265**]

To explore the dynamic behavior of $C_9H_9^+$ cations, the Progdyn script developed by Singleton was employed. [**83**] Trajectories were propagated with a 1 fs time step using the Verlet algorithm. Both downhill (initiated at transition states) and uphill trajectories (initiated from minima using the "cannonball" approach, see Appendix 7.4.5 for details) were collected. Metadynamics simulations were used to construct free energy surfaces using *ORCA 5.0.4*. [**257**, **266**], $^1$H and $^{13}$C NMR chemical shifts for the barbaralyl cation ($C_9H_9^+$) were calculated using the revTPSS functional in combination with the pcSseg-1 basis set on structures optimized with CAM-B3LYP/6-31G(d). [**267**, **268**, **269**] To convert computed isotropic values to the conventional NMR scale, isotropic shielding values computed for tetramethylsilane (TMS) were used as a reference.

The effects of tunneling were investigated using the *Gaussrate/Polyrate* package developed by Truhlar. [**105**, **106**] Calculations were performed at the CAM-B3LYP/6-31G(d) level of theory. The tunneling contributions were quantified using two methods: small curvature

[2]The exceptional delocalized structure of the barbaralyl carbocation ($C_9H_9^+$) makes CAM-B3LYP without dispersion particularly effective. Despite its lack of popularity in carbocation studies, CAM-B3LYP yields optimal results for $C_9H_9^+$ compared to the "standard" coupled cluster method. For common carbocations, which are not extremely delocalized, extensive benchmarking with many functional candidates may not be unnecessary, as M06-2X should suffice.

tunneling (SCT) and zero curvature tunneling (ZCT). [**270**] Further details regarding the computational methodology employed can be found in the Appendix 7.4.8.

## 5.3. Shapeshifting Geometries and Energies

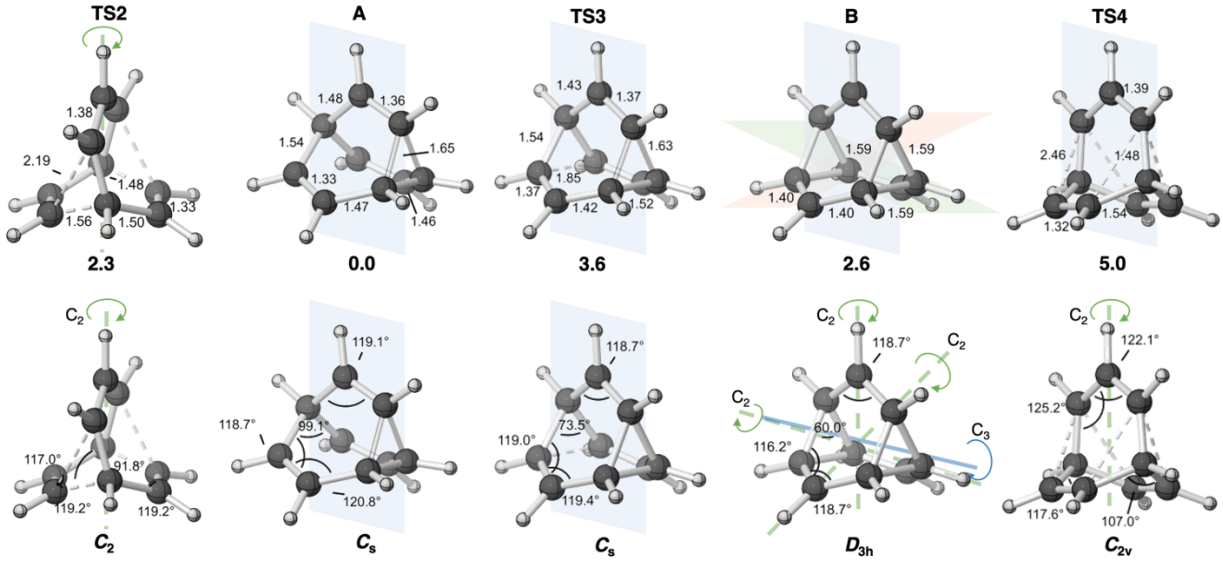


FIGURE 5.2. Geometries (selected distances in Å) of **A**, **B**, and transition structures relevant to the fluxionality of $C_9H_9^+$. Structures in top and bottom rows are the same. The rotational symmetry axis and planes of symmetry are shown along with point groups. Structures were optimized with CAM-B3LYP/6-31G(d). Relative free energies at the DLPNO-CCSD(T)/CBS//CAM-B3LYP/6-31G(d) level (thermochemical corrections from the lower level of theory included) are shown below each structure in the top row.

**5.3.1. Degenerate rearrangements.** First, we reexamined the previously described $C_9H_9^+$ PES using density functional theory (DFT). As shown in Scheme 5.1, carbocation **A** is generated following loss of water from protonated **1** *via* transition structure TS1; C–O bond breakage and C–C bond formation occur asynchronously. [**271**]

Carbocation **A** (+ $H_2O$) is connected to transition structure TS1 (Scheme 5.1) by an IRC (Appendix 7.4.2). This structure is set as the baseline for representing relative energies. The geometry of **A** is that of a "classic" non-classical carbocation with a cyclic 3-center 2-electron bonding array (highlighted in pink in line drawings). [**191**, **192**, **193**, **194**, **194**,

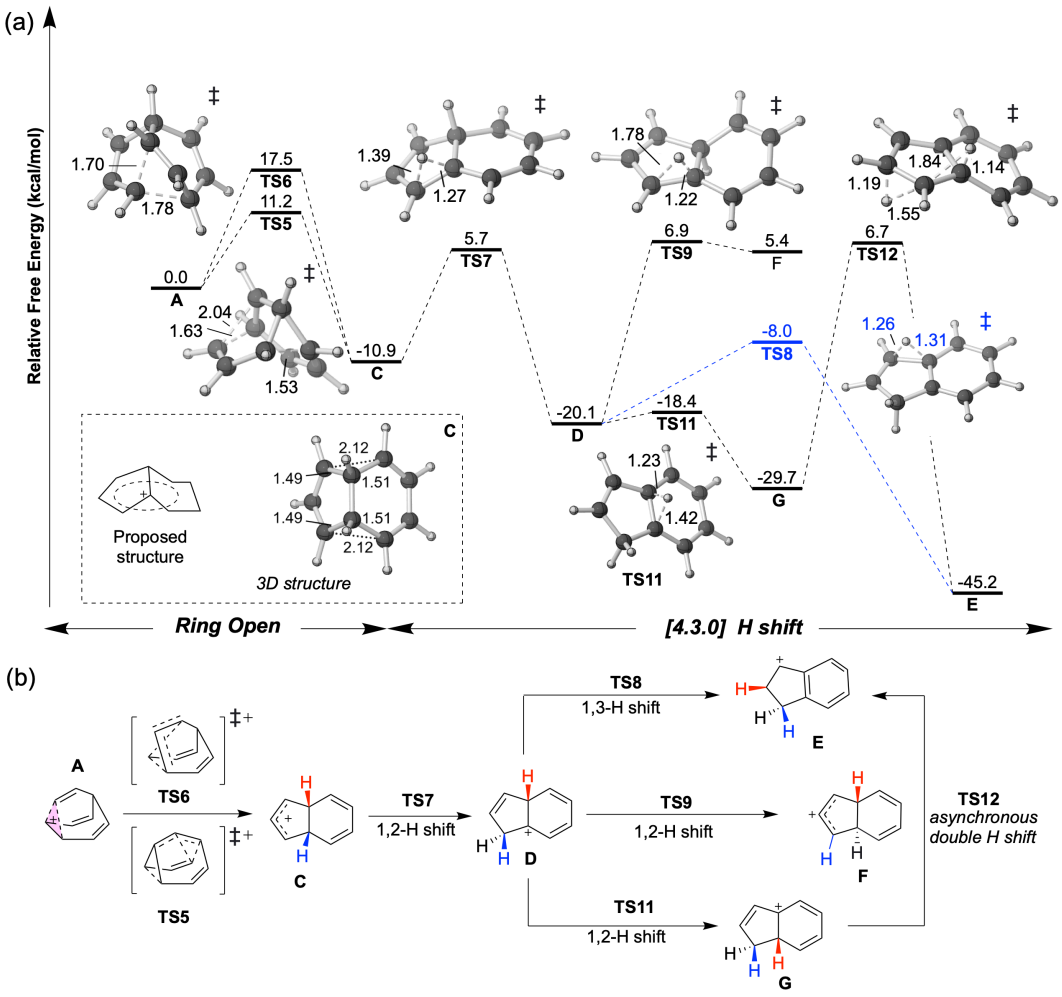


FIGURE 5.3. (a) Energy profile of ring opening and hydride shift to form [4.3.0] structures at DLPNO-CCSD(T)/CBS//CAM-B3LYP/6-31G(d) level at 138.15 K. 3D structures of transition structures (visualized by *CYLview 1.0*) [**119**] are close to their labels. The homoconjucated structure **C** is highlighted in a box. (b) Summary of the mechanism for generating [4.3.0] $C_9H_9^+$ structures discovered in this study. Shifting hydrides are color-coded, with the exception of **TS12**, where red and blue Hs are swapped.

**195**, **196**, **207**, **272**, **273**, **274**] From **A**, two distinct pathways are possible. One involves a $C_2$-symmetric transition structure (**TS2**) associated with a barrier of 2.3 kcal/mol, which converts **A** into an equivalent structure (identical in geometry but not identical in atomic positions). Alternatively, **A** can undergo ring closure *via* **TS3**, which has a relative free energy of 3.6 kcal/mol and leads to the $D_{3h}$ symmetric carbocation **B**, which is 2.6 kcal/mol higher in free energy than **A**. Only **A** and **B** were identified as minima on the portion of

the $C_9H_9^+$ PES relevant to fluxionality. The bonding in cation **B** is complex but can be formulated as involving three *p*-orbitals, one on each bridging carbon, containing a total of two electrons, that interact with each other through the cyclopropane rings that connect them. [**275**] Each **B** is connected to six **A** structures *via* **TS3**s. In this scenario, the bridging CHs cannot exchange with the bridgehead CHs (Figure 5.1a). Consequently, **TS2** and **TS3** only result in partial scrambling of the barbaralyl cation.

Complete degeneracy of all CHs is achieved through another transition structure, **TS4**, with a computed overall barrier of 5.0 kcal/mol. This transition structure corresponds to a twist of one of the three bridges, converting **B** into a degenerate structure (**B'**). Thus, the combination of **TS2**, **TS3**, and **TS4** allows for the interconversion of all nine CH groups. As illustrated in Figure 5.1a, each **TS4** enables the interconversion of groups of **A** and **B** structures. The qualitative nature of this PES matches that described by Cremer and co-workers three decades ago! [**237**]

In Cremer and co-workers' work, **TS4** was found to have lower energy than **TS3**, while our calculations indicate that **TS4** is the highest of the three transition states (see Figure 5.1b; Werstiuk's energies differed considerably). [**237**] This difference arises from the comparatively lower energies of **TS3** and **B** in our study. Nonetheless, both scenarios are consistent with the experimental observation of partial and total degeneracy at different temperatures. We also reached the same conclusion that **TS4** involves a post-transition state bifurcation (PTSB) in both directions, which connects the two **TS2** structures. [**28**, **53**, **219**, **223**, **224**, **225**, **265**]

**5.3.2. Escape from degeneracy.** At elevated temperatures, the conversion of **A** to the lower energy cation **C** can be achieved by the process shown in Figure 5.3. **TS5** and **TS6** are different transition structures that connect **A** and **C**. **TS5** corresponds to a 1,2-vinyl shift followed by cyclopropyl ring opening while **TS6** corresponds to an apparent 1,3-vinyl shift. Subsequent hydride shifts through **TS7**-**TS12** lead to other cations that are even lower in energy (**D**, **E**, **G**).[3] The computed energy barriers are consistent with the experimental

[3]It is worth noting that at the CAM-B3LYP/6-31G(d) level of theory, a minimum (**H**) and nearby transition structure (**TS10**) were optimized, suggesting a stepwise, two-step 1,2-H shift mechanism from structure **D** to

result as shown in Scheme 5.1, although the product is not homoconjugated in the manner originally proposed. [**205**, **233**] At a temperature of -135 °C, the half-life associated with the **A** to **C** conversion is $\geq$ 1.5 d, allowing **A** and **B** to be observed. When the temperature is increased to -120 °C, this predicted half-life increases to 35 minutes, allowing **C** to be observed. [**205**] The subsequent 1,2-hydride shifts initiated by passage through **TS7** are prevented by a 16.6 kcal/mol barrier relative to **C** (predicted half-life of >3000 years).

### 5.4. NMR Computations

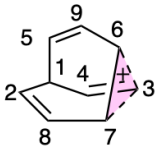


**A**

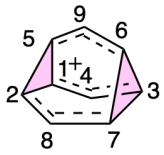


**B**

| C center | $^{13}$C shift | pred (partial) | pred (total) | $^{1}$H shift | pred (total) | C center | $^{13}$C shift (pred partial) | pred (total) | $^{1}$H shift | pred (total) |
|---|---|---|---|---|---|---|---|---|---|---|
| 4 | 221.7 | 153 | | 9.99 | | | | | | |
| 8,9 | 118.9 | | | 6.39 | | 4,8,9 | 132.8 | | 6.5 | |
| 1 | 65.5 | | 119.7 | 6.05 | 6.7 | | | 95.5 | | 6.2 |
| 2,5 | 131.0 | 103 | | 6.48 | | 1,2,3,5,6,7 | 76.8 | | 6.0 | |
| 3 | 86.3 | | | 5.14 | | | | | | |
| 6,7 | 102.1 | | | 6.56 | | | | | | |
| exp | - | 152, 101 | 118.5 | - | 6.6 | exp | 152, 101 | 118.5 | - | 6.6 |
| dev | - | **+1, +2** | **1.2** | **-** | **0.1** | dev | **-19.2, -24.2** | **-23** | **-** | **-0.4** |

TABLE 5.1. Computed $^{1}$H and $^{13}$C NMR shifts for **A** and **B** compared against the experimental results. The deviation of overall estimated chemical shifts (based on scrambling) relative to the experimental signals are in bold.

At the extremely low temperature of -150 °C, the half-life associated with complete scrambling is estimated to be 0.2 ms based on the computed overall barrier and Erying equation (w/o tunneling effect) for **A** -¿ **TS4** ($\Delta G^{\ddagger}$ = 5.0 kcal/mol). Combining the height of the barrier and dynamic NMR measurements, the partial scrambling was indeed captured by the observation of a 6:3 ratio of $^{13}C$ peak splitting. As the temperature is elevated to -135 °C, the predicted half-life for complete scrambling is reduced to 20 $\mu$s, consistent with the

structure **E**. However, when single-point energy corrections were performed using the higher-level DLPNO-CCSD(T)/CBS method, the energy of **H** was found to be higher than that of **TS10**, indicating that the stepwise mechanism is not viable. Instead, the higher-level calculations suggest that the transformation from **D** to **E** proceeds *via* a asynchronous concerted 1,3-H shift mechanism, with a relatively flat potential energy surface following the initial hydrogen shift. (See the Appendix 7.4.3 for details).

observation of a single signal representing all CHs. Although tunneling effect accelerates the scrambling process, our analysis in a subsequent section demonstrates that it contributes only about 30% to the rate constant, which is equivalent to a reducing in the effective barrier to 4.9 kcal/mol, in agreement with the estimated barrier of 5.0 kcal/mol from the NMR experiment. [**234**] In Cremer and co-workers' work, $^{13}$C NMR simulations at the IGLO/6-31G(d) level of theory suggested that the observed signals originate from the lower-energy structure **A**, but their computed difference between computed and experimental shifts was ¿ 6 ppm. [**237**] Our calculations using the revTPSS/pcSseg-1 level of theory reduced this deviation to 1.2 ppm for $^{13}$C (Table 5.1, left). In addition, the single $^{1}$H signal exhibits a deviation of only 0.1 ppm at this level of theory. In contrast, structure **B** shows much larger deviations: a 0.5 ppm underestimation of the $^{1}$H signal and a ¿ 20 ppm underestimation of the $^{13}$C signal (Table 5.1, right). Our results thus provide even more convincing evidence that the lower-energy carbocation isomer, **A**, is the species observed in the NMR experiments.

### 5.5. Further Exploration of the PES

To better understand the $C_9H_9^+$ PES, we conducted relaxed scans along the C2–C5 and C3–C6 bonds. Elongating the C2–C5 bond in B leads to the **A1** isomer, whereas extending the C3–C6 bond results in the **A2** isomer, both *via* **TS3**s (Figure 5.4a).

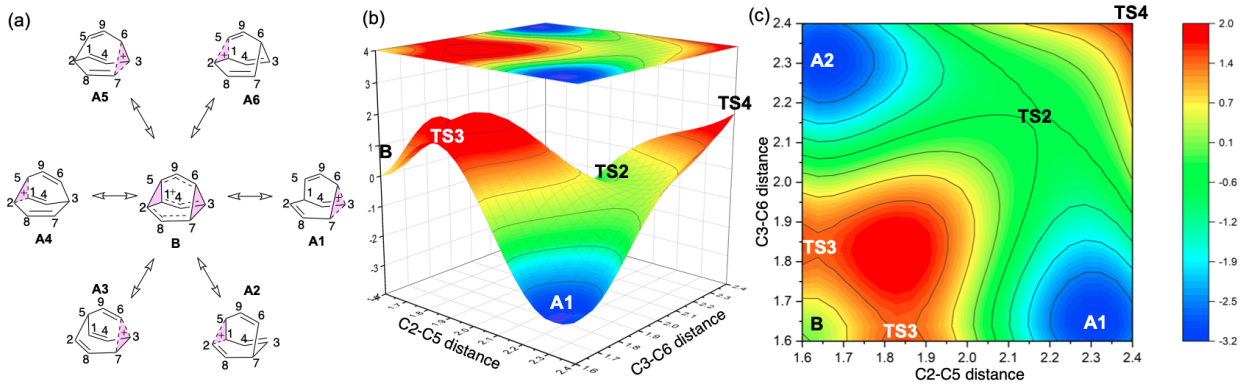


FIGURE 5.4. (a) Six-fold symmetric reaction network that converts structure **B** into six equivalent **A**s. (b) PES in terms of C2-C5 and C3-C6 distances and its 2D projection (above). (c) "top view" of the 2D projection from (b), the energy color map is scaled in kcal/mol.

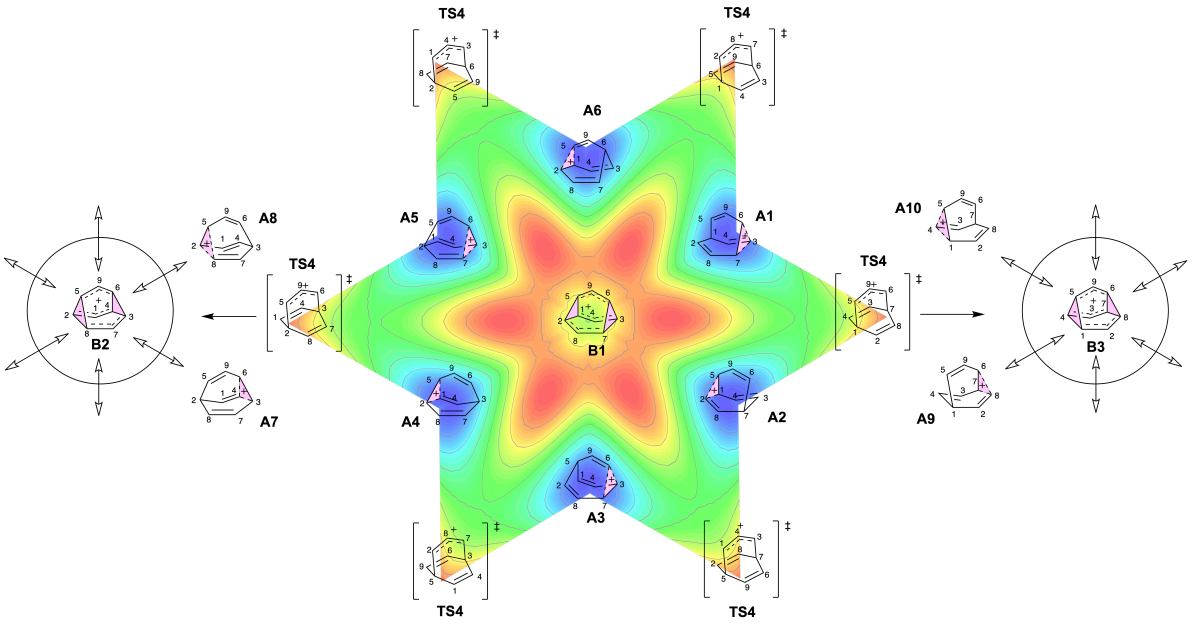


FIGURE 5.5. Six-fold symmetric 2D PES surrounding one **B**. Each 1/6 piece represents a 30-degree sheared, rescaled, and rotated 1/6 PES (Figure 5.4). Key structures that are related to MD simulations are labeled with structure names, including **A1**-**A8**, **B1** and **B2**.

These transformations lead to the symmetrical PES shown in Figure 5.4b-c, which covers the region associated with partial scrambling. This surface also captures **TS2**, which interconverts the two **A**s. **TS4** resides at one corner. From the standpoint of **TS4**, proceeding downhill in either direction corresponding to its imaginary frequency leads to a bifurcation connecting two **A**s. Metadynamics simulations gave a free energy surface of similar shape (see Appendix 7.4.6).

As the PESs shown in Figure 5.4b-c represent only 1/6 of the network from Figure 5.4a, it is instructive to duplicate and combine them to create a PES that covers the whole network. Such a PES is shown in Figure 5.5. This PES can be considered a modern view of the "pound cake" PES depicted qualitatively by Cremer and co-workers (Figure 5.1b). [**237**] Note that this surface only captures one **B**, however, with each **TS4** leading toward others.

### 5.6. Running on the Surface

To further understand the dynamic behavior governing the entire system, uphill AIMD simulations initiated from **B** were conducted. Overcoming **TS3** from **B** at the CAM-B3LYP/6-31G(d) level requires 1.0 kcal/mol of potential energy. We ran two sets of simulations, with 3 and 10 kcal/mol of energy deposited into the starting points corresponding to the cleavage of the C2–C5 bond, i.e., the conversion of **B** to **A1**.

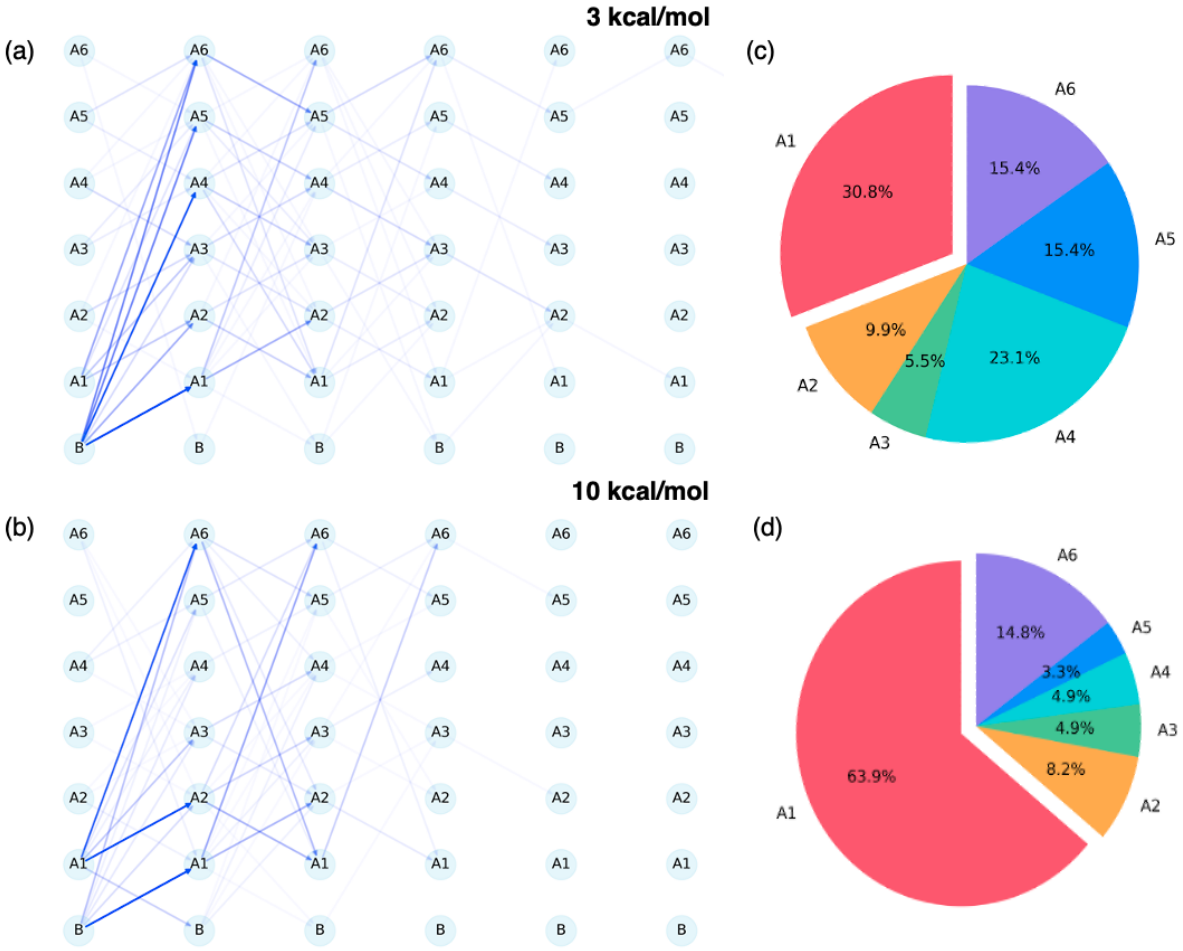


FIGURE 5.6. Left: Network visualization depicting minima encountered in uphill simulations from **B** towards **A1**. Sequential nodes from left to right denote successive minima encountered along each trajectory with (a) 3 kcal/mol and (b) 10 kcal/mol excess energy. The thickness of lines reflects the relative population for different types of pathways, with denser populations of trajectories indicated by greater thickness. Right: Distribution of the first minimum encountered for uphill simulations with (c) 3 kcal/mol and (d) 10 kcal/mol excess energy.

**5.6.1. Uphill dynamics.** Trajectories were propagated for 1000 fs and the minima encountered were recorded. The results are summarized in Figure 5.6a.

For both sets of simulations, even though energy is imparted to match the momentum associated with converting **B** to **A1**, other **A**s can be accessed through this process in various amounts. As the extra energy associated with an **A1**-forming motion is increased, selectivity for forming **A1** increases, but even with 10 kcal/mol of extra energy, less than 70% of the trajectories reach **A1** as the first minimum (Figure 5.6). Additional details can be found in the Appendix 7.4.5.1.

Does this resistance to selectivity originate simply from the PES being flat (i.e., a gain in entropy)? [**127**, **276**] Yes and no, depending on one's preferred degree of subtlety. As shown in Figure 5.7, inter-transition state roaming (through the red region of the PES) is actually observed. [**53**, **156**, **227**] For example, some trajectories initially explored the inter-transition state region between **TS3**s directly (Figure 5.7c).

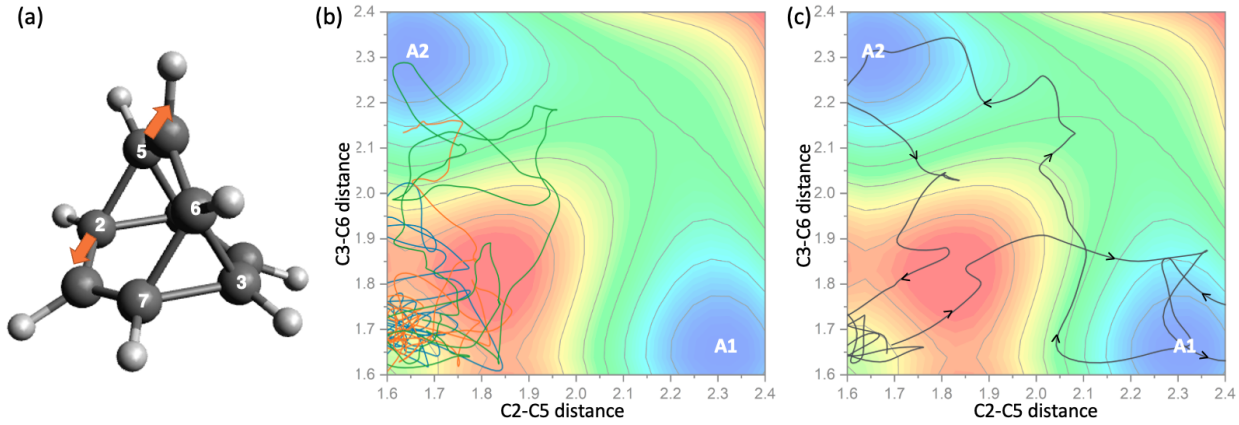


FIGURE 5.7. Projection of representative trajectories collected from uphill AIMD simulations (b and c) with 10 kcal/mol external energy given to the stretch of bond C2–C5 (a).

**5.6.2. Complete scrambling in downhill dynamics.** Given the reaction networks connected to each **TS4**, we sought to understand the dynamic behavior associated with descending from it. AIMD simulations initiated from **TS4** revealed pathways that readily

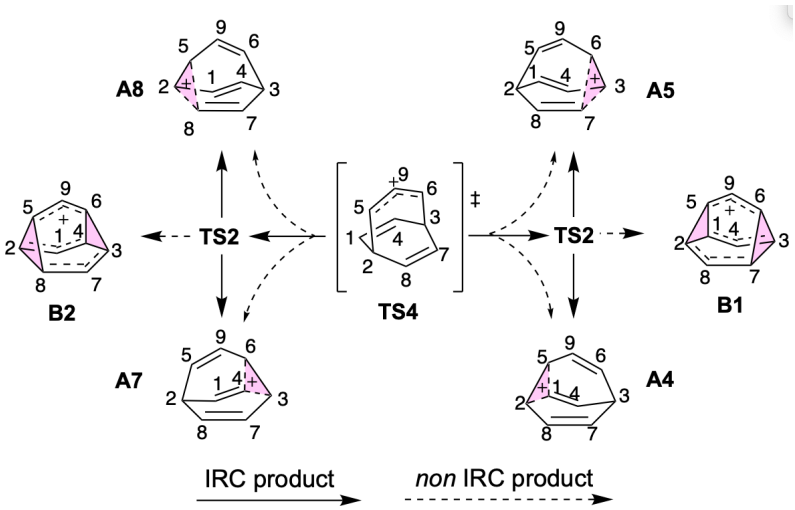


SCHEME 5.2. Illustration of the pathways observed from downhill AIMD simulation initiated from **TS4**.

bridge a total of six minima, as illustrated in Scheme 5.2 (note that the labels **A4** and **A5** in this figure are the same as those in Figure 5.4 and Figure 5.5).

The trajectories from both *quasi*-classical (with zero-point energy) and classical (without zero-point energy) AIMD simulations are visualized in Figure 5.8. The projection onto the three collective variables (CVs) clearly shows the states **A4**, **A5**, **A7**, and **A8**, as well as the associated states **B1** and **B2**, being accessed by the trajectories in our simulations. The CVs chosen to plot the trajectories are based on the four essential bonds that dominate the geometric changes at **TS4**, including the C-C distances of bonds C4–C6, C5–C8, C6–C7, and C1–C5. The 3D shape produced by the trajectories resembles a twisted "H" structure, which is more apparent in the classical trajectories (Figure 5.8a,c). Although the "cross" shape is not perfectly orthogonal(Figure 5.8b,d), the reaction pathway that generates the four **A** structures (**A4**, **A5**, **A7**, and **A8**) exhibits four-fold symmetry. The tilted appearance of the cross is a result of the specific CV selection. For instance, the C4–C6 and C5–C8 distances are equivalent between **A7** and **A8**, and consequently, the difference between these distances (CV2, C5–C8 - C4–C6) is inverted and close to, but not exactly equal to, zero.

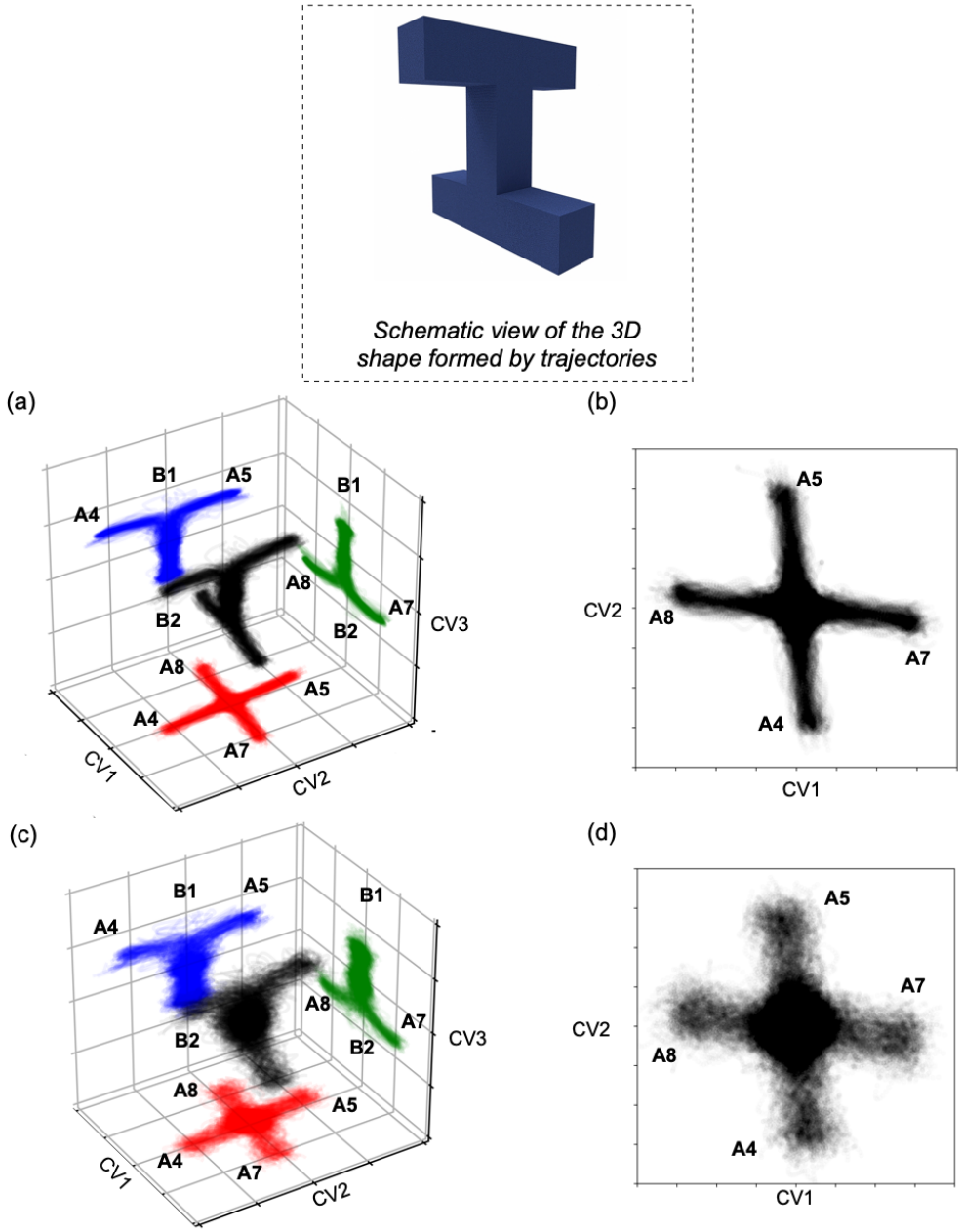


FIGURE 5.8. (a) Trajectories visualized with respect to the coordinates CV1, CV2, and CV3. CV1 is defined by R(C1,C5) - R(C6,C7); CV2 is defined by R(C5,C8) - R(C4,C6); and for CV3, (R(C1,C5) + R(C6,C7)) - (R(C5,C8) + R(C4,C6)). To better capture the six products, projections on each plane are distinctly colored in red, blue, and green. The schematic view at left describes the 3D shape of the trajectory bundle.

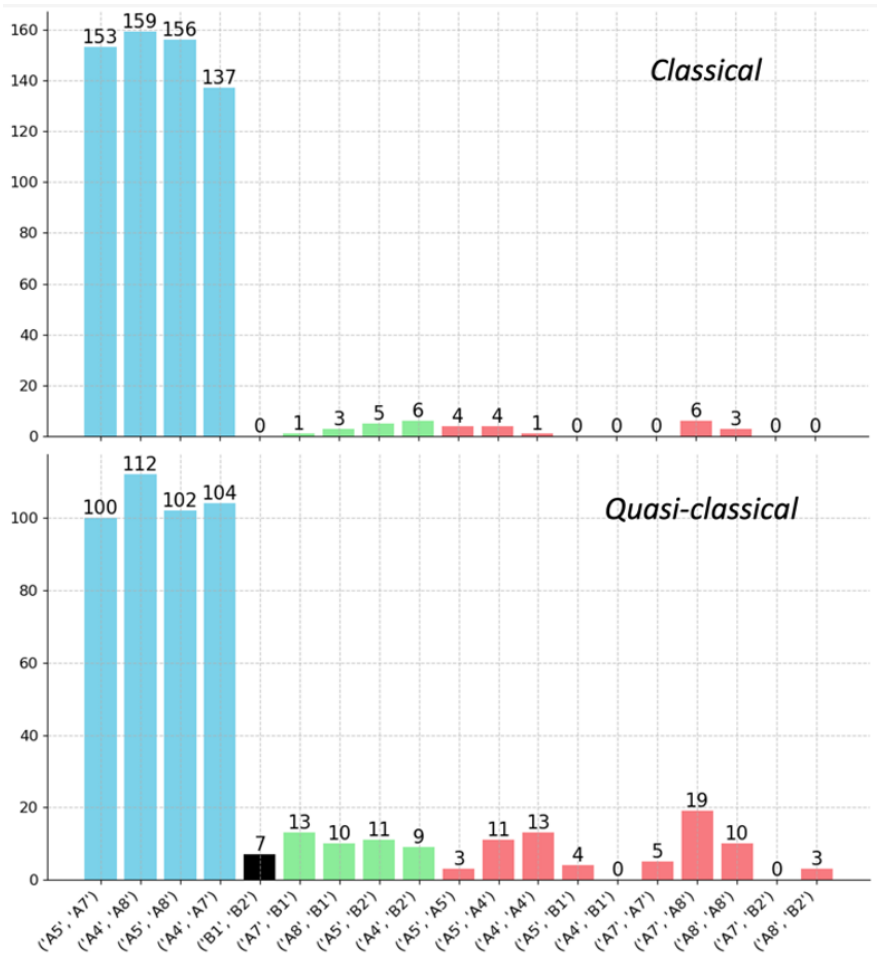


FIGURE 5.9. Histogram displaying the distribution of different trajectory types in classical and *quasi*-classical AIMD simulations initiated from TS4. Bars are colored blue (connecting two **A** structures from different sides), green (connecting an **A** structure and a **B** structure from different sides), red (recrossing), and black (connecting **B1** and **B2**). The number of trajectories in each group is labeled on each bar.

By analyzing the number of different types of trajectories, we confirmed that the ratio of trajectories connecting opposite **A** structures (**A5-A7**, **A5-A8**, **A4-A7**, **A4-A8**) is close to 1:1:1:1. As summarized in the histogram in Figure 5.9, trajectories are classified into four groups: 1) trajectories connecting two **A** structures from different sides (blue); 2) trajectories connecting an **A** structure and a **B** structure from different sides (green); 3) recrossing trajectories that connect stationary points from the same side (red); and 4) trajectories that connect the opposite **B1** and **B2**. When zero-point energy is deposited during the sampling

process, notable increases in the proportions of type-2 and type-3 trajectories are observed. These increases manifest as a blurrier shape in Figure 5.8, indicating that classical trajectories have a higher probability of following the IRC under these conditions. [**28**, **104**, **265**] Another intriguing feature of the potential energy surface in Figure 5.5 is the presence of minima **B**, which are between **TS4** and **TS3**. These minima can be directly accessed with excess momentum before encountering the two **A** structures (for a different surface topography and consequent dynamic effect encountered at the M06-2X/6-31G(d) level of theory, see Appendix 7.4.7).

## 5.7. Tunneling Effects

Although both the nature of the $C_9H_9^+$ PES and our dynamics simulations are consistent with the experimentally observed behavior of the barbaralyl cation, heavy-atom quantum mechanical tunneling may also contribute. [**?**, **228**, **230**, **231**, **277**] Tunneling in other carbocation rearrangements has been examined previously. [**230**] Here, both zero-curvature tunneling (ZCT) and small-curvature tunneling (SCT) were examined (see Supporting Information for details). Table 5.2 shows that large contributions from tunneling are expected for passage through transition structures under -135 °C, providing another route to scrambling, but the overall rate for the total scrambling process through **TS4** is only accelerated by ¡ 30%. This acceleration is not substantial enough to invalidate the conclusion that, at temperatures below -150 °C, NMR spectroscopy can capture the partially scrambled structures The tunneling effects only lower the effective barrier from 5.0 kcal/mol to 4.9 kcal/mol .

**5.7.1. Network neutrality.** Although carbocations and boranes are isoelectronic, they display both similar and different behaviors. For example, while many boranes and boron clusters support 3-center 2-electron bonding, simple $C^+ \rightarrow B$ substitution in carbocations can greatly reduce delocalization. [**278**] When performing such a replacement for $C_9H_9^+$, a greatly simplified reaction network was observed (Figure 5.10). The only transition structure

| | T (K) | $\kappa_{ZCT}$ | $\kappa_{SCT}$ | fraction of rate due to tunneling (ZCT) | (SCT) |
|---|---|---|---|---|---|
| | **138.15** | **1.08** | **1.34** | **7.49%** | **25.29%** |
| TS2 | 188.15 | 1.04 | 1.11 | 3.59% | 10.08% |
| | 273.15 | 1.02 | 1.04 | 1.62% | 4.13% |
| | **138.15** | **1.76** | **1.87** | **43.21%** | **46.58%** |
| TS3 | 188.15 | 1.35 | 1.40 | 25.97% | 28.32% |
| | 273.15 | 1.15 | 1.17 | 13.18% | 14.47% |
| | **138.15** | **1.28** | **1.39** | **22.12%** | **28.02%** |
| TS4 | 188.15 | 1.13 | 1.16 | 11.58% | 13.92% |
| | 273.15 | 1.06 | 1.07 | 5.51% | 6.53% |

TABLE 5.2. Tunneling contributions and including transmission coefficients ($\kappa$) for both ZCT and SCT. The results for temperatures used in NMR experiments are in bold

we were able to locate resembling any of the structures from Figure 5.2 was a transition structure for [3s,3s] sigmatropic shift and this reaction was predicted to have a comparatively large barrier, 12.1 kcal/mol, a classic lack of fluxionality, which results from the absence of a yearning for charge delocalization.

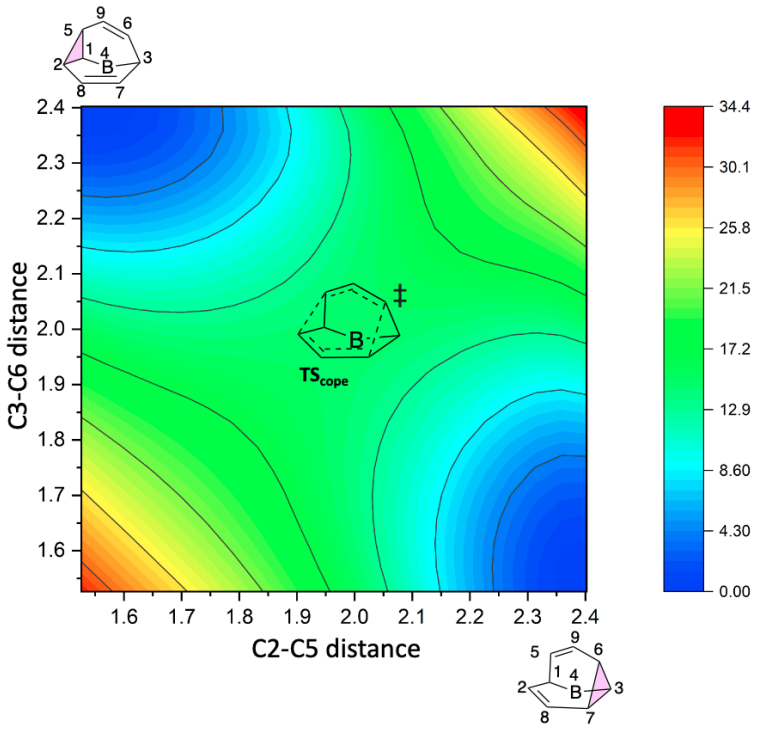


FIGURE 5.10. 2D potential energy surface for [3s,3s] sigmatropic shift of $BC_8H_9$.

## 5.8. Conclusions

We delved into the complex behavior of the non-classical barbaralyl cation, shedding light on its formation and dynamic rearrangements through a multifaceted approach that integrates analysis of barriers, thermodynamics, non-statistical dynamic effects, and tunneling. The construction of the PES and AIMD simulations unveiled the importance of dynamic effects attributable to the flat and highly symmetrical nature of the energy surface on which the cation re-sides. Our results both validate the models of previous researchers and extend them to provide a rich picture of the reactivity of a fluxional carbocation at a level only achievable with modern theoretical methods. We look forward to similar studies on additional carbocations, both classic and newly conceived.

CHAPTER 6

# Heavy Atom Quantum Mechanical Tunneling in Total Synthesis

Contributions from quantum mechanical tunneling to the rates of several radical coupling reactions between carbon $sp^2$ centers used as key steps in natural product total syntheses were computed using density functional theory. Contributions rang-ing from 15-52% from tunneling were predicted at room temperature, indicating that tunneling plays an important role in the rates of these reactions and should perhaps be considered when designing complex synthetic schemes.

## 6.1. Introduction

How can heavy atom quantum mechanical tunneling facilitate the total synthesis of complex natural products? [**279**, **280**, **281**] Other "physical organic chemistry concepts" such as kinetic isotope effects (KIE) have been put to good use in total syntheses – suppressing the formation of unwanted side products, for example [**282**, **283**, **284**] – but quantum chemical tunneling has not, to our knowledge, been intentionally employed as a tool in designing a total synthesis. [**229**, **279**, **280**, **281**, **285**, **286**] Here we describe two cases where heavy atom tunneling was responsible for a large portion of the rate of a key reaction in a total synthesis. [**287**] We hope this revelation will inspire others to add this additional tool to their synthetic toolboxes.[1]

While tunneling frequently can be a significant contributor to the rates of reactions involving H-transfer, even at non-cryogenic temperatures, [**284**] tunneling for reactions not involving H-transfer – so-called "heavy atom tunneling" – is less common. [**279**, **280**, **281**] Classic examples of heavy-atom tunneling where C–C bond formation/breakage is involved include

[1]This chapter is adapted from [**277**], with permission. The experimental work in this collaborative project with Professor Regan J Thomson is done by Emily E Robinson.

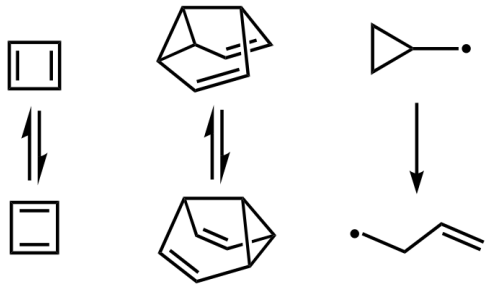

SCHEME 6.1. Representative reactions involving heavy atom tunneling and C–C bond formation/breakage.

cyclobutadiene automerization, [**288**] Cope rearrangement of semibullvalene, [**289**] and ring-opening of cyclopropyl-carbinyl radical (Scheme 6.1). [**290**] For tunneling to make a large contribution to the rate of such reactions (it always contributes a little when a thermally excited reactant nears the top of a barrier), [**285**] the barrier for reaction should be "thin", i.e., the structures of the reactant and product should be similar. [**229**, **286**] The thinner the barrier, the more of the tail of the reactant wavefunction that reaches the product.

In the context of a synthesis of (+)-7,20-diisocyanoadociane, the ring-closing reaction shown in Scheme 6.2 (top, 1b to 2b) was carried out as a key step. [**287**] Given the proximity of the methylene groups that couple in this reaction, we postulated that the barrier for ring closure would be thin, and heavy atom tunneling might make a sizable contribution to the reaction rate, even at room temperature. Here we put this hypothesis to the test using quantum chemical computations. We also examine another related reaction from the synthesis of (-)-peyssonnoside (Scheme 6.2, bottom, **3** to **4**) [**291**] to begin to probe the generality of heavy atom tunneling in synthetically useful reactions involving radical ring-closure between proximal $sp^2$ carbons.

First, we set out to examine the **1b** to **2b** reaction. To simplify our computations, we calculated **1a** to **2a**, a $C_2$-symmetric reactant forming a $C_2$-symmetric product. This exact molecule was also synthesized and shown to cyclize with a similar yield as the dimethyl compound **1b** (85% v. 92%) under the same reaction conditions (Scheme 6.2, top).

## 6.2. Computational Method

The most energetically favorable conformations for each structure were first determined using the xTB-CREST conformational searching package. [**292**] Computations on species along the cyclization reaction coordinate were then performed at the UM06-2X/6-31G(d,p) level of theory at the gas phase, which is well-known to provide reasonable accuracy for systems composed of main group elements using *Gaussian16 C.01* package. [**87**, **95**, **263**] Data set collection of opti-mized geometries are available at the ioChem-BD repository https://iochem-bd.bsc.es/browse/handle/100/319899. [**155**] The **1a** to **2a** reaction was also benchmarked using other functions, including B3LYP-D3(BJ), mPW1PW91, $\omega$B97XD and PBE0-D3(BJ) (see Appendix 7.5.1). [**293**, **294**, **295**] A standard mechanism for photoredox activation was assumed, [**296**] in which the radical shown in Scheme 6.3 (generated *via* proton transfer and electron donation to reactant 1a) is the species that undergoes cyclization. A free energy barrier of 18 kcal/mol was computed for this reaction. The associated computed IRC is shown in Figure 6.1.

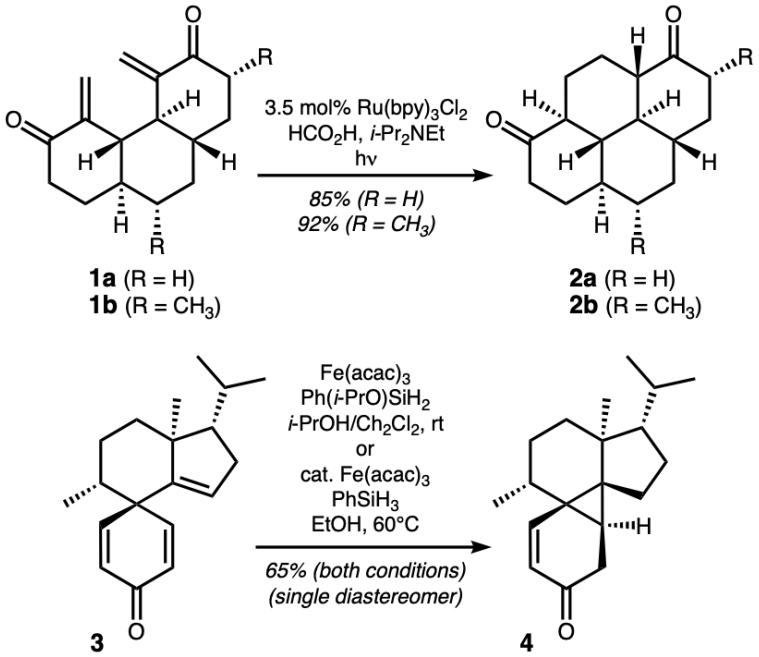


Scheme 6.2. Cyclization reactions studied herein.

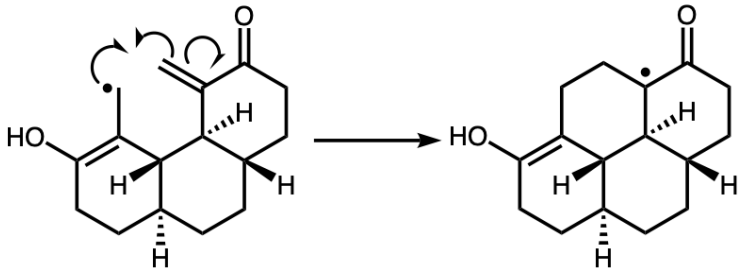


SCHEME 6.3. Radical cyclization reaction modelled for 1a to 2a

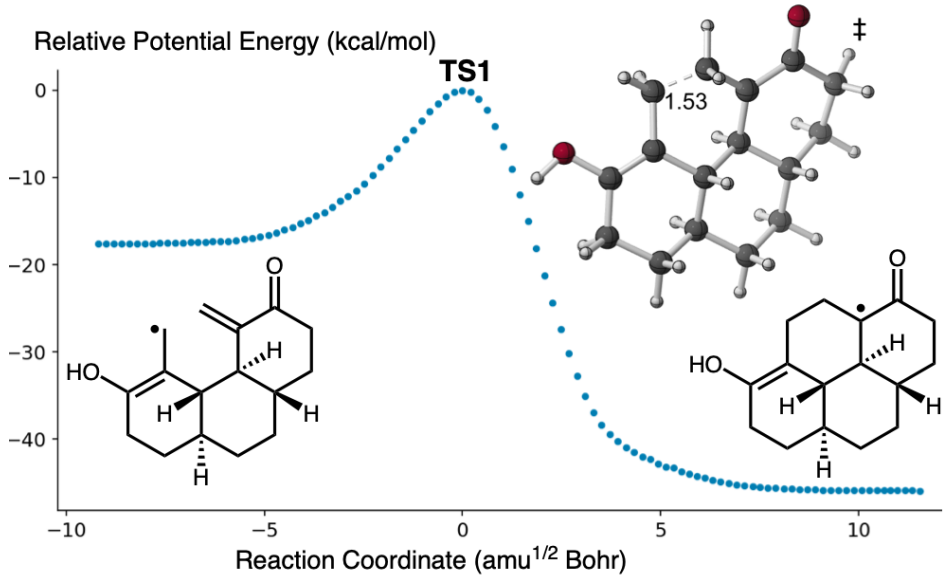


FIGURE 6.1. IRC for the cyclization reaction shown in Scheme 6.3. Structures are visualized using CYLView with the key bond distance shown in Åfor the transition structure. [**119**] The vertical axis represents potential energy (electronic energy) relative to the energy of TS1 in kcal/mol.

### 6.3. Tunneling Results

To determine the contribution of tunneling to the rate of this reaction, Truhlar's reaction-path variational transition state theory was employed using *Gaussrate/Polyrate*. [**44**, **105**, **106**] Two types of transmission constants were used to arrive at predictions with zero-curvature tunneling (ZCT) and small-curvature tunneling (SCT). So-called $\kappa$ factors, which are related to transmission coefficients (here, tunneling corrections) were calculated as the ratio of the Boltzmann average of the quantum transmission probability to the Boltzmann average of the classical transmission probability (with a threshold energy at the maximum

| T(K) | $\kappa_{ZCT}$ | $\kappa_{SCT}$ | FRACTION OF RATE DUE TO TUNNELING (ZCT) | (SCT) |
|---|---|---|---|---|
| 193.15 | 2514 | 23488 | 99.96% | 100.00% |
| 213.15 | 44.1 | 385.0 | 97.73% | 99.74% |
| 233.15 | 3.64 | 15.46 | 72.55% | 93.53% |
| 253.15 | 2.01 | 2.89 | 50.36% | 65.44% |
| 273.15 | 1.75 | 1.95 | 42.74% | 48.66% |
| **298.15** | **1.58** | **1.68** | **36.64%** | **40.54%** |
| 313.15 | 1.51 | 1.59 | 33.64% | 37.15% |
| 333.15 | 1.43 | 1.50 | 30.16% | 33.32% |

TABLE 6.1. Results of tunnelling calculations for the **1a** to **2a** reaction.

of the ground-state energy along the reaction). Results, including percentages of reaction rate predicted to arise from tunneling, are shown in Table 6.1 for a variety of temperatures. Using both ZCT and SCT, a large tunneling effect was predicted. At room temperature (bold), the temperature at which the reaction was run, we predict that approximately 40% of the rate comes from heavy atom tunneling! This value is higher than that predicted for many previously investigated reactions with heavy atom tunneling effect. [**279**, **280**, **297**]

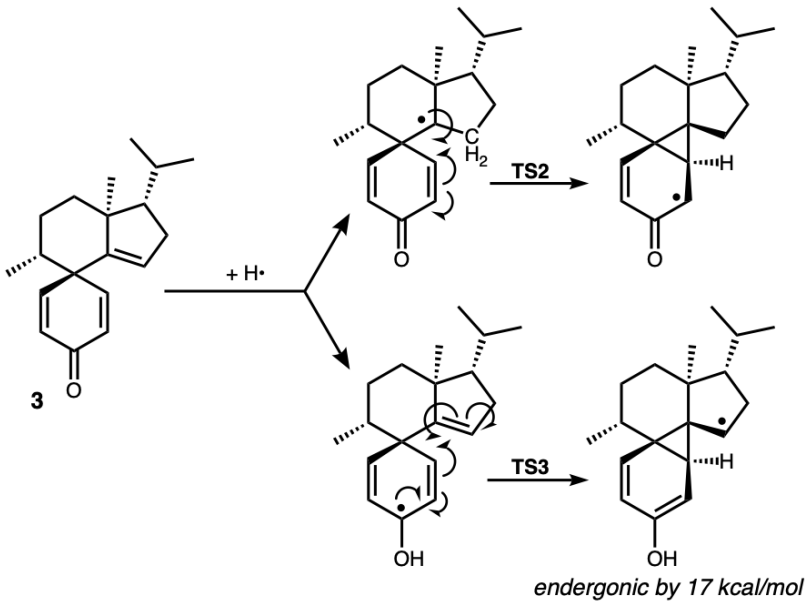


SCHEME 6.4. Radical cyclization reactions modeled for **3** to **4**.

| T(K) | $\kappa_{ZCT}$ | $\kappa_{SCT}$ | FRACTION OF RATE DUE TO TUNNELING (ZCT) | (SCT) |
|---|---|---|---|---|
| 193.15 | 1.55 | 1.76 | 35.42% | 43.29% |
| 213.15 | 1.42 | 1.57 | 29.63% | 36.16% |
| 233.15 | 1.34 | 1.44 | 25.14% | 30.70% |
| 253.15 | 1.28 | 1.36 | 21.59% | 26.39% |
| 273.15 | 1.23 | 1.30 | 18.74% | 22.93% |
| **298.15** | **1.19** | **1.24** | **15.88%** | **19.47%** |
| 313.15 | 1.17 | 1.22 | 14.47% | 17.75% |
| 333.15 | 1.15 | 1.19 | 12.85% | 15.78% |

TABLE 6.2. Results of tunnelling calculations for the **3** to **4** reaction *via* the top pathway in Scheme 6.4.

| T(K) | $\kappa_{ZCT}$ | $\kappa_{SCT}$ | FRACTION OF RATE DUE TO TUNNELING (ZCT) | (SCT) |
|---|---|---|---|---|
| 193.15 | 5.95 | 9.11 | 83.19% | 89.02% |
| 213.15 | 3.97 | 5.31 | 74.80% | 81.18% |
| 233.15 | 3.02 | 3.75 | 66.91% | 73.32% |
| 253.15 | 2.49 | 2.94 | 59.79% | 65.98% |
| 273.15 | 2.15 | 2.46 | 53.50% | 59.37% |
| **298.15** | **1.88** | **2.09** | **46.72%** | **52.13%** |
| 313.15 | 1.76 | 1.93 | 43.18% | 48.30% |
| 333.15 | 1.64 | 1.78 | 38.99% | 43.75% |

TABLE 6.3. Results of tunnelling calculations for the **3** to **4** reaction *via* the bottom pathway in Scheme 6.4.

We also explored system **3** to **4** (Scheme 6.2, bottom) using the same methods. This reaction also involves an intramolecular reductive coupling initiated through a hydrogen atom transfer, but given the asymmetry of the system, we considered two possible mechanisms (Scheme 6.4). Although the bottom pathway starts from a more stable radical (by 3.5 kcal/mol; due to conjugation), the ring-closure step for that radical was found to be endergonic by 17 kcal/mol (likely because conjugation is lost) and have a much higher barrier ($\Delta G^{\ddagger}$ = 24 kcal/mol) compared to the top pathway ($\Delta G^{\ddagger}$ = 6 kcal/mol from the higher energy radical). For both pathways, transition structures to form alternative diastereomers were

predicted to be 8 kcal/mol higher in energy than those leading to the observed diastereomer, likely the result primarily of strain (see Appendix 7.5.2 for details).

Tunneling calculations for both pathways from Scheme 6.3 were carried out. As shown in Table 6.2, the energetically preferred pathway (*via* the initial alkyl radical) is again predicted to benefit from tunneling, but to a smaller extent than does the 1a to 2a reaction (15-20% v. 40% contribution to the predicted rate at room temperature). However, the pathway *via* the initial conjugated radical benefits from tunneling to a large extent, ˜50% contribution to the predicted rate at room temperature! Although a slightly longer C· · ·C distance is found for the conjugated radical compared to the alkyl radical (2.50 v. 2.44 Å), which might be expected to result in weaker tunneling due to a wider barrier, it also has a higher activation barrier that hinders classical over-the-barrier product formation. [**229**] Although the pathway with a greater contribution from tunneling is not favored in this case (Table 6.3), both pathways benefit significantly from tunneling.

## 6.4. Conclusion

In summary, quantum chemical computations were used to provide evidence that C–C bond-forming reactions through a radical pathway featured as key steps in the total synthesis of complex natural products can benefit greatly from heavy atom tunneling. We hope that recognition of this observation will encourage synthetic chemists to utilize heavy atom tunneling as a design element in planning future syntheses.

CHAPTER 7

# Appendix

## 7.1. Supporting Information of Chapter 2

The complete information including all the raw data can be accessed at https://pubs.acs.org/doi/10.1021/jacs.2c07681

**7.1.1. Benchmark.** We performed single point energy calculations with different DFT computational to confirm the robust of level of theory we picked (M06/6-311G(d,p)+LANL2DZ, B3LYP-D3(0)/6-311G(d,p)+LANL2DZ) in this work. As shown in Figure 7.1, different level shows a good correlation on the energy of stationary points. Besides, all level of theories gives the same estimation of *cis*/*trans* ratio based on cis-TS1 and tran-TS1 barriers as presented in Table 7.1.

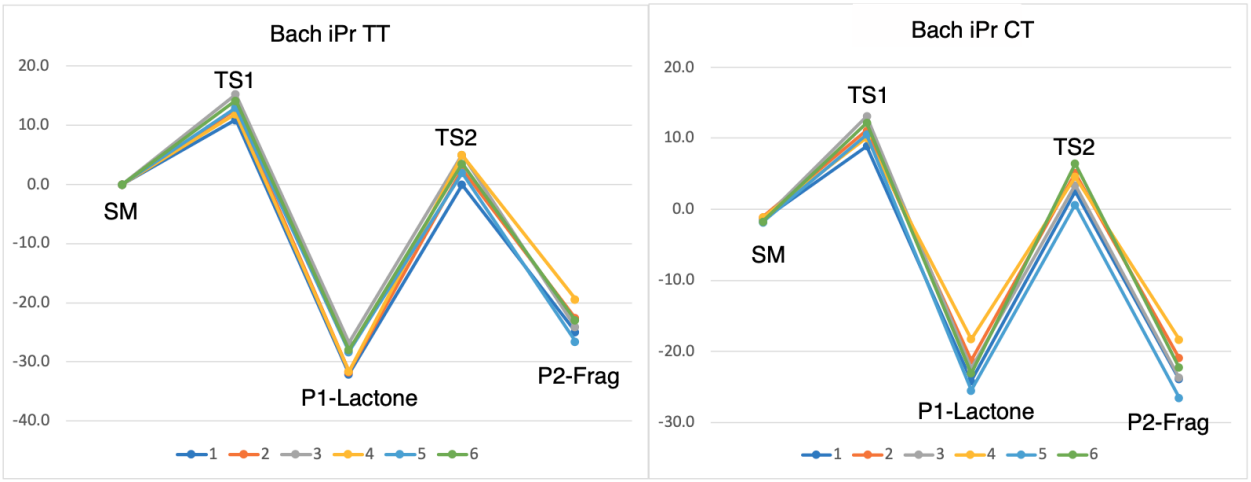


FIGURE 7.1. Potential energy of stationary points in Bach-*i*Pr-CT and Bach *i*Pr TT benchmarked with six computational levels.

| Level of theory | MN15/ 6-311G(d,p)+ LANL2DZ | MN15/ def2-TZVP | B3LYP-D3(0)/ def2-TZVP | PBE0-D3(0)/ def2-TZVP | B3LYP-D3(0)/ 6-311G(d,p)+ LANL2DZ | M06/ 6-311G(d,p)+ LANL2DZ |
|---|---|---|---|---|---|---|
| *cis*-TS1(ΔEE) | 10.9 | 12.7 | 15.2 | 11.9 | 12.9 | 14.2 |
| *trans*-TS1(ΔEE) | 8.9 | 11.1 | 13.1 | 10.1 | 10.5 | 12.2 |
| ΔΔEE (*cis*-*trans*) | 2.0 | 1.6 | 2.1 | 1.8 | 2.4 | 2.0 |

TABLE 7.1. Comparison of relative *cis* and *trans* TS1 activation energy barriers (electric energy) in kcal/mol of Bach-*i*Pr system with different levels of theory.

| Subsituent | $CBr_3$ | C-Rh | Br | C-Rh | I | C-Rh | Cl | C-Rh | Me | C-Rh | $SiH3_3$ | C-Rh |
|---|---|---|---|---|---|---|---|---|---|---|---|---|
| Away | 8.0 | 2.28Å | 7.6 | 2.29Å | 7.8 | 2.30Å | 6.6 | 2.29Å | 4.5 | 2.30Å | 1.5 | 2.19Å |
| Toward | 0.0 | 2.19Å | 0.0 | 2.18Å | 0.0 | 2.17Å | 0.0 | 2.18Å | 0.0 | 2.21Å | 0.0 | 2.18Å |

TABLE 7.2. *Trans*-away TS1 energies relative to *trans*-Toward TS1s in kcal/mol with different substituents at the *para*-position and corresponding C-Rh bond length.

In Table 7.1, the relative activation energy barrier for CT- and TT-TS1s are listed according to different computational levels. Various approaches share the same agreement that *trans*-TS1 is ˜2 kcal/mol lower than *cis*-TS1, which is consistent with the experiment observation that *cis*:*trans* is 1:20.

**7.1.2. Toward and Away.** To study the role of *para*-substituted Bromine in the carbene substrate, TA-, TT-TS1s with other substituents were optimized as well. Relative energies are summarized in Table 7.2. Interestingly, all substituents show a lower activation energy barrier when it is toward the dirhodium catalyst. Like Br, other halogens (Cl and I) prefer Toward-TS1s due to halogen bondings, but the energy difference decreases around 1kcal/mol. To increase the energy of Toward-TSS1s, we then tried methyl which has a similar Van der Waals radius but weak polar. As we changed to $SiH_3$ with appreciable steric hindrance, the relative TS1 energy difference reduced to 1.5 kcal/mol.

**7.1.3. ARC.** The two-dimensional reaction coordinate is constructed as follows (also see Figure 7.2):

- Y-axis (first dimension): Derived from the structural Cartesian coordinates of frames in the Intrinsic Reaction Coordinate (IRC).
- X-axis (second dimension): Generated from frames in the Artificial Reaction Coordinate (ARC) translation.

The process of creating this 2D reaction coordinate involves several steps:

(1) Origin setting: Translate the ARC according to the displacement vector from the artificial transition state (aTSS1) to the true transition state (TSS1). This aligns aTSS1 with TSS1, causing the two reaction coordinates to coincide at this point.

(2) Structural difference calculation: Compute the structural differences between TSS1 and subsequent frames along the IRC.

(3) Grid construction: Generate structures for each grid point by adding incremental displacements (y1, y2, etc.) to the molecular structures along the x-axis.

(4) Energy calculation: Perform single-point energy calculations on the newly generated atomic coordinates for each grid point.

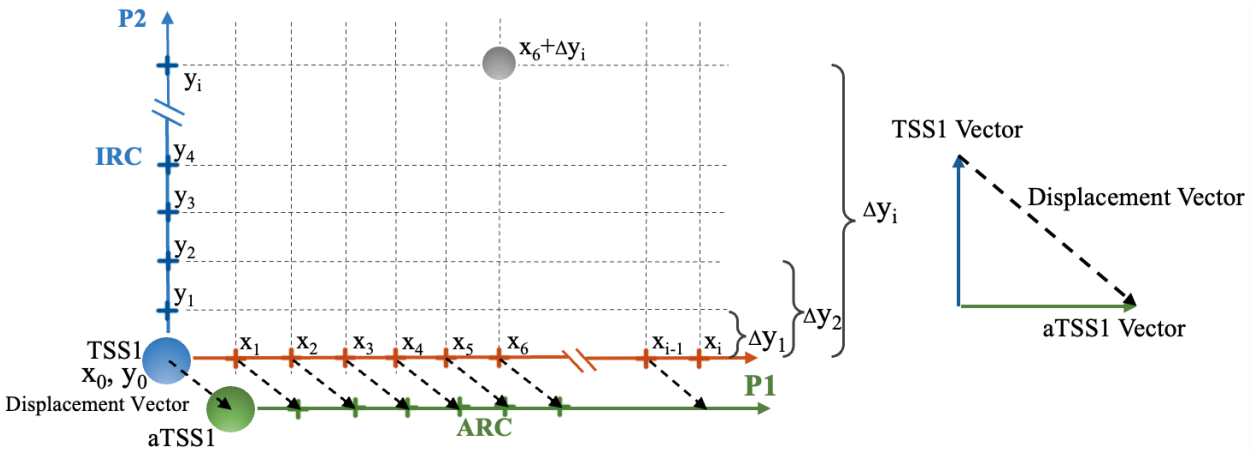


FIGURE 7.2. Illustration on how two TSS1s are aligned as well as grids generation.

While this approach successfully plotted the PES for this specific system, it is important to note that if the two coordinates are not orthogonal, this method may result in significantly incorrect structures when generating grids between the two pathways. A more accurate

approach would be to use geodesic interpolations of reaction pathways based on redundant internal coordinate spaces.

**7.1.4. EDA.** Based on the interaction/distortion methodology of studying organometallic reactions, the delicate balance of "bad" strains and "good" interactions manipulate the final geometry of different conformations. The activation energy barrier can be dissected to the relative strains and relative interactions with respect to those of the reactants. Thus, we can reckon the relative distortion energy with single point calculation on the substrate and catalyst individually in the geometry. Roughly we can get relative interaction energy by subtracting relative distortion energy from the relative potential energy barrier, as the formula describes:

$$\begin{aligned} \Delta E_{\text{energy barrier}} &= E_{\text{TS}} - E_{\text{SM}} \\ &= (E_{\text{TS-strain}} - E_{\text{SM-strain}}) + (E_{\text{TS-int}} - E_{\text{SM-int}}) \end{aligned} \tag{7.1}$$

In this work, we focus more on implementing the gap between TSS1 isomers. Instead of relative energy barrier $\Delta E_{\text{energy barrier}}$, we can rewrite the equation to the form of $\Delta\Delta E_{\text{energy barrier}}$:

$$\begin{aligned} \Delta\Delta E_{\text{energy barrier}} &= E_{\text{TSa}} - E_{\text{TSb}} \\ &= (E_{\text{TSa}} - E_{\text{SM}}) - (E_{\text{TSb}} - E_{\text{SM}}) \\ &= \Delta E_{\text{strain}} + \Delta E_{\text{int}} \end{aligned} \tag{7.2}$$

where:

$$\Delta E_{\text{int}} = E_{\text{TSa-int}} - E_{\text{TSb-int}} \tag{7.3}$$

$$\begin{aligned}\Delta E_{\text{strain}} &= (E_{\text{TSa-cat}} + E_{\text{TSa-sub}} - E_{\text{cat}} - E_{\text{sub}}) \\ &\quad - (E_{\text{TSb-cat}} + E_{\text{TSb-sub}} - E_{\text{cat}} - E_{\text{sub}}) \\ &= E_{\text{TSa-cat}} + E_{\text{TSa-sub}} - E_{\text{TSb-cat}} - E_{\text{TSb-sub}}\end{aligned} \tag{7.4}$$

To compare the dissected energies between TS isomers, we calculated relative distortion energies from the formula above. One specific isomer TT-TS1s was selected as the standard ($TSb$ in the above formula). While interaction energies are computed directly by the second generation of ALMO-EDA.

Without wave functional or force field-based interaction energy analysis, one can still get the relative interaction energy $\Delta E_{int}$ by deducting relative distortion energy $\Delta E_{strain}$ from relative barrier $\Delta\Delta E_{energybarrier}$. As shown in Figure 7.3, the sum of the EDA-derived relative interaction energy and relative strain has a good agreement with the relative energy barrier calculated by DFT comparing $\Delta E$ and $\Delta E^*$ columns.

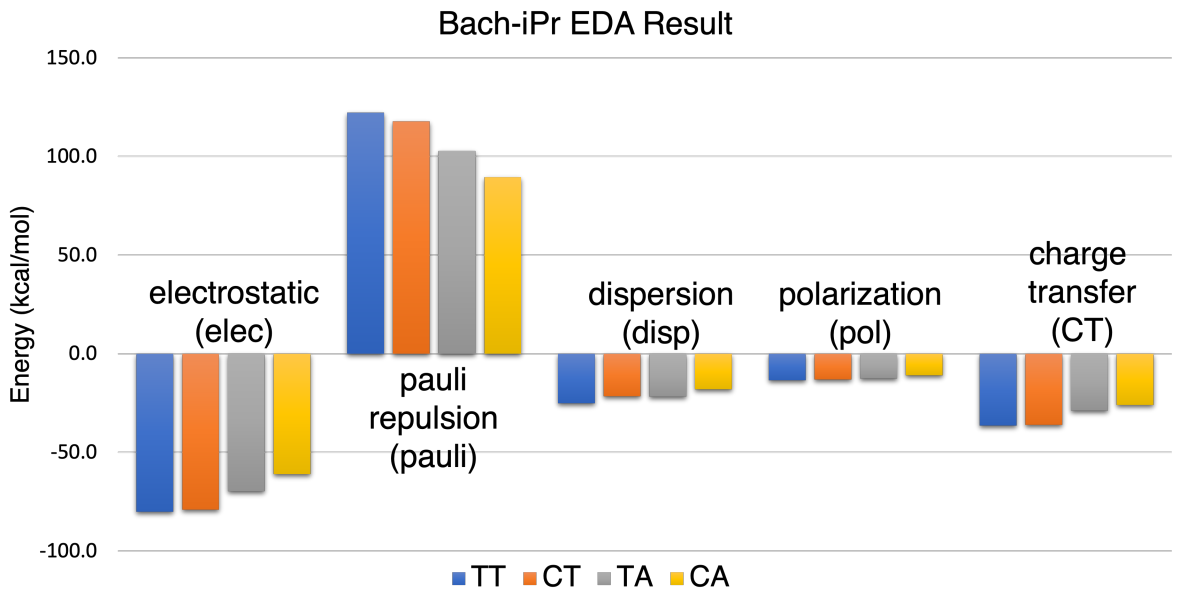


| | $E_{elec}$ | $E_{pauli}$ | $E_{disp}$ | $E_{pol}$ | $E_{CT}$ | $E_{int}$ | $\Delta E_{int}$ | $\Delta E_{strain}$ | $\Delta E$ | $\Delta E^*$ |
|---|---|---|---|---|---|---|---|---|---|---|
| **CA** | -61.1 | 89.6 | -18.1 | -11.0 | -26.0 | -26.4 | 6.5 | 1.3 | 7.8 | 8.3 |
| **CT** | -79.0 | 117.8 | -21.6 | -13.0 | -36.1 | -32.0 | 0.9 | 0.5 | 1.4 | 2.0 |
| **TA** | -69.7 | 102.9 | -21.7 | -12.5 | -28.8 | -29.8 | 3.4 | 3.6 | 7.0 | 6.6 |
| **TT** | -80.1 | 122.3 | -25.2 | -13.5 | -36.5 | -32.9 | 0.0 | 0.0 | 0.0 | 0.0 |

FIGURE 7.3. Top: EDA result of Bach-*i*Pr systems in histogram. Bottom: Summary of decomposed energies, relative interaction energy ($\Delta E_{int}$), relative strain ($\Delta E_{strain}$), and relative activation energy barriers ($\Delta E$ and $\Delta E^*$) in kcal/mol given by QChem ALMO-EDA2 under M06/6-311G(d,p)+LANL2DZ level of theory.

The EDA results for the four reaction systems have similar features. Take the Bach-*i*Pr system as an example (Figure 7.3), the primary interaction energy sources are from electrostatic and Pauli repulsion. Other interactions, including orbital interactions of polarization and charge transfer, and non-covalent interactions represented as dispersion, also play the role of balancing repulsive energy. When comparing the result of four TS1 isomers, the favored interaction is enhanced when the bromine atom is close to the catalyst, manifested by significantly increased electrostatic interactions, orbital interactions, and dispersions. However, as the catalyst and substrate are closer due to stabilizing interactions, a significant increase in the Pauli repulsion coincides. Combining the energy components describes the different

| Level of theory | conf | elec | Pauli | disp | pol | CT | int |
|---|---|---|---|---|---|---|---|
| B3LYP-D3(0)/ 6-311G(d,p) | TT | -83.8 | 126.8 | -25.1 | -13.8 | -36.1 | -32.1 |
| | CT | -82.7 | 122.4 | -22.2 | -13.5 | -35.4 | -31.4 |
| | TA | -73.5 | 107.5 | -22.1 | -13.0 | -28.5 | -29.7 |
| | CA | -64.3 | 93.7 | -19.1 | -11.5 | -25.5 | -26.7 |
| M06/ 6-311G(d,p) | TT | -80.1 | 122.3 | -25.2 | -13.5 | -36.5 | -32.9 |
| | CT | -79.0 | 117.8 | -21.6 | -13.0 | -36.1 | -32.0 |
| | TA | -69.7 | 102.9 | -21.7 | -12.5 | -28.8 | -29.8 |
| | CA | -61.1 | 89.6 | -18.1 | -11.0 | -26.0 | -26.4 |

TABLE 7.3. Energy decomposition analysis results in kcal/mol given by *QChem* ALMO-EDA2.

| conf | $E_{sub}$ (Hartree) | $E_{cat}$ (Hartree) | $E_{sub} + E_{cat}$ (Hartree) | $\Delta E_{sub}$ (kcal/mol) | $\Delta E_{cat}$ (kcal/mol) | $\Delta E_{strain}$ (kcal/mol) |
|---|---|---|---|---|---|---|
| **CA** | -3189.17822 | -1132.79929 | -4321.97751 | 1.3 | -0.1 | 1.3 |
| **CT** | -3189.17946 | -1132.79918 | -4321.97864 | 0.5 | 0.0 | 0.5 |
| **TA** | -3189.17483 | -1132.79895 | -4321.97378 | 3.4 | 0.2 | 3.6 |
| **TT** | -3189.18032 | -1132.79920 | -4321.97952 | 0.0 | 0.0 | 0.0 |

TABLE 7.4. Single point energies on substrate and catalyst individually in the geometry of TS1s in Bach-*i*Pr system under M06/6-311G(d,p)+LANL2dz level of theory.

interaction energies for TS1 isomers – compared to TT-TS1, CT-TS1 has similar interaction energies. But for TA-TS1 and CA-TS1, the overall interactions are weakened with 3.4 and 6.5 kcal/mol, respectively (see the result of M06/6-311G(d,p) in table 7.3). Nevertheless, TA and CA also feature a slightly more substantial distortion effect, elevating the energy barrier. Overall, the motive behind thermodynamically performed BrToward-TS1s is credited to stronger interactions and slighter distortion.

**7.1.5. AIMD details.** *Quasi*-classical *ab initio* dynamic simulation was implemented by Progdyn script invented by Singleton's group. The stopping criteria are defined as follows: the Rh carbene reactant is formed with C4-H5 bond lengths less than 1.10Å; the P1-lactone is formed with C1-C5 bond lengths less than 1.60Åand C1-H5 bond lengths less than 1.10Å; the P2-fragmentation is formed with C2-O3 distance greater than 2.30Å.

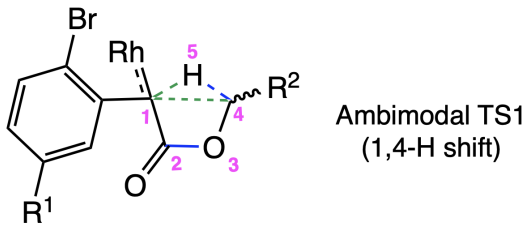


FIGURE 7.4. TS1 with critical atomic labels.

**progdyn.conf file**

method b3lyp/genecp

method2 restricted

charge 0

multiplicity 1

processors 16

memory 60GB

killcheck 1

diagnostics 2

title Rh t21 cis test

#*** initialdis – 0 (default) turns off displacement of the normal modes, so that all trajectories start from the same place

# and only the energies and signs of the motion in the modes are randomized

# 1 gives a flat distribution of displacements where all of the possible values are equally likely

# 2 (recommended) gives a QM-like gaussian distribution of displacements, so that displacements in the middle are more likely that

# those at the end by 1/e

initialdis 2 timestep 1E-15

#*** scaling – this lets you scale the gaussian frequencies by a constant

scaling 1.0

temperature 298.15

method3 empiricaldispersion=gd3

method4 iop(2/9=2000)

methodfile 10 #*** numimag –This tells the program the number of imaginary frequencies in the starting structure.

#if 0, treats as ground state and direction of all modes is random

#if 1, motion along the reaction coordinate will start out in the direction defined by searchdir

#if 2, only lowest freq will go direction of searchdir and other imag mode will go in random direction

numimag 1

#*** searchdir – This keyword says what direction to follow the mode associated with the imaginary frequency.

#The choices are "negative" and "positive". Positive moves in the direction defined in the gaussian frequency calculation

#for the imaginary frequency, while negative moves in the opposite direction. The correct choice can be made either

#by a careful inspection of the normal modes and standard orientation geometry, or by trial and error.

searchdir negative

#*** classical – for quassiclassical dynamics, the default, use 0. for classical dynamics, use 1 #if there are no normal modes and the velocities are to be generated from scratch, use classical 2 classical 0

#*** keepevery –This tells the program how often to write the gaussian output file to file dyn, after the first two points. #Use 1 for most dynamics to start with, but use a higher number to save on disk space or molden loading time.

keepevery 1

#*** highlevel –For ONIOM jobs, the following line states the number of highlevel atoms, #which must come before the medium level atoms. Use some high value such as 999 if not

using ONIOM

highlevel 999

#*** displacements – This keyword lets you set the initialdis of particular modes by using a series of lines of the format

# displacements NumberOfMode InitialDisForThatMode, as in the example below. You should be able to do as many of these as you like

# you might consider this for rotations where a straight-line displacement goes wrong at large displacements

# The choices for InitialDisForThatMode are 0, 1, 2, and 10, where 10 does the same thing as 0 but is maintained for now because

# a previous version of the program had a bug that made 0 not work.

displacements 2 0

displacements 3 0

displacements 4 0

displacements 5 0

displacements 6 0

displacements 7 0

displacements 8 0

displacements 9 0

displacements 10 0

#*** etolerance –This sets the allowable difference between the desired energy in a trajectory and the actual

#energy, known after point 1 from the potential energy + the kinetic energy in the initial velocities.

#The unit is kcal/mol and 1 is a normal value for mid-sized organic systems. For very large and floppy molecules, a larger value

#may be needed, but the value must stay way below the average thermal energy in the

molecule (not counting zpe).

#If initialdis is not 0 and few trajectories are being rejected, decrease the value.

etolerance 1.0

damping 1

reversetraj true

## 7.2. Supporting Information of Chapter 3

The complete information including all the raw data can be accessed at https://pubs.acs.org/doi/abs/10.1021/jacs.4c00382

**7.2.1. Other conformations of CH activation TS for the Model System.** Except for the eight C-H insertion TSs for the model system shown in the 3.1 derived from three pairs of geometrical possibilities, we also observed one high energetic TS for s-*cis*-chair system. This TS leads to the **elimination'** product – where the acidic H is deprotonated by terminal alkene. Below we depict the TS structure and its IRC pathway. This barrier is 3 kcal/mol higher than the other parallel transition states mentioned in the manuscript (Figure 7.5).

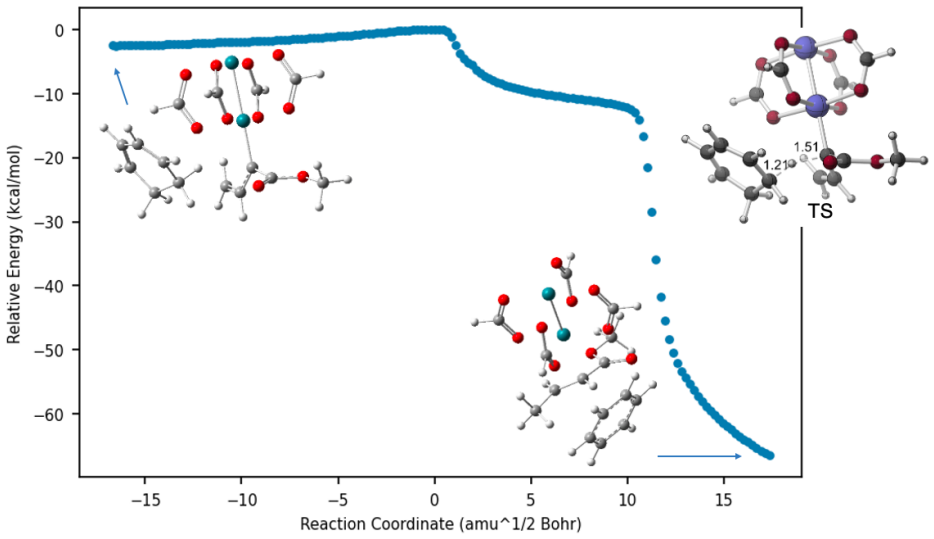


FIGURE 7.5. The IRC of the high energetic conformer of $TS4_H$, with two minima and the TS geometries depicted.

**7.2.2. Details of CCCR mechanism. TS5** (C-C activation), which competes with the **TS4** (C-H activation) was studied as well. The TS conformers can be classified in the same pattern as **TS4**s. The optimized TS structures with critical bond lengths are summarized in Figure 7.6. The following IRC study shows that different C-C activation TS conformers produce three different kinds of IRC products: 1) C-C activation product (CC); 2) cyclopropanation product (CP) and 3) cyclopropanation combined with Cope rearrangement (CCCR). Among those products, CCCR has the lowest DFT energy, which is also the

| conformation | s-*cis* | | | | s-*trans* | | | |
|---|---|---|---|---|---|---|---|---|
| | chair | | boat | | chair | | boat | |
| | in | out | in | out | in | out | in | out |
| $\Delta G^{\ddagger}$ | 9.7 | 9.2 | 8.5 | 7.9 | 7.0 | 7.1 | 11.0 | 10.8 |
| IRC product | CCCR | CCCR | CP | CP | CP | CP | CC | CC |

TABLE 7.5. $\Delta G^{\ddagger}$ and IRC products for the C-C activation TSs. Energies are in kcal/mol and are relative to the $G_{1,3-cyclohexadiene}$ + best $G_{Rh-carbene}$ at the B3LYP-D3(0)/6-311+G(d,p)+LANL2DZ//B3LYP-D3(0)/6-31G(d)+LANL2DZ level of theory.

reported C-C activation product in the experiment. The relative activation energies and corresponding IRC products are summarized in the Table 7.5 below. Only s-*cis* chair TS conformers' IRC has a flat region after the first C-C bond forms (Figure 7.7). Overall, the most favorable $\mathbf{TS5}_{H-trans-chair}$ reveals a stepwise mechanism – cyclopropanation followed by Cope rearrangement to produce CCCR product.

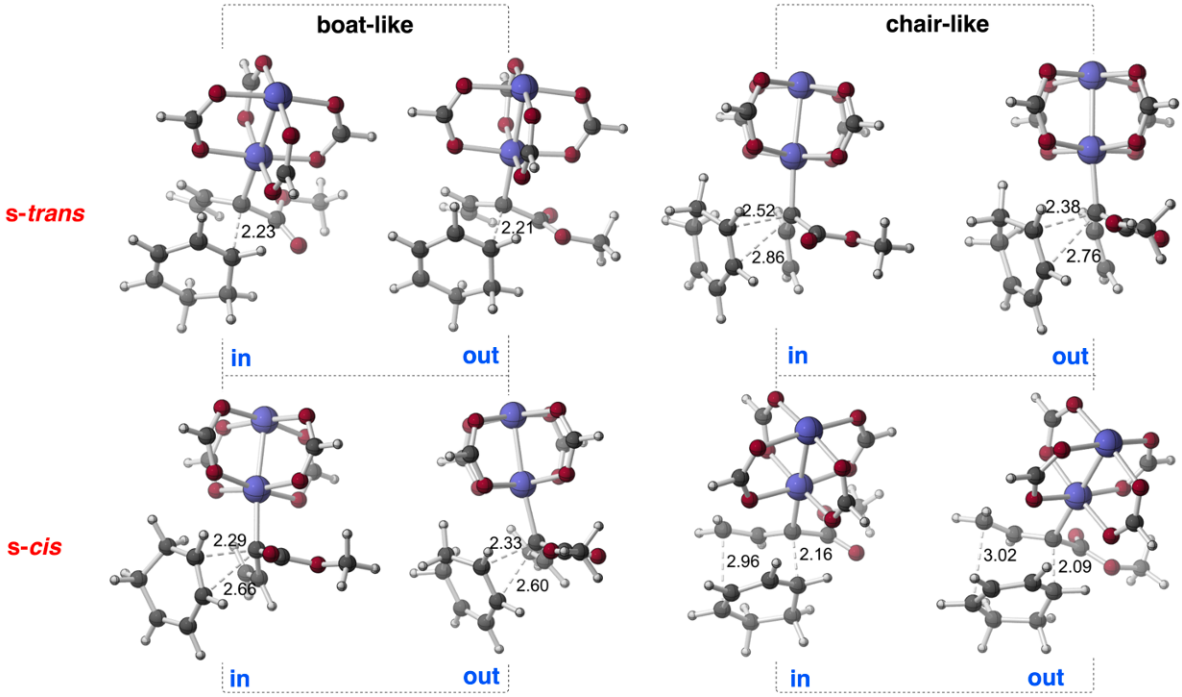


FIGURE 7.6. Model system C-C insertion TS conformations with key bond lengths in Å

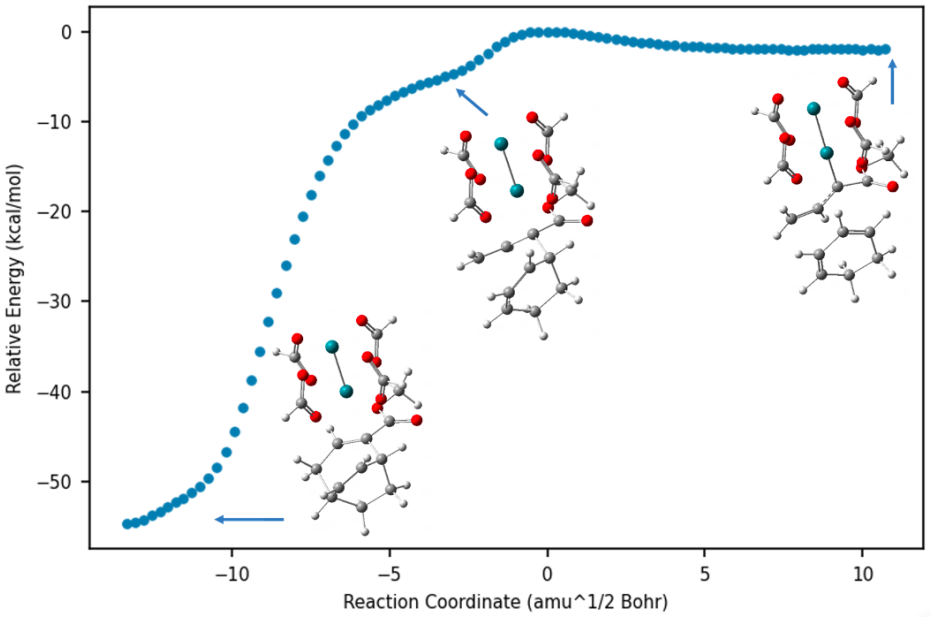


FIGURE 7.7. IRC plot of $\mathbf{TS5}_{H-cis-chair-in}$ with critical structures.

Since dynamic effect may be involved in the concerted generation of CCCR product, we performed downhill AIMD simulation with a maximum length of 1000 fs. Among the TSs given different products, only $\mathbf{TS5}_{H-cis-chair-in}$ that forms CCCR in its IRC gives three types of trajectories while others give the only IRC product. The three kinds of products include:

(1) C1-C4 bond formed intermediate;

(2) C1-C4 and C3-C7 bond formed CCCR product (IRC product shown in Figure S11) and

(3) C1-C4 and C3-C5 bond formed another cyclization product.

No CP product was observed. Similar to the dynamic mismatching involving the terminal alkene rotation that traps $\mathbf{IM}_H$ for C-H functionalization mechanism, $\mathbf{IM}_{H-CC}$ is produced due to the same reason of elongated distance between C3 and C7. The projection of trajectories is depicted in Figure 7.8.

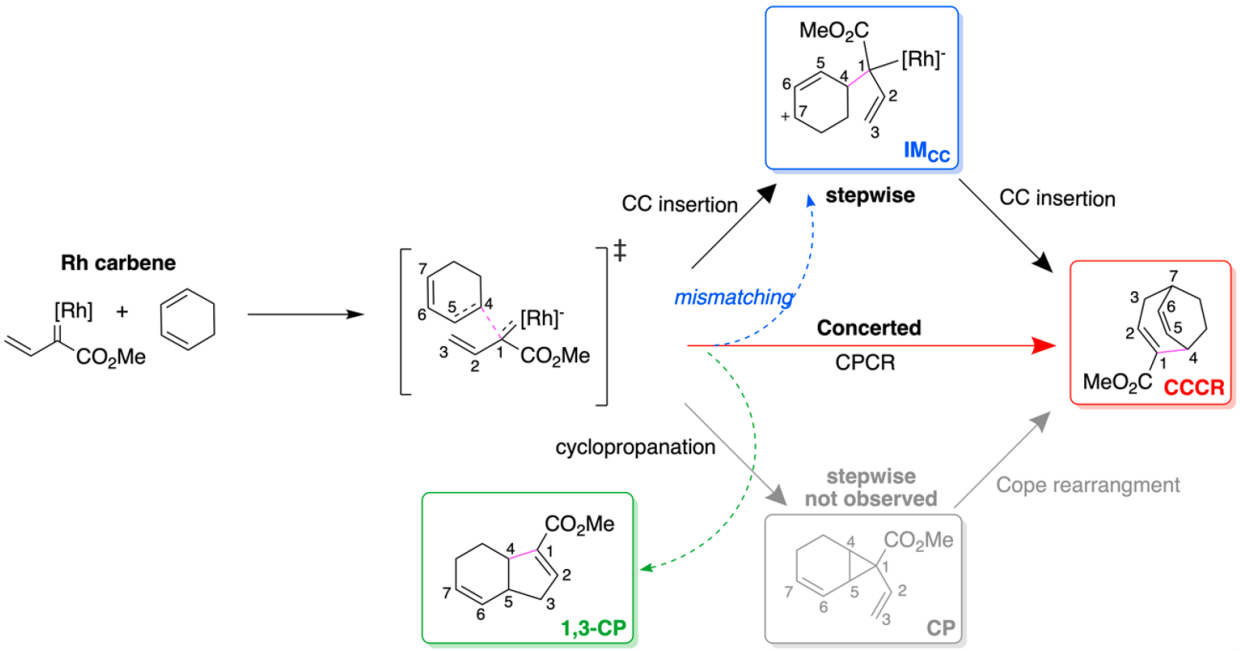


SCHEME 7.1. The reaction mechanism for $\mathbf{TS5}_{H-cis-chair}$ elucidated by the AIMD results, represented with structures that are labeled with atomic indices.

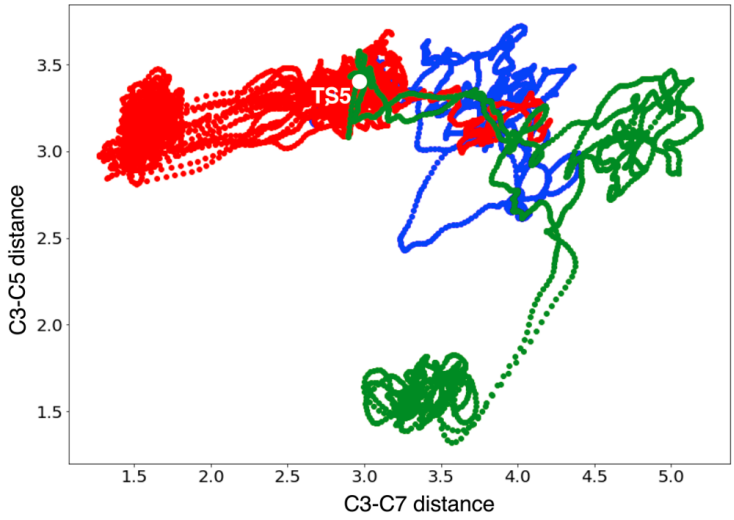


FIGURE 7.8. 2D projection of $\mathbf{TS5}_{H-cis-chair-in}$ trajectories with respect to C3-C7 distance and C3-C5 distance. The TS is highlighted as a white dot on the graph. Blue: C1-C4 bond formed intermediate; green: 1,3-CP; red: CCCR

### 7.2.3. AIMD details.

7.2.3.1. *Total number of trajectories.* **Model system**

| type | cis-chair-in | trans-boat-in | cis-chair-out | trans-chair-in |
|---|---|---|---|---|
| R-P | 62 | 68 | 14 | 27 |
| R-R | 16 | 4 | 9 | 11 |
| P-P | 8 | 0 | 3 | 4 |
| all | 86 | 72 | 26 | 42 |

TABLE 7.6. Number of trajectories for each TS conformers in the model system. R-P: reactant-product; R-R: reactant-reactant recrossing; P-P: product-product recrossing

| type | cis-chair-in (quasi-classical) | cis-chair-in (classical) | trans-chair-in (quasi-classical) | trans-chair-in (classical) |
|---|---|---|---|---|
| R-P | 97 | 54 | 72 | 91 |
| R-R | 27 | 0 | 3 | 3 |
| P-P | 25 | 0 | 16 | 3 |
| all | 149 | 54 | 91 | 97 |

TABLE 7.7. Number of trajectories for each TS conformers in the Ph system. R-P: reactant-product; R-R: reactant-reactant recrossing; P-P: product-product recrossing

The number of trajectories for the model system is summarized in Table 7.6. The model systems were run in the gas phase for both optimization and MD simulations.

**Ph system**

The number of trajectories for the model system is summarized in Table 7.7. The Ph systems were run in implicit solvent (PCM, solvent=DCM) for both optimization and MD simulations to account for the solvent used in the experiment.

7.2.3.2. *Stopping criteria.* Note that the stop criteria (Figure 7.9, Table 7.8) were initially defined solely based on the formation of the **CH** and **CHCR** products. However, as other dynamic products were captured in the model system, we began to define the subsequent minima according to the geometry observed in the unusual trajectories that were unable to terminate within 1000 fs as well as optimized structures from subsequent DFT calculations. No stop criteria were designed for ligand-assisted proton transfer situations; those **elimination*** trajectories were manually assigned. The formation of intermediate structures was also manually checked to make sure the structure was trapped due to the quick rotation of terminal alkene.

| | criteria1 | criteria2 |
|---|---|---|
| Rh-carbene | H1-C2 <1.10 | - |
| CH product | H1-C3 <1.10 | C2-C3 <1.60 |
| CHCR product | H1-C3 <1.10 | C4-C5 <1.60 |
| CH* product | H1-C3 <1.10 | C3-C6 <1.60 |
| elimination product | H8O7 <1.60 | - |
| ether | C2O7 <1.60 | - |
| max length | 1000 steps | |

TABLE 7.8. Stop criteria setup for Progdyn.

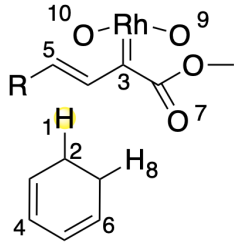


FIGURE 7.9. 2D structure with critical atomic labels related to the stopping criteria.

7.2.3.3. *Progdyn setup.* We performed both *quasi*-classical and classical MD by specifying the 'classical' command in the Progdyn script. The configuration file including details for dynamic simulations is identical to the Appendix 7.1.5. For the model system, there is no implicit solvation involved. While for the $Rh_2(OAc)_4$ Ph system, PCM solvation model was included to represent the dichloromethane environment in the experiment.

The Hessians were recomputed by *Gaussian 16* based on the variational TS structures, which were then incorporated into the normal-mode sampling process in Progdyn. The box constraint is turned off during the simulation by setting 'boxon 0'.

7.2.3.4. *Analysis of trajectories.*

CH product formation. As mentioned in the manuscript, none of the trajectories originating from either $\mathbf{TS4}_{H-trans-boat-in}$ or $\mathbf{TS4}_{H-cis-chair-in}$ directly led to the formation of the direct C–H insertion product, nor did they exhibit a tendency towards such an outcome. This conclusion is based on bond tracking results, which indicate that none of the trajectories exhibited a reduction in the C-C bond distance following the transition state structure.

The C-C distance, which indicates the formation of the **CH** product, is illustrated in the figure 7.10.

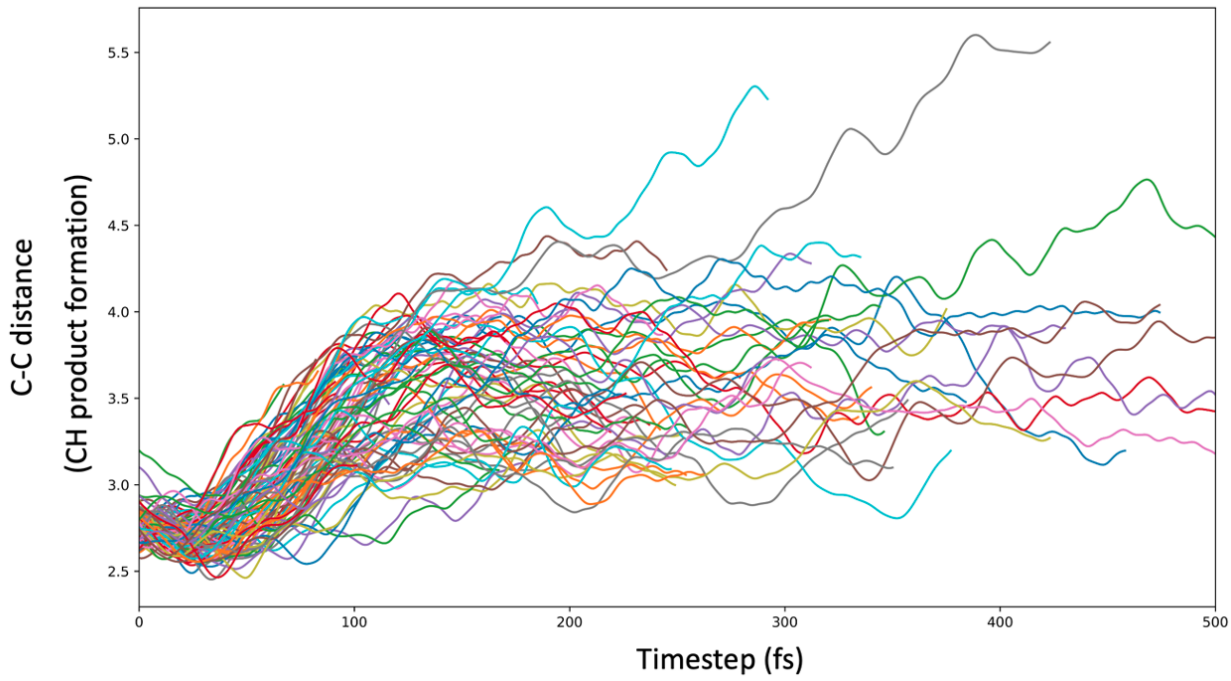


FIGURE 7.10. Plots of trajectories from $\mathbf{TS4}_{H-trans-boat-in}$ and $\mathbf{TS4}_{H-cis-chair-in}$ in terms of C-C distance that corresponds to the formation of **CH** product

Time variability. The trajectory lengths resulting in **CHCR** and **elimination** products exhibit significant variability, as depicted in the figure 7.11. The time required to generate the **CHCR** product from $\mathbf{TS4}_{H-cis-chair-in}$ varies between 60 and over 400 fs, with an average of 214 fs. In contrast, the formation of the **elimination** product from the same transition state occurs within an average of 169 fs. $\mathbf{TS4}_{H-trans-boat-in}$, displaying a narrower range of durations, takes a consistently longer time to form the **CHCR** product, with an average of 387 fs and a span ranging from 350 to 430 fs. The variability in the duration of **elimination** product formation is markedly high for both transition states. Overall, product formation takes longer when proceeding through the $\mathbf{TS4}_{H-trans-boat-in}$ transition state structure. The extended duration associated with the $\mathbf{TS4}_{H-trans-boat-in}$ can be ascribed to the dynamic mismatching effect, wherein the rotation of the terminal alkene results in a

prolonged time frame for **CHCR** product formation and increased trajectory flexibility that allows exploration of various product channels

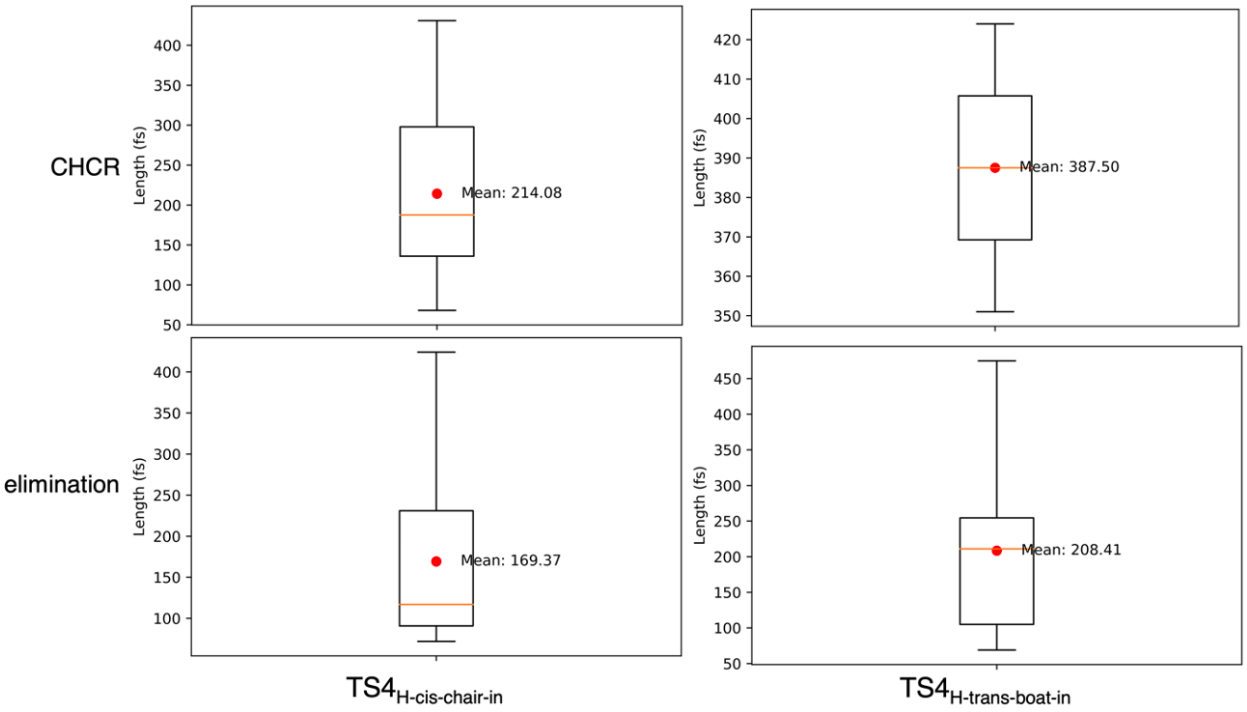


FIGURE 7.11. Box plots of trajectory lengths. The median is indicated by an orange line, and the mean is represented by a red dot, with the value noted alongside.

C-C distance distribution. In our previous study on Rh-catalyzed lactonization reactions in Chapter 2, we observed a post-transition state bifurcation effect following a similar pattern: a concerted but asynchronous hydride shift, succeeded by either bond formation or bond cleavage. To compare the AIMD trajectories of these two analogous reactions, we plotted the density distribution of the C-C bond associated with the **CHCR** product from this study against the C-C bond related to the lactone product from our prior research. In Figure 7.12 below, the bonds under investigation are highlighted in red, while the trajectories are differentiated by orange and blue colors according to their type. The C-C distance density overlap is considerably more pronounced for the **CHCR** system discussed herein, suggesting a more complex dynamic effect. This is associated with its broader and more extensive

post-transition state region, allowing for extended exploration before stabilizing into either the **CHCR** or the **elimination** product.

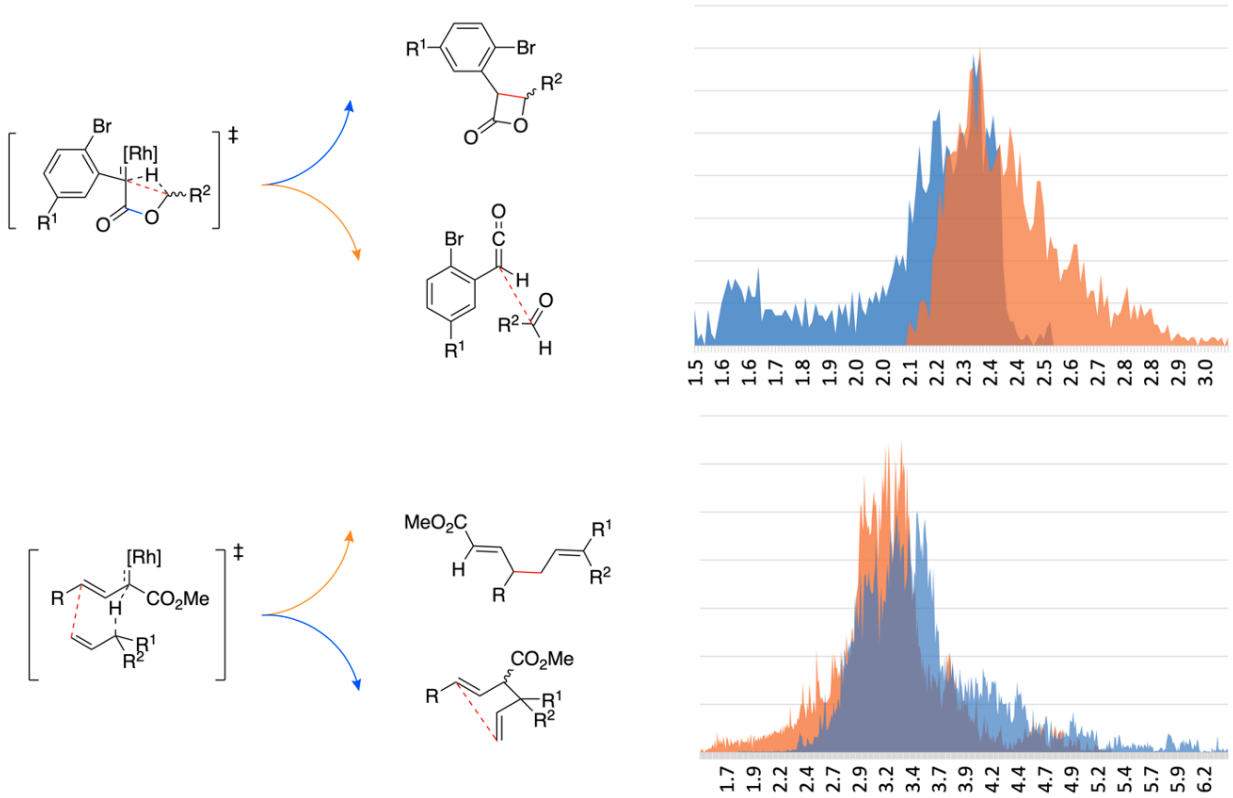


FIGURE 7.12. Left: Schematic representation of the bifurcation mechanism for the lactonization reaction detailed in our previous work and for the current study, with the critical C-C bond highlighted in red. Right: Density plot of C-C bond distances, differentiated by trajectory type. In the lactone system (referred to as the Bach-iPr CT system in the Chapter 2, which exhibited approximately a 1:1 ratio of dynamic trajectories yielding lactone and fragmentation products), orange indicates trajectories leading to fragmentation, while blue signifies those forming the lactone product. In the CHCR system presented below, orange denotes the trajectories that result in the CHCR product, and blue represents those leading to the elimination product.

7.2.3.5. *Product's distribution predicted by Newton program.* We used Newton program by Carpenter to test whether the product distribution is correlated with the vibrational mode corresponding to the reaction coordinate (which has a negative eigenvalue). The script computes the dot product of two vectors:

| TS | CHCR : CH :ketene acetal: elimination (Newton) | CHCR : CH :ketene acetal: elimination (AIMD) |
|---|---|---|
| $\mathbf{TS4}_{H-cis-chair-in}$ | 28: 0 : 19 : 53 | 61: 6: 2:31 |
| $\mathbf{TS4}_{H-trans-boat-in}$ | 4 : 37 : 21: 38 | 11:11: 3:76 |

TABLE 7.9. Product distribution predicted by Newton compared to AIMD results.

(1) the mass-weighted, normalized atomic displacement between the TS structure and the product;

(2) the mass-weighted eigenvector of the TS structure's second derivative matrix that corresponds to the reaction. The prediction given by the Newton program is far from the AIMD results, which hints that the ballistic effect is trivial for the model system's dynamic behavior.

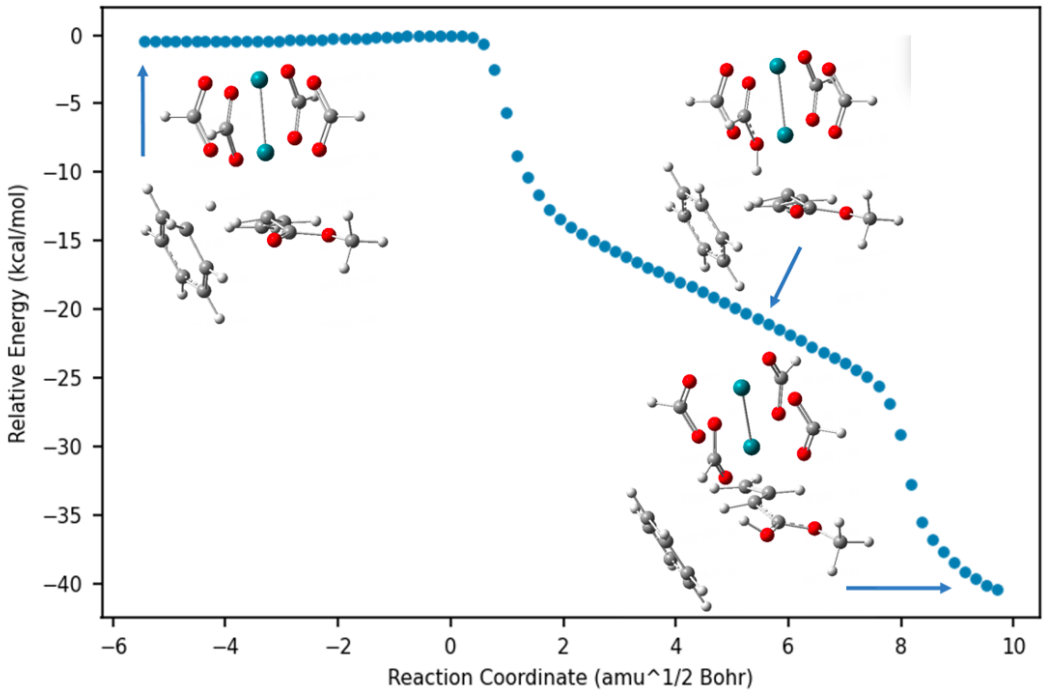


FIGURE 7.13. IRC plot of $\mathbf{TS7}_{H-cis}$

### 7.2.4. Other AIMD/IRC simulations.

7.2.4.1. *IRCs with "shoulders".* The IRCs of product conversion TSs show asynchronous aspects for several products interconversion TS. In Figure 7.13, the IRC of $\mathbf{TS7}_{H-cis}$, which corresponds to the reaction coordinate of proton transfer, connects the $\mathbf{IM}_{H-cis-chair-in}$ and

**elimination** product. The consecutive second proton transfer step happens concerted while asynchronously. The same type of **TS7** IRC that converts $\mathbf{IM}_H$ to elimination product through s-trans conformer is shown in Figure 7.14.

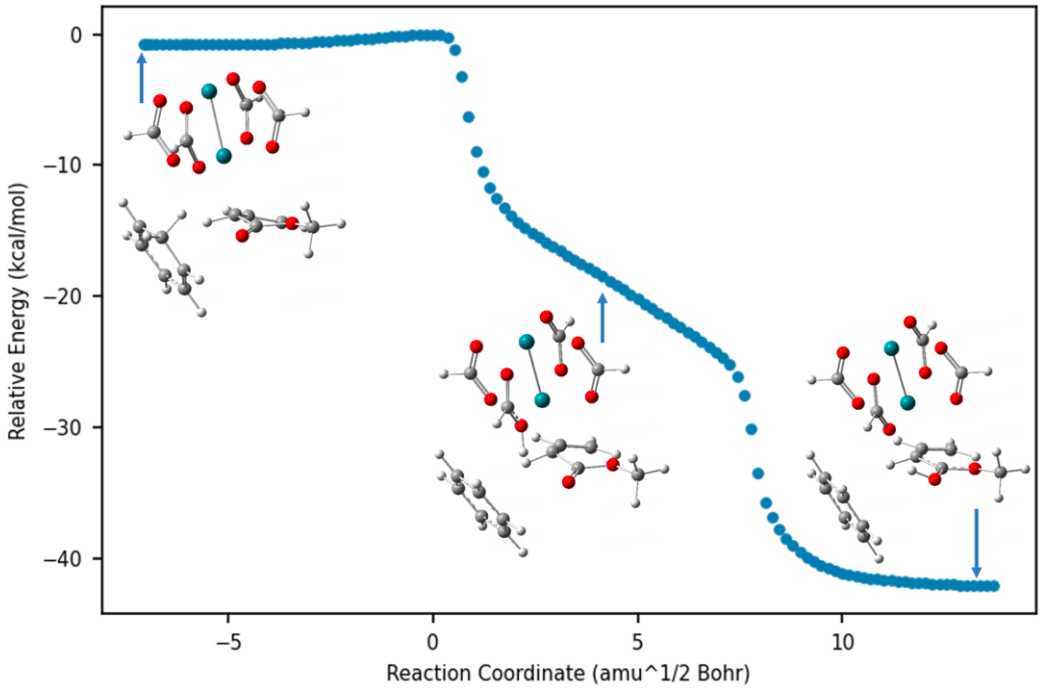


FIGURE 7.14. IRC plot of $\mathbf{TS7}_{H-trans}$

$\mathbf{TS9}_{H-trans}$ is a special transition state (TS) not found in the s-*cis* system. The reaction coordinate vibrational mode of $\mathbf{TS9}_{H-trans}$ is identical to that of $\mathbf{TS7}_{H-trans}$ and $\mathbf{TS9}_{H-cis}$, where the proton is transferred to the $HCO_2$ ligand. However, instead of being trapped at $\mathbf{IM}_H$, a subsequent C-O bond formation leads to the generation of the **ketene acetal** product.

| P1 - P2 | ratio |
|---|---|
| elimination-elimination | 83% |
| elimination - ketene acetal | 15% |
| elimination - $\mathbf{IM}_{H-trans}$ | 2% |

TABLE 7.10. Product distribution from AIMD result of $\mathbf{TS9}_{H-trans-chair-in}$

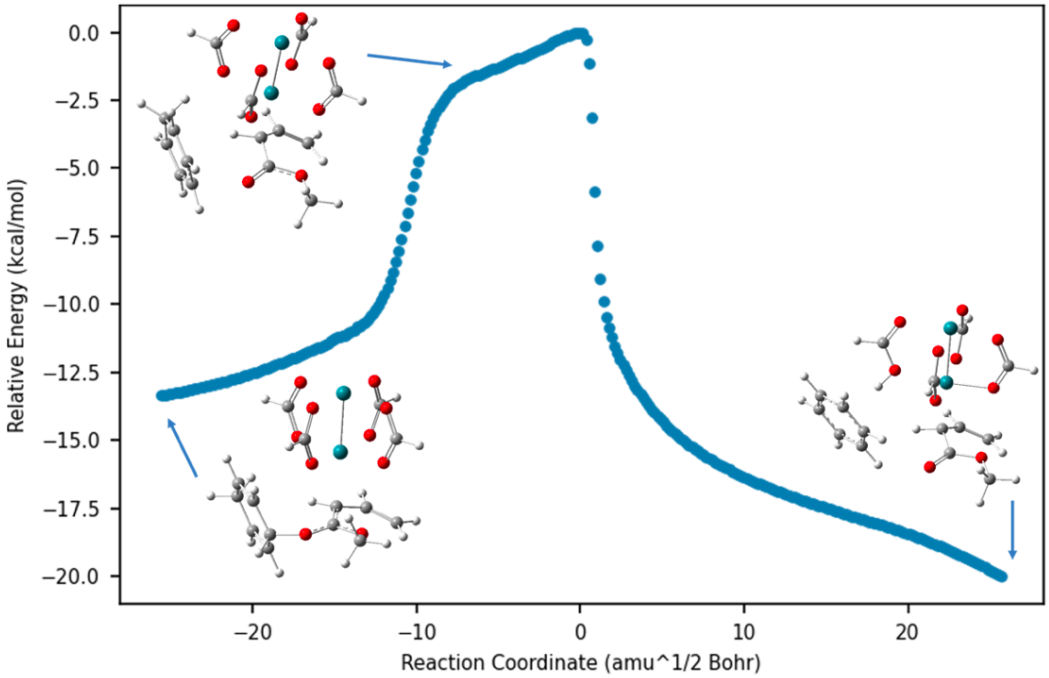


FIGURE 7.15. IRC plot of $\mathbf{TS9}_{H-trans}$.

7.2.4.2. *AIMD results of* $\boldsymbol{TS9}_{H-trans}$. In addition to the C-H insertion transition states, we also conducted AIMD simulations on TS9H-trans, which features an IRC in Figure 7.15 connecting the ketene acetal and protonated ligand. The TS structure is characterized by proton transfer, with the ketene acetal side exhibiting a flat region around the $\mathbf{IM}_{H-trans}$ structure. We collected three types of trajectories. Notably, instead of halting at the protonated ligands, the trajectories consistently progressed to the elimination product through proton shuttling to the carbanion substrate. Among these, 83% of the trajectories showed recrossing, exhibiting elimination products on both sides. Meanwhile, 15% of the trajectories aligned with the IRC results that generate the ketal acetal product, while 2% trapped at the $\mathbf{IM}_{H-trans}$ structure (see table 7.10).

**7.2.5. Projected energy profile by Sparse PCA.** To distinguish and visualize minima in a three-dimensional format using two geometric parameters as coordinates, we identified ten key bonds to serve as variables. These variables were linearly combined to represent the projection surface. For each system, we computed these ten numerical variables for the molecular geometry in every frame of the dynamic trajectories. Sparse Principal Component Analysis (SPCA) was then employed to determine the projection vectors. This method provides a mathematical approach to reduce data dimensionality while preserving maximum variance. Figure 7.16 depicts the PES of the $\mathbf{TS4}_{H-trans-chair-in}$. The dotted lines connecting the minima represent an optimized transition state structure with an IRC linking the two products. We included vertical dashed lines in the diagram to represent the energy levels of the TSs, originating from the midpoint between the connected products. Notably, these IRCs often exhibit a shoulder-like region on at least one side of the reaction pathway. While SPCA is a non-supervised process, it effectively separates the chemical space when analyzing the dynamic trajectories' frames. It distinguishes TSSs around the original point, with products dispersed on the surface and $\mathbf{IM}_{H-trans}$ positioned in between. However, the connections between stationary points remain too complex to be neatly described. Therefore, we made the connection plot according to the reaction mechanism as Scheme 3.5 in the Chapter 3.

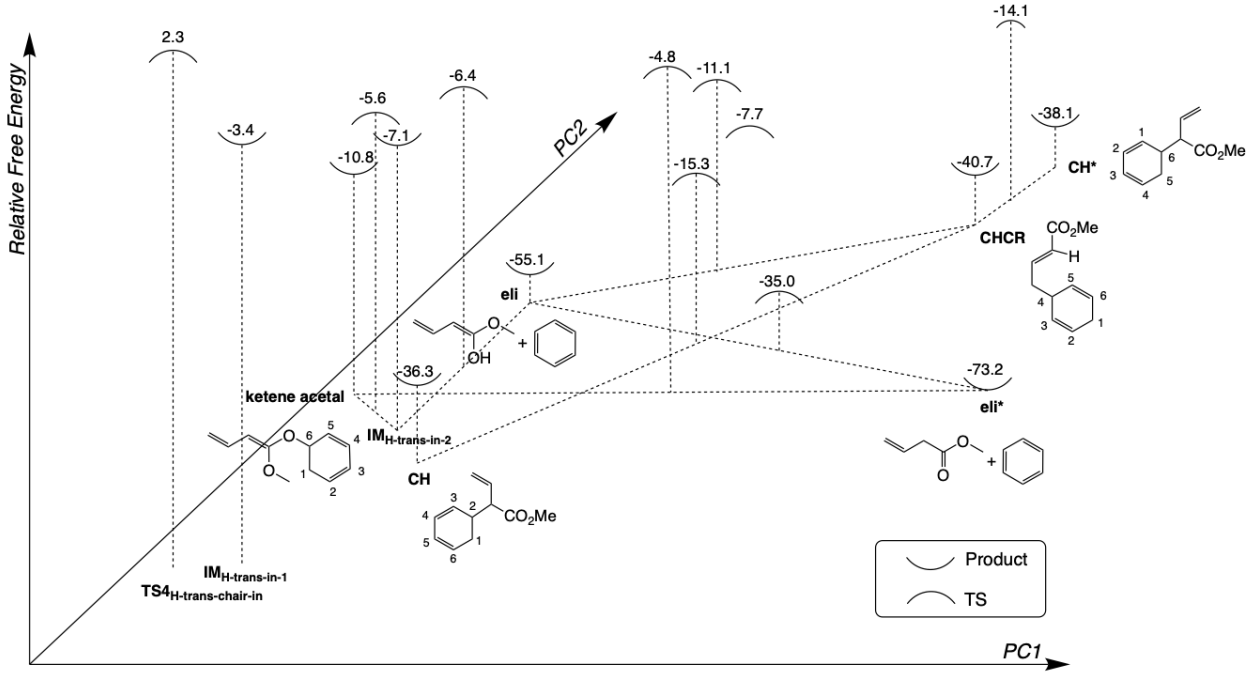


FIGURE 7.16. Energy profile of $\mathbf{TS4}_{H-trans-chair-in}$ system. The projection space is defined by the two principal components given by sparse PCA.

### 7.2.6. Geometry of $Rh_2$(s-DOSP)$_4$ systems.

7.2.6.1. *$Rh_2$(S-DOSP)$_4$.* The xTB-CREST conformational searching reveals the best conformer and the structures within a 10 kcal/mol energy window. As we have described in the manuscript, the two rotatable dihedral angles lead to different orientations of blocking ligands where $\alpha$ and $\beta$ can merely describe the exact conformation. Nonetheless, we display the representative low energetic structure of alkyl chain removed $Rh_2$($S$-DOSP)$_4$ that are classified as $\alpha\alpha\beta\beta$, $\alpha\beta\alpha\beta$, and $\alpha\alpha\alpha\beta$. Due to the steric hindrance of four bulky ligands, no $\alpha\alpha\alpha\alpha$ conformation was observed.

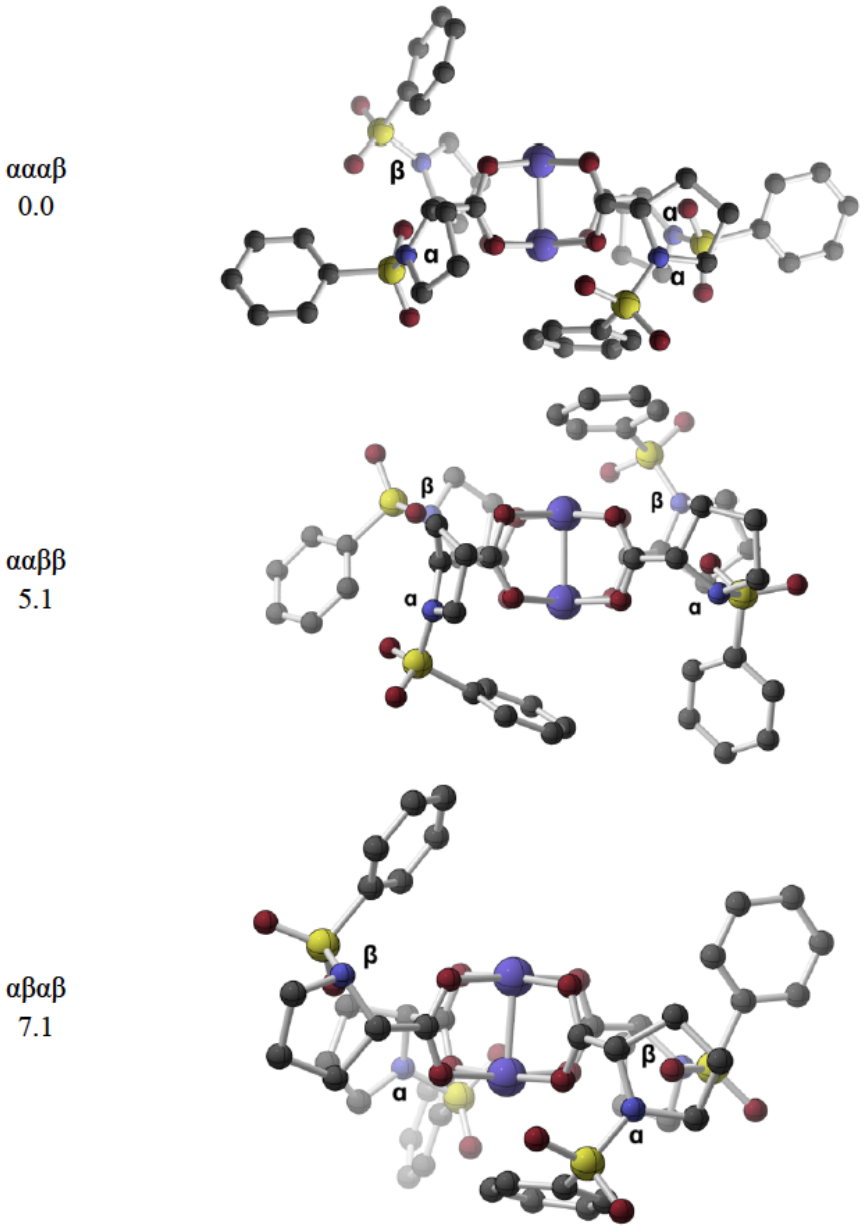


FIGURE 7.17. Representative $Rh_2(S\text{-DOSP})_4$ conformers and their relative potential energy at B3LYP-D3(0)/6-311+G(d,p)//B3LYP-D3(0)/6-31G(d)+LANL2DZ level of theory. For a clearer visual representation, hydrogen atoms are omitted.

7.2.6.2. *Rh-carbene.* The preferred arrangement of blocking ligands altered after the attachment of the carbene substrate. The optimal geometry has two adjacent ligands in an $\alpha$ orientation that anchor the styrene in the middle as shown in Figure 7.18. $\alpha\alpha\alpha\beta$, $\alpha\alpha\beta\beta$, $\alpha\beta\alpha\beta$ conformer was not observed among the low energetic Rh-carbenes. Instead, another

$\alpha\alpha\beta\beta$ structure that one side of the carbene is blocked and emerges with relatively low energy.

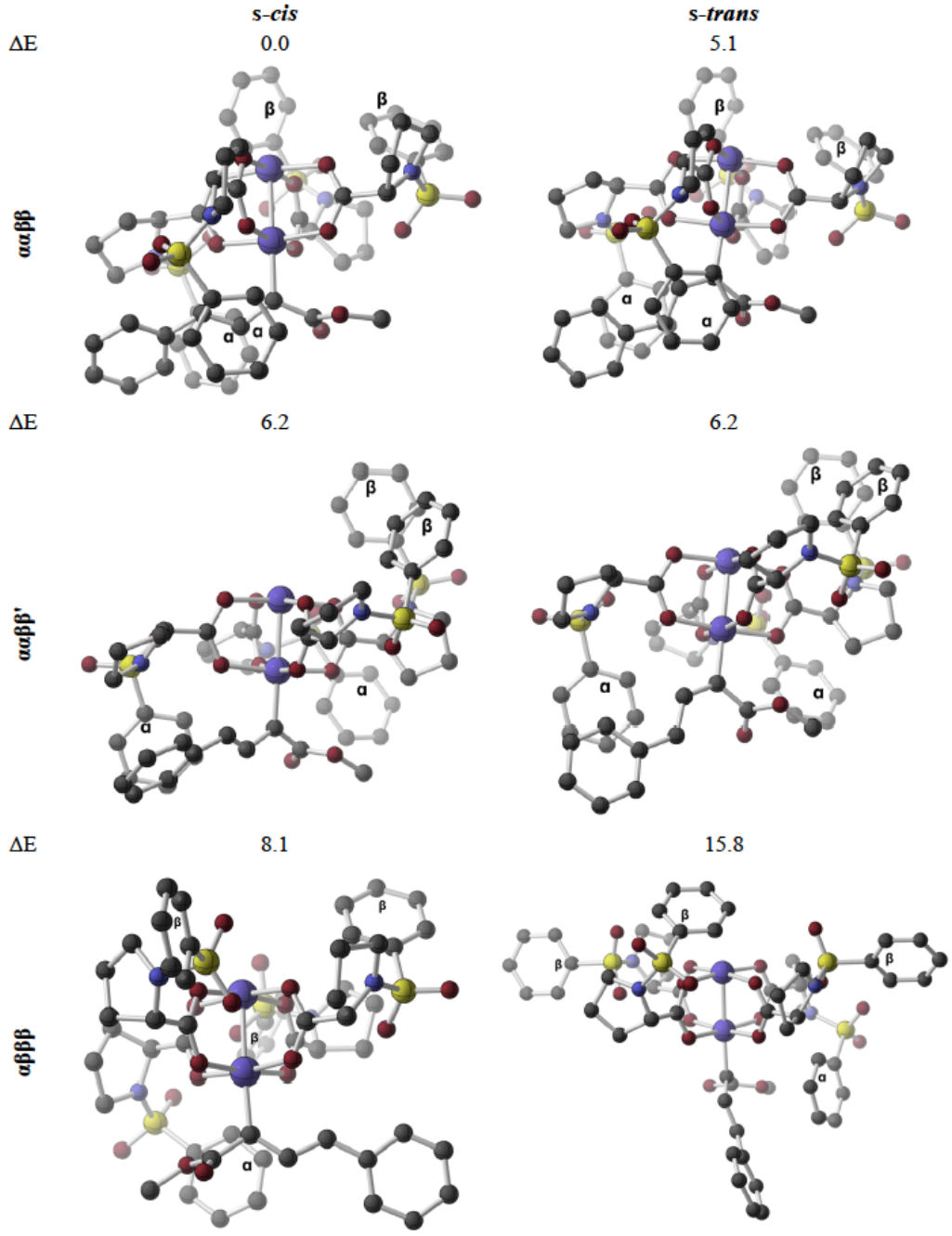


FIGURE 7.18. Representative Rh-carbene conformers and their relative potential energy at B3LYP-D3(0)/6-311+G(d,p)//B3LYP-D3(0)/6-31G(d)+LANL2DZ level of theory. Energies are related to the best conformer, which is s-*cis* $\alpha\alpha\beta\beta$. For a clearer visual representation, hydrogen atoms are omitted.

7.2.6.3. *$N_2$ extrusion TS.* Though the geometry and energies for Rh-carbene structure comparison give s-*cis* as the preferred intermediate, we performed conformational searching on $N_2$ extrusion **TS3** as it is the selective step for s-*cis*/s-*trans* Rh carbenes. When the third fragment is attached to the carbene center, the optimal conformer $\alpha\alpha\beta\beta$ at Rh-carbene stage loses its superiority. Instead, $\alpha\alpha\beta\beta'$ is favored, blocking just one side of the substrate while leaving a vacant side to accommodate the $N_2$. Similarly, one would expect that the C-H insertion and C-C activation transition state geometry is required in the same pattern that the 1,3-cyclohexadiene replaces the position of $N_2$ (Figure 7.19).

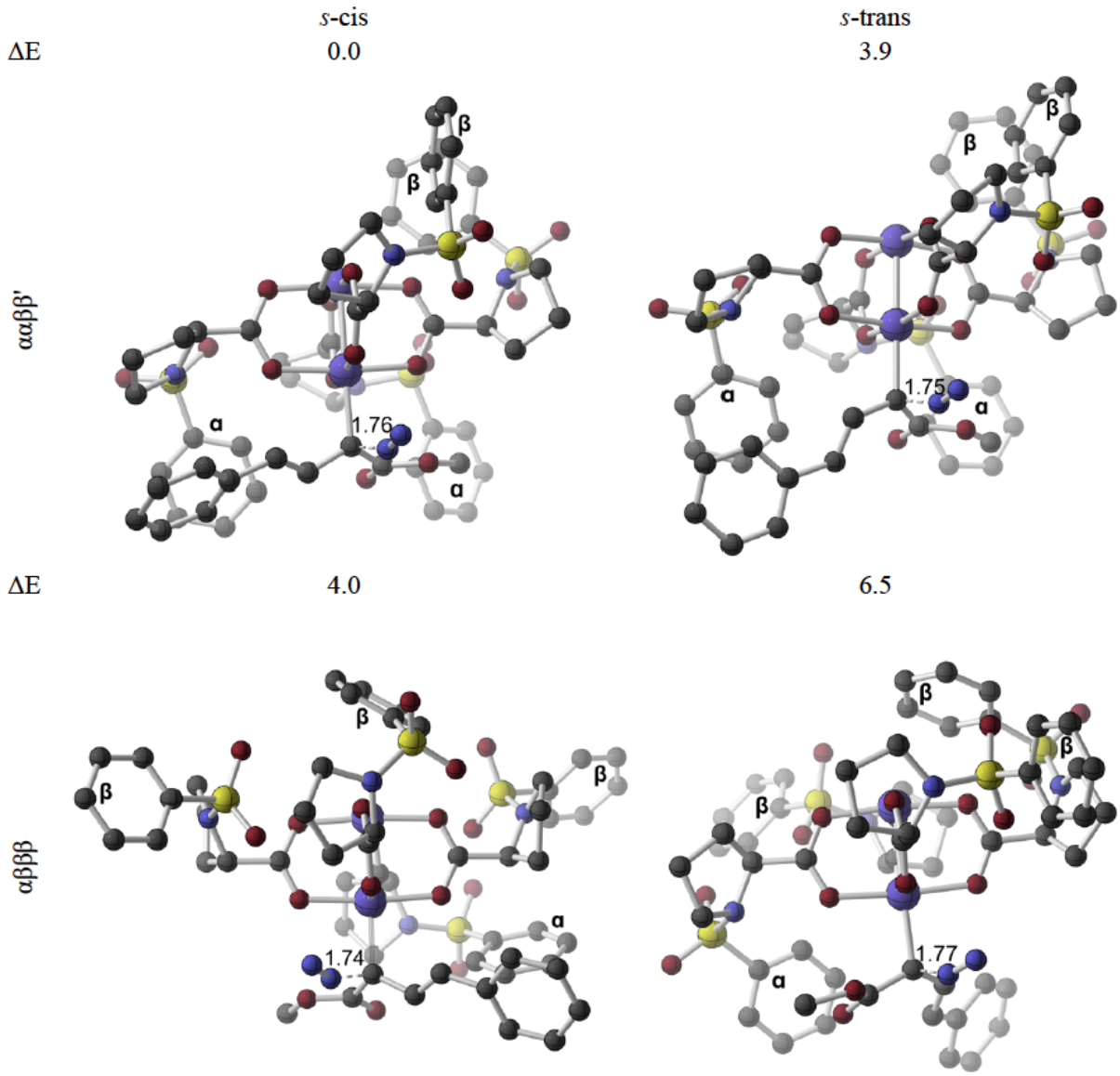


FIGURE 7.19. Representative $Rh_2(S\text{-DOSP})_4$ $N_2$ extrusion TS conformers and their relative potential energy at B3LYP-D3(0)/6-311+G(d,p)//B3LYP-D3(0)/6-31G(d)+LANL2DZ level of theory. Energies are related to the best conformer, s-*cis* $\alpha\alpha\beta\beta'$. For a clearer visual representation, hydrogen atoms are omitted.

## 7.3. Supporting Information of Chapter 4

**7.3.1. $N_2$ extrusion TS1.** The TS1-A, TS1-B and TS-D with compound **1** ($Rh_2(OAc)_3$(PHTCB)) are summarized in Figure 7.20. Based on the height of the barriers, we assume that the IM2-A is the dominant Rh-carbene conformation right after this step.

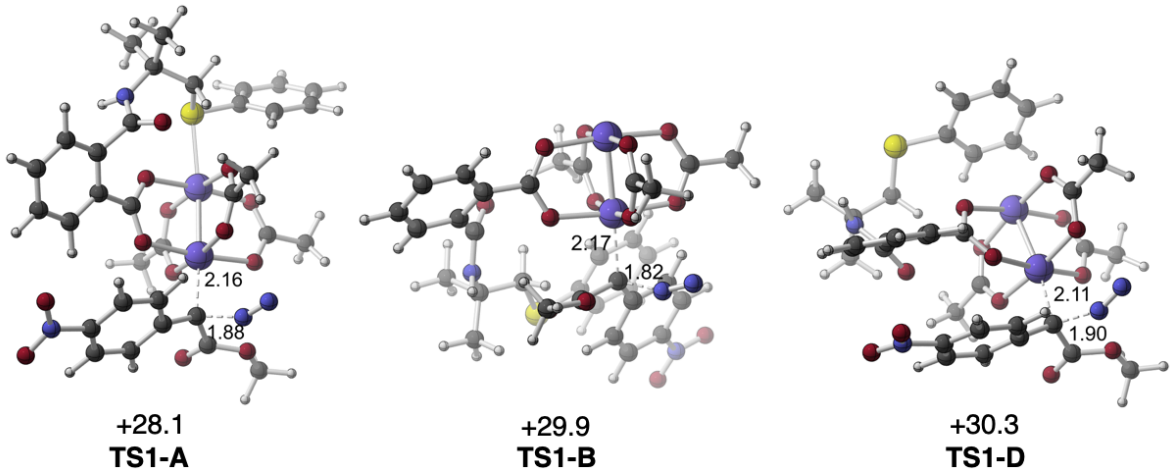


FIGURE 7.20. The $N_2$ extrusion TSs visualized by *CYLView 1.0* with critical bond length labeled. Relative free energies are related to the $G_{diazo} + G_{cat}$.

**7.3.2. You Shall Not Pass Barriers.** In the Chapter 4, Figure 4.7 displays the relative free energy profile starting from the ylide intermediate **IM2-C**. The high energetic cyclopropanation TSs and barrier heights are depicted in Figure 7.21. The optimal conformer with a "inner-sphere" geometry is depicted in Figure 7.22 after the ylide formation, not in patterns A, B, and D. The high energetic dimerization TSs and barrier heights are depicted in Figure 7.23. The energies are under SMD(DCE)-PWPB95-D4/def2-TZVPP//B3LYP-D3(0)/def2-SV(P) level of theory.

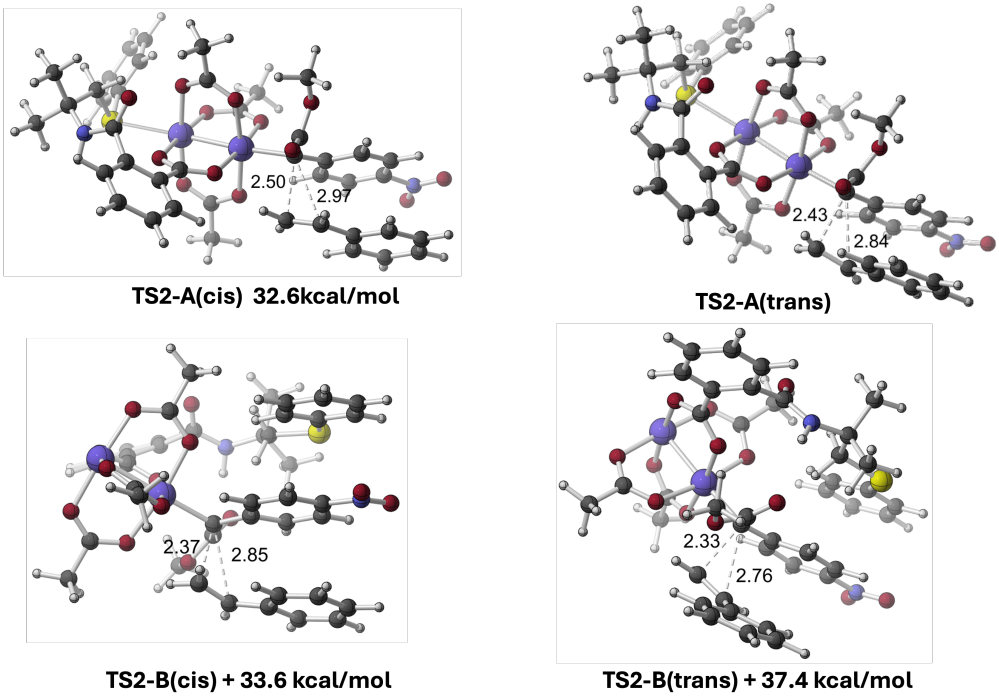


FIGURE 7.21. Cyclopropanation TS structure visualized by *CYLView 1.0* with critical bond length labeled in Å. The free energies are relative to the **IM2-C** ylide, in kcal/mol.

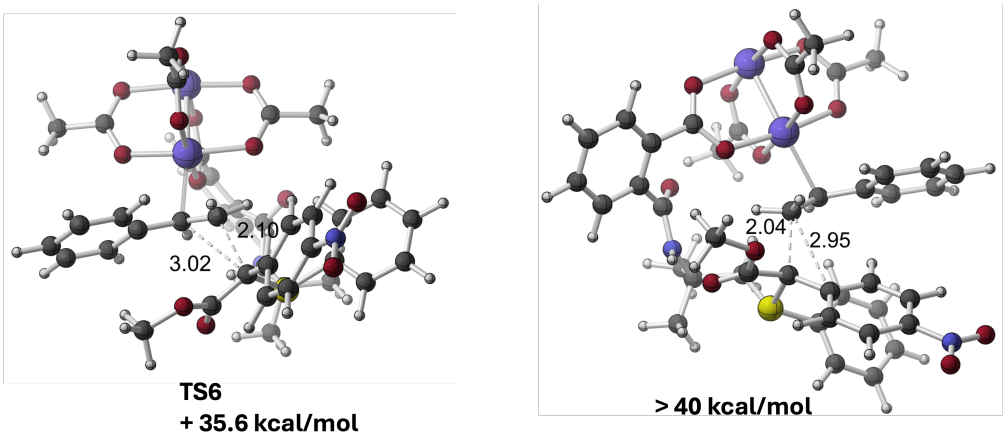


FIGURE 7.22. Inner sphere C-C activation structure visualized by *CYLView 1.0* with critical bond length labeled in Å. The free energies are relative to the **IM2-C** ylide, in kcal/mol.

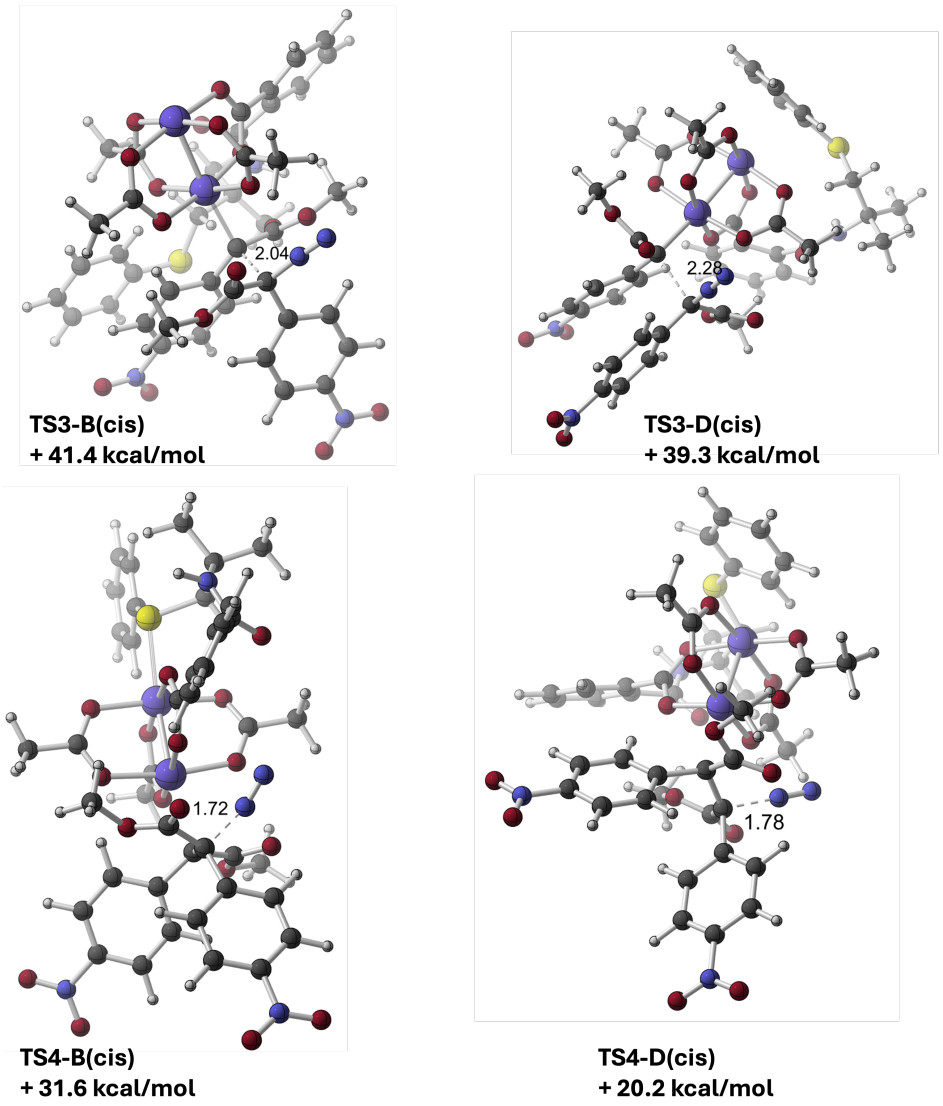


FIGURE 7.23. Dimerization TS structure visualized by *CYLView 1.0* with critical bond length labeled in Å. The free energies are relative to the **IM2-C** ylide, in kcal/mol.

## 7.4. Supporting Information of Chapter 5

**7.4.1. Benchmark.** Benchmarks herein use geometry optimized at ωB97X-D/def2-TZVP level of theory as all TS/minima previously reported for the barbaralyl cation could be optimized at this level. As we aim to find a level for AIMD simulation, we opted for 6-31G(d) and def2-SVP basis sets which are computationally efficient. We first benchmarked against relative electronic energies obtained at DLPNO-CCSD(T)/CBS level of theory against various exchange-correlation functionals in conjunction with 6-31G(d) and def2-SVP. The results are summarized below.

| | **A** | **B** | **TS2** | **TS3** | **TS4** |
|---|---|---|---|---|---|
| DLPNO-CCSD(T) | 0.00 | 3.06 | 2.66 | 4.23 | 5.41 |

TABLE 7.11. Relative potential energy relative to **A** under CCSD(T)/CBS level of theory in kcal/mol.

7.4.1.1. *Relative electronic energies.* To identify the optimal level of theory, we benchmark the relative energies of all stationary points against the energy of structure **A**, which was found to be the lowest-energy structure for the barbaralyl cation. The reference relative energies obtained using DLPNO-CCSD(T)/CBS are summarized Table 7.11. The results including mean absolute error (MAE) for the 39 density functionals with the 6-31G(d) and def2-SVP basis sets are presented in Table 7.12.

To compare the accuracy of different levels of theory, the mean absolute error (MAE), taking CCSD(T)/CBS as the standard, is visualized in Figure 7.24. CAM-B3LYP outperforms the other 38 functionals in the specific case of the barbaralyl cation. In contrast, M06-2X, which has been widely used in carbocation calculations, gives a relatively large deviation from the reference value.

Additionally, we compared the energy of structure **B** relative to structure **A**, which are the two minimum energy structures of the barbaralyl cation. As shown in Figure 7.25, the reference level CCSD(T)/CBS indicates that structure B is 2.6 kcal/mol higher in energy than structure A. Among the 39 density functionals tested, only 6 functionals correctly predicted that structure B is more than 2 kcal/mol higher in energy than structure A.

| basis set | 6-31G(d) | | | | | | def2-SVP | | | | | |
|---|---|---|---|---|---|---|---|---|---|---|---|---|
| functional | ***A*** | ***B*** | ***TS2*** | ***TS3*** | ***TS4*** | *MAE* | ***A*** | ***B*** | ***TS2*** | ***TS3*** | ***TS4*** | *MAE* |
| *APFD* | 0.0 | -1.9 | 2.8 | 0.6 | 7.9 | 2.8 | 0.0 | -2.6 | 3.1 | 0.2 | 8.2 | 3.2 |
| *B1B95* | 0.0 | -2.7 | 3.4 | 0.0 | 9.0 | 3.6 | 0.0 | -3.5 | 3.8 | -0.4 | 9.3 | 4.1 |
| *B1LYP* | 0.0 | 3.0 | 0.9 | 4.0 | 3.6 | 1.0 | 0.0 | 2.3 | 1.3 | 3.6 | 3.9 | 1.1 |
| *B3LYP* | 0.0 | 1.8 | 0.9 | 3.1 | 4.1 | 1.4 | 0.0 | 1.1 | 1.2 | 2.7 | 4.4 | 1.5 |
| *B3PW91* | 0.0 | -1.9 | 2.4 | 0.5 | 7.5 | 2.8 | 0.0 | -2.6 | 2.8 | 0.1 | 7.8 | 3.1 |
| *B97-D3* | 0.0 | -0.3 | -0.6 | 2.0 | 3.6 | 2.7 | 0.0 | -0.9 | -0.2 | 1.6 | 3.9 | 2.8 |
| *BH&HLYP* | 0.0 | 6.2 | 2.5 | 7.0 | 3.7 | 2.0 | 0.0 | 5.4 | 2.8 | 6.6 | 4.0 | 1.6 |
| *BLYP* | 0.0 | 0.6 | -0.6 | 1.7 | 3.1 | 2.7 | 0.0 | -0.1 | -0.3 | 1.3 | 3.4 | 2.8 |
| *BMK* | 0.0 | 2.6 | 2.5 | 1.6 | 7.0 | 1.2 | 0.0 | 3.2 | 2.2 | 1.6 | 6.6 | 1.1 |
| *CAM-B3LYP* | 0.0 | 3.2 | 2.7 | 4.6 | 5.2 | 0.2 | 0.0 | 2.5 | 3.0 | 4.2 | 5.5 | 0.3 |
| *B3LYP-D3(BJ)* | 0.0 | 2.5 | 0.2 | 3.8 | 3.4 | 1.3 | 0.0 | 1.8 | 0.6 | 3.4 | 3.7 | 1.5 |
| *BLYP-D3(BJ)* | 0.0 | 1.4 | -1.4 | 2.6 | 2.2 | 2.6 | 0.0 | 0.8 | -1.1 | 2.2 | 2.6 | 2.7 |
| *CAM-B3LYP-D3(BJ)* | 0.0 | 3.6 | 2.4 | 5.0 | 4.8 | 0.5 | 0.0 | 2.8 | 2.7 | 4.6 | 5.1 | 0.2 |
| *PBE0-D3(BJ)* | 0.0 | -2.2 | 2.9 | 0.6 | 8.2 | 3.0 | 0.0 | -2.9 | 3.2 | 0.2 | 8.5 | 3.4 |
| *PBE-D3(BJ)* | 0.0 | -4.4 | 1.3 | -1.6 | 7.7 | 4.2 | 0.0 | -5.1 | 1.6 | -2.0 | 7.9 | 4.5 |
| *HSEH1PBE* | 0.0 | -2.3 | 3.0 | 0.4 | 8.2 | 3.1 | 0.0 | -3.0 | 3.3 | 0.0 | 8.5 | 3.5 |
| *LC-ωHPBE* | 0.0 | 0.1 | 6.5 | 3.1 | 10.2 | 3.2 | 0.0 | -0.5 | 6.9 | 2.8 | 10.4 | 3.6 |
| *M061* | 0.0 | -3.3 | 4.5 | 0.5 | 8.7 | 3.8 | 0.0 | -3.7 | 4.9 | 0.3 | 8.9 | 4.1 |
| *M06-2X* | 0.0 | -0.8 | 4.7 | 1.6 | 8.6 | 2.9 | 0.0 | -1.5 | 5.0 | 1.3 | 8.8 | 3.3 |
| *M06-L* | 0.0 | -6.2 | 4.4 | -1.9 | 9.6 | 5.4 | 0.0 | -6.5 | 4.6 | -2.0 | 9.7 | 5.5 |
| *M11* | 0.0 | -0.7 | 5.5 | 1.3 | 9.7 | 3.5 | 0.0 | -0.9 | 5.9 | 1.3 | 9.8 | 3.6 |
| *MN12-L* | 0.0 | -0.9 | 1.5 | 1.6 | 6.2 | 2.1 | 0.0 | -2.0 | 2.0 | 1.0 | 6.6 | 2.6 |
| *MN12-SX* | 0.0 | 0.0 | 2.3 | 2.0 | 6.5 | 1.7 | 0.0 | -1.1 | 2.8 | 1.3 | 7.0 | 2.2 |
| *MN15* | 0.0 | 0.4 | 3.0 | 2.5 | 7.7 | 1.7 | 0.0 | -0.3 | 3.3 | 2.2 | 8.0 | 2.2 |
| *N12-SX* | 0.0 | -3.3 | 3.4 | -0.5 | 8.9 | 3.8 | 0.0 | -4.1 | 3.7 | -0.9 | 9.2 | 4.3 |
| *O3LYP* | 0.0 | -3.2 | 2.4 | -0.5 | 7.6 | 3.4 | 0.0 | -4.1 | 2.8 | -0.9 | 7.9 | 3.7 |
| *PBE0* | 0.0 | -2.5 | 3.2 | 0.2 | 8.6 | 3.4 | 0.0 | -3.3 | 3.5 | -0.2 | 8.9 | 3.8 |
| *PBE* | 0.0 | -4.9 | 1.7 | -2.1 | 8.1 | 4.5 | 0.0 | -5.5 | 2.0 | -2.4 | 8.3 | 4.7 |
| *PBEh1PBE* | 0.0 | -2.3 | 3.1 | 0.4 | 8.3 | 3.1 | 0.0 | -3.0 | 3.5 | 0.0 | 8.6 | 3.6 |
| *PW6B95-D3* | 0.0 | -1.1 | 2.6 | 1.2 | 7.6 | 2.3 | 0.0 | -1.9 | 3.0 | 0.8 | 7.9 | 2.8 |
| *SOGGA11X* | 0.0 | 1.1 | 3.7 | 3.2 | 7.0 | 1.4 | 0.0 | 0.4 | 4.0 | 2.9 | 7.1 | 1.8 |
| *TPSS* | 0.0 | -3.5 | 1.7 | -1.0 | 7.5 | 3.7 | 0.0 | -4.2 | 2.0 | -1.4 | 7.8 | 4.0 |
| *TPSSh* | 0.0 | -2.7 | 2.3 | -0.3 | 7.8 | 3.3 | 0.0 | -3.4 | 2.6 | -0.6 | 8.0 | 3.5 |
| *X3LYP* | 0.0 | 1.9 | 1.0 | 3.2 | 4.2 | 1.3 | 0.0 | 1.2 | 1.3 | 2.8 | 4.5 | 1.4 |
| *mPW1PW91* | 0.0 | -1.8 | 2.9 | 0.7 | 8.0 | 2.8 | 0.0 | -2.5 | 3.2 | 0.3 | 8.2 | 3.2 |
| *revTPSS* | 0.0 | -4.5 | 2.1 | -1.8 | 8.8 | 4.4 | 0.0 | -5.2 | 2.5 | -2.2 | 9.0 | 4.6 |
| *τ-HCTH hyb* | 0.0 | -0.1 | 1.1 | 1.2 | 5.7 | 2.0 | 0.0 | -0.6 | 1.4 | 0.8 | 5.9 | 2.2 |
| *ωB97X45* | 0.0 | 2.0 | 4.9 | 4.2 | 7.2 | 1.3 | 0.0 | 1.4 | 5.3 | 4.0 | 7.4 | 1.6 |
| *ωB97X-D13* | 0.0 | 1.6 | 3.1 | 3.2 | 6.4 | 1.0 | 0.0 | 0.9 | 3.5 | 2.9 | 6.6 | 1.4 |

TABLE 7.12. Benchmarking result in kcal/mol.

The benchmarking results obtained using the def2-SVP basis set are close to those obtained using the 6-31G(d) basis set (Figure 7.26 and 7.27).

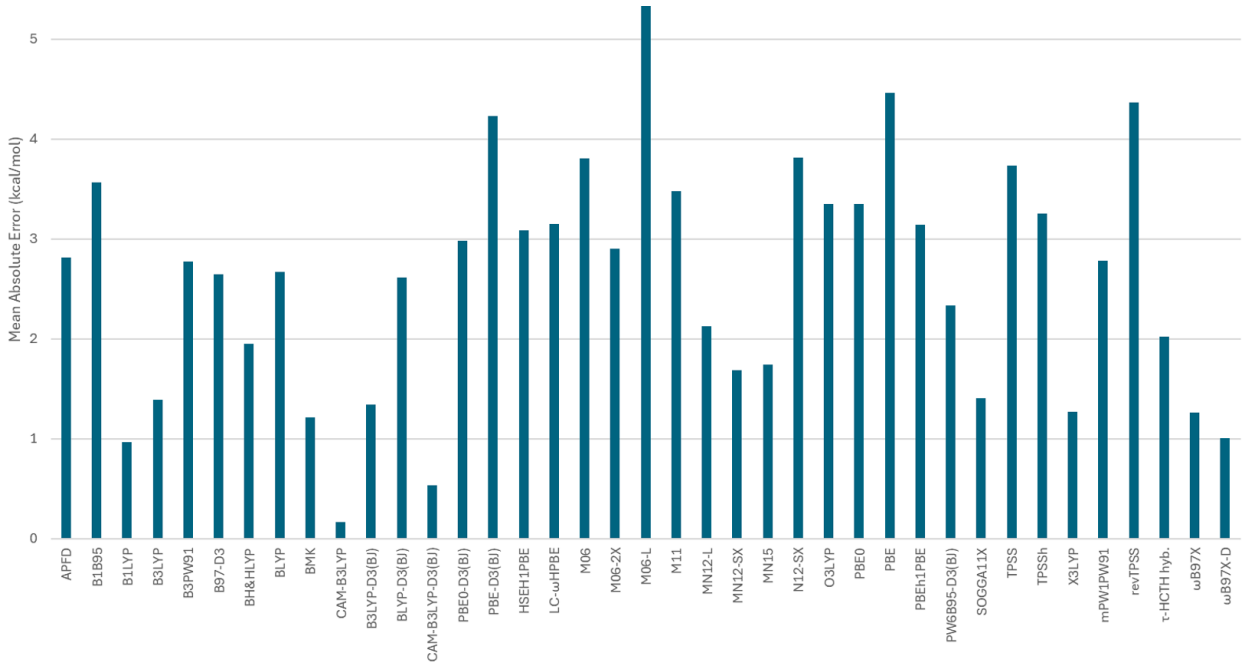


FIGURE 7.24. Mean absolute error (MAE) values for benchmarking functionals using the 6-31G(d) basis set, relative to the CCSD(T)/CBS reference energies in kcal/mol. The CAM-B3LYP functional exhibits the lowest MAE for the barbaralyl cation system.

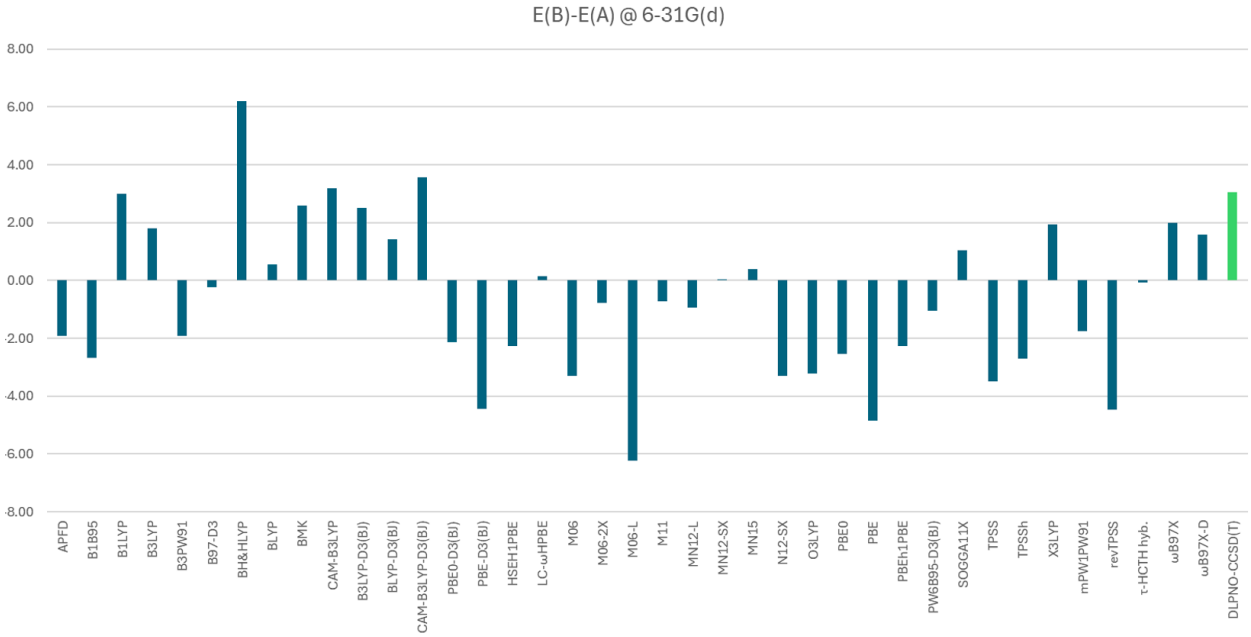


FIGURE 7.25. Relative energy of **B** (kcal/mol) for benchmarking functionals using the 6-31G(d) basis set, relative to the CCSD(T)/CBS reference energies in kcal/mol. The reference result is highlighted in green.

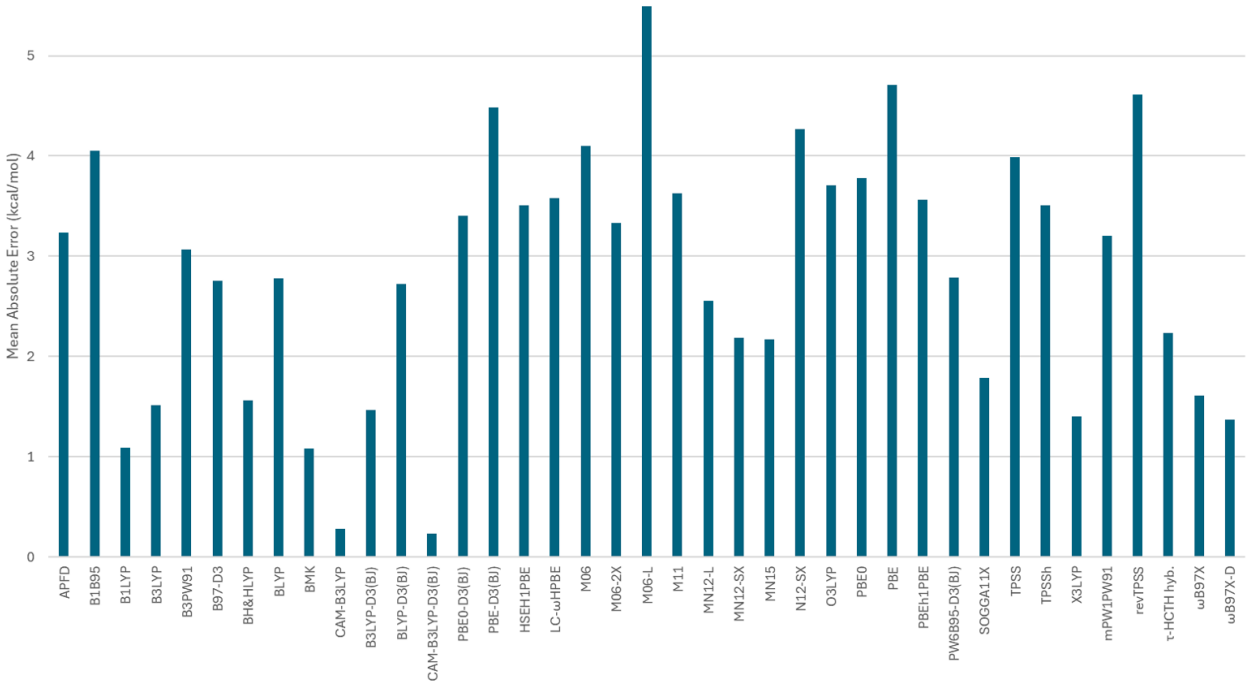


FIGURE 7.26. Mean absolute error (MAE) values for benchmarking functionals using the def2-SVP basis set, relative to the CCSD(T)/CBS reference energies in kcal/mol. The CAM-B3LYP-D3(BJ) and CAM-B3LYP exhibit outstanding accuracy for the barbaralyl.

7.4.1.2. *Divergent Results for Geometry Optimization on Barbaralyl Rearrangement.* However, as our preliminary study utilizing the Minnesota M06-2X exchange-correlation functional failed to optimize **TS2**, it is also important to benchmark the behavior of the functionals regarding whether they can optimize to correct structures and have correct local curvature about each stationary point. Here **Y** refers to optimization to a stationary point of correct nature, **N** means optimization did not converge or converged to another stationary point and **TS/MIN/2nd order** means they optimized to a TS or minimum while it should be a minimum or a TS or a 2nd order saddle point.

We discovered that a lot of functionals lead to the incorrect characterization of **TS2** as a minimum or failed to optimize to a structure like **TS2**. In particular, we realize that range-separated hybrids or (to a lesser degree) functionals with a moderate amount of exact exchange seem to have better success at predicting the correct nature of the stationary points as well as locating all key structures (Table 7.13).

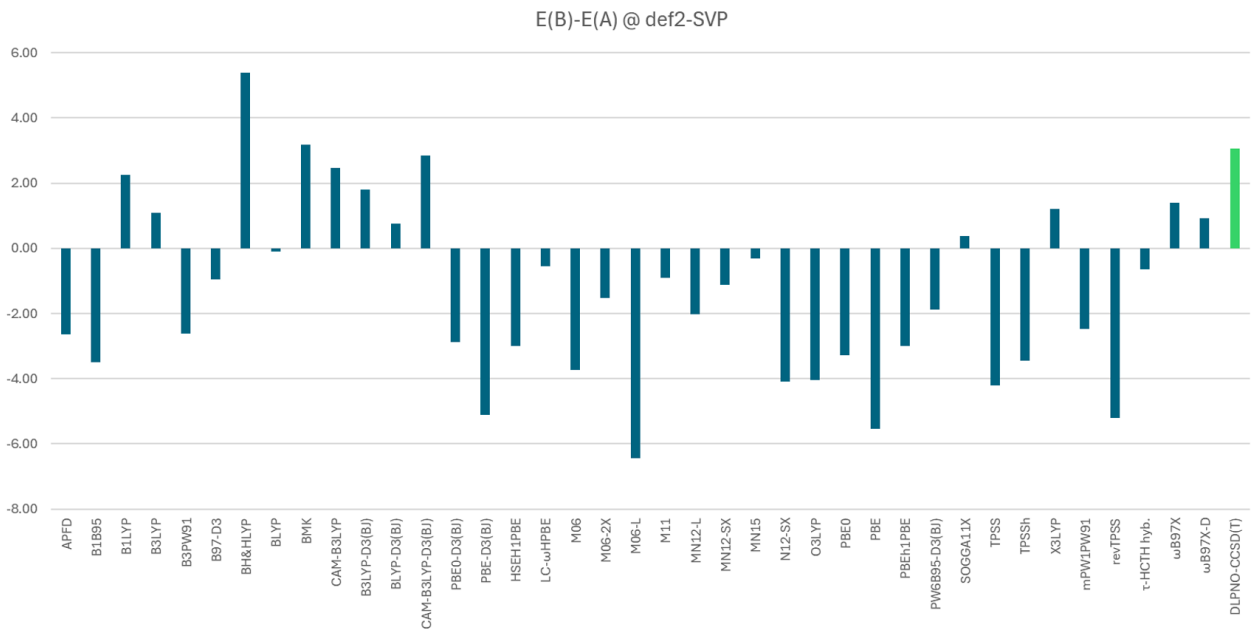


FIGURE 7.27. Relative energy of **B** (kcal/mol) for benchmarking functionals using the def2-SVP basis set, relative to the CCSD(T)/CBS reference energies in kcal/mol. The reference result is highlighted in green.

**7.4.2. Solvolysis of 1.** Scheme 5.1 in the Chapter 5 illustrates the solvolysis of compound **1** to generate the barbaralyl cation **2**. The transition state **TS1(A)** is highly asynchronous, initially dissociating to a structure resembling **TS2** (labeled as **INT**), followed by a very shallow C-C bond breaking transition state **TS1B** leading to the complex of **A**$\cdots H_2O$ on the IRC. However, single-point electronic energy correction reveals that **TS1(B)** has a lower electronic energy compared to **INT**, indicating that this solvolysis is indeed concerted but highly asynchronous on the *ab initio* PES corrected using the DLPNO-CCSD(T)/CBS method as shown in Figure 7.28.

**7.4.3. [4.3.0] Shapeshifting Rearrange Mechanism.**

7.4.3.1. *CAM-B3LYP.* As mentioned in the Chapter 5, when the barbaralyl cation undergoes ring opening to form the [4.3.0] non-classical carbocation, the potential energy surfaces calculated using the DLPNO-CCSD(T)/CBS and CAM-B3LYP/6-31G(d) level show some discrepancies regarding the existence of certain stationary points, particularly secondary carbocations, as true minima. At the CAM-B3LYP/6-31G(d) level of theory, a minimum (**H**)

| **basis set** | 6-31G(d) | | | | | def2-SVP | | | | |
|---|---|---|---|---|---|---|---|---|---|---|
| **functional** | ***A*** | ***B*** | ***TS2*** | ***TS3*** | ***TS4*** | ***A*** | ***B*** | ***TS2*** | ***TS3*** | ***TS4*** |
| *APFD* | Y | Y | Y | Y | Y | Y | Y | **N** | Y | Y |
| *B1B95* | Y | Y | **N** | Y | Y | Y | Y | **N** | Y | Y |
| *B1LYP* | Y | Y | MIN | Y | Y | Y | Y | MIN | Y | Y |
| *B3LYP* | Y | Y | MIN | Y | Y | Y | Y | MIN | Y | Y |
| *B3PW91* | Y | Y | Y | Y | Y | Y | Y | N | Y | Y |
| *B97-D3* | Y | Y | MIN | Y | Y | Y | Y | MIN | Y | Y |
| *BH&HLYP* | Y | Y | MIN | Y | Y | Y | Y | MIN | Y | Y |
| *BLYP* | Y | Y | MIN | Y | Y | Y | Y | MIN | Y | Y |
| *BMK* | TS | Y | MIN | Y | Y | TS | 2nd order | MIN | Y | Y |
| *CAM-B3LYP* | Y | Y | Y | Y | Y | Y | Y | Y | Y | Y |
| *B3LYP-D3(BJ)* | Y | Y | MIN | Y | Y | Y | Y | MIN | Y | Y |
| *BLYP-D3(BJ)* | Y | Y | MIN | Y | Y | Y | Y | MIN | Y | Y |
| *CAM-B3LYP-D3(BJ)* | Y | Y | Y | Y | Y | Y | Y | Y | Y | Y |
| *PBE0-D3(BJ)* | Y | Y | Y | Y | Y | Y | Y | **N** | Y | Y |
| *PBE-D3(BJ)* | Y | Y | **N** | Y | Y | Y | Y | **N** | Y | Y |
| *HSEH1PBE* | Y | Y | **N** | Y | Y | Y | Y | **N** | Y | Y |
| *LC-ωHPBE* | Y | Y | **N** | Y | Y | Y | Y | **N** | Y | Y |
| *M06* | Y | Y | Y | Y | Y | Y | Y | **Y** | Y | Y |
| *M06-2X* | Y | Y | **N** | Y | Y | Y | Y | **N** | Y | Y |
| *M06-L* | Y | Y | **N** | Y | Y | Y | Y | **N** | Y | Y |
| *M11* | Y | Y | **N** | Y | Y | Y | Y | **N** | Y | Y |
| *MN12-L* | Y | Y | MIN | Y | Y | Y | Y | Y | Y | Y |
| *MN12-SX* | Y | Y | Y | Y | Y | Y | Y | Y | Y | Y |
| *MN15* | Y | Y | Y | Y | Y | Y | Y | Y | Y | Y |
| *N12-SX* | Y | Y | **N** | Y | Y | Y | Y | **N** | Y | Y |
| *O3LYP* | Y | Y | **N** | Y | Y | Y | Y | **N** | Y | Y |
| *PBE0* | Y | Y | **N** | Y | Y | Y | Y | **N** | Y | Y |
| *PBE* | **N** | Y | **N** | **N** | Y | **N** | Y | **N** | **N** | Y |
| *PBEh1PBE* | Y | Y | **N** | Y | Y | Y | Y | **N** | Y | Y |
| *PW6B95-D3(BJ)* | Y | Y | Y | Y | Y | Y | Y | Y | Y | Y |
| *SOGGA11X* | Y | Y | Y | Y | Y | Y | Y | Y | Y | Y |
| *TPSS* | Y | Y | **N** | Y | Y | Y | Y | **N** | Y | Y |
| *TPSSh* | Y | Y | **N** | Y | Y | Y | Y | **N** | Y | Y |
| *X3LYP* | Y | Y | MIN | Y | Y | Y | Y | Y | Y | Y |
| *mPW1PW91* | Y | Y | **N** | Y | Y | Y | Y | **N** | Y | Y |
| *revTPSS* | **N** | Y | **N** | **N** | Y | **N** | Y | **N** | **N** | Y |
| *τ-HCTH hyb.* | Y | Y | Y | Y | Y | Y | Y | Y | Y | Y |
| *ωB97X* | Y | Y | Y | Y | Y | Y | Y | Y | Y | Y |
| *ωB97X-D* | Y | Y | Y | Y | Y | Y | Y | Y | Y | Y |

TABLE 7.13. Summary of the identification of stationary points using different density functionals with the def2-SVP basis set.

and a nearby transition structure (**TS10**) were optimized, suggesting a stepwise, two-step 1,2-H shift mechanism for the conversion of structure **D** to structure **E**. However, when single-point energy corrections were performed at the higher DLPNO-CCSD(T)/CBS level, the electronic energy of **H** was found to be higher than that of **TS10**, indicating that the

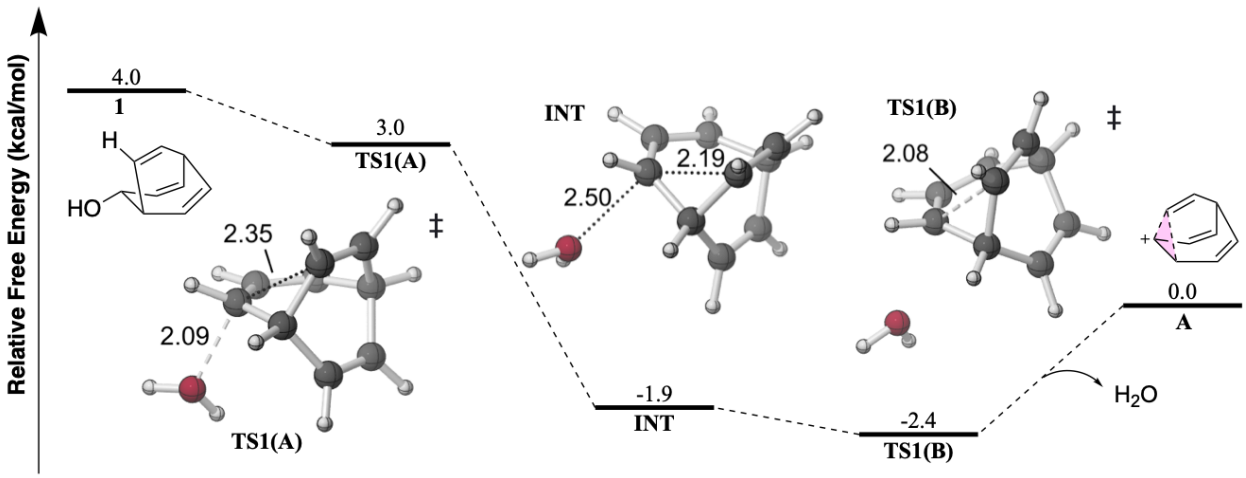


FIGURE 7.28. Energy profile of solvolysis of **1** at DLPNO-CCSD(T)/CBS//CAM-B3LYP/6-31G(d) level of theory at 138.15 K with 3D structures visualized by *CYLview1.0*.

stepwise mechanism is actually asynchronously concerted (Figure 7.29). Instead, the higher-level calculations suggest that the transformation from **D** to **E** proceeds *via* a 1,3-H shift mechanism, with a relatively flat potential energy surface following the first proton shift.

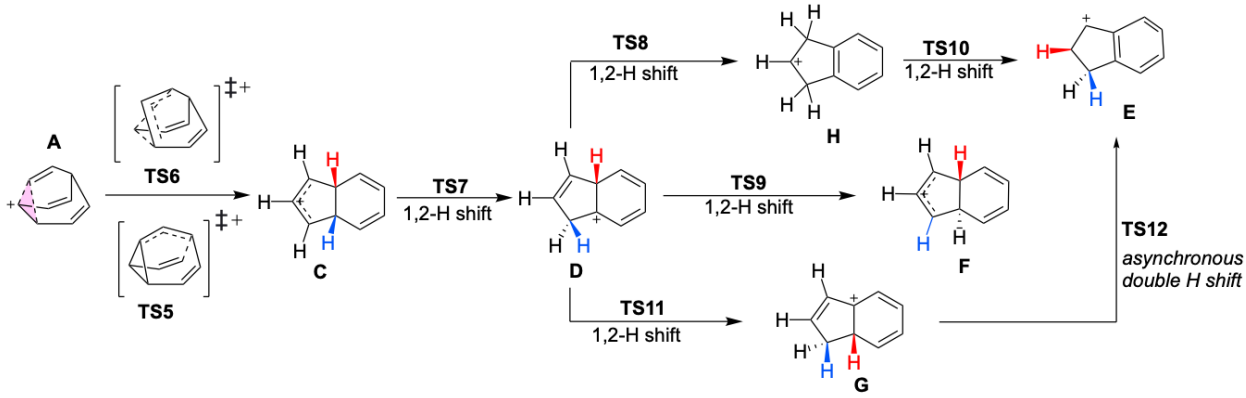


FIGURE 7.29. The mechanism predicted at CAM-B3LYP/6-31G(d) level of theory. **H** has a lower energy than **TS8** and **TS10** under this level, confirmed by IRC. While under a higher DLPNO-CCSD(T)/CBS level, **H** is higher than **TS10**.

7.4.3.2. *M06-2X.* At this ring-opening stage, the M06-2X gives a better description of the energy profile, which describes the process of **D** to **E** conversion as a 1,3 shift. As the structure **H** does not correspond to a minimum anymore, **D** is capable of isomerizing to **E**

*via* **TS8** directly. Moreover, under M06-2X functional, the structure of **H** turns to be a distinct double hydride shift transition state **TS13** where the two sequential shifts occur in a highly asynchronous manner to generate **E'**, as shown in Figure 7.30 and 7.31.

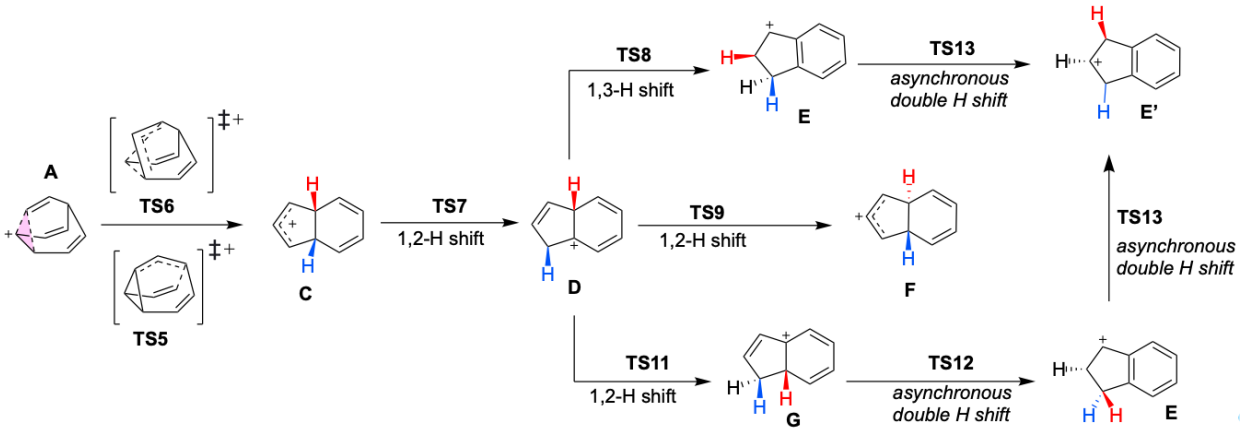


FIGURE 7.30. The mechanism predicted at M06-2X/6-31G(d) level of theory. The structure of **H** in Figure 7.29 turns out to be the transition structure **TS13** that connects **E** and **E'**.

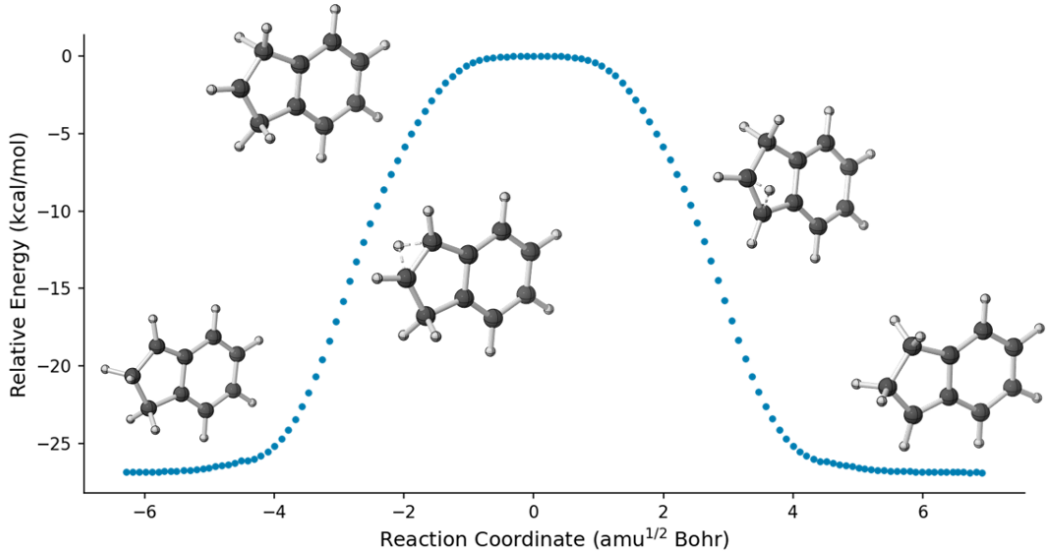


FIGURE 7.31. The intrinsic reaction coordinate of **TS13**, a double hydride shift that interconverts **E** and **E'**.

**7.4.4. PES.** Besides the CAM-B3LYP functional, we also constructed the potential energy surface in terms of C2-C5 and C3-C6 distances and its 2D projection using the

| | M06-2X/6-31G(d) | ωB97X-D/6-31G(d) | CAM-B3LYP/6-31G(d) |
|---|---|---|---|
| **B relative to A (kcal/mol)** | -0.7 | 1.6 | 3.2 |
| **TS2 located?** | No | Yes | Yes |

TABLE 7.14. Comparison of energetics for the barbaralyl cation and related structures calculated using different levels of theory.

ωB97X-D and M06-2X functionals. The difference between these three levels of theory is mainly the relative energy of **B** with respect to **A** as summarized in Table 7.14. Since the M06-2X functional predicts lower energy for **B**, the downhill pathway from **TS4** directly connects it to **B** instead of **TS2** (**TS2** is no longer a saddle point on the surface). The relative potential energy of B and the PESs are depicted below in Figure 5.4 and 7.32.

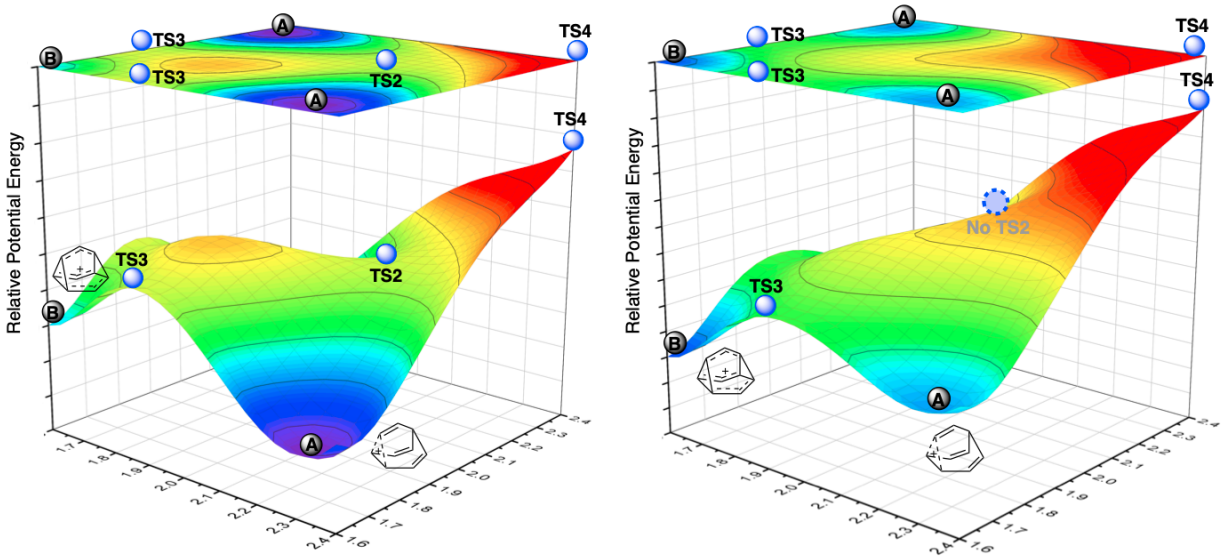


FIGURE 7.32. PES at ωB97X-D/6-31G(d) (left) and M06-2X/6-31G(d) (right) level of theory with critical structures labeled.

**7.4.5. AIMD details.** AIMD simulations were performed using the Progdyn package to investigate both downhill and uphill reaction pathways. The overall process is similar to the setup mentioned in Appendix 7.1.5 and 7.2.3.

7.4.5.1. *Uphill MD simulation.* The uphill MD simulation involves defining the potential at the initial sampling, which corresponds to the direction of breaking the C2-C5 bond, facilitating the conversion from structure **B** to **A1**. The trajectories are terminated at 1 ps

(1000 steps). Throughout the entire trajectory, the encountered minima are stored based on the following criteria in Table 7.15.

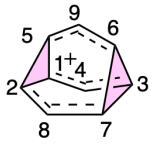


**B**

| Critical Bonds | C2-C5, C3-C6, C1-C2, C6-C7, C4-C5, C3-C3 |
|---|---|
| B | all bonds <1.60 |
| A1 | C2-C5 >2.40 |
| A2 | C3-C6 >2.40 |
| A3 | C1-C2 >2.40 |
| A4 | C6-C7 >2.40 |
| A5 | C4-C5 >2.40 |
| A6 | C3-C7 >2.40 |

other bonds <1.70

TABLE 7.15. bond length definition (Angstrom) for structure capture during uphill MD simulation

To evaluate the uphill MD simulation, we applied energy inputs of 3 kcal/mol and 10 kcal/mol to test the effect on the C2-C5 bond stretching. The results indicate that higher energy input increases the formation ratio of **A1**. This is because the increased momentum drives the molecule towards the formation that aligns with the input energy.

A total of 188 trajectories were collected for a deposit energy of 10 kcal/mol, capturing 468 minima interconversions. The scatter plot below illustrates the results for each trajectory, with the first structure encountered represented by red, followed by orange, yellow, green, blue, and purple, adhering to the order of the rainbow colors. The trajectories are arranged from left to right, with their IDs ranging from 1 to 188. This visualization provides a clear overview of the sequence of structures encountered along each trajectory.

The result agrees with the tree-shaped and pie plot in the manuscript, showing that most of the trajectories lead to **A1** as the very first product. Though some of them bounce back to **B**, even with extra energy, the following product is more likely to be **A1**. However, as the energy decreases to 3 kcal/mol (the potential barrier is 1 kcal/mol), the preference to form **A1** diminishes, as shown in the main text and figures below. A total of 174 trajectories were

collected for a deposit energy of 3 kcal/mol, capturing 441 minima interconversions. The same scatter plot is shown in Figure 7.33.

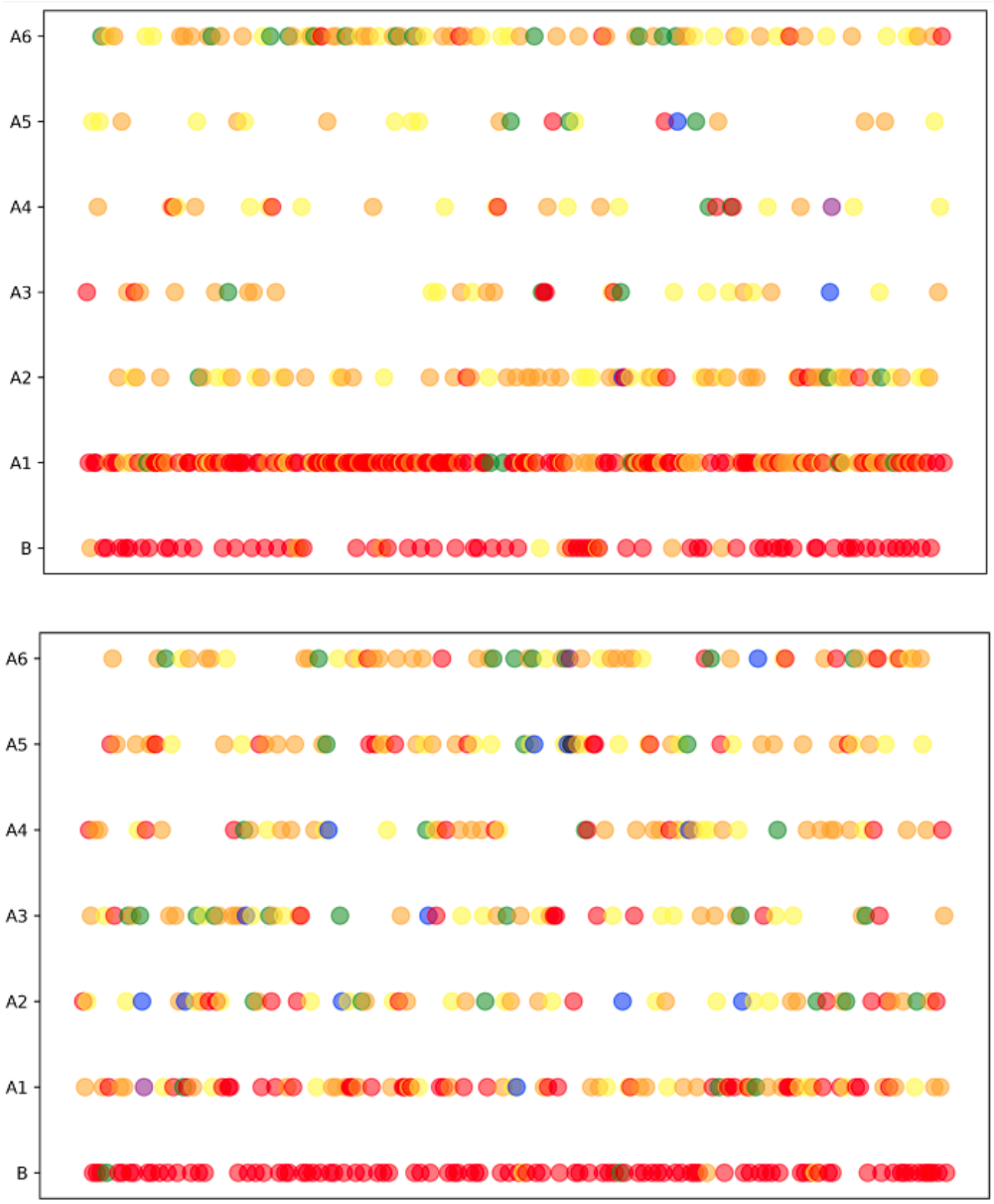


FIGURE 7.33. Scatter plot visualizing the minima encountered during each trajectory of the uphill AIMD simulation with a deposit energy of 10 kcal/mol (top) and 3 kcal/mol (bottom).

7.4.5.2. *Downhill MD simulation.* Each trajectory in the downhill AIMD simulations was set to have a maximum duration of 500 femtoseconds. However, if the geometry of the

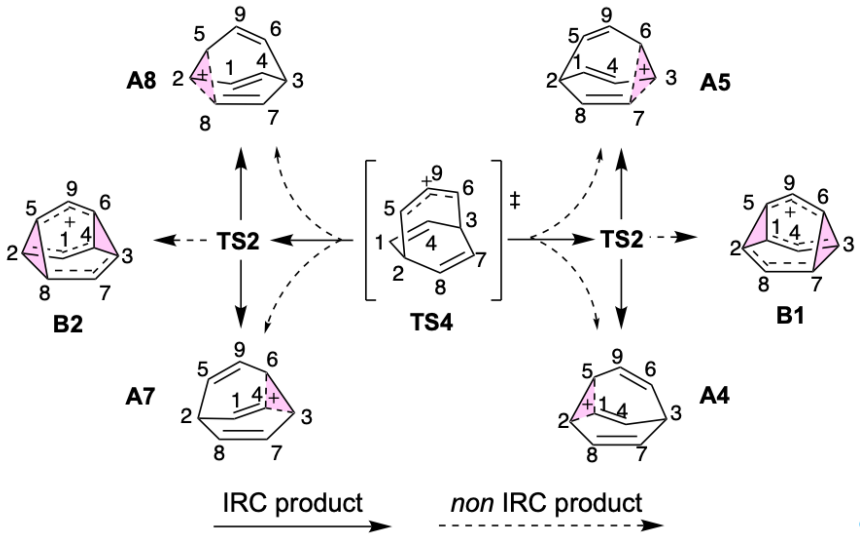


SCHEME 7.2. Illustration of the six minima connected by **TS4** with 2D structures by ChemDraw.

| Critical Bonds | C1-C5, C5-C8, C6-C7, C4-C6 | |
|---|---|---|
| B1 | C1-C5, C6-C7<1.60 | |
| B2 | C5-C8, C4-C6 <1.60 | |
| A5 | C1-C5 >2.40 | C6-C7 <1.65 |
| A4 | C6-C7 >2.40 | C1-C5 <1.65 |
| A7 | C5-C8 >2.40 | C4-C6 <1.65 |
| A8 | C4-C6 >2.40 | C5-C8 <1.65 |

TABLE 7.16. Stopping criteria of downhill AIMD simulation.

system meets the predefined stopping criteria, the trajectory is terminated immediately. The stopping criteria are summarized in Table 7.16

In total, 638 classical AIMD trajectories and 536 *quasi*-classical AIMD trajectories were generated. The number of trajectories in each group is labeled in Chapter 5 Figure 5.9.

**7.4.6. Metadynamics.** The well-tempered metadynamics simulation was carried out using *ORCA 5.0.4* using CAM-B3LYP/6-31G(d) level of theory at 138.15K with the canonical sampling velocity rescaling thermostat and propagated for 17600 fs where it appears to be reasonably converged. The slight deviation from the ideal symmetry of the free energy profile in Figure 7.34 is due to the stochastic nature of the MD simulation and the path through the phase space.

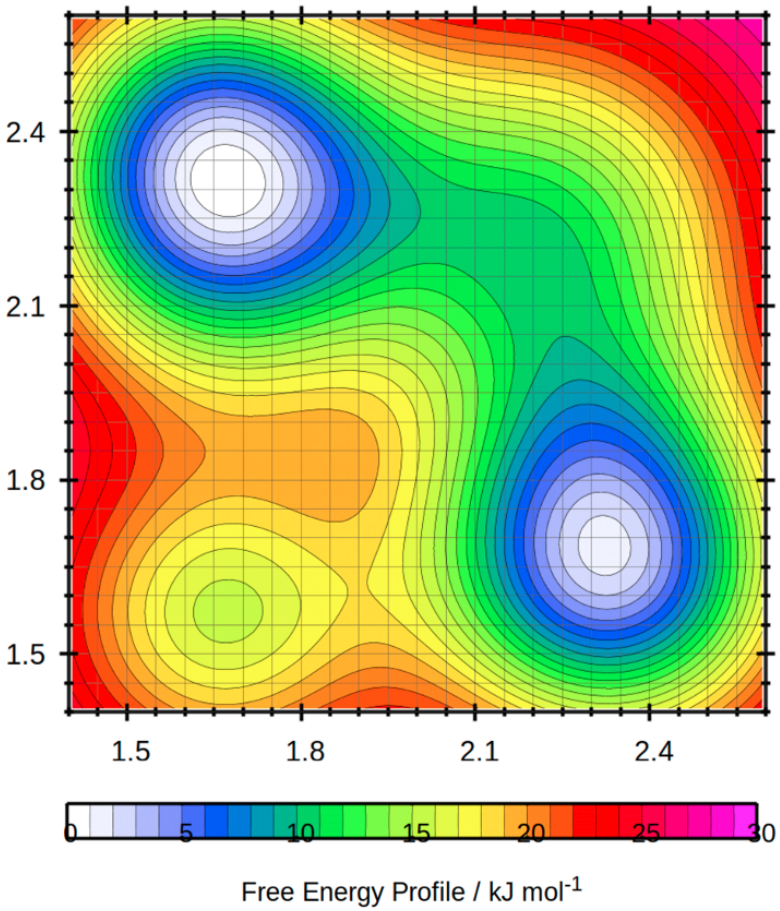


FIGURE 7.34. Free energy surface of the barbaralyl cation system constructed using metadynamics simulations. The FES is plotted based on the same geometric parameters as PES.

**7.4.7. Trifurcation under M06-2X/6-31G(d).** The unique potential energy surface topology obtained using the M06-2X functional reveals a natural trifurcation surface, which not only leads to the formation of three distinct products but also features three symmetry-related exit channels at one side. Due to the symmetry around **TS4**, the surface naturally connects six minima without encountering any additional transition states along the pathway.

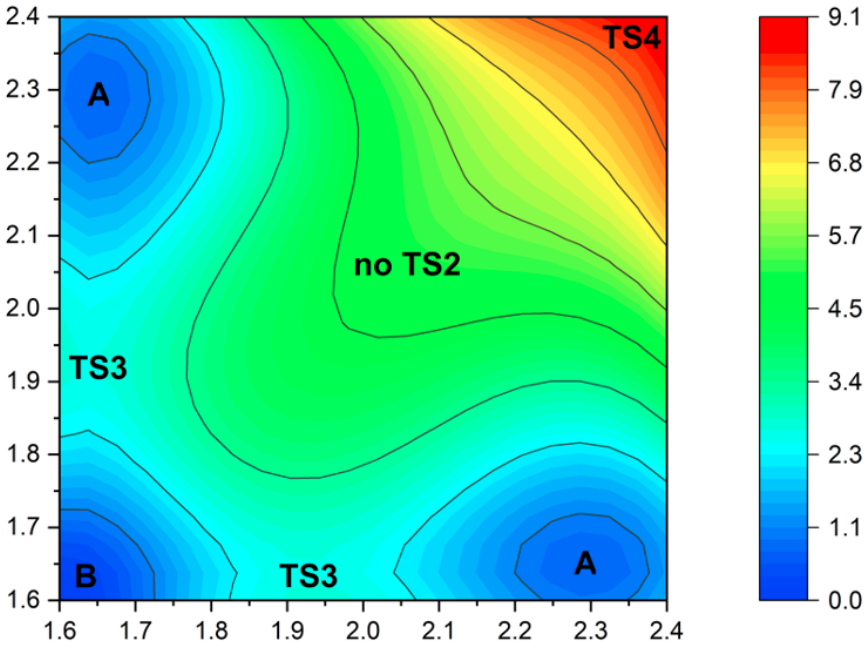


FIGURE 7.35. 2D potential energy surface calculated at the M06-2X/6-31G(d) level of theory. The steepest descent path (minimum energy pathway) from **TS4** leads directly to product **B** without encountering any stationary points. Simultaneously, the two equivalent **A** structures can be accessed *via* symmetric downhill path from **TS4**.

The downhill AIMD simulation reveals its complexity. In our *quasi*-classical downhill MD simulations initiated from **TS4**, we also uncovered pathways that directly connect various forms of **A** and **B**, as shown in Figure 7.36 and Figure 7.37. Similarly to what we reported in Chapter 5, **TS4** not only connects state **B1** to its mirrored **B2**, but also provides a direct route to **A4**, **A5**, **A7** and **A8** states on either side of the **B** states. Projections onto the CV1, CV2, and CV3 planes (same CV as Figure 5.8), clearly show six distinct minima corresponding to **B1**, **B2**, and the associated **A4**, **A5**, **A7** and **A8** being accessed. The emergence of **A**s is 'direct' from **TS4**, as the trajectories circumvent the **B1** and **B2** minima instead of traversing them. Only 133 trajectories are collected while out of the 17 distinct trajectory types identified, 43% depict a transition from one side of **B** to an opposing side of **A** (purple bins). Meanwhile, 11% connect two minima on the same side (pink bins), and only 32% bridge **B1** to **B2** (blue bins), aligning with results obtained from IRC analysis.

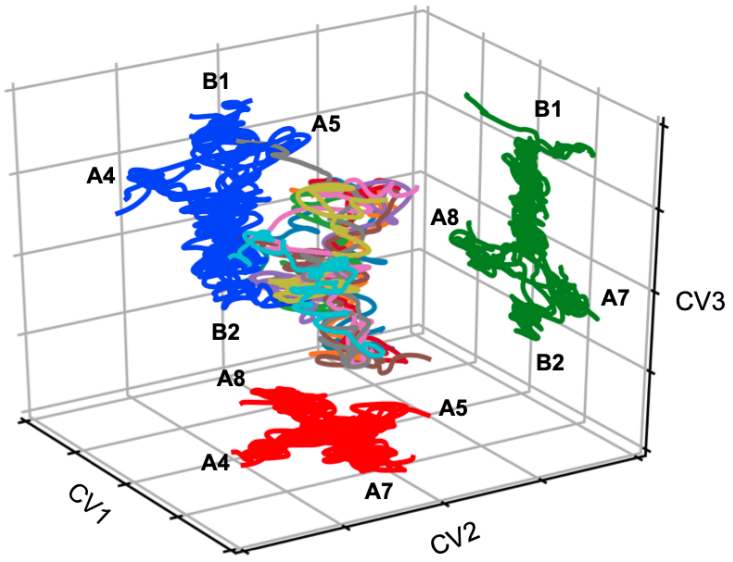


FIGURE 7.36. The trajectories are visualized with respect to the coordinates same as the setting in Figure 5.8. Projections on each plane are distinctly colored in red, blue, and green.

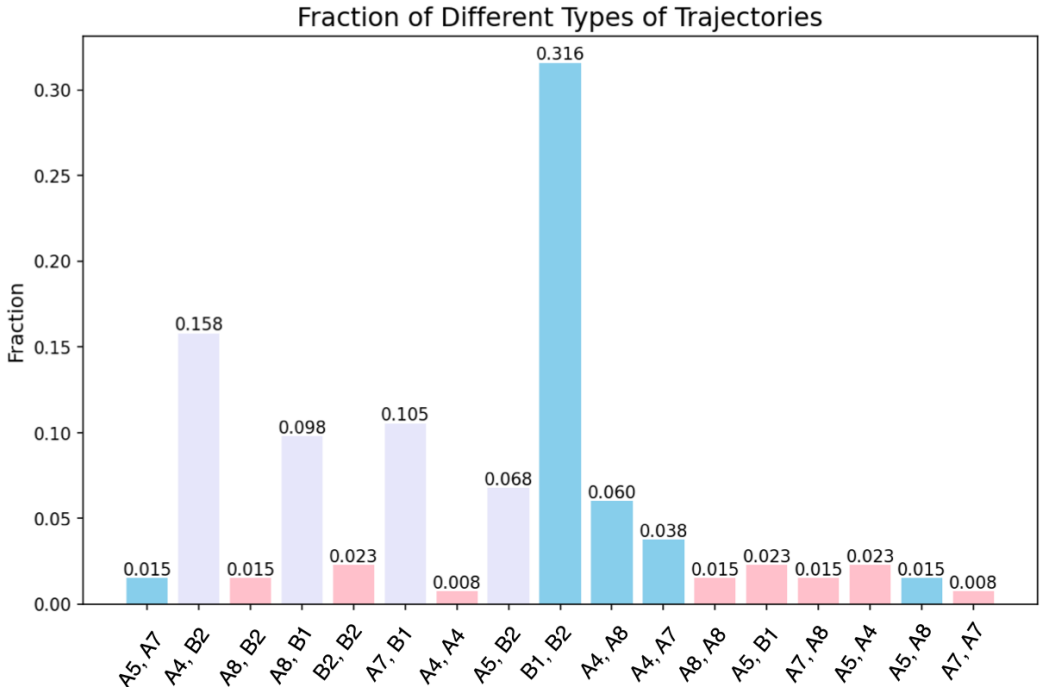


FIGURE 7.37. The proportion of trajectories collected from downhill AIMD simulations. Trajectories that connect minima from the left and right sides are depicted in blue and purple: those connecting **B** to **A** are in purple, while the rest are in blue. Trajectories in red indicate 'recrossing' events, where connections occur between two minima on the same side.

**7.4.8. Tunneling effect.** The tunneling effect was investigated using the Polyrate/ Gaussrate packages at the CAM-B3LYP/6-31G(d) level of theory under different temperatures. Both the small-curvature tunneling (SCT) and zero-curvature tunneling (ZCT) approximations were employed, and the contribution of tunneling to the overall reaction rate was determined based on the kappa factor. The kappa factor, also known as the "tunneling correction" or "transmission coefficient" in transition state theory, is calculated as the ratio of the Boltzmann average of the quantum transmission probability to the Boltzmann average of the classical transmission probability, with the threshold energy set at the peak of the adiabatic ground-state energy. The fraction of the reaction rate attributable to tunneling is given by Equation 7.5.

$$\frac{\text{quantum transmission probability}}{\text{quantum transimission probility + classical transimission probility}} = \frac{\kappa - 1}{\kappa} \tag{7.5}$$

The overall result under different temperatures is summarized in Table 7.17.

| | T(K) | ZCT | SCT | fraction of rate due to tunneling (ZCT) | (SCT) |
|---|---|---|---|---|---|
| **TS2** | 123.15 | 1.1157 | 1.6055 | 10.37% | 37.71% |
| | 138.15 | 1.0810 | 1.3385 | 7.49% | 25.29% |
| | 158.15 | 1.0564 | 1.1963 | 5.34% | 16.41% |
| | 188.15 | 1.0372 | 1.1121 | 3.59% | 10.08% |
| | 238.15 | 1.0221 | 1.0598 | 2.16% | 5.64% |
| | 273.15 | 1.0165 | 1.0431 | 1.62% | 4.13% |
| | 298.15 | 1.0137 | 1.0353 | 1.35% | 3.41% |
| **TS3** | 123.15 | 2.0486 | 2.2137 | 51.19% | 54.83% |
| | 138.15 | 1.7608 | 1.8718 | 43.21% | 46.58% |
| | 158.15 | 1.5352 | 1.6078 | 34.86% | 37.80% |
| | 188.15 | 1.3508 | 1.3951 | 25.97% | 28.32% |
| | 238.15 | 1.2049 | 1.2291 | 17.01% | 18.64% |
| | 273.15 | 1.1518 | 1.1692 | 13.18% | 14.47% |
| | 298.15 | 1.1257 | 1.1400 | 11.17% | 12.28% |
| **TS4** | 123.15 | 1.4126 | 1.6300 | 29.21% | 38.65% |
| | 138.15 | 1.2840 | 1.3892 | 22.12% | 28.02% |
| | 158.15 | 1.1978 | 1.2539 | 16.51% | 20.25% |
| | 188.15 | 1.1310 | 1.1617 | 11.58% | 13.92% |
| | 238.15 | 1.0780 | 1.0941 | 7.24% | 8.60% |
| | 273.15 | 1.0583 | 1.0699 | 5.51% | 6.53% |
| | 298.15 | 1.0485 | 1.0580 | 4.63% | 5.48% |

TABLE 7.17. The overall tunneling effects computed under CAM-B3LYP/6-31G(d) level of theory. In the manuscript, only results at 138.15, 188.15 and 273.15 K are displayed.

## 7.5. Supporting Information of Chapter 6

**7.5.1. Benchmark.** To examine the robustness of the level of theory we used in the study, we benchmarked Regan's system using five functionals. The structures were reoptimized using B3LYP-D3(BJ), mPW1PW91, PBE0-D3(BJ), and $\omega$B97X-D functionals. The relative free energies of TS and product are depicted in figure 7.38; the result shows a consistent trend among different computational levels.

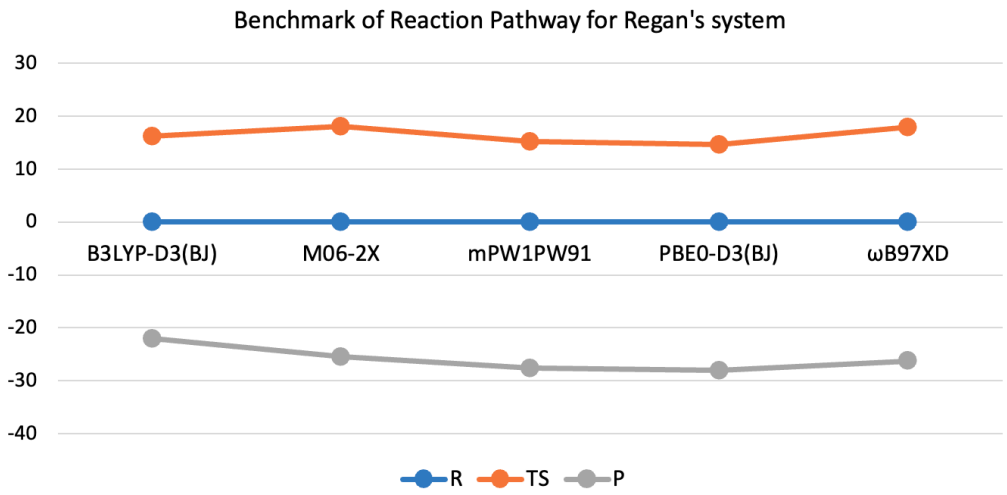


FIGURE 7.38. Summary of benchmarked results for Regan's system: TS (transition state, orange line) and product (grey line) energies, presented in kcal/mol, are relative to the reactant (blue line).

**7.5.2. Mechanistic Studies.** The overall energy profile for the key step of **1a** to **2a** is depicted in Figure 7.39, corresponding to the IRC figure in the manuscript.

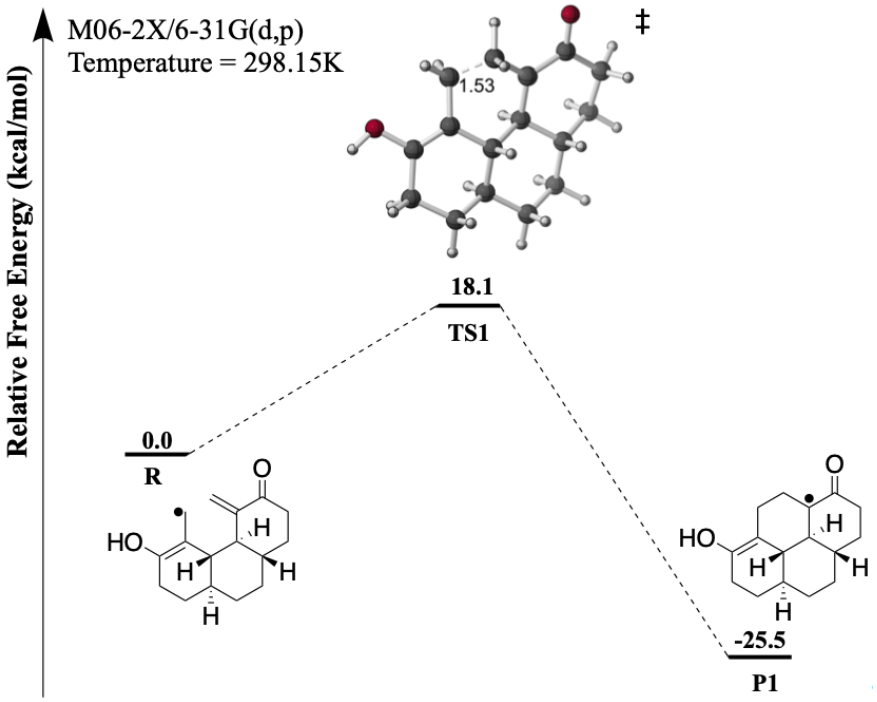


FIGURE 7.39. Free energy profile of key step from **1** to **2**.

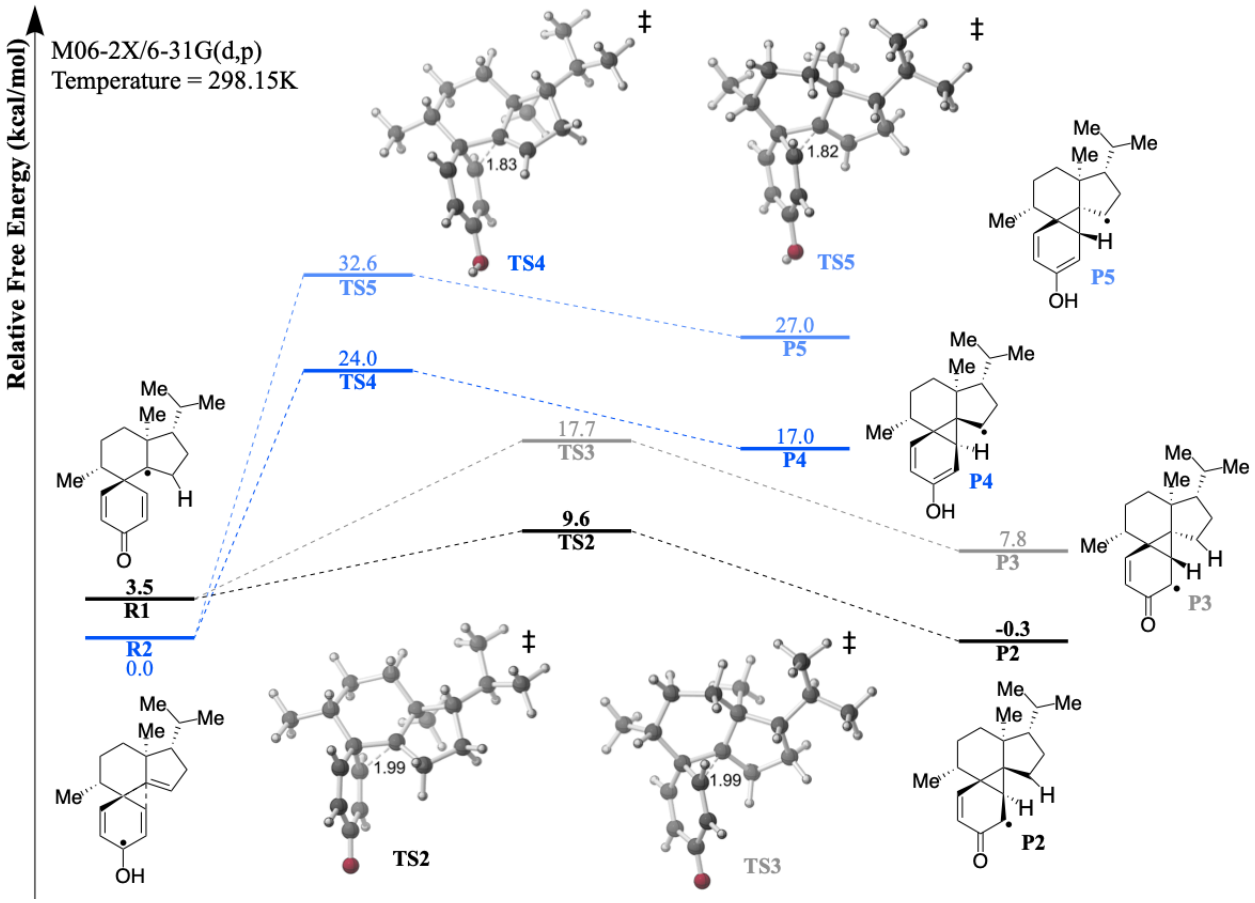


FIGURE 7.40. Free energy profile of key step from **3** to **4**

To elucidate the mechanism underlying the generation of compound **4** from **3**, our investigation extended beyond the examination of products **P2** and **P4**, which align with the stereochemistry of **4** as delineated in experimental findings. This included the consideration of the diastereomers **P3** and **P5**. The computational study revealed high enantioselectivity in the process.

The formation of the highly energetic transition states TS3 and TS5 is traced back to the initial twist-boat conformation of cyclohexane. This conformation transforms an intermediary half-chair transition state, facilitating the formation of the carbon-carbon bond. This progression results in the less stable structures of P3 and P5, attributed to the substantial strain imposed by the half-chair cyclic conformation. Conversely, the synthesis of **P2** and **P4**

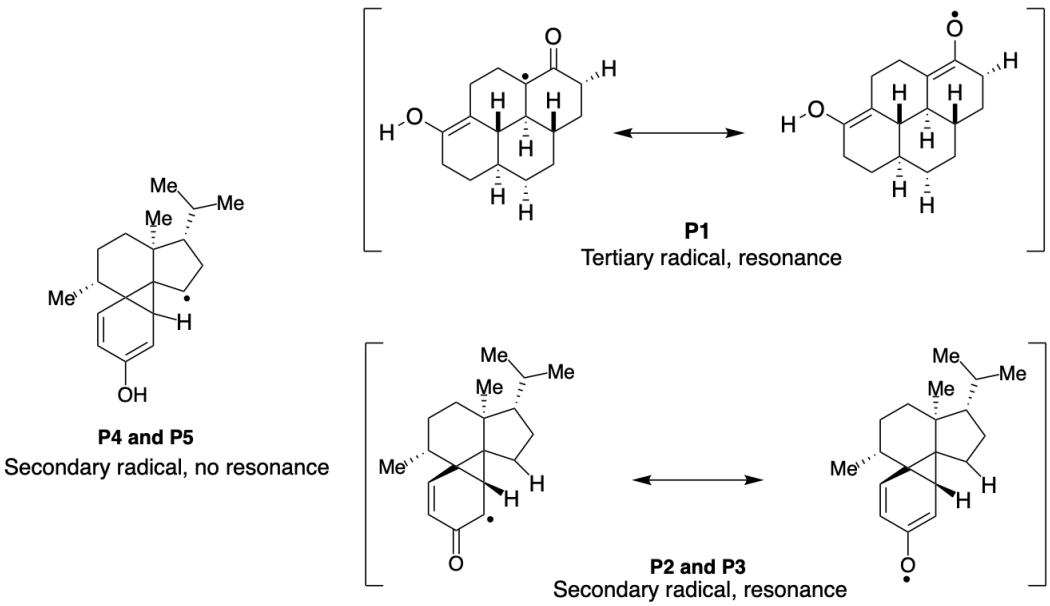


SCHEME 7.3. The resonance structure of **P1**, **P2**, **P3** and **P4**, **P5**.

is characterized by the retention of a twisted chair conformation throughout the transition, contributing to their stability.

The results also raise another question: why do the pathways involving TS4 and TS5 exhibit endothermic characteristics (with a Gibbs free energy change, $\Delta G$, exceeding 17 kcal/mol), whereas the pathway through TS1 is exothermic ($\Delta G$ less than -20 kcal/mol)? The answer lies in the structural nuances of the products. Specifically, the tertiary radical nature of P4 and P5 introduces a level of stability through a resonance structure centered around an oxygen radical. While the resonance effect similarly benefits the secondary radical structures of **P2** and **P3**, **P4** and **P5** lack comparative advantages, highlighted in Scheme 7.3.

**7.5.3. Kinetic analysis.** The below section summarizes the results of kinetic analysis for the three key TSs with significant tunneling effects reported in the manuscript. CVT refers to canonical variational transition state theory, under which the forward rate constant is obtained by minimizing the generalized transition state theory rate constant. Therefore, the rate constant obtained by CVT is smaller or equal to the results given by TST.

| FORWARD RATES (SEC**-1) | | | | | | |
|---|---|---|---|---|---|---|
| **T(K)** | **TST** | **TST/ZCT** | **TST/SCT** | **CVT** | **CVT/ZCT** | **CVT/SCT** |
| **193.15** | 4.63E-08 | 9.35E-08 | 4.61E-08 | 4.55E-08 | 4.55E-08 | 4.63E-08 |
| **213.15** | 3.21E-06 | 5.89E-06 | 3.19E-06 | 3.15E-06 | 3.15E-06 | 3.21E-06 |
| **233.15** | 1.07E-04 | 1.83E-04 | 1.07E-04 | 1.05E-04 | 1.05E-04 | 1.07E-04 |
| **253.15** | 2.07E-03 | 3.29E-03 | 2.06E-03 | 2.02E-03 | 2.02E-03 | 2.07E-03 |
| **273.15** | 2.58E-02 | 3.89E-02 | 2.57E-02 | 2.52E-02 | 2.52E-02 | 2.58E-02 |
| **298.15** | **3.75E-01** | **5.35E-01** | **3.73E-01** | **3.66E-01** | **3.66E-01** | **3.75E-01** |
| **313.15** | 1.52E+00 | 2.11E+00 | 1.52E+00 | 1.48E+00 | 1.48E+00 | 1.52E+00 |
| **333.15** | 8.09E+00 | 1.09E+01 | 8.07E+00 | 7.89E+00 | 7.89E+00 | 8.09E+00 |

TABLE 7.18. Forward reaction rates for TS1, including outcomes from generalized transition state theory (TST) and variational transition state theory (VTST). The analysis also encompasses tunneling effects, with findings provided by the zero-curvature tunneling (ZCT) and small-curvature tunneling (SCT) methods.

| FORWARD RATES (SEC**-1) | | | | | | |
|---|---|---|---|---|---|---|
| **T(K)** | **TST** | **TST/ZCT** | **TST/SCT** | **CVT** | **CVT/ZCT** | **CVT/SCT** |
| **193.15** | 5.8E+06 | 8.9E+06 | 1.0E+07 | 5.7E+06 | 8.9E+06 | 1.0E+07 |
| **213.15** | 1.9E+07 | 2.7E+07 | 2.9E+07 | 1.9E+07 | 2.7E+07 | 2.9E+07 |
| **233.15** | 5.0E+07 | 6.6E+07 | 7.2E+07 | 5.0E+07 | 6.6E+07 | 7.2E+07 |
| **253.15** | 1.1E+08 | 1.5E+08 | 1.5E+08 | 1.1E+08 | 1.4E+08 | 1.5E+08 |
| **273.15** | 2.3E+08 | 2.8E+08 | 3.0E+08 | 2.3E+08 | 2.8E+08 | 3.0E+08 |
| **298.15** | **4.9E+08** | **5.8E+08** | **6.1E+08** | **4.9E+08** | **5.8E+08** | **6.0E+08** |
| **313.15** | 7.3E+08 | 8.5E+08 | 8.8E+08 | 7.3E+08 | 8.4E+08 | 8.8E+08 |
| **333.15** | 1.2E+09 | 1.3E+09 | 1.4E+09 | 1.2E+09 | 1.3E+09 | 1.4E+09 |

TABLE 7.19. Forward reaction rates for TS2, including outcomes from generalized transition state theory (TST) and variational transition state theory (VTST). The analysis also encompasses tunneling effects, with findings provided by the zero-curvature tunneling (ZCT) and small-curvature tunneling (SCT) methods.

| FORWARD RATES (SEC**-1) | | | | | | |
|---|---|---|---|---|---|---|
| **T(K)** | **TST** | **TST/ZCT** | **TST/SCT** | **CVT** | **CVT/ZCT** | **CVT/SCT** |
| **193.15** | 4.6E-12 | 2.69E-11 | 4.13E-11 | 4.5E-12 | 2.69E-11 | 4.12E-11 |
| **213.15** | 8.1E-10 | 3.21E-09 | 4.29E-09 | 8.1E-10 | 3.20E-09 | 4.28E-09 |
| **233.15** | 6.0E-08 | 1.80E-07 | 2.23E-07 | 5.9E-08 | 1.79E-07 | 2.22E-07 |
| **253.15** | 2.3E-06 | 5.57E-06 | 6.59E-06 | 2.2E-06 | 5.55E-06 | 6.56E-06 |
| **273.15** | 5.0E-05 | 1.07E-04 | 1.22E-04 | 5.0E-05 | 1.06E-04 | 1.22E-04 |
| **298.15** | 1.4E-03 | 2.52E-03 | 2.81E-03 | 1.3E-03 | 2.50E-03 | 2.79E-03 |
| **313.15** | 7.6E-03 | 1.33E-02 | 1.46E-02 | 7.5E-03 | 1.32E-02 | 1.45E-02 |
| **333.15** | 6.0E-02 | 9.75E-02 | 1.06E-01 | 5.9E-02 | 9.67E-02 | 1.05E-01 |

TABLE 7.20. Forward reaction rates for TS4, including outcomes from generalized transition state theory (TST) and variational transition state theory (VTST). The analysis also encompasses tunneling effects, with findings provided by the zero-curvature tunneling (ZCT) and small-curvature tunneling (SCT) methods.

# Bibliography


[1] P. A. M. Dirac, *The principles of quantum mechanics*. No. 27, Oxford university press, 1981.

[2] E. Schrödinger, "An undulatory theory of the mechanics of atoms and molecules," *Physical review*, vol. 28, no. 6, p. 1049, 1926.

[3] A. Turbiner, "Perturbation theory and variation principle in quantum mechanics," *Zh. Eksp. Teor. Fiz*, vol. 79, p. 1719, 1980.

[4] J. Čížek, "On the correlation problem in atomic and molecular systems. calculation of wavefunction components in Ursell-type expansion using quantum-field theoretical methods," *The Journal of Chemical Physics*, vol. 45, no. 11, pp. 4256–4266, 1966.

[5] R. S. Mulliken, "Electronic population analysis on LCAO–MO molecular wave functions. i," *The Journal of chemical physics*, vol. 23, no. 10, pp. 1833–1840, 1955.

[6] Q. B. Zum Bezolproblem and Q. B. zum Problem, "Quantentheoretische beiträge zum benzolproblem," *Zeitschrift Fuer Physikalische Chemie*, vol. 70, pp. 204–286, 1931.

[7] T. R. Nelson, A. J. White, J. A. Bjorgaard, A. E. Sifain, Y. Zhang, B. Nebgen, S. Fernandez-Alberti, D. Mozyrsky, A. E. Roitberg, and S. Tretiak, "Non-adiabatic excited-state molecular dynamics: Theory and applications for modeling photophysics in extended molecular materials," *Chemical reviews*, vol. 120, no. 4, pp. 2215–2287, 2020.

[8] H.-D. Meyer, U. Manthe, and L. S. Cederbaum, "The multi-configurational time-dependent Hartree approach," *Chemical Physics Letters*, vol. 165, no. 1, pp. 73–78, 1990.

[9] B. O. Roos *et al.*, "The complete active space self-consistent field method and its applications in electronic structure calculations," *Advances in chemical physics*, vol. 69, pp. 399–445, 2007.

[10] D. R. Hartree, "The wave mechanics of an atom with a non-Coulomb central field. Part I. Theory and methods," in *Mathematical Proceedings of the Cambridge Philosophical Society*, vol. 24, pp. 89–110, Cambridge university press, 1928.

[11] V. Fock, "Näherungsmethode zur lösung des quantenmechanischen mehrkörperproblems," *Zeitschrift für Physik*, vol. 61, pp. 126–148, 1930.

[12] I. Shavitt, "The method of configuration interaction," in *Methods of electronic structure theory*, pp. 189–275, Springer, 1977.

[13] C. Møller and M. S. Plesset, "Note on an approximation treatment for many-electron systems," *Physical review*, vol. 46, no. 7, p. 618, 1934.

[14] P. Hohenberg and W. Kohn, "Inhomogeneous electron gas," *Physical review*, vol. 136, no. 3B, p. B864, 1964.

[15] W. Kohn and L. J. Sham, "Self-consistent equations including exchange and correlation effects," *Physical review*, vol. 140, no. 4A, p. A1133, 1965.

[16] W. Kohn and L. Sham, "Density functional theory," in *Conference Proceedings-Italian Physical Society*, vol. 49, pp. 561–572, Editrice Compositori, 1996.

[17] A. D. Becke, "Density-functional thermochemistry. I. the effect of the exchange-only gradient correction," *The Journal of chemical physics*, vol. 96, no. 3, pp. 2155–2160, 1992.

[18] J. P. Perdew and K. Schmidt, "Jacob's ladder of density functional approximations for the exchange-correlation energy," in *AIP Conference Proceedings*, vol. 577, pp. 1–20, American Institute of Physics, 2001.

[19] N. Mardirossian and M. Head-Gordon, "Thirty years of density functional theory in computational chemistry: an overview and extensive assessment of 200 density functionals," *Molecular physics*, vol. 115, no. 19, pp. 2315–2372, 2017.

[20] S. Grimme, "Density functional theory with London dispersion corrections," *Wiley Interdisciplinary Reviews: Computational Molecular Science*, vol. 1, no. 2, pp. 211–228, 2011.

[21] A. Tkatchenko and M. Scheffler, "Accurate molecular van der waals interactions from ground-state electron density¡? format?¿ and free-atom reference data," *Physical review letters*, vol. 102, no. 7, p. 073005, 2009.

[22] J.-D. Chai and M. Head-Gordon, "Systematic optimization of long-range corrected hybrid density functionals," *The Journal of chemical physics*, vol. 128, no. 8, 2008.

[23] L. Verlet, "Computer" experiments" on classical fluids. I. Thermodynamical properties of Lennard-Jones molecules," *Physical review*, vol. 159, no. 1, p. 98, 1967.

[24] R. W. Zwanzig, "High-temperature equation of state by a perturbation method. I. Nonpolar gases," *The Journal of Chemical Physics*, vol. 22, no. 8, pp. 1420–1426, 1954.

[25] M. J. Mitchell and J. A. McCammon, "Free energy difference calculations by thermodynamic integration: difficulties in obtaining a precise value," *Journal of computational chemistry*, vol. 12, no. 2, pp. 271–275, 1991.

[26] G. M. Torrie and J. P. Valleau, "Nonphysical sampling distributions in Monte Carlo free-energy estimation: Umbrella sampling," *Journal of computational physics*, vol. 23, no. 2, pp. 187–199, 1977.

[27] A. Laio and F. L. Gervasio, "Metadynamics: a method to simulate rare events and reconstruct the free energy in biophysics, chemistry and material science," *Reports on Progress in Physics*, vol. 71, no. 12, p. 126601, 2008.

[28] K. Fukui, "The path of chemical reactions-the IRC approach," *Accounts of chemical research*, vol. 14, no. 12, pp. 363–368, 1981.

[29] M. Page, C. Doubleday, and J. W. McIver Jr, "Following steepest descent reaction paths. the use of higher energy derivatives with ab initio electronic structure methods," *The Journal of chemical physics*, vol. 93, no. 8, pp. 5634–5642, 1990.

[30] S. A. Adelman, "Solvent cage effects and the dynamics of liquid state chemical reactions," *Reviews of chemical intermediates*, vol. 8, pp. 321–338, 1987.

[31] V. P. Sokhan, A. P. Jones, F. S. Cipcigan, J. Crain, and G. J. Martyna, "Signature properties of water: Their molecular electronic origins," *Proceedings of the National Academy of Sciences*, vol. 112, no. 20, pp. 6341–6346, 2015.

[32] R. Cukier and M. Morillo, "Solvent effects on proton-transfer reactions," *The Journal of chemical physics*, vol. 91, no. 2, pp. 857–863, 1989.

[33] J. Tomasi, B. Mennucci, and R. Cammi, "Quantum mechanical continuum solvation models," *Chemical reviews*, vol. 105, no. 8, pp. 2999–3094, 2005.

[34] B. Mennucci, J. Tomasi, R. Cammi, J. Cheeseman, M. Frisch, F. Devlin, S. Gabriel, and P. Stephens, "Polarizable continuum model (PCM) calculations of solvent effects on optical rotations of chiral molecules," *The Journal of Physical Chemistry A*, vol. 106, no. 25, pp. 6102–6113, 2002.

[35] A. Klamt and G. Schüürmann, "COSMO: a new approach to dielectric screening in solvents with explicit expressions for the screening energy and its gradient," *Journal of the Chemical Society, Perkin Transactions 2*, no. 5, pp. 799–805, 1993.

[36] A. V. Marenich, C. J. Cramer, and D. G. Truhlar, "Universal solvation model based on solute electron density and on a continuum model of the solvent defined by the bulk dielectric constant and atomic surface tensions," *The Journal of Physical Chemistry B*, vol. 113, no. 18, pp. 6378–6396, 2009.

[37] R. E. Bulo, C. Michel, P. Fleurat-Lessard, and P. Sautet, "Multiscale modeling of chemistry in water: Are we there yet?," *Journal of chemical theory and computation*, vol. 9, no. 12, pp. 5567–5577, 2013.

[38] H. M. Senn and W. Thiel, "QM/MM methods for biomolecular systems," *Angewandte Chemie International Edition*, vol. 48, no. 7, pp. 1198–1229, 2009.

[39] L. W. Chung, W. Sameera, R. Ramozzi, A. J. Page, M. Hatanaka, G. P. Petrova, T. V. Harris, X. Li, Z. Ke, F. Liu, *et al.*, "The ONIOM method and its applications," *Chemical reviews*, vol. 115, no. 12, pp. 5678–5796, 2015.

[40] W. Fudickar and T. Linker, "Theoretical insights into the effect of solvents on the [4+ 2] cycloaddition of singlet oxygen to substituted anthracenes: A change from a stepwise process to a concerted process," *Journal of Physical Organic Chemistry*, vol. 32, no. 7, p. e3951, 2019.

[41] A. J. Parker, "Protic-dipolar aprotic solvent effects on rates of bimolecular reactions," *Chemical Reviews*, vol. 69, no. 1, pp. 1–32, 1969.

[42] H. O. Pritchard, "Recrossings and transition-state theory," *The Journal of Physical Chemistry A*, vol. 109, no. 7, pp. 1400–1404, 2005.

[43] O. M. Gonzalez-James, E. E. Kwan, and D. A. Singleton, "Entropic intermediates and hidden rate-limiting steps in seemingly concerted cycloadditions. Observation, prediction, and origin of an isotope effect on recrossing," *Journal of the American Chemical Society*, vol. 134, no. 4, pp. 1914–1917, 2012.

[44] J. L. Bao and D. G. Truhlar, "Variational transition state theory: theoretical framework and recent developments," *Chemical Society Reviews*, vol. 46, no. 24, pp. 7548–7596, 2017.

[45] Z. Feng, W. Guo, W.-Y. Kong, D. Chen, S. Wang, and D. J. Tantillo, "Analogies between photochemical reactions and ground-state post-transition-state bifurcations shed light on dynamical origins of selectivity," *Nature Chemistry*, vol. 16, no. 4, pp. 615–623, 2024.

[46] S. R. Hare and D. J. Tantillo, "Cryptic post-transition state bifurcations that reduce the efficiency of lactone-forming rh-carbenoid C–H insertions," *Chemical science*, vol. 8, no. 2, pp. 1442–1449, 2017.

[47] W. Quapp, M. Hirsch, and D. Heidrich, "An approach to reaction path branching using valley–ridge inflection points of potential-energy surfaces," *Theoretical Chemistry Accounts*, vol. 112, pp. 40–51, 2004.

[48] J. Rehbein and B. K. Carpenter, "Do we fully understand what controls chemical selectivity?," *Physical Chemistry Chemical Physics*, vol. 13, no. 47, pp. 20906–20922, 2011.

[49] D. J. Tantillo, "Beyond transition state theory—Non-statistical dynamic effects for organic reactions," in *Advances in Physical Organic Chemistry*, vol. 55, pp. 1–16, Elsevier, 2021.

[50] W. Quapp, M. Hirsch, and D. Heidrich, "Bifurcation of reaction pathways: the set of valley ridge inflection points of a simple three-dimensional potential energy surface," *Theoretical Chemistry Accounts*, vol. 100, pp. 285–299, 1998.

[51] J. B. Thomas, J. R. Waas, M. Harmata, and D. A. Singleton, "Control elements in dynamically determined selectivity on a bifurcating surface," *Journal of the American Chemical Society*, vol. 130, no. 44, pp. 14544–14555, 2008.

[52] D. H. Ess, S. E. Wheeler, R. G. Iafe, L. Xu, N. Çelebi-Ölçüm, and K. N. Houk, "Bifurcations on potential energy surfaces of organic reactions," *Angewandte Chemie International Edition*, vol. 47, no. 40, pp. 7592–7601, 2008.

[53] B. K. Carpenter, "Energy disposition in reactive intermediates," *Chemical Reviews*, vol. 113, no. 9, pp. 7265–7286, 2013.

[54] D. J. Tantillo, "Dynamic effects on organic reactivity—Pathways to (and from) discomfort," *Journal of Physical Organic Chemistry*, vol. 34, no. 6, p. e4202, 2021.

[55] S. R. Hare and D. J. Tantillo, "Post-transition state bifurcations gain momentum – current state of the field," *Pure Appl. Chem.*, vol. 89, pp. 679–698, June 2017.

[56] Z. Wang, J. S. Hirschi, and D. A. Singleton, "Recrossing and dynamic matching effects on selectivity in a Diels-Alder reaction," *Angewandte Chemie (International ed. in English)*, vol. 48, no. 48, p. 9156, 2009.

[57] D. Boyall and K. L. Reid, "Modern studies of intramolecular vibrational energy redistribution," *Chemical society reviews*, vol. 26, no. 3, pp. 223–232, 1997.

[58] W. Guo, S. R. Hare, S.-S. Chen, C. M. Saunders, and D. J. Tantillo, "C–H insertion in dirhodium tetracarboxylate-catalyzed reactions despite dynamical tendencies toward fragmentation: implications for reaction efficiency and catalyst design," *Journal of the American Chemical Society*, vol. 144, no. 37, pp. 17219–17231, 2022.

[59] W. Guo, S. R. Hare, S.-S. Chen, C. M. Saunders, and D. J. Tantillo, "Correction to "C–H insertion in dirhodium tetracarboxylate-catalyzed reactions despite dynamical tendencies toward fragmentation: Implications for reaction efficiency and catalyst design"," *Journal of the American Chemical Society*, vol. 145, no. 46, pp. 25505–25508, 2023.

[60] F. Bernardi, A. Bottoni, and G. P. Miscione, "Metal carbene or carbenoid complexes? A theoretical study of the active form of transition metal catalysts in cyclopropanation and olefin metathesis reactions," *Organometallics*, vol. 19, no. 25, pp. 5529–5532, 2000.

[61] G. Frenking, M. Solà, and S. F. Vyboishchikov, "Chemical bonding in transition metal carbene complexes," *Journal of organometallic chemistry*, vol. 690, no. 24-25, pp. 6178–6204, 2005.

[62] D. Cardin, B. Cetinkaya, E. Cetinkaya, and M. Lappert, "Carbene complexes. Part I. Electron-rich olefins as a source of carbene complexes of platinum (II) and palladium (II); and some experiments with $(CF_3)_2CN_2$," *Journal of the Chemical Society, Dalton Transactions*, no. 5, pp. 514–522, 1973.

[63] M. P. Doyle, "Catalytic methods for metal carbene transformations," *Chemical Reviews*, vol. 86, no. 5, pp. 919–939, 1986.

[64] H. M. Davies and S. A. Panaro, "Effect of rhodium carbenoid structure on cyclopropanation chemoselectivity," *Tetrahedron*, vol. 56, no. 28, pp. 4871–4880, 2000.

[65] S. Chuprakov, S. W. Kwok, L. Zhang, L. Lercher, and V. V. Fokin, "Rhodium-catalyzed enantioselective cyclopropanation of olefins with N-sulfonyl 1, 2, 3-triazoles," *Journal of the American Chemical Society*, vol. 131, no. 50, pp. 18034–18035, 2009.

[66] R. J. Ross, R. Jeyaseelan, and M. Lautens, "Rhodium-catalyzed intermolecular cyclopropanation of benzofurans, indoles, and alkenes via cyclopropene ring opening," *Organic Letters*, vol. 22, no. 12, pp. 4838–4843, 2020.

[67] D. F. Taber and E. H. Petty, "General route to highly functionalized cyclopentane derivatives by intramolecular C–H insertion," *The Journal of Organic Chemistry*, vol. 47, no. 24, pp. 4808–4809, 1982.

[68] J. P. Lutz, C. M. Rathbun, S. M. Stevenson, B. M. Powell, T. S. Boman, C. E. Baxter, J. M. Zona, and J. B. Johnson, "Rate-limiting step of the rh-catalyzed carboacylation of alkenes: C–C bond activation or migratory insertion?," *Journal of the American Chemical Society*, vol. 134, no. 1, pp. 715–722, 2012.

[69] Y. Xiang, C. Wang, Q. Ding, and Y. Peng, "Diazo compounds: Versatile synthons for the synthesis of nitrogen heterocycles via transition metal-catalyzed cascade C–H activation/carbene insertion/annulation reactions," *Advanced Synthesis & Catalysis*, vol. 361, no. 5, pp. 919–944, 2019.

[70] H. M. Davies and K. Liao, "Dirhodium tetracarboxylates as catalysts for selective intermolecular C–H functionalization," *Nature Reviews Chemistry*, vol. 3, no. 6, pp. 347–360, 2019.

[71] J. He, X.-S. Liu, M. Li, S. Peng, Z.-Y. Si, and L. Liu, "A rhodium-catalyzed ylide formation/Smiles rearrangement reaction of chalcogenide ether and triazoles," *Organic Chemistry Frontiers*, vol. 10, no. 9, pp. 2198–2203, 2023.

[72] A. Padwa, "Domino reactions of rhodium (II) carbenoids for alkaloid synthesis," *Chemical Society Reviews*, vol. 38, no. 11, pp. 3072–3081, 2009.

[73] Z. Li and H. M. Davies, "Enantioselective C-C bond formation by rhodium-catalyzed tandem ylide formation/[2, 3]-sigmatropic rearrangement between donor/acceptor carbenoids and allylic alcohols," *Journal of the American Chemical Society*, vol. 132, no. 1, pp. 396–401, 2010.

[74] J. Hansen and H. M. Davies, "High symmetry dirhodium (II) paddlewheel complexes as chiral catalysts," *Coordination chemistry reviews*, vol. 252, no. 5-7, pp. 545–555, 2008.

[75] R. Wu, D. Zhu, and S. Zhu, "Dirhodium: carbene transformations and beyond," *Organic Chemistry Frontiers*, vol. 10, no. 11, pp. 2849–2878, 2023.

[76] F. G. Adly, "On the structure of chiral dirhodium (II) carboxylate catalysts: Stereoselectivity relevance and insights," *Catalysts*, vol. 7, no. 11, p. 347, 2017.

[77] A. Lledós, "Computational organometallic catalysis: Where we are, where we are going," *European journal of inorganic chemistry*, vol. 2021, no. 26, pp. 2547–2555, 2021.

[78] D. F. Taber, K. K. You, and A. L. Rheingold, "Predicting the diastereoselectivity of rh-mediated intramolecular C-H insertion," *Journal of the American Chemical Society*, vol. 118, no. 3, pp. 547–556, 1996.

[79] E. Nakamura, N. Yoshikai, and M. Yamanaka, "Mechanism of C-H bond activation/C-C bond formation reaction between diazo compound and alkane catalyzed by dirhodium tetracarboxylate," *Journal of the American Chemical Society*, vol. 124, no. 24, pp. 7181–7192, 2002.

[80] M. Zhou and M. Springborg, "Theoretical study of the mechanism behind the site-and enantioselectivity of C–H functionalization catalysed by chiral dirhodium catalyst," *Physical Chemistry Chemical Physics*, vol. 22, no. 17, pp. 9561–9572, 2020.

[81] A. I. Green, C. P. Tinworth, S. Warriner, A. Nelson, and N. Fey, "Computational mapping of dirhodium (II) catalysts," *Chemistry–A European Journal*, vol. 27, no. 7, pp. 2402–2409, 2021.

[82] B. K. Carpenter, "Dynamic matching: The cause of inversion of configuration in the [1, 3] sigmatropic migration?," *Journal of the American Chemical Society*, vol. 117, no. 23, pp. 6336–6344, 1995.

[83] B. R. Ussing, C. Hang, and D. A. Singleton, "Dynamic effects on the periselectivity, rate, isotope effects, and mechanism of cycloadditions of ketenes with cyclopentadiene," *Journal of the American Chemical Society*, vol. 128, no. 23, pp. 7594–7607, 2006.

[84] U. Lourderaj, K. Park, and W. L. Hase, "Classical trajectory simulations of post-transition state dynamics," *International Reviews in Physical Chemistry*, vol. 27, no. 3, pp. 361–403, 2008.

[85] D. H. Ess, "Quasiclassical direct dynamics trajectory simulations of organometallic reactions," *Accounts of Chemical Research*, vol. 54, no. 23, pp. 4410–4422, 2021.

[86] L. Eun, W. J. Kyung, and S. K. Yong, "Selectivity in the lactone formation via C-H insertion reaction of diazomalonates," *Tetrahedron letters*, vol. 31, no. 7, pp. 1023–1026, 1990.

[87] M. J. Frisch, G. W. Trucks, H. B. Schlegel, G. E. Scuseria, M. A. Robb, J. R. Cheeseman, G. Scalmani, V. Barone, G. A. Petersson, H. Nakatsuji, X. Li, M. Caricato, A. V. Marenich, J. Bloino, B. G. Janesko,

R. Gomperts, B. Mennucci, H. P. Hratchian, J. V. Ortiz, A. F. Izmaylov, J. L. Sonnenberg, D. Williams-Young, F. Ding, F. Lipparini, F. Egidi, J. Goings, B. Peng, A. Petrone, T. Henderson, D. Ranasinghe, V. G. Zakrzewski, J. Gao, N. Rega, G. Zheng, W. Liang, M. Hada, M. Ehara, K. Toyota, R. Fukuda, J. Hasegawa, M. Ishida, T. Nakajima, Y. Honda, O. Kitao, H. Nakai, T. Vreven, K. Throssell, J. A. Montgomery, Jr., J. E. Peralta, F. Ogliaro, M. J. Bearpark, J. J. Heyd, E. N. Brothers, K. N. Kudin, V. N. Staroverov, T. A. Keith, R. Kobayashi, J. Normand, K. Raghavachari, A. P. Rendell, J. C. Burant, S. S. Iyengar, J. Tomasi, M. Cossi, J. M. Millam, M. Klene, C. Adamo, R. Cammi, J. W. Ochterski, R. L. Martin, K. Morokuma, O. Farkas, J. B. Foresman, and D. J. Fox, "Gaussian˜16 Revision C.01," 2016. Gaussian Inc. Wallingford CT.

[88] A. D. Becke, "Density-functional exchange-energy approximation with correct asymptotic behavior," *Physical review A*, vol. 38, no. 6, p. 3098, 1988.

[89] C. Lee, W. Yang, and R. G. Parr, "Development of the Colle-Salvetti correlation-energy formula into a functional of the electron density," *Physical review B*, vol. 37, no. 2, p. 785, 1988.

[90] A. D. Becke, "A new mixing of Hartree–Fock and local density-functional theories," *The Journal of chemical physics*, vol. 98, no. 2, pp. 1372–1377, 1993.

[91] T. Sperger, I. A. Sanhueza, I. Kalvet, and F. Schoenebeck, "Computational studies of synthetically relevant homogeneous organometallic catalysis involving Ni, Pd, Ir, and Rh: an overview of commonly employed dft methods and mechanistic insights," *Chemical Reviews*, vol. 115, no. 17, pp. 9532–9586, 2015.

[92] R. Ditchfield, W. J. Hehre, and J. A. Pople, "Self-consistent molecular-orbital methods. IX. An extended Gaussian-type basis for molecular-orbital studies of organic molecules," *The Journal of Chemical Physics*, vol. 54, no. 2, pp. 724–728, 1971.

[93] V. A. Rassolov, M. A. Ratner, J. A. Pople, P. C. Redfern, and L. A. Curtiss, "6-31g* basis set for third-row atoms," *Journal of Computational Chemistry*, vol. 22, no. 9, pp. 976–984, 2001.

[94] P. J. Hay and W. R. Wadt, "Ab initio effective core potentials for molecular calculations. potentials for K to Au including the outermost core orbitals," *The Journal of chemical physics*, vol. 82, no. 1, pp. 299–310, 1985.

[95] Y. Zhao and D. G. Truhlar, "The M06 suite of density functionals for main group thermochemistry, thermochemical kinetics, noncovalent interactions, excited states, and transition elements: two new functionals and systematic testing of four m06-class functionals and 12 other functionals," *Theoretical chemistry accounts*, vol. 120, pp. 215–241, 2008.

[96] L. A. Curtiss, M. P. McGrath, J.-P. Blaudeau, N. E. Davis, R. C. Binning, and L. Radom, "Extension of Gaussian-2 theory to molecules containing third-row atoms Ga–Kr," *The Journal of Chemical Physics*, vol. 103, no. 14, pp. 6104–6113, 1995.

[97] M. Kumar, R. V. Chaudhari, B. Subramaniam, and T. A. Jackson, "Ligand effects on the regioselectivity of rhodium-catalyzed hydroformylation: Density functional calculations illuminate the role of long-range noncovalent interactions," *Organometallics*, vol. 33, no. 16, pp. 4183–4191, 2014.

[98] Y.-S. Xue, Y.-P. Cai, and Z.-X. Chen, "Mechanism and stereoselectivity of the Rh (II)-catalyzed cyclopropanation of diazooxindole: a density functional theory study," *RSC advances*, vol. 5, no. 71, pp. 57781–57791, 2015.

[99] X. Qi, D. G. Kohler, K. L. Hull, and P. Liu, "Energy decomposition analyses reveal the origins of catalyst and nucleophile effects on regioselectivity in nucleopalladation of alkenes," *Journal of the American Chemical Society*, vol. 141, no. 30, pp. 11892–11904, 2019.

[100] B. A. Shiekh, "Hierarchy of commonly used DFT methods for predicting the thermochemistry of Rh-mediated chemical transformations," *ACS omega*, vol. 4, no. 13, pp. 15435–15443, 2019.

[101] J. M. del Campo, J. L. Gázquez, S. Trickey, and A. Vela, "Non-empirical improvement of PBE and its hybrid PBE0 for general description of molecular properties," *The Journal of chemical physics*, vol. 136, no. 10, 2012.

[102] S. Y. Haoyu, X. He, S. L. Li, and D. G. Truhlar, "MN15: A Kohn–Sham global-hybrid exchange–correlation density functional with broad accuracy for multi-reference and single-reference systems and noncovalent interactions," *Chemical science*, vol. 7, no. 8, pp. 5032–5051, 2016.

[103] F. Weigend and R. Ahlrichs, "Balanced basis sets of split valence, triple zeta valence and quadruple zeta valence quality for h to rn: Design and assessment of accuracy," *Physical Chemistry Chemical Physics*, vol. 7, no. 18, pp. 3297–3305, 2005.

[104] S. Maeda, Y. Harabuchi, Y. Ono, T. Taketsugu, and K. Morokuma, "Intrinsic reaction coordinate: Calculation, bifurcation, and automated search," *International Journal of Quantum Chemistry*, vol. 115, no. 5, pp. 258–269, 2015.

[105] J. Zheng, J. L. Bao, R. Meana-Pañeda, S. Zhang, B. J. Lynch, J. C. Corchado, Y.-Y. Chuang, P. L. Fast, W.-P. Hu, Y.-P. Liu, G. C. Lynch, K. A. Nguyen, C. F. Jackels, A. Fernandez Ramos, B. A. Ellingson, V. S. Melissas, I. V. J. Rossi, E. L. Coitiño, J. Pu, T. V. Albu, A. Ratkiewicz, R. Steckler, B. C. Garrett, A. D. Isaacson, and D. G. Truhlar, *Polyrate-version 2017-C*. PhD thesis, University of Minnesota: Minneapolis, 2017.

[106] J. Zheng, J. L. Bao, S. Zhang, J. C. Corchado, R. Meana-Pañeda, Y.-Y. Chuang, E. L. Coitiño, B. A. Ellingson, and D. G. Truhlar, *Gaussrate 17*. PhD thesis, University of Minnesota: Minneapolis, 2017.

[107] E. R. Johnson, S. Keinan, P. Mori-Sánchez, J. Contreras-García, A. J. Cohen, and W. Yang, "Revealing noncovalent interactions," *Journal of the American Chemical Society*, vol. 132, no. 18, pp. 6498–6506, 2010.

[108] J. Contreras-García, R. A. Boto, F. Izquierdo-Ruiz, I. Reva, T. Woller, and M. Alonso, "A benchmark for the non-covalent interaction (NCI) index or... is it really all in the geometry?," *Theoretical Chemistry Accounts*, vol. 135, pp. 1–14, 2016.

[109] C. Lefebvre, G. Rubez, H. Khartabil, J.-C. Boisson, J. Contreras-García, and E. Hénon, "Accurately extracting the signature of intermolecular interactions present in the NCI plot of the reduced density gradient versus electron density," *Physical Chemistry Chemical Physics*, vol. 19, no. 27, pp. 17928–17936, 2017.

[110] T. Lu and F. Chen, "Multiwfn: A multifunctional wavefunction analyzer," *Journal of computational chemistry*, vol. 33, no. 5, pp. 580–592, 2012.

[111] F. M. Bickelhaupt and K. N. Houk, "Analyzing reaction rates with the distortion/interaction-activation strain model," *Angewandte Chemie International Edition*, vol. 56, no. 34, pp. 10070–10086, 2017.

[112] P. Yu, Z. Yang, Y. Liang, X. Hong, Y. Li, and K. Houk, "Distortion-controlled reactivity and molecular dynamics of dehydro-Diels–Alder reactions," *Journal of the American Chemical Society*, vol. 138, no. 26, pp. 8247–8252, 2016.

[113] P. Vermeeren, T. A. Hamlin, and F. M. Bickelhaupt, "Chemical reactivity from an activation strain perspective," *Chemical Communications*, vol. 57, no. 48, pp. 5880–5896, 2021.

[114] Y. Shao, Z. Gan, E. Epifanovsky, A. T. Gilbert, M. Wormit, J. Kussmann, A. W. Lange, A. Behn, J. Deng, X. Feng, *et al.*, "Advances in molecular quantum chemistry contained in the Q-Chem 4 program package," *Molecular Physics*, vol. 113, no. 2, pp. 184–215, 2015.

[115] R. Z. Khaliullin, E. A. Cobar, R. C. Lochan, A. T. Bell, and M. Head-Gordon, "Unravelling the origin of intermolecular interactions using absolutely localized molecular orbitals," *The Journal of Physical Chemistry A*, vol. 111, no. 36, pp. 8753–8765, 2007.

[116] P. R. Horn and M. Head-Gordon, "Polarization contributions to intermolecular interactions revisited with fragment electric-field response functions," *The Journal of Chemical Physics*, vol. 143, no. 11, 2015.

[117] L. Fu, H. Wang, and H. M. Davies, "Role of ortho-substituents on rhodium-catalyzed asymmetric synthesis of $\beta$-lactones by intramolecular C–H insertions of aryldiazoacetates," *Organic letters*, vol. 16, no. 11, pp. 3036–3039, 2014.

[118] M. Wamser and T. Bach, "Regioselectivity of intramolecular rhodium-catalyzed C–H insertion reactions of $\alpha$-aryl-$\alpha$-diazocarboxylates: Influence of the aryl substituent," *Synlett*, vol. 25, no. 08, pp. 1081–1084, 2014.

[119] C. Y. Legault, "CYLview, 1.0b." http://www.cylview.org, 2009. Accessed: NA-NA-NA.

[120] I. Mayer, "Bond order and valence indices: A personal account," *Journal of computational chemistry*, vol. 28, no. 1, pp. 204–221, 2007.

[121] P. Politzer, J. S. Murray, and T. Clark, "Halogen bonding: an electrostatically-driven highly directional noncovalent interaction," *Physical Chemistry Chemical Physics*, vol. 12, no. 28, pp. 7748–7757, 2010.

[122] K. E. Riley, J. S. Murray, P. Politzer, M. C. Concha, and P. Hobza, "Br···O complexes as probes of factors affecting halogen bonding: interactions of bromobenzenes and bromopyrimidines with acetone," *Journal of Chemical Theory and Computation*, vol. 5, no. 1, pp. 155–163, 2009.

[123] S. Kozuch and J. M. Martin, "Halogen bonds: Benchmarks and theoretical analysis," *Journal of chemical theory and computation*, vol. 9, no. 4, pp. 1918–1931, 2013.

[124] G. Cavallo, P. Metrangolo, R. Milani, T. Pilati, A. Priimagi, G. Resnati, and G. Terraneo, "The halogen bond," *Chemical reviews*, vol. 116, no. 4, pp. 2478–2601, 2016.

[125] W. Wang and P. Hobza, "Origin of the X-Hal (Hal= Cl, Br) bond-length change in the halogen-bonded complexes," *The Journal of Physical Chemistry A*, vol. 112, no. 17, pp. 4114–4119, 2008.

[126] W. Humphrey, A. Dalke, and K. Schulten, "VMD: visual molecular dynamics," *Journal of molecular graphics*, vol. 14, no. 1, pp. 33–38, 1996.

[127] M. Bai, Z. Feng, J. Li, and D. J. Tantillo, "Bouncing off walls–widths of exit channels from shallow minima can dominate selectivity control," *Chemical science*, vol. 11, no. 36, pp. 9937–9944, 2020.

[128] M. Kpante and L. M. Wolf, "Pathway bifurcations in the activation of allylic halides by palladium and their influence on the dynamics of $\eta$1 and $\eta$3 allyl intermediates," *The Journal of Organic Chemistry*, vol. 86, no. 14, pp. 9637–9650, 2021.

[129] S. R. Hare, R. P. Pemberton, and D. J. Tantillo, "Navigating past a fork in the road: carbocation-$\pi$ interactions can manipulate dynamic behavior of reactions facing post-transition-state bifurcations," *Journal of the American Chemical Society*, vol. 139, no. 22, pp. 7485–7493, 2017.

[130] H. B. Schlegel, "Exploring potential energy surfaces for chemical reactions: an overview of some practical methods," *Journal of computational chemistry*, vol. 24, no. 12, pp. 1514–1527, 2003.

[131] S. R. Hare, L. A. Bratholm, D. R. Glowacki, and B. K. Carpenter, "Low dimensional representations along intrinsic reaction coordinates and molecular dynamics trajectories using interatomic distance matrices," *Chemical science*, vol. 10, no. 43, pp. 9954–9968, 2019.

[132] H.-H. Chuang, D. J. Tantillo, and C.-P. Hsu, "Construction of two-dimensional potential energy surfaces of reactions with post-transition-state bifurcations," *Journal of Chemical Theory and Computation*, vol. 16, no. 7, pp. 4050–4060, 2020.

[133] Z. Yang, X. Dong, Y. Yu, P. Yu, Y. Li, C. Jamieson, and K. Houk, "Relationships between product ratios in ambimodal pericyclic reactions and bond lengths in transition structures," *Journal of the American Chemical Society*, vol. 140, no. 8, pp. 3061–3067, 2018.

[134] S. Lee and J. M. Goodman, "Rapid route-finding for bifurcating organic reactions," *Journal of the American Chemical Society*, vol. 142, no. 20, pp. 9210–9219, 2020.

[135] T. H. Peterson and B. K. Carpenter, "Estimation of dynamic effects on product ratios by vectorial decomposition of a reaction coordinate. application to thermal nitrogen loss from bicyclic azo compounds," *Journal of the American Chemical Society*, vol. 114, no. 2, pp. 766–767, 1992.

[136] V. N. Lindsay and A. B. Charette, "Design and synthesis of chiral heteroleptic rhodium (II) carboxylate catalysts: experimental investigation of halogen bond rigidification effects in asymmetric cyclopropanation," *Acs Catalysis*, vol. 2, no. 6, pp. 1221–1225, 2012.

[137] H. Tsutsui, Y. Yamaguchi, S. Kitagaki, S. Nakamura, M. Anada, and S. Hashimoto, "Dirhodium (II) tetrakis [N-tetrafluorophthaloyl-(S)-tert-leucinate]: an exceptionally effective Rh (II) catalyst for enantiotopically selective aromatic c-h insertions of diazo ketoesters," *Tetrahedron: Asymmetry*, vol. 14, no. 7, pp. 817–821, 2003.

[138] B. Biswas and D. A. Singleton, "Controlling selectivity by controlling the path of trajectories," *Journal of the American Chemical Society*, vol. 137, no. 45, pp. 14244–14247, 2015.

[139] R. B. Campos and D. J. Tantillo, "Designing reactions with post-transition-state bifurcations: asynchronous nitrene insertions into C–C $\sigma$ bonds," *Chem*, vol. 5, no. 1, pp. 227–236, 2019.

[140] W. Guo and D. J. Tantillo, "Running wild through dirhodium Tetracarboxylate-Catalyzed combined CH(C)-Functionalization/Cope rearrangement landscapes: Does Post-Transition-State dynamic mismatching influence product distributions?," *J. Am. Chem. Soc.*, vol. 146, pp. 7039–7051, Mar. 2024.

[141] X. Qi and Y. Lan, "Recent advances in theoretical studies on transition-metal-catalyzed carbene transformations," *Accounts of Chemical Research*, vol. 54, no. 14, pp. 2905–2915, 2021.

[142] M. Lee, Z. Ren, D. G. Musaev, and H. M. Davies, "Rhodium-stabilized diarylcarbenes behaving as donor/acceptor carbenes," *ACS catalysis*, vol. 10, no. 11, pp. 6240–6247, 2020.

[143] R. C. Cammarota, W. Liu, J. Bacsa, H. M. Davies, and M. S. Sigman, "Mechanistically guided workflow for relating complex reactive site topologies to catalyst performance in C–H functionalization reactions," *Journal of the American Chemical Society*, vol. 144, no. 4, pp. 1881–1898, 2022.

[144] Z. Ren, D. G. Musaev, and H. M. Davies, "Key selectivity controlling elements in rhodium-catalyzed C–H functionalization with donor/acceptor carbenes," *ACS Catalysis*, vol. 12, no. 21, pp. 13446–13456, 2022.

[145] D. J. Tantillo, "Quantum chemical interrogation of reactions promoted by dirhodium tetracarboxylate catalysts - mechanism, selectivity, and nonstatistical dynamic effects," *Accounts of Chemical Research*, pp. 829–839, 2024.

[146] C. J. Laconsay, A. Pla-Quintana, and D. J. Tantillo, "Effects of axial solvent coordination to dirhodium complexes on the reactivity and selectivity in C–H insertion reactions: A computational study," *Organometallics*, vol. 40, no. 24, pp. 4120–4132, 2021.

[147] H. M. Davies and Y. Lian, "The combined C–H functionalization/cope rearrangement: discovery and applications in organic synthesis," *Accounts of Chemical Research*, vol. 45, no. 6, pp. 923–935, 2012.

[148] J. H. Hansen, T. M. Gregg, S. R. Ovalles, Y. Lian, J. Autschbach, and H. M. Davies, "On the mechanism and selectivity of the combined C-H activation/Cope rearrangement," *Journal of the American Chemical Society*, vol. 133, no. 13, pp. 5076–5085, 2011.

[149] J. L. Thompson and H. M. Davies, "Enhancement of cyclopropanation chemistry in the silver-catalyzed reactions of aryldiazoacetates," *Journal of the American Chemical Society*, vol. 129, no. 19, pp. 6090–6091, 2007.

[150] H. M. Davies, D. G. Stafford, and T. Hansen, "Catalytic asymmetric synthesis of diarylacetates and 4,4-diarylbutanoates. A formal asymmetric synthesis of (+)-sertraline," *Organic letters*, vol. 1, no. 2, pp. 233–236, 1999.

[151] H. M. Davies, D. G. Stafford, B. D. Doan, and J. H. Houser, "Tandem asymmetric cyclopropanation/cope rearrangement. A highly diastereoselective and enantioselective method for the construction of 1, 4-cycloheptadienes," *Journal of the American Chemical Society*, vol. 120, no. 14, pp. 3326–3331, 1998.

[152] K. O. Marichev, H. Zheng, and M. P. Doyle, "Metal carbene cycloaddition reactions," *Transition Metal-Catalyzed Carbene Transformations*, pp. 139–168, 2022.

[153] M. Cossi, V. Barone, R. Cammi, and J. Tomasi, "Ab initio study of solvated molecules: a new implementation of the polarizable continuum model," *Chemical Physics Letters*, vol. 255, no. 4-6, pp. 327–335, 1996.

[154] S. Miertuš, E. Scrocco, and J. Tomasi, "Electrostatic interaction of a solute with a continuum. A direct utilizaion of ab initio molecular potentials for the prevision of solvent effects," *Chemical Physics*, vol. 55, no. 1, pp. 117–129, 1981.

[155] M. Álvarez-Moreno, C. de Graaf, N. López, F. Maseras, J. M. Poblet, and C. Bo, "Managing the computational chemistry big data problem: the ioChem-BD platform," *J. Chem. Inf. Model.*, vol. 55, pp. 95–103, Jan. 2015.

[156] Z. Feng and D. J. Tantillo, "Dynamic effects on migratory aptitudes in carbocation reactions," *Journal of the American Chemical Society*, vol. 143, no. 2, pp. 1088–1097, 2021.

[157] Y. Nieves-Quinones and D. A. Singleton, "Dynamics and the regiochemistry of nitration of toluene," *Journal of the American Chemical Society*, vol. 138, no. 46, pp. 15167–15176, 2016.

[158] M. T. Tremblay and Z. J. Yang, "The effect of zero-point energy in simulating organic reactions with post-transition state bifurcation," *Journal of Physical Organic Chemistry*, vol. 35, no. 11, p. e4322, 2022.

[159] Z. Yang, C. S. Jamieson, X.-S. Xue, M. Garcia-Borràs, T. Benton, X. Dong, F. Liu, and K. Houk, "Mechanisms and dynamics of reactions involving entropic intermediates," *Trends in Chemistry*, vol. 1, no. 1, pp. 22–34, 2019.

[160] J. Joy and D. H. Ess, "Direct dynamics trajectories demonstrate dynamic matching and nonstatistical radical pair intermediates during Fe-Oxo-mediated C–H functionalization reactions," *Journal of the American Chemical Society*, vol. 145, no. 13, pp. 7628–7637, 2023.

[161] L. Törk, G. Jiménez-Osés, C. Doubleday, F. Liu, and K. Houk, "Molecular dynamics of the Diels–Alder reactions of tetrazines with alkenes and n2 extrusions from adducts," *Journal of the American Chemical Society*, vol. 137, no. 14, pp. 4749–4758, 2015.

[162] Z. Chen, Y. Nieves-Quinones, J. R. Waas, and D. A. Singleton, "Isotope effects, dynamic matching, and solvent dynamics in a wittig reaction. betaines as bypassed intermediates," *Journal of the American Chemical Society*, vol. 136, no. 38, pp. 13122–13125, 2014.

[163] H. M. Davies and D. Morton, "Guiding principles for site selective and stereoselective intermolecular C–H functionalization by donor/acceptor rhodium carbenes," *Chemical Society Reviews*, vol. 40, no. 4, pp. 1857–1869, 2011.

[164] J. F. Briones, J. Hansen, K. I. Hardcastle, J. Autschbach, and H. M. Davies, "Highly enantioselective $Rh_2$(S-DOSP)$_4$-catalyzed cyclopropenation of alkynes with styryldiazoacetates," *Journal of the American Chemical Society*, vol. 132, no. 48, pp. 17211–17215, 2010.

[165] C. Werlé, R. Goddard, P. Philipps, C. Farès, and A. Fürstner, "Stabilization of a chiral dirhodium carbene by encapsulation and a discussion of the stereochemical implications," *Angewandte Chemie*, vol. 128, no. 36, pp. 10918–10923, 2016.

[166] S. Grimme, "Exploration of chemical compound, conformer, and reaction space with Meta-dynamics simulations based on tight-binding quantum chemical calculations," *Journal of chemical theory and computation*, vol. 15, no. 5, pp. 2847–2862, 2019.

[167] Q. Feng, H. Wu, X. Li, L. Song, L. W. Chung, Y.-D. Wu, and J. Sun, "Ru-catalyzed geminal hydroboration of silyl alkynes via a new gem-addition mechanism," *Journal of the American Chemical Society*, vol. 142, no. 32, pp. 13867–13877, 2020.

[168] Y. Yang, X. Zhang, L.-P. Zhong, J. Lan, X. Li, C.-C. Li, and L. W. Chung, "Unusual KIE and dynamics effects in the Fe-catalyzed hetero-Diels-Alder reaction of unactivated aldehydes and dienes," *Nature communications*, vol. 11, no. 1, p. 1850, 2020.

[169] M. S. Teynor, W. Scott, and D. H. Ess, "Catalysis with a skip: Dynamically coupled addition, proton transfer, and elimination during Au-and Pd-catalyzed diol cyclizations," *ACS Catalysis*, vol. 11, no. 16, pp. 10179–10189, 2021.

[170] J. Joy, A. J. Schaefer, M. S. Teynor, and D. H. Ess, "Dynamical origin of rebound versus dissociation selectivity during Fe-Oxo-Mediated C–H functionalization reactions," *Journal of the American Chemical Society*, vol. 146, no. 4, pp. 2452–2464, 2024.

[171] T. Ziegler and J. Autschbach, "Theoretical methods of potential use for studies of inorganic reaction mechanisms," *Chemical reviews*, vol. 105, no. 6, pp. 2695–2722, 2005.

[172] Y. Liu, X. Liu, and X. Feng, "Recent advances in metal-catalysed asymmetric sigmatropic rearrangements," *Chemical Science*, vol. 13, no. 42, pp. 12290–12308, 2022.

[173] M. Liao and J. Wang, "Highly efficient [2, 3]-sigmatropic rearrangement of sulfur ylide derived from Rh (II) carbene and sulfides in water," *Green Chemistry*, vol. 9, no. 2, pp. 184–188, 2007.

[174] Z. Zhang, Z. Sheng, W. Yu, G. Wu, R. Zhang, W.-D. Chu, Y. Zhang, and J. Wang, "Catalytic asymmetric trifluoromethylthiolation via enantioselective [2, 3]-sigmatropic rearrangement of sulfonium ylides," *Nature Chemistry*, vol. 9, no. 10, pp. 970–976, 2017.

[175] S. Jana, Y. Guo, and R. M. Koenigs, "Recent perspectives on rearrangement reactions of ylides via carbene transfer reactions," *Chemistry–A European Journal*, vol. 27, no. 4, pp. 1270–1281, 2021.

[176] Y. Li, Z. Huang, X. Wu, P.-F. Xu, J. Jin, Y. Zhang, and J. Wang, "Rh(II)-catalyzed [2,3]-sigmatropic rearrangement of sulfur ylides derived from n-tosylhydrazones and sulfides," *Tetrahedron*, vol. 68, no. 26, pp. 5234–5240, 2012.

[177] Z. Yang, Y. Guo, and R. M. Koenigs, "Solvent-dependent, rhodium catalysed rearrangement reactions of sulfur ylides," *Chemical Communications*, vol. 55, no. 58, pp. 8410–8413, 2019.

[178] H. Zhang, B. Wang, H. Yi, Y. Zhang, and J. Wang, "Rh(II)-catalyzed [2,3]-sigmatropic rearrangement of sulfur ylides derived from cyclopropenes and sulfides," *Organic letters*, vol. 17, no. 13, pp. 3322–3325, 2015.

[179] C. J. Laconsay and D. J. Tantillo, "Metal bound or free ylides as reaction intermediates in metal-catalyzed [2,3]-sigmatropic rearrangements? it depends," *ACS Catal.*, vol. 11, pp. 829–839, Jan. 2021.

[180] V. N. Nair and U. K. Tambar, "Catalytic rearrangements of onium ylides in aromatic systems," *Organic & biomolecular chemistry*, vol. 20, no. 17, pp. 3427–3439, 2022.

[181] J. S. Clark and K. E. Hansen, "Intramolecular reactions of metal carbenoids with allylic ethers: is a free ylide involved in every case?," *Chemistry–A European Journal*, vol. 20, no. 18, pp. 5454–5459, 2014.

[182] K. J. Hock and R. M. Koenigs, "Enantioselective [2, 3]-sigmatropic rearrangements: metal-bound or free ylides as reaction intermediates?," *Angewandte Chemie (International ed. in English)*, vol. 56, no. 44, pp. 13566–13568, 2017.

[183] B. G. Anderson, D. Cressy, J. J. Patel, C. F. Harris, G. P. Yap, J. F. Berry, and A. Darko, "Synthesis and catalytic properties of dirhodium paddlewheel complexes with tethered, axially coordinating thioether ligands," *Inorganic Chemistry*, vol. 58, no. 3, pp. 1728–1732, 2019.

[184] D. T. Boruta, O. Dmitrenko, G. P. Yap, and J. M. Fox, "$Rh_2$(s-pttl)$_3$ TPA—a mixed-ligand dirhodium (II) catalyst for enantioselective reactions of $\alpha$-alkyl-$\alpha$-diazoesters," *Chemical science*, vol. 3, no. 5, pp. 1589–1593, 2012.

[185] B. Hong, L. Shi, L. Li, S. Zhan, and Z. Gu, "Paddlewheel dirhodium (II) complexes with n-heterocyclic carbene or phosphine ligand: New reactivity and selectivity," *Green Synthesis and Catalysis*, vol. 3, no. 2, pp. 137–149, 2022.

[186] S. Rej and N. Chatani, "Effect of sulfonamide and carboxamide ligands on the structural diversity of bimetallic Rh(II)–Rh(II) cores: Exploring the catalytic activity of these newly synthesized $Rh_2$ complexes," *Inorganic Chemistry*, vol. 60, no. 6, pp. 3534–3538, 2021.

[187] S. Grimme, "Supramolecular binding thermodynamics by dispersion-corrected density functional theory," *Chemistry–A European Journal*, vol. 18, no. 32, pp. 9955–9964, 2012.

[188] L. Goerigk and S. Grimme, "Efficient and accurate Double-Hybrid-Meta-GGA density functionals: Evaluation with the extended GMTKN30 database for general main group thermochemistry, kinetics,

and noncovalent interactions," *Journal of chemical theory and computation*, vol. 7, no. 2, pp. 291–309, 2011.

[189] V. N. Nair, V. Kojasoy, C. J. Laconsay, W. Y. Kong, D. J. Tantillo, and U. K. Tambar, "Catalyst-controlled regiodivergence in rearrangements of indole-based onium ylides," *Journal of the American Chemical Society*, vol. 143, no. 24, pp. 9016–9025, 2021.

[190] Y. Zhao, H. T. Ng, R. Peverati, and D. G. Truhlar, "Benchmark database for ylidic bond dissociation energies and its use for assessments of electronic structure methods," *Journal of Chemical Theory and Computation*, vol. 8, no. 8, pp. 2824–2834, 2012.

[191] H. C. Brown, *The nonclassical ion problem*. New York, NY: Springer, 1997.

[192] R. V. Williams, "Homoaromaticity," *Chem. Rev.*, vol. 101, pp. 1185–1204, May 2001.

[193] C. A. Grob, "Inductivity and bridging in carbocations," *Acc. Chem. Res.*, vol. 16, pp. 426–431, Dec. 1983.

[194] H. C. Brown, "The energy of the transition states and the intermediate cation in the ionization of 2-norbornyl derivatives. where is the nonclassical stabilization energy?," *Acc. Chem. Res.*, vol. 16, pp. 432–440, Dec. 1983.

[195] C. Walling, "An innocent bystander looks at the 2-norbornyl cation," *Acc. Chem. Res.*, vol. 16, pp. 448–454, Dec. 1983.

[196] G. A. Olah, G. K. S. Prakash, and M. Saunders, "Conclusion of the classical-nonclassical ion controversy based on the structural study of the 2-norbornyl cation," *Acc. Chem. Res.*, vol. 16, pp. 440–448, Dec. 1983.

[197] A. K. Cheng, F. A. L. Anet, J. Mioduski, and J. Meinwald, "Determination of the fluxional barrier in semibullvalene by proton and carbon-13 nuclear magnetic resonance spectroscopy," *J. Am. Chem. Soc.*, vol. 96, pp. 2887–2891, May 1974.

[198] R. V. Williams, "Semibullvalenes and related molecules: Ever closer approaches to neutral homoaromaticity," *European J. Org. Chem.*, vol. 2001, pp. 227–235, Jan. 2001.

[199] M. Seefelder, M. Heubes, H. Quast, W. D. Edwards, J. R. Armantrout, R. V. Williams, C. J. Cramer, A. C. Goren, D. A. Hrovat, and W. T. Borden, "Experimental and theoretical study of stabilization of delocalized forms of semibullvalenes and barbaralanes by dipolar and polarizable solvents. Observation of a delocalized structure that is lower in free energy than the localized form," *J. Org. Chem.*, vol. 70, pp. 3437–3449, Apr. 2005.

[200] R. V. Williams, A. G. Al-Sehemi, A. K. Meier, Z. Z. Brown, and J. R. Armantrout, "The role of strain in the homoaromatization of semibullvalenes," *J. Org. Chem.*, vol. 82, pp. 4136–4147, Apr. 2017.

[201] C. J. Laconsay and D. J. Tantillo, "Modulating escape channels of cycloheptatrienyl rhodium carbenes to form semibullvalene," *J. Org. Chem.*, vol. 88, pp. 9056–9065, July 2023.

[202] Y. J. Hong and D. J. Tantillo, "Viability of nonclassical carbocations proposed as intermediates in the biosynthesis of atiserene, beyerene, kaurene, and trachylobane diterpenes," *Helv. Chim. Acta*, vol. 97, pp. 1475–1480, Nov. 2014.

[203] M. Castiñeira Reis, C. S. López, O. Nieto Faza, and D. J. Tantillo, "Pushing the limits of concertedness. A waltz of wandering carbocations," *Chem. Sci.*, vol. 10, pp. 2159–2170, Feb. 2019.

[204] R. Properzi, P. S. J. Kaib, M. Leutzsch, G. Pupo, R. Mitra, C. K. De, L. Song, P. R. Schreiner, and B. List, "Catalytic enantiocontrol over a non-classical carbocation," *Nat. Chem.*, vol. 12, pp. 1174–1179, Dec. 2020.

[205] P. Ahlberg, D. L. Harris, and S. Winstein, "1-methylbicyclo[4.3.0]nonatrienyl cation. a 1,4-bishomotropylium ion," *J. Am. Chem. Soc.*, vol. 92, pp. 2146–2147, Apr. 1970.

[206] R. S. Mulliken, C. A. Rieke, and W. G. Brown, "Hyperconjugation*," *J. Am. Chem. Soc.*, vol. 63, pp. 41–56, Jan. 1941.

[207] I. V. Alabugin, G. dos Passos Gomes, and M. A. Abdo, "Hyperconjugation," *WIREs Comput. Mol. Sci.*, vol. 9, p. e1389, Mar. 2019.

[208] R. Hoffmann, "Interaction of orbitals through space and through bonds," *Acc. Chem. Res.*, vol. 4, pp. 1–9, Jan. 1971.

[209] H. Jiao, P. v. R. Schleyer, and M. N. Glukhovtsev, "Are the $d_{mh}$ symmetric Hxq rings with 4n+2 $\sigma$-electrons and hydrogen clusters aromatic?," *The Journal of Physical Chemistry*, vol. 100, no. 30, pp. 12299–12304, 1996.

[210] G. Merino, M. Solà, I. Fernández, C. Foroutan-Nejad, P. Lazzeretti, G. Frenking, H. L. Anderson, D. Sundholm, F. P. Cossío, M. A. Petrukhina, J. Wu, J. I. Wu, and A. Restrepo, "Aromaticity: Quo vadis," *Chem. Sci.*, vol. 14, no. 21, pp. 5569–5576, 2023.

[211] R. Hoffmann, "The many guises of aromaticity," *Am. Sci*, vol. 103, no. 18.10, p. 1511, 2015.

[212] W. J. Hehre, "Theoretical approaches to rearrangements in carbocations. II. Degenerate rearrangements in bicyclo[3.1.0]hexenyl and homotropylium cations. Stability of homoaromatic molecules," *J. Am. Chem. Soc.*, vol. 96, pp. 5207–5217, Aug. 1974.

[213] D. J. Tantillo, "Speeding up sigmatropic shifts: To halve or to hold," *Acc. Chem. Res.*, vol. 49, no. 4, pp. 741–749, 2016.

[214] W. T. Borden, R. J. Loncharich, and K. N. Houk, "Synchronicity in multibond reactions," *Annu. Rev. Phys. Chem.*, vol. 39, pp. 213–236, Jan. 1988.

[215] D. J. Tantillo, "Recent excursions to the borderlands between the realms of concerted and stepwise: carbocation cascades in natural products biosynthesis," *J. Phys. Org. Chem.*, vol. 21, pp. 561–570, July 2008.

[216] Y.-Y. Ma, M. Yan, H.-R. Li, Y.-B. Wu, X.-X. Tian, H.-G. Lu, and S.-D. Li, "Probing the fluxional bonding nature of rapid cope rearrangements in bullvalene C10H10 and its analogs C8H8, C9H10, and C8BH9," *Sci. Rep.*, vol. 9, p. 17074, Nov. 2019.

[217] R. Wodraszka and U. Manthe, "CH+5: Symmetry and the entangled rovibrational quantum states of a fluxional molecule," *J. Phys. Chem. Lett.*, vol. 6, pp. 4229–4232, Nov. 2015.

[218] M. Sanz-Novo, M. Mato, Í. León, A. M. Echavarren, and J. L. Alonso, "Shape-shifting molecules: Unveiling the valence tautomerism phenomena in bare barbaralones," *Angew. Chem. Int. Ed Engl.*, vol. 61, p. e202117045, Apr. 2022.

[219] B. K. Carpenter, "Nonstatistical dynamics in thermal reactions of polyatomic molecules," *Annu. Rev. Phys. Chem.*, vol. 56, no. 1, pp. 57–89, 2005.

[220] R. Hoffmann, S. Swaminathan, B. G. Odell, and R. Gleiter, "Potential surface for a nonconcerted reaction. Tetramethylene," *J. Am. Chem. Soc.*, vol. 92, pp. 7091–7097, Dec. 1970.

[221] W. v. E. Doering, J. L. Ekmanis, K. D. Belfield, F.-G. Klärner, and B. Krawczyk, "Thermal reactions of anti- and syn-dispiro[5.0.5.2]tetradeca-1,8-dienes: Stereomutation and fragmentation to 3-methylenecyclohexenes. Entropy-dictated product ratios from diradical intermediates?," *J. Am. Chem. Soc.*, vol. 123, pp. 5532–5541, June 2001.

[222] C. Doubleday, "Unusual potential energy surfaces and nonstatistical dynamic effects," in *Applied Theoretical Organic Chemistry*, pp. 351–369, WORLD SCIENTIFIC (EUROPE), May 2018.

[223] D. H. Ess, S. E. Wheeler, R. G. Iafe, L. Xu, N. Celebi-Olçüm, and K. N. Houk, "Bifurcations on potential energy surfaces of organic reactions," *Angew. Chem. Int. Ed Engl.*, vol. 47, no. 40, pp. 7592–7601, 2008.

[224] J. Rehbein and B. Wulff, "Chemistry in motion—off the MEP," *Tetrahedron Lett.*, vol. 56, pp. 6931–6943, Dec. 2015.

[225] D. J. Tantillo, "Beyond transition state theory–Non-statistical dynamic effects for organic reactions," in *Advances in Physical Organic Chemistry*, Advances in physical organic chemistry, pp. 1–16, Elsevier, 2021.

[226] D. Tantillo, "Wiggling and jiggling: As chemists incorporate molecular vibrations into their study of reactions, they are learning that many pathways are entangled," *American Scientist*, vol. 107, no. 1, pp. 22–26, 2019.

[227] D. Townsend, S. A. Lahankar, S. K. Lee, S. D. Chambreau, A. G. Suits, X. Zhang, J. Rheinecker, L. B. Harding, and J. M. Bowman, "The roaming atom: straying from the reaction path in formaldehyde decomposition," *Science*, vol. 306, pp. 1158–1161, Nov. 2004.

[228] M. Saunders and H. A. Jimenez-Vazquez, "Recent studies of carbocations," *Chem. Rev.*, vol. 91, pp. 375–397, May 1991.

[229] P. R. Schreiner, "Quantum mechanical tunneling is essential to understanding chemical reactivity," *Trends in Chemistry*, vol. 2, no. 11, pp. 980–989, 2020.

[230] S. Kozuch, A. Karton, S. Jalife, and G. Merino, "Fluxionality by quantum tunnelling: nonclassical 21-homododecahedryl cation rearrangement re-revisited," *Chemical Communications*, vol. 57, pp. 10735–10738, Oct. 2021.

[231] S. Kozuch, "On the tunneling instability of a hypercoordinated carbocation," *Phys. Chem. Chem. Phys.*, vol. 17, pp. 16688–16691, July 2015.

[232] J. C. Barborak, J. Daub, D. M. Follweiler, and P. v. R. Schleyer, "Degenerate rearrangements of the 9-barbaralyl cation," *J. Am. Chem. Soc.*, vol. 91, pp. 7760–7761, Dec. 1969.

[233] P. Ahlberg, C. Engdahl, and G. Jonsaell, "The 9-barbaralyl cation. isotopic perturbation by eight deuteriums of a totally degenerate carbon-13-labeled C9H9+ carbonium ion," *J. Am. Chem. Soc.*, vol. 103, pp. 1583–1584, Mar. 1981.

[234] C. Engdahl, G. Jonsaell, and P. Ahlberg, "The totally degenerate (CH)9+ ion 9-barbaralyl cation studied by carbon-13 labeling and isotopic perturbation by eight deuteriums," *J. Am. Chem. Soc.*, vol. 105, pp. 891–897, Feb. 1983.

[235] D. Ajami, O. Oeckler, A. Simon, and R. Herges, "Synthesis of a möbius aromatic hydrocarbon," *Nature*, vol. 426, pp. 819–821, Dec. 2003.

[236] G. Schröder, "Preparation and properties of tricyclo[3,3,2,$0^{4,6}$]deca-2,7,9-triene (bullvalene)," *Angew. Chem., Int. Ed. Engl.*, vol. 2, pp. 481–482, Aug. 1963.

[237] D. Cremer, P. Svensson, E. Kraka, and P. Ahlberg, "Exploration of the potential energy surface of C9H9+ by ab initio methods. 1. the barbaralyl cation," *J. Am. Chem. Soc.*, vol. 115, pp. 7445–7456, Aug. 1993.

[238] J. Bella, J. M. Poblet, A. Demoulliens, and F. Volatron, "A new MINDO/3 study of rearrangements in barbaralyl cations," *J. Chem. Soc., Perkin Trans. 2*, pp. 37–42, Jan. 1989.

[239] N. H. Werstiuk, "The 9-barbaralyl and related C9H9+ carbocations — a QTAIM-DI-VISAB computational study," *Can. J. Chem.*, vol. 88, pp. 1195–1204, Nov. 2010.

[240] P. E. Larsson and J. Linderberg, "Topology and least motion," *Theoret. Chim. Acta*, vol. 93, pp. 79–85, Feb. 1996.

[241] A. Karton, "Shapeshifting radicals," *Chem. Phys.*, vol. 552, p. 111373, Jan. 2022.

[242] A. Sanchez, A. Gurajapu, W. Guo, W.-Y. Kong, C. J. Laconsay, N. S. Settineri, D. J. Tantillo, and T. J. Maimone, "A shapeshifting roadmap for polycyclic skeletal evolution," *J. Am. Chem. Soc.*, vol. 145, pp. 13452–13461, June 2023.

[243] M. V. Makarova and S. G. Semenov, "Quantum-chemical study of barbaralone in singlet and triplet states," *Russ. J. Gen. Chem.*, vol. 85, pp. 589–594, Mar. 2015.

[244] D. J. Tantillo, "Dynamic effects on organic reactivity—pathways to (and from) discomfort," *J. Phys. Org. Chem.*, vol. 34, p. e4202, June 2021.

[245] D. A. Singleton, C. Hang, M. J. Szymanski, and E. E. Greenwald, "A new form of kinetic isotope effect. Dynamic effects on isotopic selectivity and regioselectivity," *J. Am. Chem. Soc.*, vol. 125, pp. 1176–1177, Feb. 2003.

[246] G. Rasul, G. K. Surya Prakash, and G. A. Olah, "Comparative study of the hypercoordinate carbonium ions and their boron analogs: A challenge for spectroscopists," *Chem. Phys. Lett.*, vol. 517, pp. 1–8, Nov. 2011.

[247] D. A. Hrovat, E. C. Brown, R. V. Williams, H. Quast, and W. T. Borden, "How important is bishomoaromatic stabilization in determining the relative barrier heights for the degenerate cope rearrangements of semibullvalene, barbaralane, bullvalene, and dihydrobullvalene?," *J. Org. Chem.*, vol. 70, pp. 2627–2632, Apr. 2005.

[248] M. L. McKee, "Fluctional molecules: Fluctional molecules," *WIREs Comput. Mol. Sci.*, vol. 1, pp. 943–951, Nov. 2011.

[249] Y. Wang, P. Verma, X. Jin, D. G. Truhlar, and X. He, "Revised M06 density functional for main-group and transition-metal chemistry," *Proc. Natl. Acad. Sci. U. S. A.*, vol. 115, pp. 10257–10262, Oct. 2018.

[250] H. Sato, B.-X. Li, T. Takagi, C. Wang, K. Miyamoto, and M. Uchiyama, "DFT study on the biosynthesis of verrucosane diterpenoids and mangicol sesterterpenoids: Involvement of secondary-carbocation-free reaction cascades," *JACS Au*, vol. 1, pp. 1231–1239, Aug. 2021.

[251] H. Sato, T. Hashishin, J. Kanazawa, K. Miyamoto, and M. Uchiyama, "DFT study of a missing piece in brasilane-type structure biosynthesis: An unusual skeletal rearrangement," *J. Am. Chem. Soc.*, vol. 142, pp. 19830–19834, Nov. 2020.

[252] X. Tang, F. Zhang, T. Zeng, W. Li, S. Yin, and R. Wu, "Enzymatic plasticity inspired by the diterpene cyclase CotB2," *ACS Chem. Biol.*, vol. 15, pp. 2820–2832, Oct. 2020.

[253] D. T. Major, "Electrostatic control of chemistry in terpene cyclases," *ACS Catal.*, vol. 7, pp. 5461–5465, Aug. 2017.

[254] N. Tarannam, P. K. Gupta, S. Zev, and D. T. Major, "Stability trends in carbocation intermediates stemming from germacrene a and hedycaryol," *Beilstein J. Org. Chem.*, vol. 20, pp. 1189–1197, May 2024.

[255] C. Riplinger and F. Neese, "An efficient and near linear scaling pair natural orbital based local coupled cluster method," *J. Chem. Phys.*, vol. 138, p. 034106, Jan. 2013.

[256] C. Riplinger, B. Sandhoefer, A. Hansen, and F. Neese, "Natural triple excitations in local coupled cluster calculations with pair natural orbitals," *J. Chem. Phys.*, vol. 139, p. 134101, Oct. 2013.

[257] F. Neese, "Software update: The ORCA program system—version 5.0," *WIREs Comput. Mol. Sci.*, vol. 12, p. e1606, Sept. 2022.

[258] F. Neese and E. F. Valeev, "Revisiting the atomic natural orbital approach for basis sets: Robust systematic basis sets for explicitly correlated and conventional correlated ab initio methods?," *J. Chem. Theory Comput.*, vol. 7, pp. 33–43, Jan. 2011.

[259] S. Zhong, E. C. Barnes, and G. A. Petersson, "Uniformly convergent n-tuple-zeta augmented polarized (nZaP) basis sets for complete basis set extrapolations. I. Self-consistent field energies," *J. Chem. Phys.*, vol. 129, p. 184116, Nov. 2008.

[260] Y. Guo, C. Riplinger, U. Becker, D. G. Liakos, Y. Minenkov, L. Cavallo, and F. Neese, "Communication: An improved linear scaling perturbative triples correction for the domain based local pair-natural orbital based singles and doubles coupled cluster method [DLPNO-CCSD(T)]," *J. Chem. Phys.*, vol. 148, p. 011101, Jan. 2018.

[261] G. Luchini, J. V. Alegre-Requena, I. Funes-Ardoiz, and R. S. Paton, "GoodVibes: automated thermochemistry for heterogeneous computational chemistry data," *F1000Res.*, vol. 9, p. 291, Apr. 2020.

[262] T. Yanai, D. P. Tew, and N. C. Handy, "A new hybrid exchange–correlation functional using the Coulomb-attenuating method (CAM-B3LYP)," *Chem. Phys. Lett.*, vol. 393, pp. 51–57, July 2004.

[263] P. C. Hariharan and J. A. Pople, "The influence of polarization functions on molecular orbital hydrogenation energies," *Theor. Chim. Acta*, vol. 28, pp. 213–222, Sept. 1973.

[264] W. J. Hehre, R. Ditchfield, and J. A. Pople, "Self—consistent molecular orbital methods. XII. further extensions of Gaussian—type basis sets for use in molecular orbital studies of organic molecules," *J. Chem. Phys.*, vol. 56, pp. 2257–2261, Mar. 1972.

[265] C. Gonzalez and H. B. Schlegel, "Reaction path following in mass-weighted internal coordinates," *J. Phys. Chem.*, vol. 94, pp. 5523–5527, July 1990.

[266] A. Barducci, G. Bussi, and M. Parrinello, "Well-tempered metadynamics: a smoothly converging and tunable free-energy method," *Phys. Rev. Lett.*, vol. 100, p. 020603, Jan. 2008.

[267] M. T. de Oliveira, J. M. A. Alves, A. A. C. Braga, D. J. D. Wilson, and C. A. Barboza, "Do double-hybrid exchange–correlation functionals provide accurate chemical shifts? a benchmark assessment for proton NMR," *J. Chem. Theory Comput.*, vol. 17, pp. 6876–6885, Nov. 2021.

[268] J. P. Perdew, A. Ruzsinszky, G. I. Csonka, L. A. Constantin, and J. Sun, "Workhorse semilocal density functional for condensed matter physics and quantum chemistry," *Phys. Rev. Lett.*, vol. 103, p. 026403, July 2009.

[269] F. Jensen, "Segmented contracted basis sets optimized for nuclear magnetic shielding," *J. Chem. Theory Comput.*, vol. 11, pp. 132–138, Jan. 2015.

[270] W.-P. Hu, Y.-P. Liu, and D. G. Truhlar, "Variational transition-state theory and semiclassical tunnelling calculations with interpolated corrections: A new approach to interfacing electronic structure theory and dynamics for organic reactions," *Journal of the Chemical Society, Faraday Transactions*, vol. 90, no. 12, pp. 1715–1725, 1994.

[271] P. R. Schreiner, P. v. R. Schleyer, and H. F. Schaefer, 3rd, "Why the classical and nonclassical norbornyl cations do not resemble the 2-endo- and 2-exo-norbornyl solvolysis transition states," *J. Org. Chem.*, vol. 62, pp. 4216–4228, June 1997.

[272] C. J. Collins, "Nonclassical ions. reprints and commentary," *J. Am. Chem. Soc.*, vol. 88, pp. 4117–4118, Sept. 1966.

[273] B. P. Coppola, "Deeper beneath the surface of the chemical article: Richard g. lawton and the norbornyl cation problem," *Chemical Intelligencer*, vol. 4, no. 2, pp. 40–49, 1998.

[274] G. A. Olah, G. K. Surya Prakash, and M. Saunders, "Conclusion of the classical non-classical ion controversy based on the structural study of the 2-norbornyl cation," *Acc. Chem. Res.*, vol. 16, no. 12, pp. 440–448, 1983.

[275] G. A. Olah, V. P. Reddy, and G. K. S. Prakash, "Long-lived cyclopropylcarbinyl cations," *Chem. Rev.*, vol. 92, pp. 69–95, Jan. 1992.

[276] D. J. Tantillo, "Portable models for entropy effects on kinetic selectivity," *J. Am. Chem. Soc.*, vol. 144, pp. 13996–14004, Aug. 2022.

[277] W. Guo, E. E. Robinson, R. J. Thomson, and D. J. Tantillo, "Heavy atom quantum mechanical tunneling in total synthesis," *Org. Lett.*, vol. 26, pp. 4606–4609, June 2024.

[278] T. A. Hamlin, C. S. Hamann, and D. J. Tantillo, "Delocalization of charge and electron density in the humulyl cation - implications for terpene biosynthesis," *J. Org. Chem.*, vol. 80, pp. 4046–4053, 2015.

[279] C. Doubleday, R. Armas, D. Walker, C. V. Cosgriff, and E. M. Greer, "Heavy-atom tunneling calculations in thirteen organic reactions: Tunneling contributions are substantial, and Bell's formula closely approximates multidimensional tunneling at 250 K," *Angewandte Chemie*, vol. 129, no. 42, pp. 13279–13282, 2017.

[280] C. Castro and W. L. Karney, "Heavy-atom tunneling in organic reactions," *Angewandte Chemie*, vol. 132, no. 22, pp. 8431–8442, 2020.

[281] M. J. Vetticatt and D. A. Singleton, "Isotope effects and heavy-atom tunneling in the roush allylboration of aldehydes," *Organic letters*, vol. 14, no. 9, pp. 2370–2373, 2012.

[282] K. W. Quasdorf, A. D. Huters, M. W. Lodewyk, D. J. Tantillo, and N. K. Garg, "Total synthesis of oxidized welwitindolinones and (-)-N-methylwelwitindolinone C isonitrile," *Journal of the American Chemical Society*, vol. 134, no. 3, pp. 1396–1399, 2012.

[283] Y. Kanda, H. Nakamura, S. Umemiya, R. K. Puthukanoori, V. R. Murthy Appala, G. K. Gaddamanugu, B. R. Paraselli, and P. S. Baran, "Two-phase synthesis of taxol," *Journal of the American Chemical Society*, vol. 142, no. 23, pp. 10526–10533, 2020.

[284] M. Goldstein, "Kinetic isotope effects and organic reaction mechanisms: A fruitful application of quantum theory to organic chemistry has now been strengthened.," *Science*, vol. 154, no. 3757, pp. 1616–1621, 1966.

[285] E. M. Greer, K. Kwon, A. Greer, and C. Doubleday, "Thermally activated tunneling in organic reactions," *Tetrahedron*, vol. 72, no. 47, pp. 7357–7373, 2016.

[286] D. J. Tantillo, "Tunnel vision: In outer space and within living cells, quantum mechanics allows molecules to take mind-bending journeys that would be impossible by the rules of classical physics.," *American Scientist*, vol. 109, no. 5, pp. 274–278, 2021.

[287] E. E. Robinson and R. J. Thomson, "A strategy for the convergent and stereoselective assembly of polycyclic molecules," *Journal of the American Chemical Society*, vol. 140, no. 5, pp. 1956–1965, 2018.

[288] M. J. Huang and M. Wolfsberg, "Tunneling in the automerization of cyclobutadiene," *Journal of the American Chemical Society*, vol. 106, no. 14, pp. 4039–4040, 1984.

[289] T. Schleif, J. Tatchen, J. F. Rowen, F. Beyer, E. Sanchez-Garcia, and W. Sander, "Heavy-atom tunneling in semibullvalenes: How driving force, substituents, and environment influence the tunneling rates," *Chemistry–A European Journal*, vol. 26, no. 46, pp. 10452–10458, 2020.

[290] O. M. Gonzalez-James, X. Zhang, A. Datta, D. A. Hrovat, W. T. Borden, and D. A. Singleton, "Experimental evidence for heavy-atom tunneling in the ring-opening of cyclopropylcarbinyl radical

from intramolecular $^{12}c/^{13}c$ kinetic isotope effects," *Journal of the American Chemical Society*, vol. 132, no. 36, pp. 12548–12549, 2010.

[291] B. Xu, C. Liu, and M. Dai, "Catalysis-enabled 13-step total synthesis of (-)-peyssonnoside a," *Journal of the American Chemical Society*, vol. 144, no. 43, pp. 19700–19703, 2022.

[292] P. Pracht, F. Bohle, and S. Grimme, "Automated exploration of the low-energy chemical space with fast quantum chemical methods," *Physical Chemistry Chemical Physics*, vol. 22, no. 14, pp. 7169–7192, 2020.

[293] C. Adamo and V. Barone, "Exchange functionals with improved long-range behavior and adiabatic connection methods without adjustable parameters: The mPW and mPW1PW models," *The Journal of chemical physics*, vol. 108, no. 2, pp. 664–675, 1998.

[294] C. Adamo and V. Barone, "Toward reliable density functional methods without adjustable parameters: The PBE0 model," *The Journal of chemical physics*, vol. 110, no. 13, pp. 6158–6170, 1999.

[295] J.-D. Chai and M. Head-Gordon, "Long-range corrected hybrid density functionals with damped atom–atom dispersion corrections," *Physical Chemistry Chemical Physics*, vol. 10, no. 44, pp. 6615–6620, 2008.

[296] J. Du, L. R. Espelt, I. A. Guzei, and T. P. Yoon, "Photocatalytic reductive cyclizations of enones: Divergent reactivity of photogenerated radical and radical anion intermediates," *Chemical Science*, vol. 2, no. 11, pp. 2115–2119, 2011.

[297] E. M. Greer, V. Siev, A. Segal, A. Greer, and C. Doubleday, "Computational evidence for tunneling and a hidden intermediate in the biosynthesis of tetrahydrocannabinol," *Journal of the American Chemical Society*, vol. 144, no. 17, pp. 7646–7656, 2022.